

Summer 2024

Coherent Backscattering Under Conditions of Electromagnetically Induced Transparency in Ultracold Rubidium

Joshua D. Carter
Old Dominion University, joshcarter067@gmail.com

Follow this and additional works at: https://digitalcommons.odu.edu/physics_etds



Part of the [Atomic, Molecular and Optical Physics Commons](#), [Optics Commons](#), and the [Quantum Physics Commons](#)

Recommended Citation

Carter, Joshua D.. "Coherent Backscattering Under Conditions of Electromagnetically Induced Transparency in Ultracold Rubidium" (2024). Doctor of Philosophy (PhD), Dissertation, Physics, Old Dominion University, DOI: 10.25777/etdj-3f77
https://digitalcommons.odu.edu/physics_etds/210

This Dissertation is brought to you for free and open access by the Physics at ODU Digital Commons. It has been accepted for inclusion in Physics Theses & Dissertations by an authorized administrator of ODU Digital Commons. For more information, please contact digitalcommons@odu.edu.

COHERENT BACKSCATTERING UNDER CONDITIONS OF
ELECTROMAGNETICALLY INDUCED TRANSPARENCY IN
ULTRACOLD RUBIDIUM

by

Joshua D. Carter
B.S. August 2016, Old Dominion University
M.S. May 2018, Old Dominion University

A Dissertation Submitted to the Faculty of
Old Dominion University in Partial Fulfillment of the
Requirements for the Degree of

DOCTOR OF PHILOSOPHY

PHYSICS

OLD DOMINION UNIVERSITY
August 2024

Approved by:

Charles Sukenik (Director)

Peter Bernath (Member)

Stephen Bueltmann (Member)

Ted Rogers (Member)

Richard Zimmerman (Member)

ABSTRACT

COHERENT BACKSCATTERING UNDER CONDITIONS OF ELECTROMAGNETICALLY INDUCED TRANSPARENCY IN ULTRACOLD RUBIDIUM

Joshua D. Carter
Old Dominion University, 2024
Director: Dr. Charles Sukenik

This dissertation presents experimental results of coherent backscattering of light in an ultracold ensemble of rubidium atoms confined in a magneto optical trap under conditions of electromagnetically induced transparency (EIT) in a cascade-type system. Electromagnetically induced transparency was investigated experimentally in both a counterpropagating and orthogonal laser geometry and compared to theory. The experimental results were largely in good agreement with theory. Coherent backscattering was then measured with and without an EIT control field present to investigate the modification, if any, that EIT has on the enhancement of the coherent backscattering cone. The results indicated that the electromagnetically induced transparency reduced incoherent and coherent scattering differently, with a greater reduction in the coherent scattering processes.

Copyright, 2024, by Joshua D. Carter, All Rights Reserved.

This dissertation is dedicated to my dad, along with the others lost along the way.

ACKNOWLEDGMENTS

I would like to give great thanks to Dr. Sukenik for stepping up and taking on both Brent and me after Dr. Havey's unfortunate passing and for being a top-of-the-line advisor over the years in all possible ways, while also providing plenty of comic relief as well. I was truly lucky to be taken in by Dr. Sukenik. I am eternally grateful for Dr. Havey providing me with the opportunity to join the physics Ph.D. program, almost on a whim, and for being a great advisor in the time that we shared. Thanks also to Dima Kupriyanov for insight on theoretical aspects of the project. Many thanks go out to those in the physics department as well that provided assistance over the years (Justin, Lisa, Annette, Delicia, Tom H., and everyone else), whether that be help with administrative issues, lab equipment, etc. I am also grateful for all of the graduate student friends I've come to know over the years, previous and current. They provided invaluable knowledge, advice, insight, and anything else an inexperienced graduate student could need. The ODU physics department, students and faculty, treated me well and I will be forever thankful. I'd also like to express my gratitude to my committee members for taking me on and being flexible and communicative.

I would also like to thank my friend and coworker, Brent Jones, for all of the ridiculousness and help along the way, could not have gotten here and made it through this journey without the endless help with Mathematica code and so on.

Last, but certainly not least, I would like to thank my friends and family for their patience with me over this arduous journey. I could not have come this far in life without them, their insight, and their guidance.

TABLE OF CONTENTS

	Page
LIST OF TABLES	vii
LIST OF FIGURES.....	viii
Chapter	
1. INTRODUCTION.....	1
1.1 ELECTROMAGNETICALLY INDUCED TRANSPARENCY.....	1
1.2 COHERENT BACKSCATTERING	3
2. THEORY AND BACKGROUND.....	6
2.1 TWO LEVEL ATOM	6
2.2 ELECTROMAGNETICALLY INDUCED TRANSPARENCY.....	10
2.3 COHERENT BACKSCATTERING OVERVIEW	16
3. EXPERIMENTAL OVERVIEW	30
3.1 LASER ARRANGEMENT	30
3.2 ELECTROMAGNETICALLY INDUCED TRANSPARENCY DATA AC- QUISITION	37
3.3 COHERENT BACKSCATTERING DATA ACQUISITION	38
4. ELECTROMAGNETICALLY INDUCED TRANSPARENCY.....	47
4.1 EXPERIMENTAL EIT RESULTS.....	47
4.2 NUMERICAL EIT RESULTS.....	69
4.3 EXPERIMENTAL AND NUMERICAL RESULTS COMPARISON	80
5. COHERENT BACKSCATTERING EXPERIMENTAL RESULTS.....	95
5.1 ATOMIC CBS WITHOUT EIT	96
5.2 CBS WITH EIT	102
6. CONCLUSIONS.....	128
BIBLIOGRAPHY	130
APPENDICES	
A. OTHER OPTICAL BLOCH NUMERICAL SOLUTIONS	136
B. OPTICAL DIAGRAM LEGEND.....	138
VITA	139

LIST OF TABLES

Table	Page
1. Atomic transition properties	32
2. Experimental polarization channel description	42
3. Corresponding values and intensity for each detection channel.....	44
4. Enhancement and CBS cone FWHM for the three measured control polarizations at $\Omega_c = 0.91\Gamma_p$	125

LIST OF FIGURES

Figure	Page
1. Three level EIT configurations	3
2. One of many multiply scattered paths possible for a wave incident on a scattering medium with k_i , k_e representing the incoming and emitted wave directions	4
3. Three level EIT in weak probe regime ($\Omega_{12} = 0.01\Gamma_{12}$) with control detuning $\Delta_{23} = 0$	15
4. Three level EIT in weak probe regime ($\Omega_{12} = 0.01\Gamma_{12}$) with control detuning $\Delta_{23} = \Gamma_{12}$	16
5. Contributions to the total complex amplitude $f(\mathbf{r}_1, \mathbf{r}_2)$	18
6. Scattering paths of classical average intensity and coherent backscattering	19
7. Scattering path of the Diffuson.....	22
8. Diffuson albedo α_D as a function of angle	23
9. Scattering paths of the Cooperon contribution to the total albedo.....	24
10. The Cooperon albedo added to Diffuson albedo as a function of angle.....	25
11. Rubidium 85 and 87 hyperfine energy splittings for the $5S_{1/2}$, $5P_{3/2}$, and $5D_{5/2}$ states.....	31
12. Rubidium 85 levels of experiment associated with this experiment	32
13. 780 nm laser optics	34
14. 776 nm laser optics	35
15. Experimental table layout	36
16. Sample signals observed during the EIT experiment	37
17. Photo of LN CCD	39
18. Coherent backscattering optical layout	40
19. A sample image from a ray diagram Mathematica program used to determine angular resolution	41
20. General geometry of light detection with Euler angles ϕ , θ , and χ	43

Figure	Page
21. Graphical representation of polarized light emission as function of angle.....	45
22. Experimental timing diagram	46
23. All data represented as a function of probe detuning with σ_- probe polarization and horizontal π control polarization in the counterpropagating EIT geometry	48
24. Counterpropagating EIT control intensity dependence	49
25. Counterpropagating EIT at various polarizations	51
26. Counterpropagating EIT polarization dependence	52
27. Counterpropagating EIT at various control detunings.....	53
28. Counterpropagating EIT at various control detunings comparison	54
29. Counterpropagating EIT at various probe Rabi frequencies	56
30. Counterpropagating EIT probe intensity dependence in terms of probe Rabi fre- quency	57
31. Orthogonal EIT at various control Rabi frequencies	59
32. Orthogonal EIT control intensity dependence in terms of Rabi frequency.....	60
33. Orthogonal EIT at various probe and control polarizations.....	62
34. Orthogonal EIT polarization dependence.....	63
35. Orthogonal EIT at various control detunings	64
36. Orthogonal EIT at various control detunings comparison	65
37. Orthogonal EIT at various probe Rabi frequencies	66
38. Orthogonal EIT probe intensity dependence in terms of Rabi frequency	67
39. Comparison of optimized alignment vs unoptimized alignment	68
40. Energy level description of numerical simulation of optical Bloch equations.....	69
41. Numerical solutions of the OBE simulated probe absorption channel with $\Delta_c = 0$ MHz and $\Omega_p = 0.18\Gamma_p$ at various control field Rabi frequencies.....	71

Figure	Page
42. Numerical solutions of the OBE simulated $6P_{3/2}$ state fluorescence with $\Delta_c = 0$ MHz at various control field Rabi frequencies	72
43. Numerical solutions of the OBE simulated probe channel with $\Delta_c = 9.5$ MHz and $\Omega_p = 0.18\Gamma_p$ at various control field Rabi frequencies	73
44. Numerical solutions of the OBE simulated $6P_{3/2}$ state fluorescence with $\Delta_c = 9.5$ MHz and $\Omega_p = 0.18\Gamma_p$ at various control field Rabi frequencies.....	74
45. Numerical solutions of the OBE simulated probe channel with $\Delta_c = 18.5$ MHz and $\Omega_p = 0.18\Gamma_p$ at various control field Rabi frequencies	75
46. Numerical solutions of the OBE simulated $6P_{3/2}$ state fluorescence with $\Delta_c = 18.5$ MHz and $\Omega_p = 0.18\Gamma_p$ at various control field Rabi frequencies.....	76
47. Numerical solutions of the OBE simulated probe absorption channel at various probe Rabi frequencies and $\Omega_c = 2.22\Gamma_p$ with $\Delta_c = 0$	78
48. Numerical solutions of the OBE simulated $6P_{3/2}$ state fluorescence with control Rabi frequency $\Omega_c = 2.22\Gamma_p$ with control detuning $\Delta_c = 0$	79
49. Numerical solutions of the OBE simulated $6P_{3/2}$ state fluorescence as a function of probe detuning at various control detunings overlaid for comparison.....	80
50. Comparison of orthogonal EIT probe absorption data as a function of probe detuning to theory	82
51. Comparison of orthogonal EIT $6P_{3/2}$ fluorescence data as a function of probe detuning to theory	83
52. Comparison of orthogonal EIT probe absorption to theory as a function of probe detuning at multiple control detunings and control Rabi frequencies.....	84
53. Comparison of orthogonal EIT $6P_{3/2}$ fluorescence to theory as a function of probe detuning at multiple control detunings and control Rabi frequencies.....	85
54. Comparison of orthogonal EIT probe absorption to theory as a function of probe detuning at multiple probe intensities	86
55. Comparison of orthogonal EIT $6P_{3/2}$ fluorescence to theory as a function of probe detuning at multiple probe intensities	87
56. Comparison of counterpropagating EIT probe absorption data as a function of probe detuning to theory	88

Figure	Page
57. Comparison of counterpropagating EIT $6P_{3/2}$ fluorescence data as a function of probe detuning to theory	89
58. Comparison of counterpropagating EIT probe absorption to theory as a function of probe detuning at multiple control detunings and control Rabi frequencies	90
59. Comparison of counterpropagating EIT $6P_{3/2}$ fluorescence to theory as a function of probe detuning at multiple control detunings and control Rabi frequencies	91
60. Comparison of counterpropagating EIT probe absorption to theory as a function of probe detuning at multiple probe intensities displayed in terms of the Rabi frequency	92
61. Comparison of counterpropagating EIT $6P_{3/2}$ fluorescence to theory as a function of probe detuning at multiple probe intensities displayed in terms of the Rabi frequency	93
62. Coherent backscattering from atoms vs Styrofoam	96
63. Comparison of the four channels of coherent backscattering.....	97
64. CBS profile of the four standard polarization channels.....	98
65. CCD images and CBS profiles from the H_{\perp} channel probe detuning dependence.....	99
66. Data corresponding to the H_{\perp} channel with no control beam present	100
67. CCD images and CBS profiles from the L_{\parallel} channel probe detuning dependence with no control beam present.....	101
68. Data corresponding to the L_{\parallel} channel with no control beam present	102
69. Control beam intensity dependence of the H_{\perp} channel with control beam intensities in ascending order	103
70. CBS profiles corresponding to the images in Fig. 69 as CCD counts vs pixel.	104
71. Control power dependence of the H_{\perp} channel.....	104
72. CCD images and CBS profiles of vertically polarized control field intensity dependence of H_{\perp} channel.....	105
73. Control power dependence of the H_{\perp} channel with a vertically polarized control field.....	106
74. CCD images and CBS profiles of circularly polarized control field intensity dependence of H_{\perp} channel.....	107

Figure	Page
75. Control power dependence of the H_{\perp} channel with a circularly polarized control field	108
76. CCD images and CBS profiles of horizontally polarized control field intensity dependence of L_{\parallel} channel	109
77. Control power dependence of the L_{\parallel} channel with a horizontally polarized control field	110
78. CCD images and CBS profiles of horizontally polarized control field power dependence of L_{\perp} channel	111
79. Control power dependence of the L_{\perp} channel with a horizontally polarized control field	112
80. CCD images and CBS profiles from the H_{\perp} channel probe detuning dependence with $\Omega_c = 0.64\Gamma_p$ (0.5 mW) control beam present	113
81. H_{\perp} CBS channel with a $\Omega_c = 0.64\Gamma_p$ (0.5 mW) control beam present	114
82. CCD images and CBS profiles from the H_{\perp} CBS channel probe detuning dependence with $\Omega_c = 0.91\Gamma_p$ (1 mW) control beam present	115
83. H_{\perp} CBS channel with a $\Omega_c = 0.91\Gamma_p$ (1 mW) control beam present	116
84. CCD images and CBS profiles from the H_{\perp} channel probe detuning dependence with $\Omega_c = 1.28\Gamma_p$ (2 mW) control beam present	117
85. H_{\perp} CBS channel with a $\Omega_c = 1.28\Gamma_p$ (2 mW) control beam present	118
86. CCD images and CBS profiles from the H_{\perp} channel probe detuning dependence with $\Omega_c = 1.82\Gamma_p$ (4 mW) control beam present	119
87. H_{\perp} CBS channel with a $\Omega_c = 1.82\Gamma_p$ (4 mW) control beam present	120
88. CCD images and CBS profiles from the H_{\perp} channel probe detuning dependence with $\Omega_c = 0.91\Gamma_p$ vertically polarized control beam present	121
89. H_{\perp} CBS channel with a $\Omega_c = 0.91\Gamma_p$ vertically polarized beam present	122
90. CCD images and CBS profiles from the H_{\perp} channel probe detuning dependence with $\Omega_c = 0.91\Gamma_p$ circularly polarized control beam present	123
91. H_{\perp} CBS channel with a $\Omega_c = 0.91\Gamma_p$ circularly polarized beam present	124

Figure	Page
92. Control beam detuning dependence of H_{\perp} channel.....	126
93. Index of refraction as a function of probe detuning at various control Rabi frequencies with $\Delta_c = 0$	136
94. Numerical solution of probe absorption as a function of probe detuning at various probe intensities with $\Delta_c = 0$ and $\Omega_c = 2.22\Gamma_p$. Simulated fluorescence of the $6P_{3/2}$ state as a function of probe detuning at various probe intensities with $\Delta_c = 0$	137
95. Legend for optical diagrams used in this dissertation	138

CHAPTER 1

INTRODUCTION

In recent years, the study of light-matter interactions has led to a vast number of fields (and many more sub-fields) of research topics with the desire to further probe the nature of such interactions, and more importantly to control and alter interactions, especially at the quantum level. The manipulation of light interacting with a medium, whether that be a cold atomic gas, trapped ions, crystalline materials, or molecules, allows for a step closer to exotic concepts such as quantum computing and other quantum information sciences.

In this dissertation, we study light scattering in the cold atom regime with an emphasis on the quantum optical response of the system. More specifically, we look to use the quantum nature of the atoms in a cold atomic rubidium cloud to manipulate the amount of incoherent and coherent scattering processes that ultimately occur. To investigate this topic, we measure coherent backscattering under conditions of electromagnetically induced transparency.

1.1 ELECTROMAGNETICALLY INDUCED TRANSPARENCY

Electromagnetically induced transparency (EIT) is a method that modifies the transport of an electromagnetic wave through a medium by the mechanism of quantum interference. This technique utilizes a strong dressing field, commonly denoted as the control field, which alters absorption of a weak probe field within a medium. With its quantum nature and ability to manipulate light scattering in gases, EIT has been extensively studied [1–23] and continues to be studied and utilized for further applications such as slowed and stopped light, quantum memories, lasing without inversion, stabilization of atomic clocks, and a vast number of additional applications [24–35]. The conceptual basis of EIT can even be applied in nuclear systems [36]. The simplest implementation of EIT involves systems of three quantum states, first observed in the Λ -type scheme [37], but can be constructed in a V and Ξ (ladder) systems as well. Figure 1 shows each of the EIT schemes for three level systems.

Specifically focusing on EIT in rubidium, Olson *et al.* [38] studied ladder-type transparency in a room temperature rubidium gas cell and achieved 34% reduction in absorption with a low power coupling beam. Thaicharoen *et al.* [39] investigated the ladder system

in a rubidium vapor cell extending up to a Rydberg state beyond the $5D_{5/2}$, studying EIT and electromagnetically induced absorption (EIA) as a potential device for calibration of microwave frequency stabilization. Li *et al.* [40] demonstrated EIT in a three level Λ system with an absorption reduction of more than 85% in a vapor cell of ^{87}Rb on the D1 line. Nath *et al.* [41] investigated EIT and Autler-Townes splitting (ATS) in a rubidium vapor by utilizing a ladder-type scheme, experimentally discerning the two effects while also observing 420 nm fluorescence from the $6P_{3/2}$ state. In their description, they associate EIT with a strong coupling field between the $5P_{3/2}$ and $5D_{5/2}$, whereas ATS occurs with strong coupling between the ground and first excited state $5S_{1/2} \rightarrow 5P_{3/2}$.

Following more closely to the constraints of the experiment at hand, Yan *et al.* [42] demonstrated EIT in cold ^{87}Rb atoms in a Λ -type and ladder-type system on the D1 line. Their study showed complete transparency in the Λ -type system, while the ladder-type system does not achieve complete transparency due to strong field AC Stark effect, also known as Autler-Townes splitting. Their claim was also that destructive quantum interference occurs for the Λ -type system with constructive interference for the ladder-type system. The work done by Wang *et al.* [43] was performed in a ^{85}Rb MOT, studying EIT in a ladder configuration, measuring transparency from the $5P_{3/2}F = 3 \rightarrow 5D_{5/2}F = 4, 3, 2$ hyperfine transitions. In our EIT experiment, we expand upon the work done by Wang *et al.*, measuring probe absorption in a ladder type configuration instead on the $5P_{3/2}F = 4 \rightarrow 5D_{5/2}F = 5, 4, 3$ transitions, while simultaneously measuring fluorescence emitted at 420 nm from the $6P_{3/2}$ state. We measure the control intensity dependence, polarization dependence of probe and control, probe intensity dependence, and control detuning dependence in terms of probe absorption. In this study, we use a ladder-type EIT (Fig. 1(b)) configuration due to the constraints of the overarching goal of the research, that being the inclusion of coherent backscattering, described in the next section.

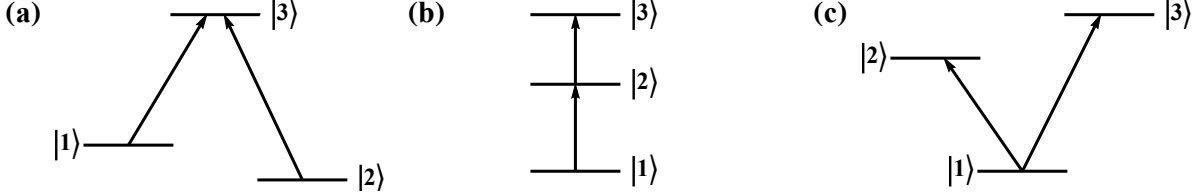


FIG. 1: (a) Three level representation of a Λ -type EIT configuration. (b) Three level representation of a ladder-type EIT configuration. (c) Three level representation of a V-type EIT configuration.

Among research topics in this area, there is ambiguity between EIT and ATS [44]. In the most general sense, EIT is a narrow window of transparency, due purely to destructive quantum interference competing between states. Autler-Townes splitting is attributed to the AC Stark effect, which is level splitting due to the presence of an electric field, resulting in a window of reduced absorption that increases in width with increasing electric field. The lack of absorption on “resonance” due to ATS gives rise to an effect similar to that of EIT, which is where much of the ambiguity arises. This is also the interpretation of Anisimov *et al.* [45, 46] and Finkelstein *et al.* [47] in their description of EIT and ATS. There has been a number of studies dedicated to characterizing the overlap and quantitatively discerning the behaviors of both effects, which rely on the particular state configuration [44–46, 48–57]. Furthermore, the ladder-type system (Fig. 1(b)) as used in this dissertation, can be broken into two regimes, depending on if the stronger coupling field is applied to the lower or upper transition, where our experimental configuration is the latter. The ladder-type system with strong coupling on the bottom transition and the V-scheme are predominantly or exclusively ATS, whereas the Λ -type and strong upper cascade-type system, as used in this experiment, are predominantly EIT [48], provided the control field is not too strong. Separating EIT from ATS is outside the scope of this investigation however, therefore when referring to EIT, we are attributing the transparency that is observed due to the combination of both effects.

1.2 COHERENT BACKSCATTERING

Similar to EIT, coherent backscattering (CBS) is also a well studied subject matter, especially considering at its core, coherent backscattering is a classical wave phenomena. It is predicted in physical media where wave propagation can occur, usually regarding light and

electron propagation, but also demonstrated with acoustic waves [58]. Coherent backscattering is attributed to time-reversed scattering paths constructively interfering, which will be explained in detail in Chapter 2. An example of an individual scattering path that a wave could take is shown in Fig. 2, where k_i represents incident wave direction and k_e is the emitted light direction.

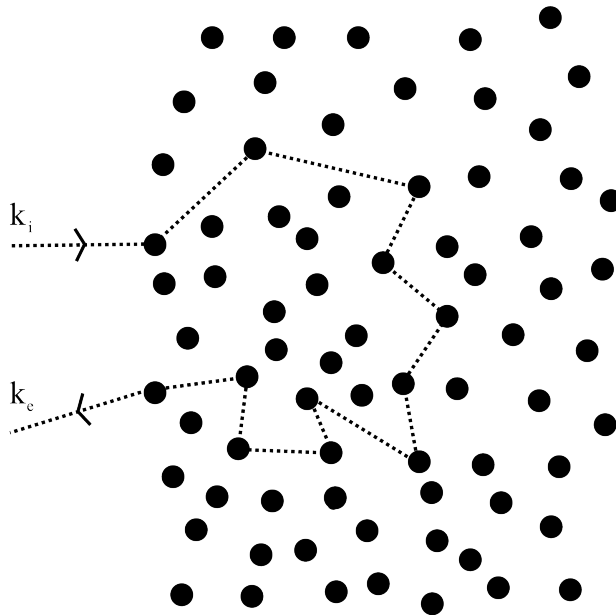


FIG. 2: One of many multiply scattered paths possible for a wave incident on a scattering medium with k_i , k_e representing the incoming and emitted wave directions.

Multiply scattered paths such as these are the fundamental mechanism of coherent effects such as CBS. Here the term “multiply scattered” refers to the incident wave scattering with more than one scatterer, for example an atom, before leaving the medium.

Due to the somewhat analogous behavior of coherent backscattering to Anderson localization and its potential application to control of quantum systems, interest has increased within the field of cold atom light scattering. Anderson localization refers to the strong localization of a field within a medium, i.e. a standing wave in a small localized zone, trapped due to strong disorder within the medium [59], or as Anderson states in his seminal paper: the absence of diffusion [60]. For light scattering, this would be radiation trapping of the highest

degree, which has not been achieved yet in three dimensions. However, coherent backscattering is referred to as the weak localization of light, which is a step closer to the elusive strong localization of light in three dimensions. Other applications of coherent backscattering include using it as a tool on biological tissue to avoid more destructive measurement processes [61], a measurement device of entangled photon pairs [62], and numerous other theoretical and experimental studies since its discovery [63–72]. The first observation of coherent backscattering in a cold rubidium gas was performed by Labeyrie *et al.* [73], along with further analysis in their work in Ref. [74], where they discuss the influence of sample and probe geometry on the CBS signals obtained and give some explanation to the small CBS signals obtained in cold atoms, as opposed to what is classically observed. Following on the work of Labeyrie *et al.*, Sigwarth *et al.* [75] determined a method of enhancing CBS signals by use of magnetic field, where strong fields can give rise to large enough Zeeman splitting to reduce degeneracy, creating an effective two-level system in the scattering atoms. Furthermore, the work by Wilkowski *et al.* [76] demonstrated that the CBS enhancement obtained in cold atoms depends on the atomic transition the probe is interacting with, along with further internal structure of the atom being studied.

Studies from our group began soon after the first observation of CBS in cold atoms [77–82]. Fundamental theoretical work associated with our group [83] has shown an expected reduction of coherent enhancement for CBS under the effect of EIT, which we look to investigate experimentally.

In this dissertation, the effect of ladder-type EIT on the coherent backscattering of cold rubidium 85 will be discussed primarily on the H_{\perp} channel. In reference to CBS, most texts refer to the observable polarization channels of CBS as $H_{\perp}H$, $H_{\parallel}H$, $L_{\perp}L$, and $L_{\parallel}L$, but we will not use that redundancy in this dissertation and simplify notation to H_{\perp} , H_{\parallel} , L_{\perp} , and L_{\parallel} . In this context, H refers to polarization of light with helicity, namely circular polarization (σ_{+} , σ_{-}), and L refers to linearly polarized light. Combining two expansive topics such as EIT and CBS allows for a nearly unlimited phase space of parameters to explore. With that being said, the focus of this research was reporting dependence of control field intensity, probe and control field detunings, and control and probe field polarizations and the effect of such parameters on coherently backscattered signals. Quantitatively, the effect of CBS will be described using the value of enhancement, which is the ratio of of total light scattered to incoherent background light scattered, which will be expanded upon in Chapter 2.

CHAPTER 2

THEORY AND BACKGROUND

2.1 TWO LEVEL ATOM

The following section follows closely to the quantum mechanical formulation of atoms interacting with classical radiation fields in [84–86]. Starting with the Schrödinger equation, we have

$$\hat{\mathcal{H}}\Psi(\mathbf{r}, t) = i\hbar\Psi(\mathbf{r}, t) , \quad (1)$$

where $\hat{\mathcal{H}}$ is the full quantum mechanical Hamiltonian and $\Psi(\mathbf{r}, t)$ is the wavefunction. The solution of the Schrödinger equation without the presence of external fields is the following:

$$\Psi_n(\mathbf{r}, t) = \psi_n(\mathbf{r})e^{-iE_n t/\hbar} . \quad (2)$$

Furthermore, substituting the solution into Eq. (1) results in the energy eigenvalue equation:

$$\hat{H}_0\psi_n(\mathbf{r}) = E_n\psi_n(\mathbf{r}) , \quad (3)$$

where $\hat{\mathcal{H}} = H_0$ in this case due to no external fields being present. Simplifying now to two atomic energy levels, we have

$$\Psi_1(\mathbf{r}, t) = \psi_1(\mathbf{r})e^{-iE_1 t/\hbar} \quad \text{and} \quad \Psi_2(\mathbf{r}, t) = \psi_2(\mathbf{r})e^{-iE_2 t/\hbar} , \quad (4)$$

where we define the energy separation

$$\hbar\omega_0 = E_2 - E_1 . \quad (5)$$

Now, introducing a light field, the Hamiltonian gains a time dependent interaction term \hat{H}_I , which modifies the full Hamiltonian into the form

$$\hat{\mathcal{H}} = \hat{H}_0 + \hat{H}_I . \quad (6)$$

With the newly added time dependence, solutions of the form in Eq. (4), require modification. If we assume the frequency of the light to be near the transitional frequency ω_0 , the wavefunction can be written as a superposition

$$\Psi(\mathbf{r}, t) = c_1(t)\Psi_1(\mathbf{r}, t) + c_2(t)\Psi_2(\mathbf{r}, t) , \quad (7)$$

where $c_1(t)$ and $c_2(t)$ are time dependent probability amplitudes that the atom is in the ground and excited state respectively, with the typical normalization condition of

$$\int |\Psi(\mathbf{r}, t)|^2 d^3\mathbf{r} = |c_1(t)|^2 + |c_2(t)|^2 = 1 . \quad (8)$$

Substituting Eq. (7) into Eq. (1), dropping the explicit time dependence of $c_i(t)$, and changing to bra-ket representation for convenience where $\Psi_i(\mathbf{r}, t) \rightarrow |i\rangle$, we obtain equations in the form

$$\langle 1|\hat{H}_I|1\rangle c_1 + e^{-i\omega_0 t} \langle 1|\hat{H}_I|2\rangle c_2 = i\hbar \frac{dc_1}{dt} , \quad (9)$$

and

$$e^{i\omega_0 t} \langle 2|\hat{H}_I|1\rangle c_1 + \langle 2|\hat{H}_I|2\rangle c_2 = i\hbar \frac{dc_2}{dt} . \quad (10)$$

If we treat the interaction to be a polarized traveling electric field wave, i.e. like that of a laser, the interaction Hamiltonian takes the form

$$\hat{H}_I = e\mathbf{d} \cdot \mathbf{E}_0 \cos(\omega t) , \quad (11)$$

where e is the charge of the electron, \mathbf{d} is the total electric dipole moment of the atom, \mathbf{E}_0 is the amplitude of the electric field, and ω is the frequency of the light. For electric dipole transitions such as discussed here

$$\langle 1|\hat{H}_I|1\rangle = \langle 2|\hat{H}_I|2\rangle = 0 , \quad (12)$$

and

$$\langle 1|\hat{H}_I|2\rangle = \langle 2|\hat{H}_I|1\rangle^* . \quad (13)$$

For E_0 in the x-direction, we can represent the product

$$\langle 1|\hat{H}_I|2\rangle = eE_0 X_{12} \cos(\omega t) , \quad (14)$$

with X_{12} representing the spatial wavefunction integral in terms of the unit vector of the electric field $\hat{\mathbf{e}}$ and the transition dipole moment \mathbf{d}_{12}

$$X_{12} = \int \psi_1^*(\mathbf{r}) X \psi_2(\mathbf{r}) d^3\mathbf{r} = \int \psi_1^*(\mathbf{r}) [\hat{\mathbf{e}} \cdot \mathbf{d}] \psi_2(\mathbf{r}) d^3\mathbf{r} = \hat{\mathbf{e}} \cdot \mathbf{d}_{12} . \quad (15)$$

Then introducing the Rabi frequency, Ω_{12} , as

$$\Omega_{12} = \frac{eE_0 X_{12}}{\hbar} , \quad (16)$$

we can simplify Eqs. (9) and (10) to the form:

$$\Omega_{12} \cos(\omega t) e^{-i\omega_0 t} c_2 = i \frac{dc_1}{dt} , \quad (17)$$

and

$$\Omega_{12}\cos(\omega t)e^{i\omega_0 t}c_1 = i\frac{dc_2}{dt} . \quad (18)$$

These are exact equations, but to solve, approximations must be made. If we make the assumption that the driving field is weak, which is the approximation that $c_1(t) = 1$ and $|c_2(t)| \ll 1$, the integration of Eq. (18) results in

$$c_2(t) = \frac{\Omega_{12}}{2} \left[\frac{1 - e^{i(\omega_0 + \omega)t}}{\omega_0 + \omega} + \frac{1 - e^{i(\omega_0 - \omega)t}}{\omega_0 - \omega} \right] . \quad (19)$$

Applying a further approximation, namely the rotating wave approximation (RWA) [87], eliminating the first highly oscillatory term, the time dependent amplitude of the probability that the atom is excited becomes

$$|c_2(t)|^2 = \Omega_{12}^2 \frac{\sin^2 \left[\frac{1}{2}(\omega_0 - \omega)t \right]}{(\omega_0 - \omega)^2} . \quad (20)$$

While this is a nice result, in reality atoms have the property of spontaneous emission, which is not included in the above derivation. To include spontaneous emission, Eq. (18) must include an additional term with the spontaneous decay rate γ in the following way:

$$\Omega_{12}\cos(\omega t)e^{i\omega_0 t}c_1 - i\gamma c_2 = i\frac{dc_2}{dt} . \quad (21)$$

As expected, if the applied electric field is removed, the excited state amplitude decays as

$$c_2(t) = c_2(0)e^{-\gamma t} . \quad (22)$$

If we expand this formulation to that of a gas with N two level atoms, the number of atoms in each state is represented by the probability of the atoms in each state, times the total number of atoms.

$$N_1(t) = N|c_1(t)|^2 \text{ and } N_2(t) = N|c_2(t)|^2 . \quad (23)$$

Then, the number of atoms in the excited state can be represented by

$$N_2(t) = N_2(0)e^{-2\gamma t} . \quad (24)$$

The radiative decay Γ then can be given by relation of the Einstein coefficient A_{21} in the following way for a two level non-degenerate system:

$$\Gamma = 2\gamma = A_{21} = \frac{1}{\tau} = \frac{e^2\omega_0^3 d_{12}^2}{3\pi\epsilon_0 \hbar c^3} , \quad (25)$$

with ϵ_0 being the free space permittivity, c the speed of light, and d_{12} is referred to as the transition dipole moment as mentioned before in Eq. (15). For transitions with degenerate

states $d_{12}^2 \rightarrow (g_1/g_2)d_{12}^2$, where g_1, g_2 is the degeneracy of the ground and excited state respectively.

Reformulating some from here, we can present the radiative decay in a more typical atomic physics representation [86]. First, we must obtain a proper description of the angular momentum of the atom. The total electron angular momentum is

$$\mathbf{J} = \mathbf{L} + \mathbf{S} , \quad (26)$$

where \mathbf{L} is the orbital angular momentum of the outer electron in a single electron system and \mathbf{S} is the spin angular momentum of the electron that follow the typical quantum mechanics convention

$$|L - S| \leq J \leq L + S . \quad (27)$$

Furthermore, the total angular momentum of the atom is represented by

$$\mathbf{F} = \mathbf{J} + \mathbf{I} , \quad (28)$$

where \mathbf{I} is the total angular momentum of the atomic nucleus. Similar to Eq. (27), the values of F are between

$$|J - I| \leq F \leq J + I . \quad (29)$$

In the particular case of this work, ^{85}Rb is used, which has a nonzero nuclear angular momentum ($I = 5/2$), therefore we must start with the coupling of hyperfine F levels and magnetic sublevels m_F in our description of the dipole matrix elements. For any hyperfine level F , there are $2F + 1$ magnetic sublevels that are degenerate in the absence of an external magnetic field and range from $-F$ to F . The m_F levels determine angular distribution of the electronic wave function. While not discussed here, there are magnetic sublevels for the other previously mentioned quantum numbers as well.

We start with the dipole matrix element

$$\langle Fm_F | er_q | F'm'_F \rangle , \quad (30)$$

where q is a spherical basis index related ultimately to the polarization of the excitation field. Here and in further description, primed quantum numbers denote excited states and unprimed numbers are the ground state. By use of Wigner-Eckart theorem, these matrix elements can be broken into a reduced matrix element (represented with double absolute value bars) and a Clebsch-Gordon coefficient, which will be broken down further in terms of

Wigner 3-j and 6-j symbols. The dipole matrix element in Eq. (30) in terms of the reduced matrix element and Wigner 3-j symbol becomes

$$\langle Fm_F|er_q|F'm'_F\rangle = \langle F||e\mathbf{r}||F'\rangle(-1)^{F'-1+m_F}\sqrt{2F+1} \begin{pmatrix} F' & 1 & F \\ m'_F & q & -m_F \end{pmatrix}. \quad (31)$$

The reduced matrix element can then be broken down further in terms of a Wigner 6-j symbol in the following way:

$$\langle F||e\mathbf{r}||F'\rangle = \langle J||e\mathbf{r}||J'\rangle(-1)^{F'+J+I+1}\sqrt{(2F'+1)(2J+1)} \begin{Bmatrix} J & J' & 1 \\ F' & F & I \end{Bmatrix}. \quad (32)$$

With the substitution of the reduced matrix element in terms of F in Eq. (32) into Eq. (31), the dipole matrix element can be calculated based on the experimentally measured radiative lifetime, as portrayed in Eq. (25), but now in the following way

$$\frac{1}{\tau} = \frac{\omega_0^3}{3\pi\epsilon_0\hbar c^3} \frac{2J+1}{2J'+1} |\langle J||e\mathbf{r}||J'\rangle|^2, \quad (33)$$

where the transition dipole moment from before is replaced with the reduced dipole matrix element in terms of the quantum number J and J' and degeneracy ratio factor. If necessary, the matrix element can be broken down again in terms of the orbital angular momentum L , but is not necessary for the system in discussion here.

2.2 ELECTROMAGNETICALLY INDUCED TRANSPARENCY

2.2.1 OPTICAL BLOCH EQUATIONS

For describing EIT, generally the approach of the optical Bloch equations are used which is a density matrix formulation. In the physical system in this experiment, simulating the effect with qualitative accuracy requires a 9 level system, which then implies 81 equations of motion. Here in this fundamental discussion, we will use avoid using a complicated situation such as that and turn a much simpler system to express the general behavior of an atom subject to multiple electric fields. To better describe the quantum three level system dynamics, we must move to a density matrix approach for the system. Under the assumption that the system is comprised of a pure ensemble, we have the density matrix operator

$$\rho = |\Psi\rangle\langle\Psi|, \quad (34)$$

with the quantum states represented by:

$$|\Psi\rangle = \sum_k c_k |\psi_k\rangle . \quad (35)$$

In a three level system, which will be discussed briefly here, the density matrix takes the following form:

$$\rho = \begin{pmatrix} \rho_{11} & \rho_{12} & \rho_{13} \\ \rho_{21} & \rho_{22} & \rho_{23} \\ \rho_{31} & \rho_{32} & \rho_{33} \end{pmatrix} , \quad (36)$$

with matrix elements

$$\rho_{ij} = \langle \psi_i | \rho | \psi_j \rangle = c_i c_j^* . \quad (37)$$

In a pure system, the diagonal elements ρ_{ii} represent the population of the state $|\psi_i\rangle$ and meet the condition:

$$\sum_i \rho_{ii} = \sum_i |c_i|^2 = 1 . \quad (38)$$

Off diagonal terms in the density matrix are referred to as coherence terms and are an expression of interference between states. More explicitly, $c_i c_j^*$ expresses the interference between the states $|\psi_i\rangle$ and $|\psi_j\rangle$ and ρ_{ij} is called the coherence between the aforementioned states. With the formalities of the density matrix taken care of, we now can move to the calculation of the optical Bloch equations (OBEs), also known as the Maxwell-Bloch equations. We start with the Liouville equation, which describes the time evolution of the density matrix:

$$\frac{\partial \rho}{\partial t} = \frac{i}{\hbar} [\rho, \hat{\mathcal{H}}] , \quad (39)$$

where $\hat{\mathcal{H}}$ is the full Hamiltonian which can be written as the following:

$$\hat{\mathcal{H}} = \hat{H}_0 + \hat{H}_I , \quad (40)$$

with \hat{H}_0 representing the pure atomic Hamiltonian with no radiation present, and \hat{H}_I representing the interaction Hamiltonian that describes the interaction of the (classically treated) radiation field with the atom by means of electric dipole transition.

To obtain the optical Bloch equations, we must simplify the Liouville equation in terms of the individual matrix elements of the density matrix. For reduction of clutter in the calculation, generalize $|\psi_k\rangle = |k\rangle$ and $\frac{\partial \rho}{\partial t} = \dot{\rho}$. The Liouville equation then becomes

$$\dot{\rho}_{ij} = \frac{i}{\hbar} \langle i | (\rho \hat{\mathcal{H}} - \hat{\mathcal{H}} \rho) | j \rangle . \quad (41)$$

Using the relation $\rho = \sum_{m,n} \rho_{mn} |m\rangle\langle n|$, eq. (41) becomes

$$\dot{\rho}_{ij} = \frac{i}{\hbar} \left[\sum_{m,n} \rho_{mn} \langle i|m\rangle\langle n|\hat{\mathcal{H}}|j\rangle - \sum_{m,n} \rho_{mn} \langle i|\hat{\mathcal{H}}|m\rangle\langle n|j\rangle \right]. \quad (42)$$

Changing the dummy index to l and reducing further leads to

$$\dot{\rho}_{ij} = \frac{i}{\hbar} \left[\sum_l \rho_{il} \langle l|\hat{\mathcal{H}}|j\rangle - \sum_l \rho_{lj} \langle i|\hat{\mathcal{H}}|l\rangle \right]. \quad (43)$$

Evaluation of the atomic Hamiltonian and substituting $E_k = \hbar\omega_k$ leads to

$$\dot{\rho}_{ij} = i\rho_{ij}(\omega_j - \omega_i) + \frac{i}{\hbar} [\rho, \hat{H}_I]_{ij}. \quad (44)$$

Before evaluating the interaction Hamiltonian, we define

$$\tilde{\rho}_{ij} = \rho_{ij} e^{-i(\omega_j - \omega_i)t}, \quad (45)$$

in order to simplify calculations. Thus, we have

$$\dot{\tilde{\rho}}_{ij} = \dot{\rho}_{ij} e^{-i(\omega_j - \omega_i)t} - i(\omega_j - \omega_i) \tilde{\rho}_{ij}. \quad (46)$$

Now substituting eq. (44) into eq. (46) yields

$$\dot{\tilde{\rho}}_{ij} = \frac{i}{\hbar} [\rho, \hat{H}_I]_{ij} e^{-i(\omega_j - \omega_i)t} = \frac{i}{\hbar} \left[\sum_l \rho_{il} \langle l|\hat{H}_I|j\rangle - \sum_l \rho_{lj} \langle i|\hat{H}_I|l\rangle \right] e^{-i(\omega_j - \omega_i)t}. \quad (47)$$

Using the definition from eq. (45) leads to

$$\dot{\tilde{\rho}}_{ij} = \frac{i}{\hbar} \left[\sum_l \tilde{\rho}_{il} e^{i(\omega_l - \omega_j)t} \langle l|\hat{H}_I|j\rangle - \sum_l \tilde{\rho}_{lj} e^{i(\omega_i - \omega_l)t} \langle i|\hat{H}_I|l\rangle \right]. \quad (48)$$

We treat the interaction Hamiltonian as the electric dipole interaction between the atom's electron and an oscillating monochromatic electric field with frequency ω_α , where α is representative of the laser field for the specific transition ($\alpha = 1$ is the probe, $\alpha = 2$ is the control in the case to be discussed). The interaction Hamiltonian is the following:

$$\hat{H}_I = -\mathbf{d} \cdot \mathbf{E} = -e\mathbf{r} \cdot \mathbf{E}_0(\mathbf{r}) \cos(\omega_\alpha t) = -\frac{eE_0}{2} \mathbf{r} \cdot \hat{\boldsymbol{\epsilon}} [e^{i\omega_\alpha t} + e^{-i\omega_\alpha t}]. \quad (49)$$

To further reduce clutter in calculations, we represent the radial matrix elements as a factor of the Rabi frequency Ω_{ij}^α in the following way

$$\frac{1}{\hbar} \langle i|\hat{H}_I|j\rangle = -\frac{eE_0}{2\hbar} \langle i|\mathbf{r} \cdot \hat{\boldsymbol{\epsilon}}|j\rangle [e^{i\omega_\alpha t} + e^{-i\omega_\alpha t}] = -\frac{\Omega_{ij}^\alpha}{2} [e^{i\omega_\alpha t} + e^{-i\omega_\alpha t}]. \quad (50)$$

Now, continuing from eq. (50), and utilizing $R_{ij}^\alpha = \Omega_{ij}^\alpha/2$ and $\omega_\alpha = \omega_i - \omega_l + \Delta_{il}$ along with the rotating wave approximation to further simplify the expression, we reach the form of

$$\dot{\rho}_{ij} = i \sum_l [\tilde{\rho}_{lj} R_{il}^\alpha e^{i\Delta_{il}^\alpha t} - \tilde{\rho}_{il} R_{lj}^\alpha e^{i\Delta_{lj}^\alpha t}] . \quad (51)$$

Until this point, we have assumed that the system is closed, but now we must also consider non-interacting decay terms based on the radiative lifetime of the atomic states. Simply, we must add terms that incorporate the atomic decay to lower energy states. This can be represented by the Linblad master equation, which is an alteration of the Liouville equation with the addition of a term [39], as shown in the following:

$$\frac{\partial \rho}{\partial t} = \frac{i}{\hbar} [\rho, \hat{\mathcal{H}}] + L(\rho) . \quad (52)$$

In the case of eq. (48), with the Linblad term added, we have diagonal terms in the form of

$$\dot{\rho}_{ii} = i \sum_l [\tilde{\rho}_{li} R_{il}^\alpha e^{i\Delta_{il}^\alpha t} - \tilde{\rho}_{il} R_{li}^\alpha e^{i\Delta_{li}^\alpha t} + A_{li} \tilde{\rho}_{ll}] - \Gamma_i \tilde{\rho}_{ii} , \quad (53)$$

where

$$\Gamma_n = \sum_k A_{nk} \quad \text{for } k < n . \quad (54)$$

In eq. (54), Γ_n refers to the total rate of decay of the state $|n\rangle$ and A_{nk} represents the rate of decay from the states $|n\rangle \rightarrow |k\rangle$. As for the off diagonal terms, we have

$$\dot{\rho}_{ij} = i \sum_l [\tilde{\rho}_{lj} R_{il}^\alpha e^{i\Delta_{il}^\alpha t} - \tilde{\rho}_{il} R_{lj}^\alpha e^{i\Delta_{lj}^\alpha t}] - \frac{\Gamma_i + \Gamma_j}{2} \tilde{\rho}_{ij} . \quad (55)$$

In general, the sum over the lasers, α , must be accounted for all states in the Bloch equations, but for the specific case we are describing, the probe field only couples states $|1\rangle$ to $|2\rangle$ and the control field only couples states $|2\rangle$ to $|3\rangle$. Therefore we can drop the α superscripts on the Rabi frequency and detuning. To simplify the Rabi frequency terms further, we can make use of the fact $R_{ij} = R_{ji}$. Now, using eqs. (53) and (55), the set of optical Bloch

equations is:

$$\begin{aligned}
\dot{\tilde{\rho}}_{11} &= i [\tilde{\rho}_{21}e^{i\Delta_{12}t} - \tilde{\rho}_{12}e^{i\Delta_{21}t}] R_{12} - \Gamma_{21}\tilde{\rho}_{22} \\
\dot{\tilde{\rho}}_{12} &= i [(\tilde{\rho}_{22} - \tilde{\rho}_{11}) R_{12}e^{i\Delta_{12}t} - \tilde{\rho}_{13}R_{32}e^{i\Delta_{21}t}] - \frac{\Gamma_{21}}{2}\tilde{\rho}_{12} \\
\dot{\tilde{\rho}}_{13} &= i [\tilde{\rho}_{23}R_{12}e^{i\Delta_{12}t} - \tilde{\rho}_{12}R_{23}e^{i\Delta_{12}t}] - \frac{\Gamma_{32}}{2}\tilde{\rho}_{13} \\
\dot{\tilde{\rho}}_{21} &= \dot{\tilde{\rho}}_{12}^* \\
\dot{\tilde{\rho}}_{22} &= i [(\tilde{\rho}_{12}e^{i\Delta_{21}t} - \tilde{\rho}_{21}e^{i\Delta_{12}t})R_{12} + (\tilde{\rho}_{32}e^{i\Delta_{23}t} - \tilde{\rho}_{23}e^{i\Delta_{32}t})R_{23}] + \Gamma_{32}\tilde{\rho}_{33} - \Gamma_{21}\tilde{\rho}_{22} \quad (56) \\
\dot{\tilde{\rho}}_{23} &= i [\tilde{\rho}_{13}R_{21}e^{i\Delta_{21}t} + (\tilde{\rho}_{33} - \tilde{\rho}_{22}) R_{23}e^{i\Delta_{23}t}] - \frac{\Gamma_{21} + \Gamma_{32}}{2}\tilde{\rho}_{23} \\
\dot{\tilde{\rho}}_{31} &= \dot{\tilde{\rho}}_{13}^* \\
\dot{\tilde{\rho}}_{32} &= \dot{\tilde{\rho}}_{23}^* \\
\dot{\tilde{\rho}}_{33} &= iR_{23} [\tilde{\rho}_{23}e^{i\Delta_{32}t} - \tilde{\rho}_{32}e^{i\Delta_{23}t}] - \Gamma_{32}\tilde{\rho}_{33} .
\end{aligned}$$

To further simplify calculations, we introduce the form

$$\sigma_{ij} = \tilde{\rho}_{ij}e^{-i\Delta_{ij}t} , \quad (57)$$

which leads to

$$\dot{\sigma}_{ij} = \dot{\tilde{\rho}}_{ij}e^{-i\Delta_{ij}t} - i\Delta_{ij}\tilde{\rho}_{ij}e^{-i\Delta_{ij}t} . \quad (58)$$

Also, it must be noted that Δ_{ij} must be treated carefully in systems with more complicated structure than that of the three level system like in this case. For cases in which there are multiple pathways from state i to j, only the shortest path is considered.

$$\begin{aligned}
\dot{\sigma}_{11} &= i [\sigma_{21} - \sigma_{12}] R_{12} + \Gamma_{21}\sigma_{22} \\
\dot{\sigma}_{12} &= i [(\sigma_{22} - \sigma_{11}) R_{12} - \sigma_{13}R_{32}] - \left[\frac{\Gamma_{21}}{2} + i\Delta_{12} \right] \sigma_{12} \\
\dot{\sigma}_{13} &= i [\sigma_{23}R_{12} - \sigma_{12}R_{23}] - \left[\frac{\Gamma_{32}}{2} + i(\Delta_{12} + \Delta_{23}) \right] \sigma_{13} \\
\dot{\sigma}_{21} &= \dot{\sigma}_{12}^* \\
\dot{\sigma}_{22} &= i [(\sigma_{12} - \sigma_{21})R_{12} + (\sigma_{32} - \sigma_{23})R_{23}] + \Gamma_{32}\sigma_{33} - \Gamma_{21}\sigma_{22} \quad (59) \\
\dot{\sigma}_{23} &= i [\sigma_{13}R_{21} + (\sigma_{33} - \sigma_{22}) R_{23}] - \left[\frac{\Gamma_{21} + \Gamma_{32}}{2} + i\Delta_{23} \right] \sigma_{23} \\
\dot{\sigma}_{31} &= \dot{\sigma}_{13}^* \\
\dot{\sigma}_{32} &= \dot{\sigma}_{23}^* \\
\dot{\sigma}_{33} &= iR_{23} [\sigma_{23} - \sigma_{32}] - \Gamma_{32}\sigma_{33} .
\end{aligned}$$

At this point, the equations in (59) can be solved numerically, with the solutions for the real and imaginary of σ_{12} shown in Fig. 3. Solutions for σ_{12} with a control detuning of $\Delta_{23} = \Gamma_{12}$

is shown in Fig. 4. Alternatively to solving numerically, some assumptions for specific cases can be made to solve the system analytically. For example, under the assumption that the probe laser and control laser are on resonance, with the probe field being much weaker than the control field, and also the system is in steady state, the interference between state $|1\rangle$ and $|2\rangle$ is

$$\sigma_{12} = -\frac{i\Omega_{12}}{\Gamma_{21} + \frac{\Gamma_{21}\Omega_{12}^2}{\Gamma_{32}(\Gamma_{21} + \Gamma_{32})} + \frac{\Omega_{23}^2}{\Gamma_{32}}}. \quad (60)$$

The notable result is that $\text{Im}(\sigma_{12})$ is proportional to the probe absorption in the system, therefore with a weak probe and strong coupling field ($\Omega_{12} \ll \Omega_{23}$), the absorption of the probe strongly decreases.

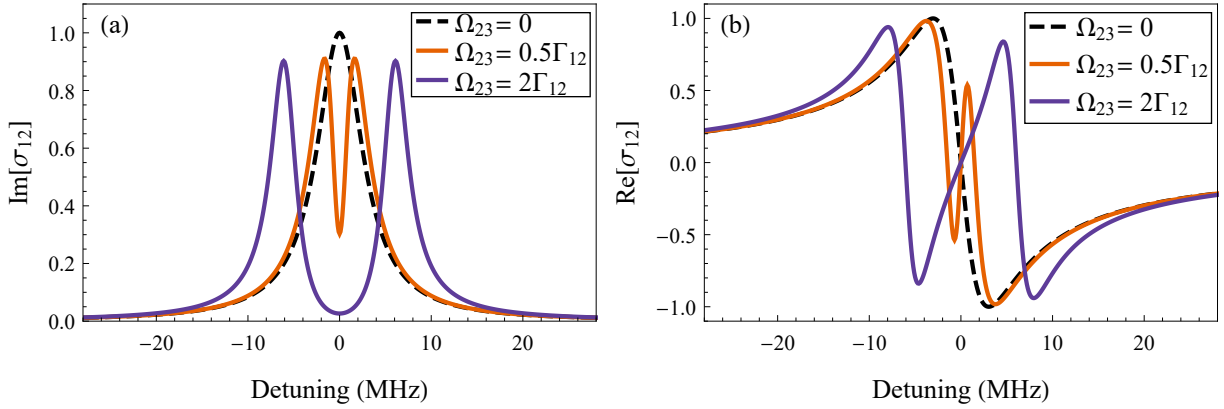


FIG. 3: Three level EIT in weak probe regime ($\Omega_{12} = 0.01\Gamma_{12}$) with control detuning $\Delta_{23} = 0$. (a) $\text{Im}[\sigma_{12}]$ corresponding to probe absorption. (b) $\text{Re}[\sigma_{12}]$ corresponding to index of refraction.

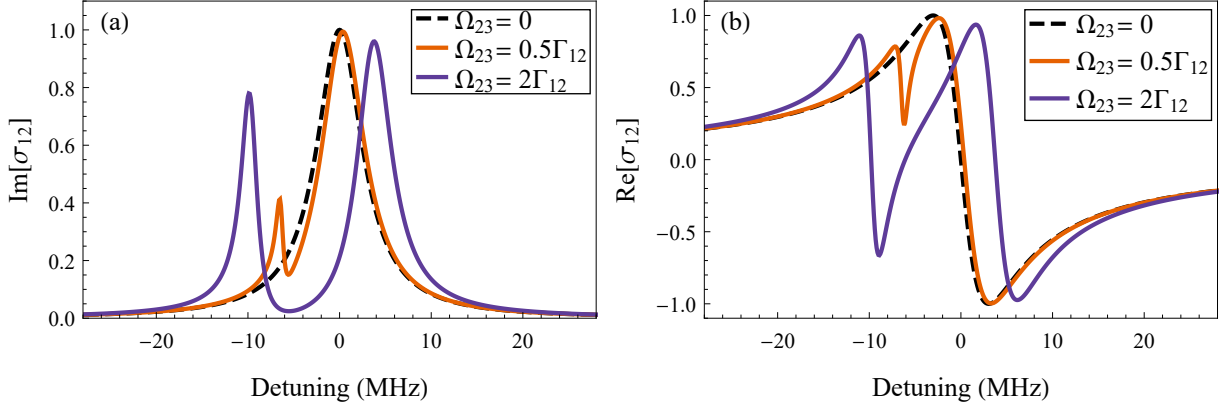


FIG. 4: Three level EIT in weak probe regime ($\Omega_{12} = 0.01\Gamma_{12}$) with control detuning $\Delta_{23} = \Gamma_{12}$. (a) $\text{Im}[\sigma_{12}]$ corresponding to probe absorption. (b) $\text{Re}[\sigma_{12}]$ corresponding to index of refraction.

Furthermore, while not directly related to what was studied here, one can relate the real part of the coherence terms to the susceptibility of the gas, thus the index of refraction which can give an expression for slowed light. The susceptibility is given by

$$\chi(\omega) = \frac{2\pi c^3 N_d \Gamma_{21}}{\omega_0^3 \Omega_{12}} \tilde{\rho}_{21} , \quad (61)$$

where N_d is the density of the gas and c is the speed of light. The group velocity of light in a dielectric is represented by

$$v_g = \frac{c}{n + \omega \frac{\partial n}{\partial \omega}} . \quad (62)$$

With the index of refraction n being proportional to $\text{Re}(\chi)$ one can surmise the effect on group velocity by solving the optical Bloch equations.

2.3 COHERENT BACKSCATTERING OVERVIEW

As previously mentioned in Chapter 1, coherent backscattering is a well studied physical phenomena that can occur in presumably any system where waves interact with a disordered medium or object, where the constructive interference of time-reversed paths lead to an enhancement in the backwards direction. The discussion in this section will describe this effect in more rigorous mathematical detail following closely to the excellent description of CBS (and many other effects) in Akkermans' and Montambaux's *Mesoscopic Physics of Electrons and Photons* [88].

2.3.1 SPECKLE AND WAVE SCATTERING CONTRIBUTIONS

Speckle patterns occur when a coherent, monochromatic light source encounters an obstacle that scatters the incoming wave, creating a unique diffraction pattern based on the physical properties of the obstacle, whether it be a solid object or a medium. A classic example of a speckle pattern can be observed by shining a laser pointer on a wall, which shows bright and dark areas due to constructive and destructive interference.

However, if the ensemble of scatterers is “averaged over”, the speckle phenomena disappears. For solid objects, the averaging consists of physically moving or rotating the object under consideration. For turbid, optically thick media, such as a suspension of particles in liquid or a cold atomic gas, the averaging occurs naturally with the motion of the scatterers within the medium. With a random medium and an incident wave undergoing multiple scattering in the medium, it would classically be expected that no coherence effects would remain, but that is not the case. However, it must be added here that this is only the case when a system is such that it is smaller than the phase coherence length, L_ϕ . A sample that is smaller than L_ϕ is said to be a mesoscopic system, i.e., small enough to retain coherence effects, where a significantly larger system will eventually lose the coherent effects. The description here also assumes coherent multiple scattering in the limit $\lambda = \frac{2\pi}{k}$ is small compared to the elastic mean free path l_e , which is referred to as the limit of weak disorder. In this text, elastic mean free path l_e represents the average distance a wave packet travels between two scattering events with no energy change.

For a generalized mathematical description, consider an optically thick medium of N randomly distributed point scatterers. Then consider a plane wave from a coherent source located outside the medium, that propagates in the medium and elastically scatters off of the particles in the medium. For the purposes of this study, we want to analyze the complex amplitude of the re-emitted wave $A(\mathbf{k}, \mathbf{k}')$, where \mathbf{k} is the incident plane wave direction and \mathbf{k}' is the direction of the re-emitted wave. The scattered wave amplitude is thus defined as

$$A(\mathbf{k}, \mathbf{k}') = \sum_{\mathbf{r}_1, \mathbf{r}_2} f(\mathbf{r}_1, \mathbf{r}_2) e^{i(\mathbf{k} \cdot \mathbf{r}_1 - \mathbf{k}' \cdot \mathbf{r}_2)} , \quad (63)$$

where $f(\mathbf{r}_1, \mathbf{r}_2)$ is the complex amplitude corresponding to propagation between two scattering events located at \mathbf{r}_1 and \mathbf{r}_2 . Breaking this down further, this amplitude can be represented in the form

$$\sum_j a_j = \sum_j |a_j| e^{i\delta_j} , \quad (64)$$

with a_j being the amplitude of the j -th path and δ_j the associated phase with that same

path, where each path is a sequence of scattering events between points \mathbf{r}_1 and \mathbf{r}_2 (Fig. 5). Amplitudes such as these are vital in the description of light characteristics within a disordered medium. Much of the following consists of the probability of diffusion as the average of a product of such complex amplitudes as

$$P(\mathbf{r}, \mathbf{r}') \sim \overline{\sum_{i,j} a_i^*(\mathbf{r}, \mathbf{r}') a_j(\mathbf{r}, \mathbf{r}')}, \quad (65)$$

where the subscript defines the trajectory as before from \mathbf{r} to \mathbf{r}' . With the trajectories playing an important role in coherence effects, the probability can be rewritten for identical trajectories and for those that are different

$$P(\mathbf{r}, \mathbf{r}') \sim \sum_j |a_j(\mathbf{r}, \mathbf{r}')|^2 + \sum_{i \neq j} |a_i^*(\mathbf{r}, \mathbf{r}') a_j(\mathbf{r}, \mathbf{r}')|. \quad (66)$$

The first term with identical trajectories will be referred to as the Diffuson in later sections and its probability will be denoted as P_D , where the second term will give rise to coherent effects.

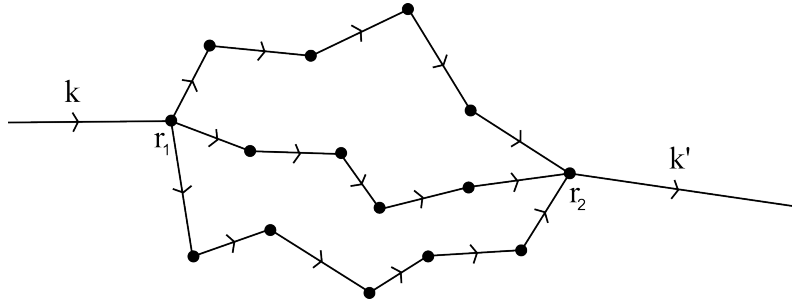


FIG. 5: Contributions to the total complex amplitude $f(\mathbf{r}_1, \mathbf{r}_2)$ over three paths. Diagram inspiration from [88].

With the wave amplitude established, the associated intensity of the wave therefore is:

$$|A(\mathbf{k}, \mathbf{k}')|^2 = \sum_{\mathbf{r}_1, \mathbf{r}_2} \sum_{\mathbf{r}_3, \mathbf{r}_4} f(\mathbf{r}_1, \mathbf{r}_2) f^*(\mathbf{r}_3, \mathbf{r}_4) e^{i(\mathbf{k} \cdot \mathbf{r}_1 - \mathbf{k}' \cdot \mathbf{r}_2)} e^{-i(\mathbf{k} \cdot \mathbf{r}_3 - \mathbf{k}' \cdot \mathbf{r}_4)}, \quad (67)$$

where the product of the complex amplitudes are defined by

$$f(\mathbf{r}_1, \mathbf{r}_2) f^*(\mathbf{r}_3, \mathbf{r}_4) = \sum_{j, j'} a_j(\mathbf{r}_1, \mathbf{r}_2) a_{j'}^*(\mathbf{r}_3, \mathbf{r}_4) = \sum_{j, j'} |a_j| |a_{j'}| e^{i(\delta_j - \delta_{j'})}. \quad (68)$$

To achieve a physically measurable quantity for such a system, the average intensity must be calculated. In order to calculate the value averaged over the position of the scatterers, it is useful to note that most of the terms in Eq. (68) and thus, Eq. (67), vanish on average provided that the phase $\delta_j - \delta_{j'}$, which measures the difference in the lengths of the trajectories, is random. This leaves only the terms in which the phase difference is zero that contribute to the average of the intensity $|A(\mathbf{k}, \mathbf{k}')|^2$, that is when pairs of identical trajectories occur, whether that be in the same direction or opposite directions as portrayed in Fig. 6.

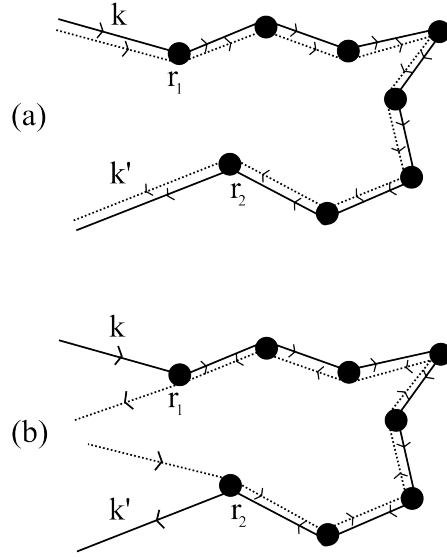


FIG. 6: (a) Representation of scattering paths of classical average intensity. (b) Representation of the source of the scattering paths that occur during coherent backscattering, i.e., time-reversed scattering paths. Diagram inspiration from [88].

With identical trajectories, eq. (67) simplifies with $\mathbf{r}_1 = \mathbf{r}_3$ and $\mathbf{r}_2 = \mathbf{r}_4$ when the paths are in the same direction, while $\mathbf{r}_1 = \mathbf{r}_4$ and $\mathbf{r}_2 = \mathbf{r}_3$ for paths of the opposite direction. Presuming that the system is invariant under time reversal, which in reality is not always true, these two processes contribute identically to the average intensity. Expressing the average intensity more specifically after these simplifications leads to

$$|\overline{A(\mathbf{k}, \mathbf{k}')})|^2 = \overline{\sum_{\mathbf{r}_1, \mathbf{r}_2} |f(\mathbf{r}_1, \mathbf{r}_2)|^2 [1 + e^{i(\mathbf{k}+\mathbf{k}') \cdot (\mathbf{r}_1 - \mathbf{r}_2)}]} , \quad (69)$$

where the first term, unity, is a result of the co-propagating process in Fig. 6(a), while the second term accounts for the opposite directional paths as in Fig. 6(b). More explicitly, the first term of unity consists of the averaged, what will be referred to as incoherent background light, and the second term will be the source of the coherent effects, specifically, coherent backscattering. Lastly in this basic description, we can represent the intensity as the following:

$$I(\mathbf{k}, \mathbf{k}') \sim \int d\mathbf{r} d\mathbf{r}' P_D(\mathbf{r}, \mathbf{r}') \left[1 + e^{i(\mathbf{k}+\mathbf{k}') \cdot (\mathbf{r} - \mathbf{r}')} \right] , \quad (70)$$

where the complex squared amplitude from Eq. (69) is represented by the Diffuson probability, and \mathbf{r} and \mathbf{r}' are close to the interface separating the diffusive medium and vacuum.

2.3.2 COHERENT BACKSCATTERING OF LIGHT

Now we aim to use the description in the previous section to give a rigorous mathematical representation specifically in the terms of light scattering. For the sake of simplicity, we treat the field as a scalar wave in this description and will elaborate further on the effect of polarization afterwards.

The mathematical description follows that of the description in chapter 8 of Akkermans et al. The physical description goes as follows: an incident monochromatic plane wave is directed towards in interface in the direction represented by the unit vector $\hat{\mathbf{s}}_i$. The interface is separated by vacuum, the source of the monochromatic plane wave, and a diffusive medium. The diffusive medium is in the semi-infinite space of $z > 0$, with the vacuum in the space $z < 0$. The assumption of the semi infinite medium allows for an analytic solution that also matches closely to the observed effect in reality with objects of finite size. The resulting scattered wave from the medium re-emerges and is detected far from the interface as intensity along the $\hat{\mathbf{s}}_e$ direction at a distance R . We look to calculate the angular dependence of reflection coefficient, referred to as the albedo, where albedo is defined as the unitless quantity

$$\alpha(\hat{\mathbf{s}}_e) = \frac{R^2}{S} \frac{I(R\hat{\mathbf{s}}_e)}{I_0} , \quad (71)$$

with S corresponding to the surface area in which scattering occurs. With this definition, the intensity $I(R\hat{\mathbf{s}}_e)$ must be calculated. Complications arise due to accounting for the intensity emanating from the last scatterer within the medium and propagating to the detector. However, the approach of radiative transfer can be used to describe this process. Treating

the scattered wave as a spherical wave emitted from a point, the solution of the Helmholtz equation corresponds to a Green's function, which portrays the intensity in the following way:

$$I(\mathbf{r}) = \frac{4\pi}{c} |\psi(\mathbf{r})|^2 = \frac{4\pi}{c} G^R(\mathbf{r}_0, \mathbf{r}) G^A(\mathbf{r}, \mathbf{r}_0) . \quad (72)$$

Here, the R and A refer to the retarded and advanced Green's functions, with the field emanating from a point source at \mathbf{r}_0 . Also the Drude-Boltzmann approximation given by

$$\overline{G^R(\mathbf{r}_0, \mathbf{r}) G^A(\mathbf{r}, \mathbf{r}_0)} = \overline{G^R(\mathbf{r}_0, \mathbf{r})} \overline{G^A(\mathbf{r}, \mathbf{r}_0)} , \quad (73)$$

is used in the the average intensity calculation involving Green's functions. The intensity and thus albedo for the incoherent light, i.e. Diffuson, and for that of the coherent light, the Cooperon, must be calculated independently. The total albedo therefore will be represented as the contribution from both terms added together as

$$\alpha(\theta) = \alpha_D(\theta) + \alpha_C(\theta) . \quad (74)$$

2.3.2.1 Diffuson Contribution

Starting with the Diffuson, the corresponding intensity is

$$I_D(R\hat{\mathbf{s}}_e) = \frac{4\pi}{c} \int d\mathbf{r}_1 d\mathbf{r}_2 |\overline{\psi}_i(\mathbf{r}_1)|^2 \Gamma(\mathbf{r}_1, \mathbf{r}_2) |\overline{G^R}(\mathbf{r}_2, \mathbf{R})|^2 , \quad (75)$$

where \mathbf{r}_1 and \mathbf{r}_2 is the point of the first and last scatterer respectively. The term $|\overline{\psi}_i(\mathbf{r}_1)|^2$ can be thought of as the average intensity of the wave to travel up to the point \mathbf{r}_1 with no collision, $\Gamma(\mathbf{r}_1, \mathbf{r}_2)$ is referred to as the structure or vertex function and takes into account all scattering processes between \mathbf{r}_1 and \mathbf{r}_2 , and the product of the Green's functions can be thought of as the intensity of the light traveling from the final scatterer \mathbf{r}_2 to the location of the detector \mathbf{R} , without further collision. The squared terms arise due to the Diffuson describing identical wave scattering paths throughout the process, as shown in Fig. 7.

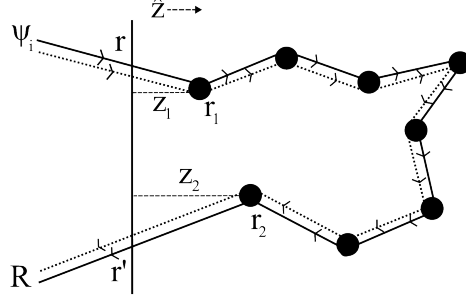


FIG. 7: Scattering path of the Diffuson, inspired by diagrams from [88]. Distances z_1 , z_2 are the distances of the first and last scatterers at \mathbf{r}_1 , \mathbf{r}_2 from the scattering interface.

For the geometry described here and shown in Fig. 7, the plane wave takes the form

$$\bar{\psi}_i(\mathbf{r}_1) = \sqrt{\frac{cI_0}{4\pi}} e^{-|\mathbf{r}_1 - \mathbf{r}|/2l_e} e^{-ik\hat{\mathbf{s}}_i \cdot \mathbf{r}_1}, \quad (76)$$

in which the decaying exponential term is analogous to Beer's law accounting for attenuation when the wave passes through the interface and is inside the medium. The definition of the *average* Green's function in the describe medium is given by

$$\bar{G}^R(\mathbf{r}_2, \mathbf{R}) = e^{-|\mathbf{r}_1 - \mathbf{r}|/2l_e} \frac{e^{ik|\mathbf{R} - \mathbf{r}_2|}}{4\pi|\mathbf{R} - \mathbf{r}_2|}, \quad (77)$$

where we can use the Fraunhofer approximation to simplify the Green's function further into the form of

$$\bar{G}^R(\mathbf{r}_2, \mathbf{R}) = e^{-|\mathbf{r}_1 - \mathbf{r}|/2l_e} e^{-ik\hat{\mathbf{s}}_e \cdot \mathbf{r}_2} \frac{e^{ikR}}{4\pi R}. \quad (78)$$

As is done in the experiment, we take the incoming wave unit vector $\hat{\mathbf{s}}_i$ to be normal to the interface, and then define the projection of the emitted wave unit vector $\hat{\mathbf{s}}_e$ onto the z -axis $\hat{\mathbf{s}}_e \cdot \hat{\mathbf{z}} = \cos\theta = \eta$ such that for the particle at \mathbf{r}_1 and \mathbf{r}_2 respectively, we have

$$|\mathbf{r}_1 - \mathbf{r}| = z_1 \text{ and } |\mathbf{r}_2 - \mathbf{r}'| = \frac{z_2}{\eta}. \quad (79)$$

The Diffuson intensity, therefore the Diffuson albedo α_D can be expressed as

$$\alpha_D = \frac{R^2}{S} \frac{I_D(R\hat{\mathbf{s}}_e)}{I_0} = \frac{1}{(4\pi)^2 S} \int d\mathbf{r}_1 d\mathbf{r}_2 e^{-z_1/l_e} e^{-z_2/\eta l_e} \Gamma(\mathbf{r}_1, \mathbf{r}_2), \quad (80)$$

As for determining the structure factor $\Gamma(\mathbf{r}_1, \mathbf{r}_2)$, which is normally an iterative integral equation, chapter 4 of Akkermans *et al.* gives a thorough explanation of how in the diffusion

approximation, with small spatial variations, the structure factor can be related to the probability of diffusion in the following way:

$$P_D(\mathbf{r}_1, \mathbf{r}_2) = \frac{l_e^2}{4\pi c} \Gamma(\mathbf{r}_1, \mathbf{r}_2) . \quad (81)$$

The probability of diffusion here is a solution to the diffusion equation, which can be conveniently calculated in this case using the method of images formulation, where the Dirichlet condition that the probability vanishes is at the point $-z_0$ outside the scattering medium. Using this technique, the probability of diffusion is expressed as

$$P_D(z_1, z_2) = \frac{1}{2D} [(z_1 + z_2 + 2z_0) - |z_1 - z_2|] , \quad (82)$$

where D is referred to as the diffusion constant which is proportional to the elastic mean free path and group velocity. Finally, Eq. (80) can be solved and results in

$$\alpha_D = \frac{3}{4\pi} \eta \left[\frac{z_0}{l_e} + \frac{\eta}{\eta + 1} \right] , \quad (83)$$

with the plot of the Diffuson albedo in Fig. 8, plotted in the range of $\theta = (-\frac{\pi}{2}, \frac{\pi}{2})$.

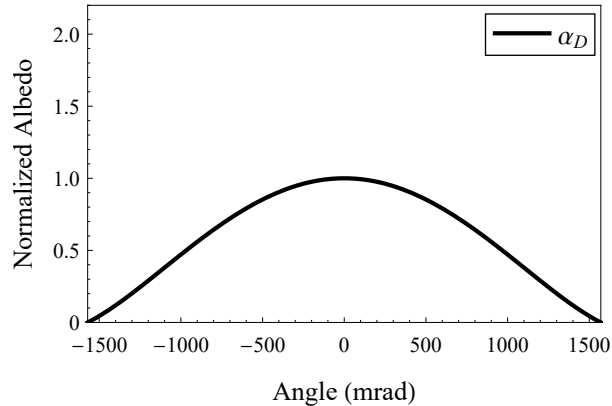


FIG. 8: The Diffuson albedo α_D as a function of angle.

While there is an angular dependence to the Diffuson albedo, it is not very pronounced, especially at small angles as how it is generally measured. The Diffuson albedo α_D can generally be considered constant at small angles, which will be elaborated on when comparing the Cooperon.

2.3.2.2 Cooperon Contribution

Now turning to the Cooperon, that is, the intensity contribution due to coherent effects as shown in the trajectory diagram in Fig. 9, we have

$$I_C(R\hat{\mathbf{s}}_e) = \frac{4\pi}{c} \int d\mathbf{r}_1 d\mathbf{r}_2 \bar{\psi}_i(\mathbf{r}_1) \bar{\psi}_i^*(\mathbf{r}_2) \Gamma(\mathbf{r}_1, \mathbf{r}_2) \bar{G}^R(\mathbf{r}_2, \mathbf{R}) \bar{G}^A(\mathbf{R}, \mathbf{r}_1) , \quad (84)$$

where now the differences from the Diffuson intensity in Eq. (75) are due to the waves following in time-reversed trajectories.

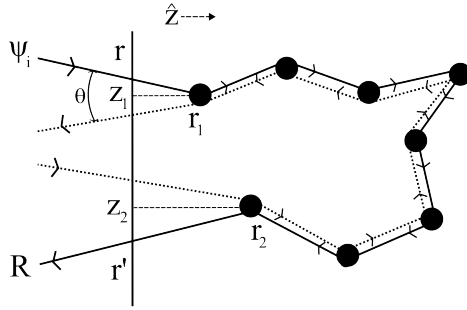


FIG. 9: Scattering paths of the Cooperon contribution to the total albedo. The values of z_1 , z_2 are the dashed lines connecting from the plane at $z = 0$ to the points \mathbf{r}_1 , \mathbf{r}_2 respectively. Inspired by diagrams from [88]

With the same assumptions as before with the incoming plane wave, the Fraunhofer approximation for the Green's function, and projecting the first and last scatterers coordinates on the interface, we have the average Cooperon albedo

$$\alpha_C = \frac{1}{(4\pi)^2 S} \int d\mathbf{r}_1 d\mathbf{r}_2 e^{-\frac{\eta+1}{2\eta} \frac{z_1+z_2}{l_e}} \Gamma(\mathbf{r}_1, \mathbf{r}_2) e^{ik(\hat{\mathbf{s}}_i + \hat{\mathbf{s}}_e) \cdot (\mathbf{r}_1 - \mathbf{r}_2)} . \quad (85)$$

At this point, it is straightforward to see that if you take the direction of incoming and outgoing light to be equal and opposite, i.e., $\hat{\mathbf{s}}_e + \hat{\mathbf{s}}_i = 0$ and therefore $\eta = 0$, the integral of the Cooperon and Diffuson are exactly equivalent. This is what gives rise to the peak of the coherent backscattering cone being twice that of the background light in theory. Displayed in terms of the total averaged albedo:

$$\alpha(\theta = 0) = \alpha_D(0) + \alpha_C(0) = 2\alpha_D . \quad (86)$$

Now to continue solving for the Cooperon albedo: projecting the wave vectors onto the x - y plane as $\mathbf{k}_\perp = [\mathbf{k}_i + \mathbf{k}_e]_\perp = k[\hat{\mathbf{s}}_i + \hat{\mathbf{s}}_e]_\perp$, and replacing the structure factor with the diffusive probability as before, we have the form of the Cooperon albedo as

$$\alpha_C = \frac{c}{4\pi l_e^2} \int_0^\infty dz_1 dz_2 e^{-\frac{\eta+1}{2\eta} \frac{z_1+z_2}{l_e}} P_D(z_1, z_2) e^{i\mathbf{k}_\perp \cdot \boldsymbol{\rho}}, \quad (87)$$

where $\boldsymbol{\rho}$ here is the projection of the vector $\mathbf{r}_1 - \mathbf{r}_2$ onto the x - y plane. Following the same logic as that in solving the Diffuson and integrating, the albedo of the Cooperon becomes

$$\alpha_C = \frac{3}{8\pi} \frac{1}{\left[k_\perp l_e + \frac{\eta+1}{2\eta}\right]^2} \left[\frac{1 - e^{-2k_\perp z_0}}{k_\perp l_e} + \frac{2\eta}{\eta+1} \right]. \quad (88)$$

In Fig. 10, the Cooperon albedo is shown, added to the nearly constant background Diffuson albedo, with the Diffuson contribution being the dashed line. In the specific case of Fig. 10, the parameters consist of those in a typical magneto optical trap (MOT) with a peak density of $5 \cdot 10^{10}$ atoms/cm³ and the atomic cross section of ⁸⁵Rb on the $5S_{1/2}F = 3 \rightarrow 5P_{3/2}F = 4'$ transition.

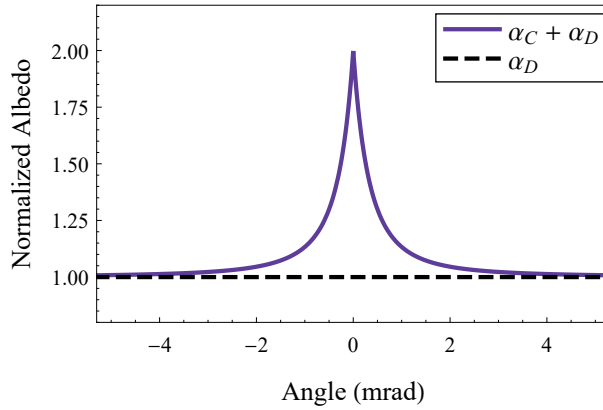


FIG. 10: The Cooperon albedo added to Diffuson albedo as a function of angle.

Where the disagreements occur in an experimental measurement compared to this theoretical calculation are due to the MOT gas cloud being spherical distribution of atoms and not a semi-infinite plane interface with classical scatterers as in the previous mathematical consideration. There are also the effects of depolarization reducing the total backscattering, non-elastic Raman scattering, dephasing of reciprocal paths due to the movement of

the scatterers, and due to the Zeeman sublevels of the atom not allowing for time reversed symmetry for initial and reciprocal paths of a given polarization of light [74, 77, 88].

2.3.2.3 Polarization Effects

To briefly discuss the effect that polarization takes upon the backscattered light, we must first take into account the time dependent albedo of classical scatterers for both the coherent and diffusive terms. Here we assume that the angular dependence is very small, which leaves the value of $\eta = 1$ and $k_{\perp} = k\sin\theta \approx k|\theta|$. From Eqs. (80) and (87), the time dependent albedo contributions can be represented as

$$\alpha_D(t) = \frac{c}{4\pi l_e^2} \int_0^{\infty} dz dz' e^{-z/l_e} e^{-z'/l_e} P_D(z, z', t) , \quad (89)$$

and

$$\alpha_C(t) = \frac{c}{4\pi l_e^2} \int_0^{\infty} dz dz' e^{-z/l_e} e^{-z'/l_e} P_D(k_{\perp}, z, z', t) , \quad (90)$$

where the respective now time dependent probabilities are represented by

$$P_D(z, z', t) = \int d^2\rho \frac{e^{-\rho^2/4Dt}}{(4\pi Dt)^{3/2}} \left[e^{-(z-z')^2/4Dt} - e^{-(z+z'+2z_0)^2/4Dt} \right] , \quad (91)$$

and

$$P_D(k_{\perp}, z, z', t) = \frac{e^{-Dk_{\perp}^2 t}}{\sqrt{4\pi Dt}} \left[e^{-(z-z')^2/4Dt} - e^{-(z+z'+2z_0)^2/4Dt} \right] . \quad (92)$$

In the long time limit, the time dependent albedo contributions can be approximated and expressed as

$$\alpha_D(t) \approx c(z_0 + l_e)^2 \frac{1}{(4\pi Dt)^{3/2}} , \quad (93)$$

and

$$\alpha_C(\theta, t) = \alpha_D(t) e^{-Dk_{\perp}^2 t} . \quad (94)$$

Furthermore, there is an additional factor included in the temporal integral to determine the angular distribution of the coherent albedo to force the integral vanish at small times, leaving the purely angular dependence in the form of

$$\alpha_C(\theta) \sim \int_0^{\infty} e^{-\frac{1}{3}(kl_e\theta)^2 t/\tau} \frac{1}{t^{3/2}} [1 - e^{-t/\tau}] dt , \quad (95)$$

where τ is the average time between single scattering events. The form of this integral will be used when including polarization effects.

Now to include the effects of polarization, we introduce the depolarization coefficients in terms of the polarization channels that CBS is observed, with $||$ representing channels that are

analyzed with the same polarization as the incoming light, i.e., the H_{\parallel} and L_{\parallel} channels and \perp representing the perpendicularly analyzed CBS channels H_{\perp} and L_{\perp} channels, where H corresponds to polarizations with helicity such as σ_+ , σ_- , and L refers to linear polarization. The depolarization coefficients are given as

$$d_{\parallel}(t) = \frac{\Gamma_{\parallel}^D(t)}{\Gamma_{\parallel}^D(t) + \Gamma_{\perp}^D(t)} \quad \text{and} \quad d_{\perp}(t) = \frac{\Gamma_{\perp}^D(t)}{\Gamma_{\parallel}^D(t) + \Gamma_{\perp}^D(t)}. \quad (96)$$

To determine the structure factor contributions in the parallel and perpendicular channels, we must turn to the tensor equation representation of the structure factor. We will not go into the derivation of this tensor equation, but state that its form is

$$\Gamma_{\alpha\beta,\gamma\delta} = \frac{1}{2}(\Gamma_1 + \Gamma_2)\delta_{\alpha\gamma}\delta_{\beta\delta} + \frac{1}{2}(\Gamma_2 - \Gamma_1)\delta_{\alpha\delta}\delta_{\beta\gamma} + \frac{1}{3}(\Gamma_0 - \Gamma_2)\delta_{\alpha\beta}\delta_{\gamma\delta}. \quad (97)$$

In the case of analyzing the light in the diffusive regime of the same polarization as the incident light, corresponding to the parallel channels, we have

$$\Gamma_{\alpha\alpha,\alpha\alpha} = \Gamma_{\parallel}^D = \frac{1}{3}(\Gamma_0 + 2\Gamma_2). \quad (98)$$

For perpendicular channels in the diffusive case

$$\Gamma_{\alpha\alpha,\beta\beta} = \Gamma_{\perp}^D = \frac{1}{3}(\Gamma_0 - \Gamma_2). \quad (99)$$

As for the coherent contributions, the structure factor in the parallel case matches that of the diffusive contribution, and the perpendicular polarization structure factor is

$$\Gamma_{\alpha\beta,\beta\alpha} = \Gamma_{\perp}^C = \frac{1}{2}(\Gamma_2 - \Gamma_1). \quad (100)$$

In general, the structure factor modes Γ_1 and Γ_2 decay rapidly compared to Γ_0 , which will be used in the calculation of depolarization effects that occur at large times. Now with the specific channels in this representation, the depolarization coefficients can be determined and thus are

$$d_{\parallel}(t) = \frac{\Gamma_0 + 2\Gamma_2}{2\Gamma_0 + \Gamma_2} \quad \text{and} \quad d_{\perp}(t) = \frac{\Gamma_0 - \Gamma_2}{2\Gamma_0 + \Gamma_2}. \quad (101)$$

At long times, with Γ_1 , Γ_2 rapidly decaying, it is clear that the depolarization coefficients approach $\frac{1}{2}$. Now with the depolarization coefficients and their behavior established, we define the factors

$$Q_{\parallel}(t) = \frac{\Gamma_{\parallel}^C(t)}{\Gamma_{\parallel}^D(t)} \quad \text{and} \quad Q_{\perp}(t) = \frac{\Gamma_{\perp}^C(t)}{\Gamma_{\perp}^D(t)}, \quad (102)$$

which describe the attenuation of coherence effects over time. The effect of these factors can be shown more explicitly with the definitions of the channel specific structure factors inserted, giving the following relations:

$$Q_{\parallel}(t) = \frac{\Gamma_0 + 2\Gamma_2}{\Gamma_0 + 2\Gamma_2} \quad \text{and} \quad Q_{\perp}(t) = \frac{\frac{1}{2}(\Gamma_2 - \Gamma_1)}{\frac{1}{3}(\Gamma_0 - \Gamma_2)}. \quad (103)$$

Clearly, for the parallel channel this factor is one and for the perpendicular channel goes to zero at large times. We can finally write the albedo of the Cooperon for the parallel channel

$$\alpha_C^{\parallel}(\theta) = \int_0^{\infty} \alpha_D(t) d_{\parallel}(t) e^{-Dt(\frac{2\pi}{\lambda}\theta)^2} [1 - e^{-t/\tau}] dt, \quad (104)$$

and for the perpendicular channel

$$\alpha_C^{\perp}(\theta) = \int_0^{\infty} \alpha_D(t) d_{\perp}(t) Q_{\perp}(t) e^{-Dt(\frac{2\pi}{\lambda}\theta)^2} [1 - e^{-t/\tau}] dt, \quad (105)$$

where the factor $Q_{\parallel} = 1$ in the parallel integral. The diffusive contributions are simply

$$\alpha_D^{\parallel} = \int_0^{\infty} \alpha_D(t) d_{\parallel}(t) dt \quad \text{and} \quad \alpha_D^{\perp} = \int_0^{\infty} \alpha_D(t) d_{\perp}(t) dt. \quad (106)$$

At large times ($t \gg \tau$), the ratio of coherent contributions to incoherent contributions in the exact backwards direction can be written

$$r_{\parallel} = \frac{\int_0^{\infty} \alpha_D(t) d_{\parallel}(t) dt}{\int_0^{\infty} \alpha_D(t) d_{\parallel}(t) dt}, \quad (107)$$

in the parallel case. For the perpendicular, we have

$$r_{\perp} = \frac{\int_0^{\infty} \alpha_D(t) d_{\perp}(t) Q_{\perp}(t) dt}{\int_0^{\infty} \alpha_D(t) d_{\perp}(t) dt}. \quad (108)$$

This ultimately expresses that due to polarization, for *classical scatterers* the perpendicularly analyzed channels, L_{\perp} and H_{\perp} , have a reduction in the CBS cone height compared to the parallel channels, based on the total time accrued over scattering paths. As for the light scattering of atoms, somewhat unexpectedly, the opposite is true, as will be shown in experiment. Atoms, due to their internal structure show sensitivity to the polarization of the excitation field, which thus suggests that the quantum mechanical nature of the light-atom interaction must be considered. Atoms also interact with linearly polarized light and circularly polarized light differently, therefore in the consideration of the contributions to the Cooperon and Diffuson albedos, the parallel and perpendicularly analyzed channels must be calculated separately for linearly and circularly polarized light.

The structure factor for the atomic case, analogous to Eq. (97), is given as

$$\Gamma^D(\hat{\epsilon}, \hat{\epsilon}') = \frac{1}{2} (\Gamma_1^D + \Gamma_2^D) |\hat{\epsilon} \cdot \hat{\epsilon}'|^2 + \frac{1}{2} (\Gamma_2^D - \Gamma_1^D) |\hat{\epsilon} \cdot \hat{\epsilon}'|^2 + \frac{1}{3} (\Gamma_0^D - \Gamma_2^D) , \quad (109)$$

for the Diffuson contribution, and for the Cooperon contribution we have

$$\Gamma^C(\hat{\epsilon}, \hat{\epsilon}') = \frac{1}{2} (\Gamma_1^C + \Gamma_2^C) |\hat{\epsilon} \cdot \hat{\epsilon}'|^2 + \frac{1}{3} (\Gamma_0^C - \Gamma_2^C) |\hat{\epsilon} \cdot \hat{\epsilon}'|^2 + \frac{1}{2} (\Gamma_2^C - \Gamma_1^C) , \quad (110)$$

where $\hat{\epsilon}$ is the unit vector in spherical basis coordinates of the incoming light polarization and $\hat{\epsilon}'$ is the outgoing polarization unit vector. From the previous discussion on classical scatterers, we determined that the factor $Q(t)$ was the determining factor of the loss of coherence at long times, therefore with the calculation with atoms, we have four different factors. For the two linearly polarized channels we have

$$Q_{\parallel}^L = \frac{\Gamma_0^C + 2\Gamma_2^C}{\Gamma_0^D + 2\Gamma_2^D} \quad \text{and} \quad Q_{\perp}^L = \frac{3}{2} \cdot \frac{\Gamma_2^C - \Gamma_1^C}{\Gamma_0^D - \Gamma_2^D} . \quad (111)$$

The assumptions previously for the classical scatterers do not necessarily apply here since the modes of the Cooperon and Diffuson are not directly comparable and are determined by propagators based on polarization relaxation times [89], but under the approximation that they behave similarly, that is Γ_0 dominating at long times, it would appear that $Q_{\perp}^L < Q_{\parallel}^L$, which experimentally is observed to be true for atoms and also is similar to the polarization effects of classical scatterers.

As for the circularly polarized light channels, the factors are

$$Q_{\parallel}^H = \frac{6\Gamma_2^C}{2\Gamma_0^D + 3\Gamma_1^D + \Gamma_2^D} \quad \text{and} \quad Q_{\perp}^H = \frac{2\Gamma_0^C - 3\Gamma_1^C + \Gamma_2^C}{2\Gamma_0^D - 3\Gamma_1^D + \Gamma_2^D} . \quad (112)$$

Making similar assumptions as before implies now that $Q_{\parallel}^H < Q_{\perp}^H$, which does not align with the classical expectation. This result is experimentally observed to be true as well, namely with the H_{\perp} channel displaying the best CBS signals in cold ^{85}Rb . However, it must be stated that the enhancement observed in each channel of polarization depends on the atomic states that the probe is interacting with and internal structure of the element that backscattering is occurring from, as shown in Ref. [76].

CHAPTER 3

EXPERIMENTAL OVERVIEW

This experiment utilizes a standard 3D rubidium 85 magneto optical trap (MOT) as the light scattering medium. The laser and optical setup, experimental timing, and other relevant information for this dissertation will be discussed in this chapter.

3.1 LASER ARRANGEMENT

Before describing the finer details of the laser setup, we must establish the necessary atomic transitions required for the experiment. The full atomic energy levels of ^{85}Rb relevant to the laser transitions of this experiment are shown in Fig. 11, with the energy levels of ^{87}Rb shown for comparison. The atomic transition used for the MOT beam is the $5S_{1/2} F = 3 \rightarrow 5P_{3/2} F' = 4$, with the beam 12 MHz ($\sim 2\Gamma$) negatively detuned for laser cooling of the ^{85}Rb atoms within the vacuum chamber. A magnetic field generated by anti-Helmholtz coils exploits the Zeeman splitting of the atoms in combination with circularly polarized light, to spatially confine the atoms. The probe is tuned near the $5S_{1/2} F = 3 \rightarrow 5P_{3/2} F' = 4$. The control beam in this experiment is tuned near the $5P_{3/2} F' = 4 \rightarrow 5D_{5/2} F'' = 5$. In this text the shorthand may be used where F (without a prime) represents hyperfine levels in the $5S_{1/2}$ state, F' references those in the $5P_{3/2}$ excited state, and F'' refers to hyperfine levels in the $5D_{5/2}$ excited state.

When discussing the probe and control fields in the later analysis sections, subscripts will be used to differentiate the two beams, for example Ω_p , Ω_c are the Rabi frequencies of the probe and control respectively. Also, while not a property of the probe beam itself, the natural linewidth of the $5P_{3/2}$ state will be referred to as Γ_p due to that excited state being associated with the transition of the probe laser.

Simplifying the system from Fig. 11 to the atomic states corresponding to lasers used in this experiment, we have the states shown in Fig. 12, where ω_p , ω_c are the frequencies of the probe and control respectively. The decay rate Γ_{5D} corresponds to decay from the $5D_{5/2}$ to the $6P_{3/2}$ and Γ_{6P} represents the decay rate of the $6P_{3/2}$ to the ground state, spontaneously emitting 420 nm light. Table 1 gives the values of the transition rates (Γ), radiative lifetimes (τ), and vacuum wavelength (λ) of the states involved in the experiment.

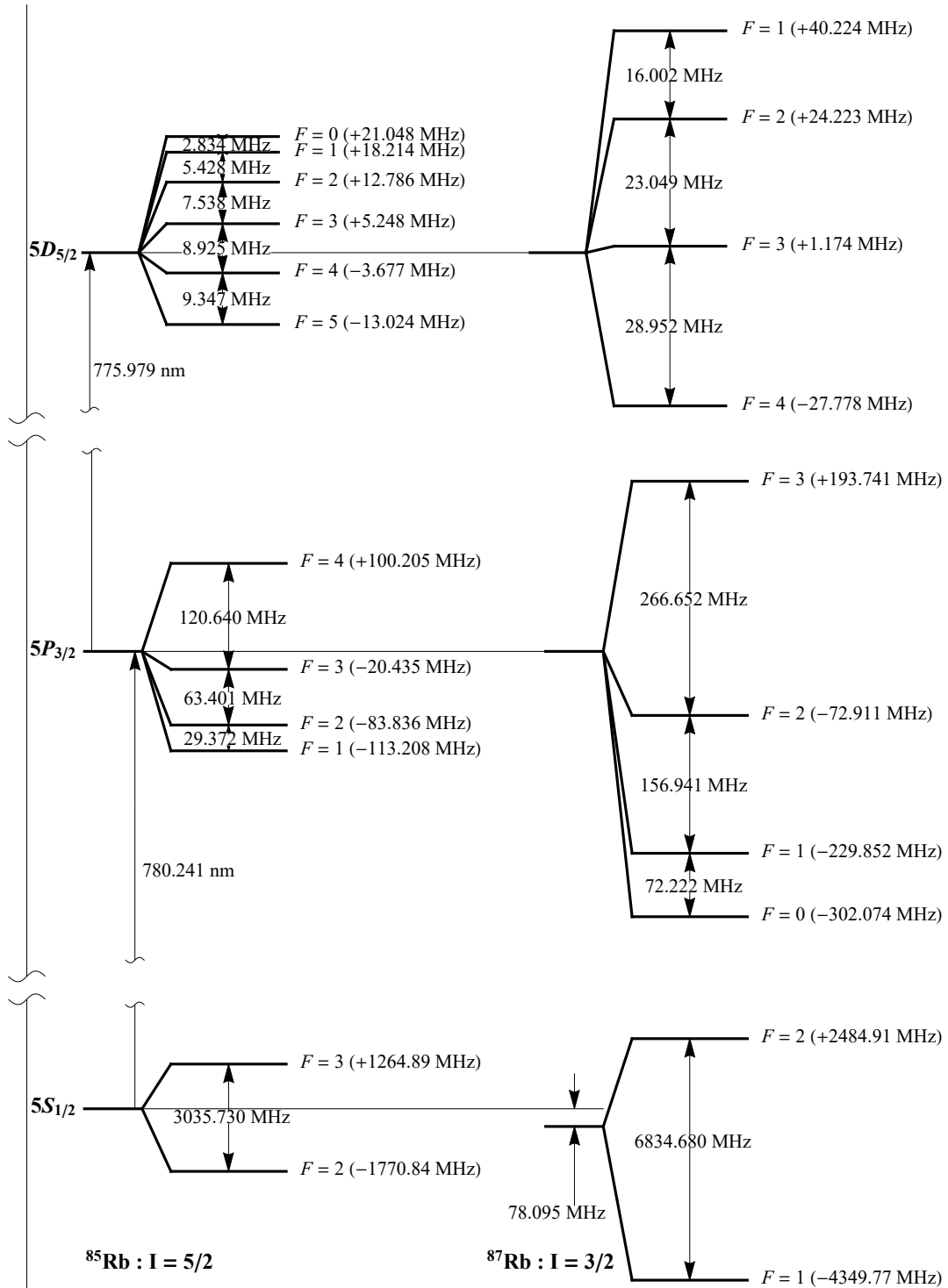


FIG. 11: Rubidium 85 and 87 hyperfine energy splittings for the $5S_{1/2}$, $5P_{3/2}$, and $5D_{5/2}$ states.

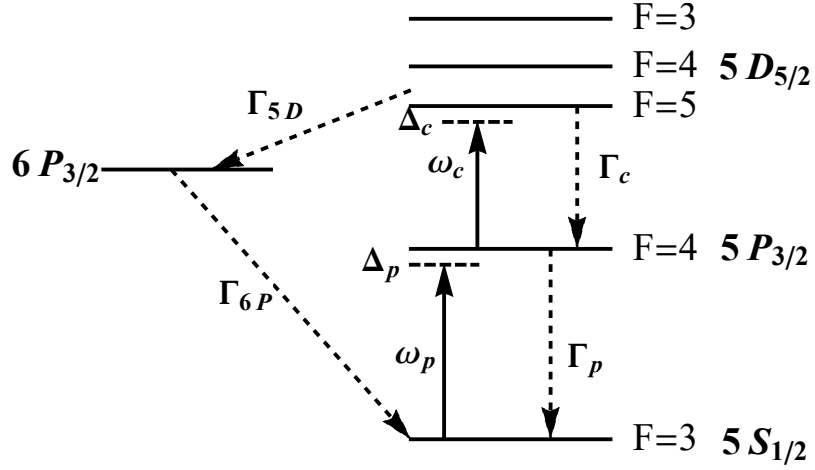


FIG. 12: Energy levels associated with this experiment, omitting hyperfine levels that are not directly accessed. The angular frequencies of the probe and control are ω_p and ω_c . Corresponding decay rates in Table 1.

TABLE 1: Atomic transition properties.

Atomic Transition	Γ (MHz)	τ (ns)	λ (nm)
$5P_{3/2} \rightarrow 5S_{1/2}$	$2\pi \cdot 6.07^a$	26.23^a	780.24^a
$5D_{5/2} \rightarrow 5P_{3/2}$	$2\pi \cdot 0.66^b$	254^c	775.98^c
$5D_{5/2} \rightarrow 6P_{1/2}$	$2\pi \cdot 0.225^c$	707.5^c	5233^c
$6P_{3/2} \rightarrow 5S_{1/2}$	$2\pi \cdot 0.318^c$	500.8^c	420.3^c

^aReference [86].

^bReference [39].

^cReference [90].

Four laser beam sources are used in this experiment, two operating at 780 nm in a master-slave configuration, and two operating at 776 nm in a master-slave configuration.

The master 780 nm laser is a home built external cavity diode laser (ECDL) that is frequency stabilized via Doppler-free saturated absorption spectroscopy. The master 780 nm

laser is frequency stabilized to the $F' = 2/4$ crossover from the $5S_{1/2}F = 3$ ground state, corresponding to about -92 MHz from the $5P_{3/2}F' = 4$ level. The beam is split initially to feed into the injection locked laser diode, and then with the remainder of the light splitting again to the saturated absorption spectroscopy and probe optics.

The portion of the beam going to the probe optics passes through a 80 MHz acousto-optic modulator (AOM) in a double pass optical arrangement and then a single pass through a second 80 MHz AOM to act as a light switching mechanism, and to shift the frequency of the laser near the $5S_{1/2}F = 3 \rightarrow 5P_{3/2}F = 4'$ atomic transition to act as the experimental probe. A representative diagram of the 780 nm laser optics is shown in Fig. 13. A legend for all optical diagrams is in Appendix B Fig. 95.

The injection locked laser passes through a 80 MHz AOM for switching and frequency adjustment and is then fiber launched to the vacuum chamber to be split into the 6 individual MOT beams. Acting as a repumper, 3 GHz sidebands are applied to the injection locked MOT laser to keep atoms in the cycling transition. A small amount of the beam is picked off before the AOM to send to the 776 nm laser optics.

The 776 nm laser system starts with a master ECDL that splits to a rubidium cell for frequency reference with the remainder of the beam going into the injection locked 776 nm laser. The frequency reference uses the previously mentioned picked off portion of the 780 nm laser overlapped with the 776 nm laser to excite atoms in the rubidium cell to the $5D_{5/2}$ energy state. Once excited to that state, the atoms can decay to the $6P_{3/2}$ state which then can decay at 420 nm to the ground state and is detected by a PMT with a 420 nm coated filter as shown in Fig. 14.

The 776 nm injection locked laser passes through an 80 MHz AOM for switching and fine frequency adjustment before being fiber launched to act as the experimental control beam.

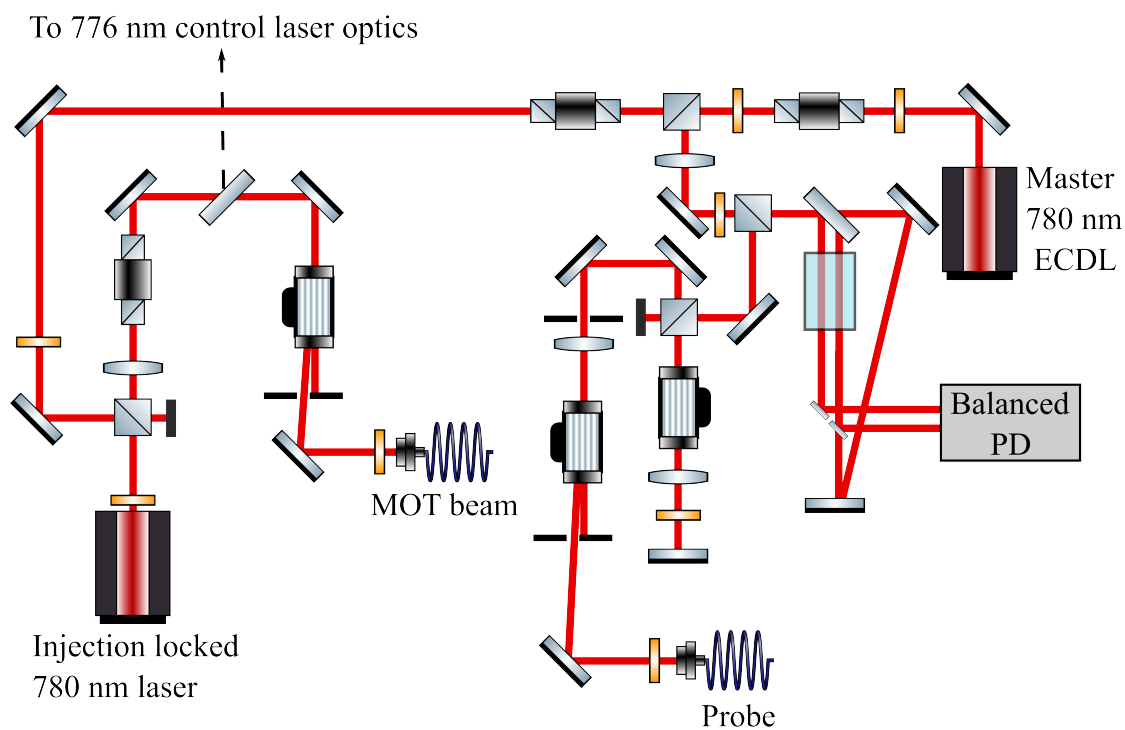


FIG. 13: Representative diagram of the optical setup of the 780 nm laser system. Beam pickoffs for spectrum analyzer not shown.

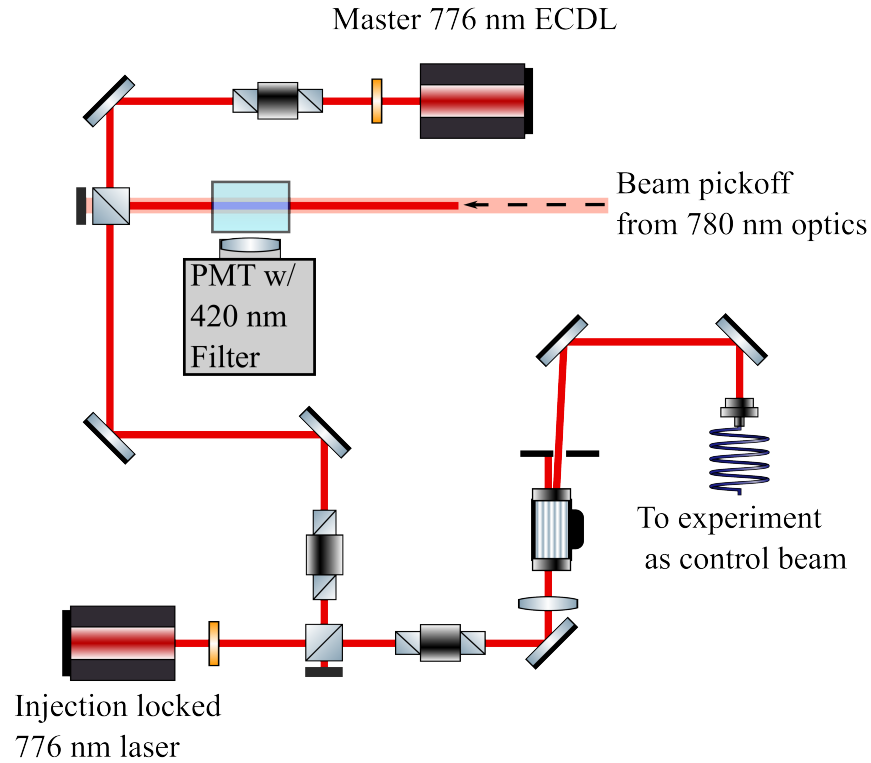


FIG. 14: Representative diagram of the optical setup of the 776 nm laser system. Beam pickoffs for spectrum analyzer not shown.

An optical diagram of the experimental optics is shown in Fig 15. The MOT beam is represented in green, probe in red, and control in blue. Dashed lines show alternative paths when the flip mirror is engaged and also the path of the CBS signal. When the flip mirror is engaged, the control is reflected into the chamber, counterpropagating with the probe beam, which is what will be referred to as counterpropagating EIT in later sections. In this setup, EIT can be measured but CBS cannot be recorded due to the control beam being directed into the path of CBS detection. When the flip mirror is disengaged, the control beam passes by and is directed into the side window of the chamber, orthogonal to the probe beam. When the control beam is orthogonal to the probe, EIT can be recorded simultaneously with CBS signals, which is the primary experimental focus of this study.

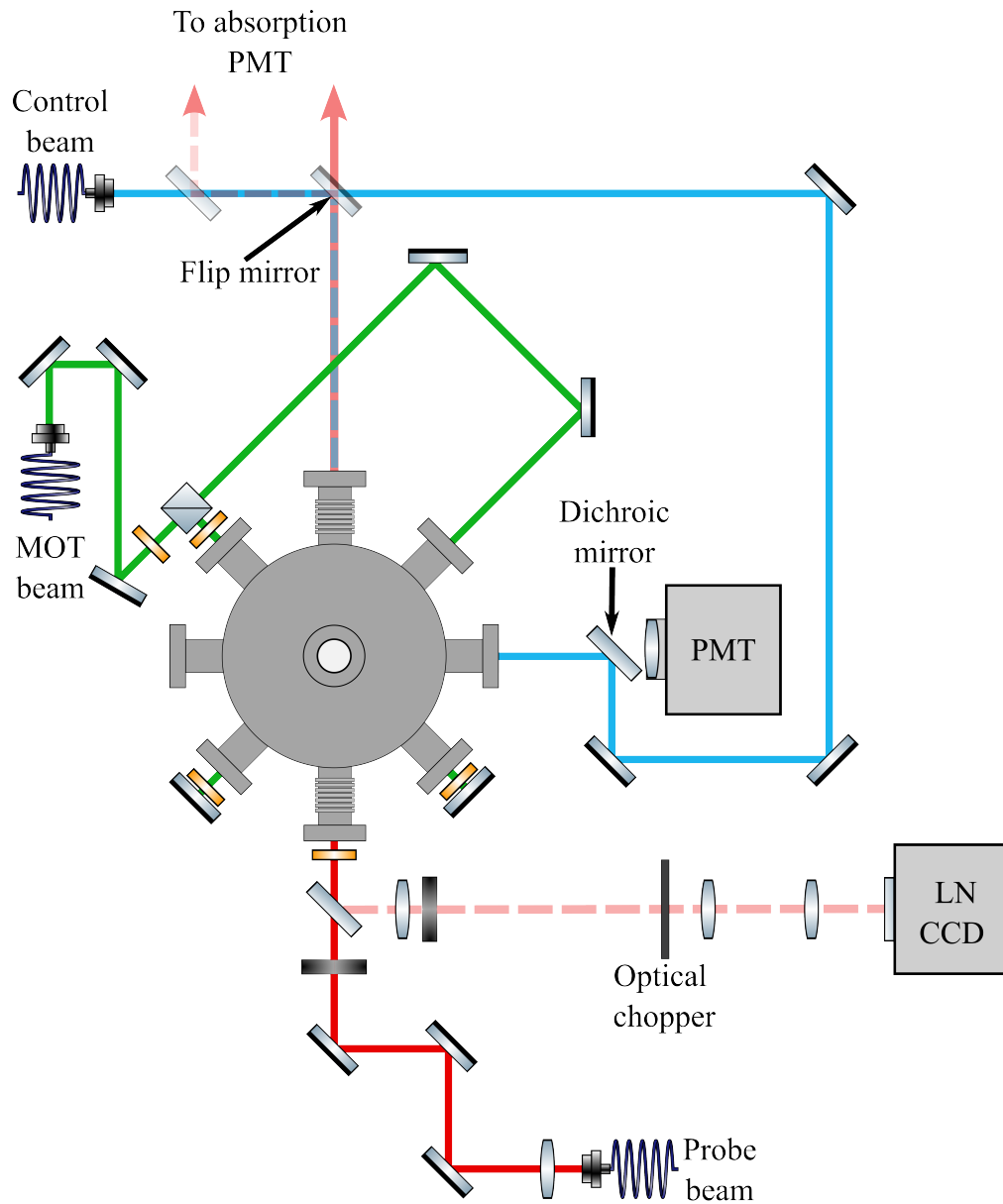


FIG. 15: Representative diagram of experimental table optical system. Each beam represented by a different color with the third dimension (up/down) of the MOT beam not shown for simplicity. Dashed line towards the LN CCD represents the path of CBS detection. Beam dumps not shown.

3.2 ELECTROMAGNETIC INDUCED TRANSPARENCY DATA ACQUISITION

To measure the effect of EIT in this particular case, a photomultiplier tube was implemented to detect the small amounts of probe transmission through the cold atomic sample. The PMT signal for each probe pulse was recorded and then averaged over 128 acquisitions for each of the three measurements needed to determine and analyze EIT effects.

The first consists of the probe beam without the cold atoms and without control beam present as a baseline pulse, corresponding to the signals in black in Fig. 16. The second is with the cold atoms present and no control beam for directly measuring probe transmission signals through the atomic cloud. Subtracting the second standard transmission signal from the first baseline measurement results in a mapping of the absorption which corresponds to the signals in 16(a). The third measurement is with the cold atoms and control beam present to detect the probe transmission under EIT conditions. Subtracting the third transmission signal under EIT conditions again from the probe with no atoms present results in mapping of the absorption as well, but due to the presence of the control, is modified from that of the standard absorption. An example EIT signal and the corresponding subtraction from the probe is shown in Fig. 16(b). These signals were then integrated over the pulse time to give a value for each detuning, corresponding to a single data point in the results presented later.

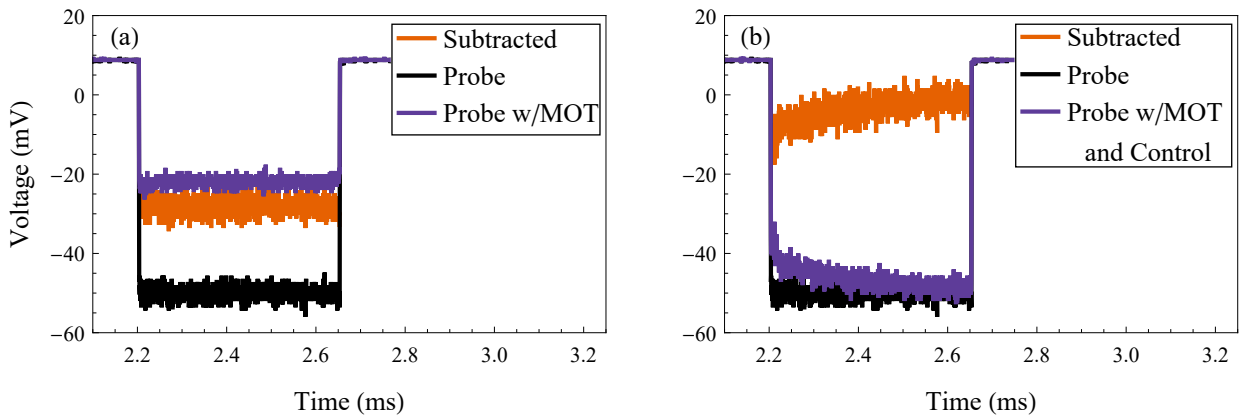


FIG. 16: Sample signals observed during the EIT experiment averaged 128 times with (a) showing signals for determining probe absorption and (b) showing signals for EIT.

It must be stated that when measuring EIT on these respective transitions over the 450 μs pulse time, there is a time dependence, with the effect mitigating over time. This is likely due to an optical pumping mechanism of atoms excited to the $5D_{5/2}F = 4, 3$ states decaying to the $6P_{3/2}$ state, then decaying to the $5S_{1/2}F = 2$, resulting in less available atoms in the $F = 3$ ground state to be scattered. There will also be loss corresponding to quadrupole transitions to the $F = 2$ ground state, due to the lack of a repumper during the EIT measurements. This time dependence is the reasoning for the integration of the signals as mentioned.

A second PMT was used to collect 420 nm fluorescence orthogonal to the probe beam during the pulses with the control beam present. To collect 420 nm fluorescence from the $6P_{3/2}$ state, a dichroic shortpass mirror (Thorlabs DMSP490) was used to allow light collection by a PMT placed behind the mirror, while reflecting the control beam at 776 nm, as shown in Fig. 15.

3.3 COHERENT BACKSCATTERING DATA ACQUISITION

To properly detect coherently backscattered signals, great care must be taken to reduce any light that is not due to backscattering, i.e. reflections of the probe beam, reflections of light from within the chamber from other lasers, to even small light sources within the room, such as LEDs on lab equipment. For the path of the probe beam, the beam first passes through an initial polarizer and then a wedged 70:30 (Reflection:Transmission) anti-reflection coated beam splitter (Thorlabs BST17). The wedge of the beam splitter allows for separation of reflections from the surface of the splitter from that of the back surface of the splitter. The beam passes through the splitter with 30% transmission and through a removable quarter wave plate and into the chamber to interact with the MOT. Coherently backscattered light off of the MOT returns to the splitter, with 70% reflected to the optical detection system. The windows on both sides of the chamber that the probe passes through are wedged, to minimize reflections from the front and back side of the windows going directly backwards, and are anti-reflection coated (AR) for further reflection minimization. The AR coated windows are also on bellows to fine adjust the angle in case of excess light scattering in the backwards direction. Carefully placed beam dumps are located on the side reflecting the probe opposite to the CBS detection optics, and on the far side of the chamber past the flip mirror in Fig. 15, to further ensure that no probe light other than that of the backscattered light of the MOT is detected. It cannot be overstated how arduous of a process minimizing unwanted reflections and light was for proper signal detection. An experiment of this type

cannot be performed with the slightest of external light contaminating any of the optical setup.

3.3.1 OPTICAL DETECTION SYSTEM

A charged coupled device (CCD) was used to obtain coherent backscattering signals. To achieve the levels of signal to noise necessary, a liquid nitrogen cooled CCD was used (Princeton Instruments). Without the liquid nitrogen cooling, the inherent dark count noise overtakes the coherently backscattered light. A photo of the CCD is included in its enclosure in Fig. 17. The CCD array is 512x512 pixels, with each pixel being a square $24 \times 24 \mu\text{m}$ in size. The pixel size is the limiting value in determining the angular resolution of the optical system, once lenses are accounted for.



FIG. 17: Photograph of the LN CCD during liquid nitrogen filling.

A representative diagram of the optics is shown in Fig. 18. For the coherent backscattering collection optics, the first lens of the system acts as a collection lens, with a focal length of 450 mm, referred to as L1 in Fig. 18. With this focal length, the approximate angular resolution is 0.053 mrad. This resolution is determined by the inverse sine of the ratio of height of a pixel to the focal length of the collection lens. More specifically $\theta \approx \sin^{-1} \left(\frac{24 \cdot 10^{-3} \text{ mm}}{450 \text{ mm}} \right)$.

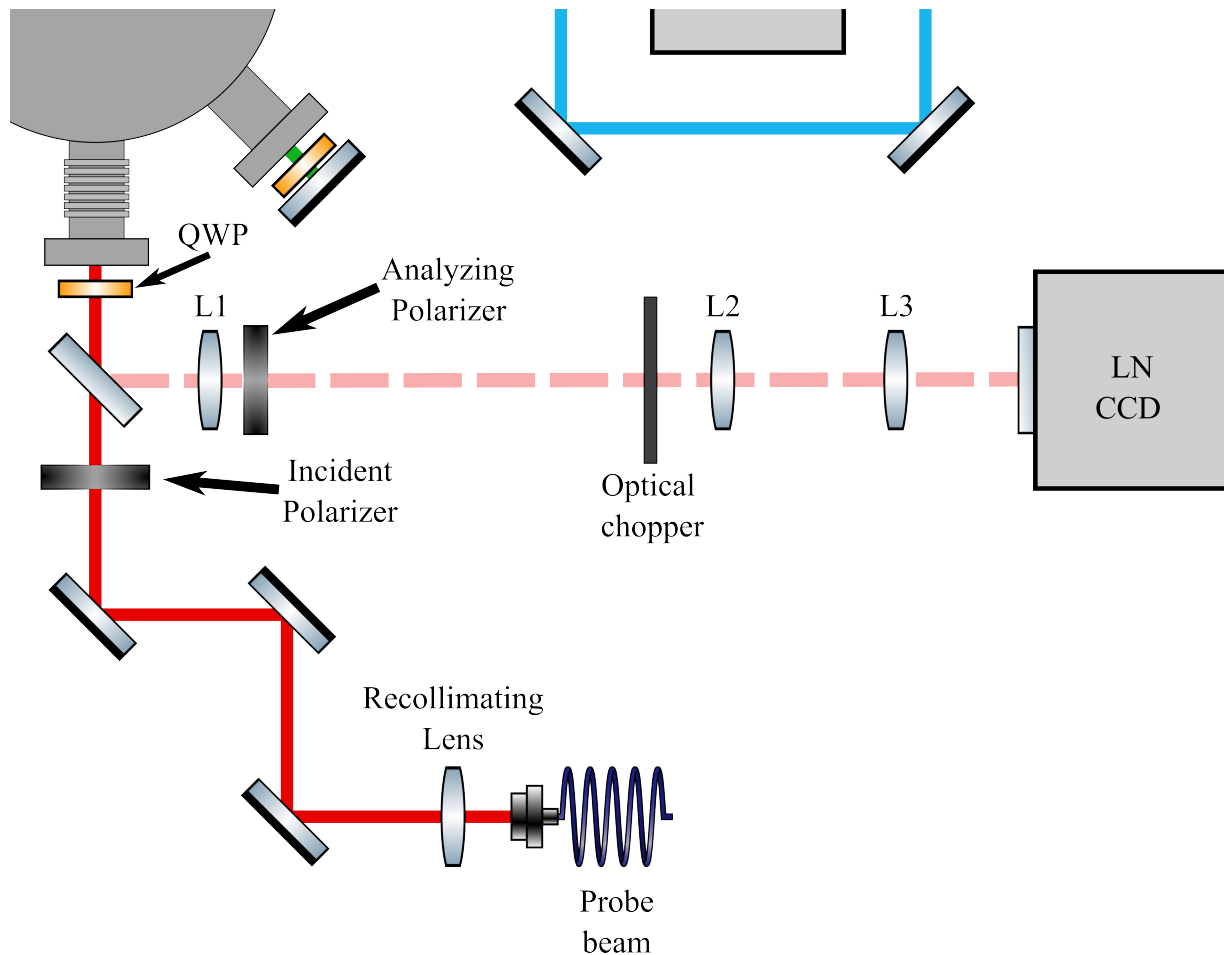


FIG. 18: Representative diagram of the CBS optical layout. L1 is 450 mm collection lens, L2 is 90 mm collimating lens, L3 is 90 mm refocusing lens. Dashed line towards the LN CCD represents the path of CBS detection. Optical iris in front of chopper omitted in diagram.

At the focal point of the 450 mm lens, an optical chopper is placed for experimental timing purposes and to prevent unwanted fluorescence from the MOT during probe pulses, to be discussed later. Also near the focal point of the collection lens is an optical iris (not shown in diagram), to eliminate stray off axis rays for better signal to noise. Positioned 90 mm further from the focus of the collection lens is a collimation lens with a focal length of 90 mm (L2), followed by a second 90 mm focal length lens (L3). The CCD is then placed at the focal point (90 mm) of the last lens to image the angular displacement. An example of the lens system ray diagram is shown in Fig. 19 from a Mathematica program used to visualize the mapping of the angular resolution of the lens system. However, if the second and third lenses are positioned properly, the angular resolution is only determined by the collection lens focal length and pixel size as previously mentioned.

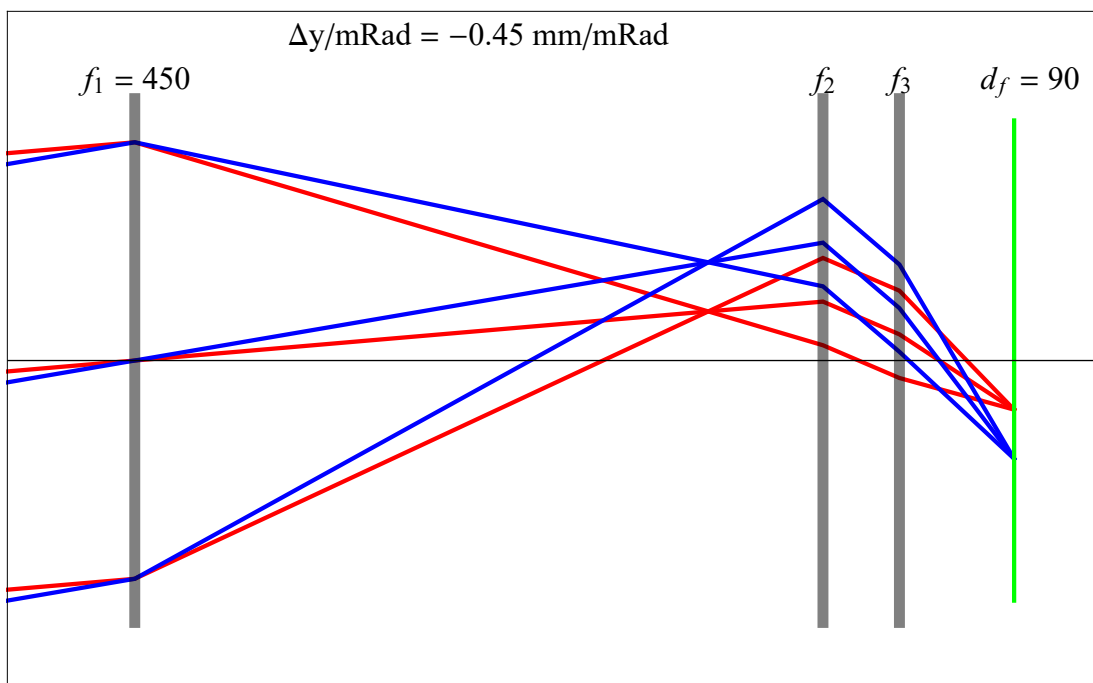


FIG. 19: A sample image from a ray diagram Mathematica program used to determine angular resolution. In units of mm.

3.3.2 CBS POLARIZATION CHANNELS

There are four observable polarization channels of CBS: H_{\perp} , H_{\parallel} , L_{\perp} , and L_{\parallel} . These channels correspond to the incident vs analyzing polarizer degree angles as shown in Table 2. The H_{\perp} and H_{\parallel} channels begin as vertically polarized light, then pass through a quarter waveplate (QWP) to induce the light into circular polarized light. The retro-reflection refers to the amount of light transmitted through the analyzing polarizer if the incident light were to be retro-reflected towards the analyzer with a mirror. For example, with the QWP in, the vertical linear polarized light becomes circular, then when retro-reflected, the circular polarization becomes reversed. The reversed circularly polarized light goes back through the QWP which makes the polarization perpendicular to the initial polarization, hence why H_{\perp} results in maximum transmission and H_{\parallel} results in minimal transmission. This is used as a device of understanding the role of the incident and analyzing polarizer in this experiment.

TABLE 2: Experimental polarization channel description.

Channel	QWP	Analyzer wrt. Incident	Retro-reflection
H_{\perp}	helicity non-preserving	\rightarrow	max
H_{\parallel}	helicity preserving	\uparrow	min
L_{\perp}	none	\rightarrow	min
L_{\parallel}	none	\uparrow	max

While it is useful to understand, an atomic gas does not scatter light in the same manner as a retro-reflecting mirror. Next, we look to determine the angular dependence of scattered light intensity from a gas [91]. The intensity detected is dependent on incident polarization of the excitation field, the physical location of the detector, and the angle of the analyzing polarizer. The detector is assumed to be along the transmission axis of the analyzer. This process is also under the assumption of fluorescence due to single scattering events and not multiple scattering. The geometry of light detection in general is shown in Fig 20, with rotations corresponding to Euler angles.

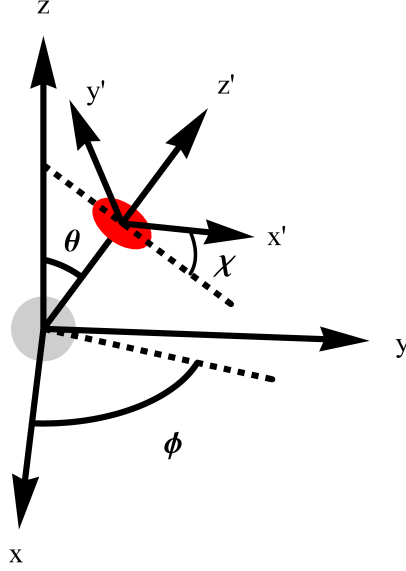


FIG. 20: General geometry of light detection with Euler angles ϕ , θ , and χ . [92]

In this experiment we take the Euler angle $\phi = 0$. The scattered light intensity, based on the detection angle θ , the analyzing polarizer angle χ , and light polarization β is determined by the following equation:

$$I(\theta, \chi, \beta) = \frac{1}{3}I_0 \left[1 - A_0 h^{(2)}(F', F) \left(\frac{1}{2}P_2(\cos\theta) - \frac{3}{4}\sin^2\theta \cos 2\chi \cos 2\beta \right) + \frac{3}{2}h^{(1)}(F', F) \mathcal{O}_0 \cos\theta \sin 2\beta \right], \quad (113)$$

where $h^{(k)}(F', F)$ are referred to as geometric factors and A_0 and \mathcal{O}_0 are parameters based on the alignment and orientation respectively. The form of the geometric factors $h^{(k)}(F', F)$ is given by the following:

$$h^{(1)}(F', F) = \frac{F' + 1}{\sqrt{F'(F' + 1)}}, \quad (114)$$

$$h^{(2)}(F', F) = -\frac{F' + 1}{2F' - 1}. \quad (115)$$

In the case of this experiment, $F' = 4$, $F = 3$, which gives $h^{(1)}(4, 3) = 5/\sqrt{20}$ and $h^{(2)}(4, 3) = -5/7$. The value A_0 is referred to as an alignment parameter and is given to be

$$A_0 = -(-1)^q \left(1 - \frac{1}{2}q^2 \right) \frac{2F' + 3}{5F'}. \quad (116)$$

The value \mathcal{O}_0 is denoted as the orientation vector, which is the average value of the angular momentum pseudovector \mathbf{F} in a case such as this when treated with cylindrical symmetry and is represented by

$$\mathcal{O}_0 = \frac{\frac{1}{2}q(F' + 1)}{\sqrt{F'(F' + 1)}}, \quad (117)$$

where q is the spherical basis representation of the light polarization [91].

For the linear case, the Euler angles rotating the frame must correspond to the quantization axis which is the axis of light polarization. In the case of circularly polarized light, the Euler angles correspond to the propagation axis of the light [93]. Therefore in the situation of detecting linearly polarized light, $q = 0$ and the detection angle is $\theta = \frac{\pi}{2}$ in the backwards direction which gives

$$I_{\text{Lin}}(\chi, \beta) = \frac{I_0}{3} \left[1 + \frac{11}{112} (1 + 3\cos 2\chi \cos 2\beta) \right]. \quad (118)$$

For the circular case, the backwards direction corresponds to $\theta = \pi$ and $q = \pm 1$ which results in

$$I_{\sigma}(\chi, \beta) = \frac{I_0}{3} \left[\frac{123}{112} \mp \frac{15}{16} \sin 2\beta \right]. \quad (119)$$

It is interesting to note that the result for circularly polarized light does not show a dependence on the analyzing polarizer angle χ . The angles for each channel are shown in Table 3.

TABLE 3: Corresponding values and intensity for each detection channel.

Channel	θ	χ	β	$I(\theta, \chi, \beta)$
H_{\perp}	π	$\frac{\pi}{2}$	$\frac{\pi}{4}$	$0.05I_0$
H_{\parallel}	π	0	$\frac{\pi}{4}$	$0.05I_0$
L_{\perp}	$\frac{\pi}{2}$	$\frac{\pi}{2}$	0	$0.27I_0$
L_{\parallel}	$\frac{\pi}{2}$	0	0	$0.46I_0$

It is worth noting again that these are the predicted values for single scatters, whereas coherent backscattering is a multiple scattering effect. Therefore, channels with less scattered intensity theoretically should produce better backscattered signals vs noise. The channels

with helicity also show a minimum in the backwards direction, which can be seen in Fig. 21(b).

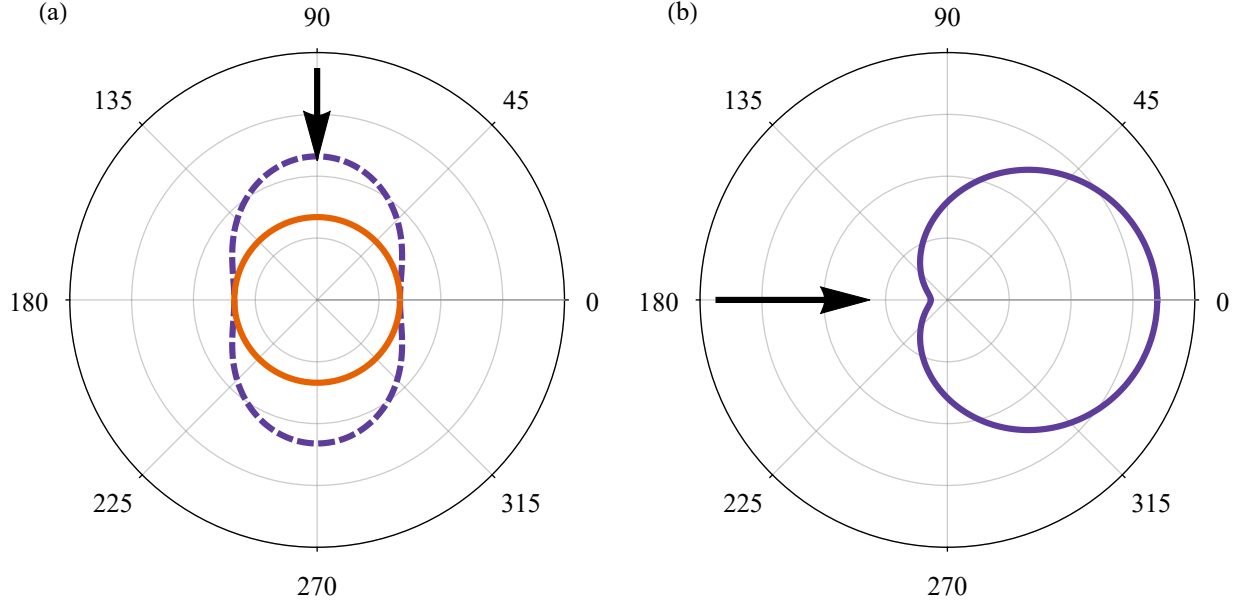


FIG. 21: Graphical representation of Eq. (113) as a function of θ . Black arrows indicate direction of probe with detection being in the opposite direction, i.e., backwards. (a) Linear polarized light with dashed purple representing the L_{\parallel} channel ($\chi = 0$) and orange representing the L_{\perp} channel ($\chi = \frac{\pi}{2}$). (b) Circularly polarized σ_+ light, representing the H_{\perp} and H_{\parallel} detection channels.

3.3.3 EXPERIMENTAL TIMING

The timing of this experiment is constrained to that of obtaining coherent backscattering signals therefore, the observed EIT must be within this timing window as well. A representative timing diagram is shown in Fig. 22. The experiment utilizes the optical chopper timing window to maximize signal to noise for CBS signals. Timing for the MOT, probe, and control are all dictated by the aforementioned AOMs being used as a switching mechanism. The MOT beam and magnetic field of the MOT are shut off well before the optical chopper

window opens, to prevent fluorescence from the MOT leaking into CCD images, roughly 1.75 ms and 2 ms respectively before the optical chopper allows light through. The optical chopper window is open for roughly 2.2 ms, with the probe and control pulsing for 450 μs in the center of the chopper opening window. The pulses were controlled by a Quantum Composers model 9614, with the optical chopper providing an output signal to act as a trigger. The signal from the MOT channel was used as a timing trigger sent to an oscilloscope for the EIT measurements. The chopper was set at 41 Hz, therefore a timing sequence as in Fig. 22 occurred 41 times per second. With the CCD collecting light for 10 minutes for all images and data points presented, which corresponds to roughly 11 seconds of CBS light collection.

A 10 minute background image is subtracted from the CBS signal to optimize the signal, under the same conditions, except with the magnetic trapping field off. The MOT beams remain pulsing at their usual time in case they are exciting atoms in the non trapped and cooled atomic vapor within the vacuum chamber. With the magnetic field off, the MOT does not form, therefore the background image should subtract off all scattering that does not occur from the MOT on average.

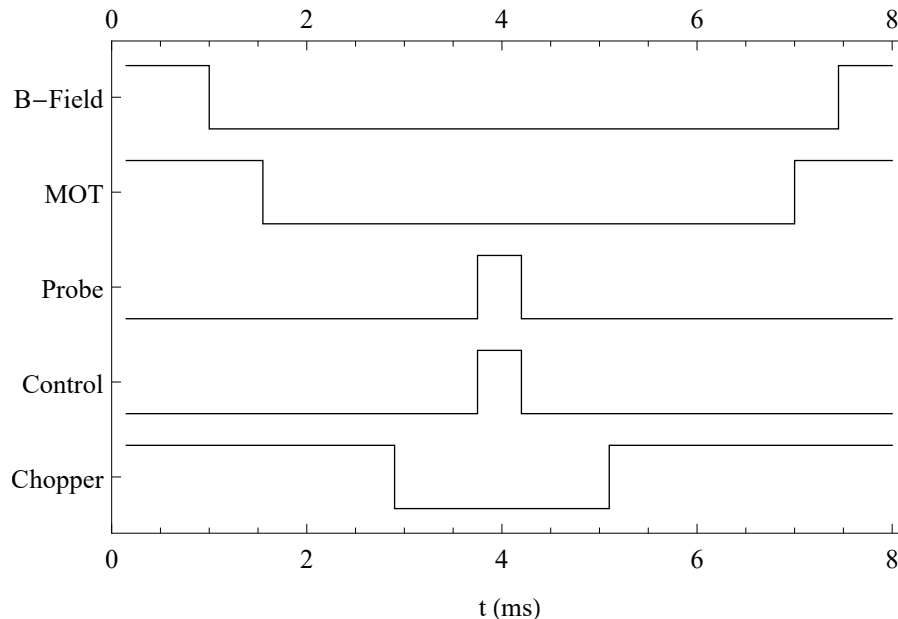


FIG. 22: Experimental timing diagram with up representing on and down representing off for each signal.

CHAPTER 4

ELECTROMAGNETICALLY INDUCED TRANSPARENCY

As a reminder from the discussion in Chapter 1, the observed effects due to the presence of a strong control field result in quantum destructive interference, along with Autler-Townes splitting, which occur simultaneously and are not clearly discernible. Thus, the window of transparency in the discussed data will be referred to as EIT, but will be encompassing both the effects of EIT and ATS. In this chapter, the experimental EIT and theoretical EIT results will be presented and compared.

4.1 EXPERIMENTAL EIT RESULTS

Here, the results from the experimental EIT in the counterpropagating regime will be displayed, to be compared to the orthogonal geometry that is implemented during CBS data collection, to ensure consistency, and to determine if there are any geometrical effects on EIT beam geometry. Each data point in the following experimental results section is from the average of 128 pulses. All corresponding EIT data is in terms of probe detuning. The standard probe Rabi frequency unless otherwise stated is $\Omega_p = 0.18\Gamma_p$ for all measurements.

4.1.1 COUNTERPROPAGATING EIT GEOMETRY

Recall that the collected data for EIT is limited to the timing window of the CBS experiment, due to having to fit the physical constraints to collect CBS signals. While CBS signals are not obtainable during the counterpropagating EIT experimental arrangement, we still maintain the proper timing to compare the physical effects to those of the orthogonal EIT arrangement.

4.1.1.1 Control Intensity Dependence

The dependence of the control intensity was one of the primary focus points of studying the effects of EIT, with the Rabi frequencies of the respective fields predicted to show a large dependence in the overall effect. Due to this intensities will be represented in the form of Rabi frequency, in terms of Γ_p . The results of EIT in the counterpropagating scheme are shown in Fig. 23, with ascending control field Rabi frequency from (a) to (f). Each plot

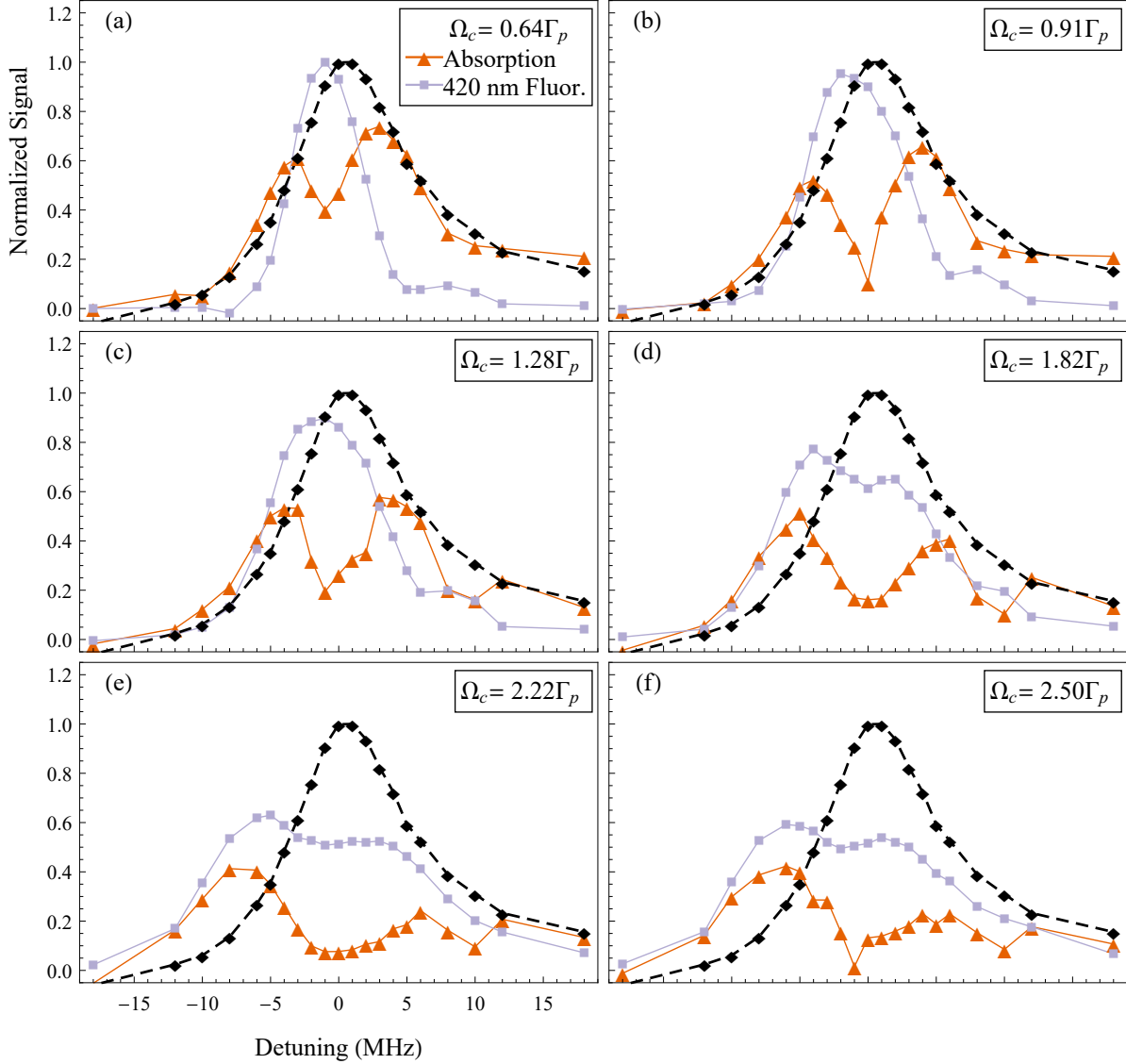


FIG. 23: All data represented as a function of probe detuning with σ_- probe polarization and horizontal π control polarization in the counterpropagating EIT geometry with probe Rabi frequency $\Omega_p = 0.18\Gamma_p$ and control detuning $\Delta_c = 0$. Black: probe absorption with no control field present. Orange: Probe with control field present. Purple: Fluorescence of the $6P_{3/2}$ state. (a)-(f) display various control Rabi frequencies specified in the legends.

shows the probe absorption with no control field present (black dashed), probe absorption with the control field present (orange), and the resulting 420 nm fluorescence from the $6P_{3/2}$

state (purple) recorded during EIT measurements, all as functions of detuning.

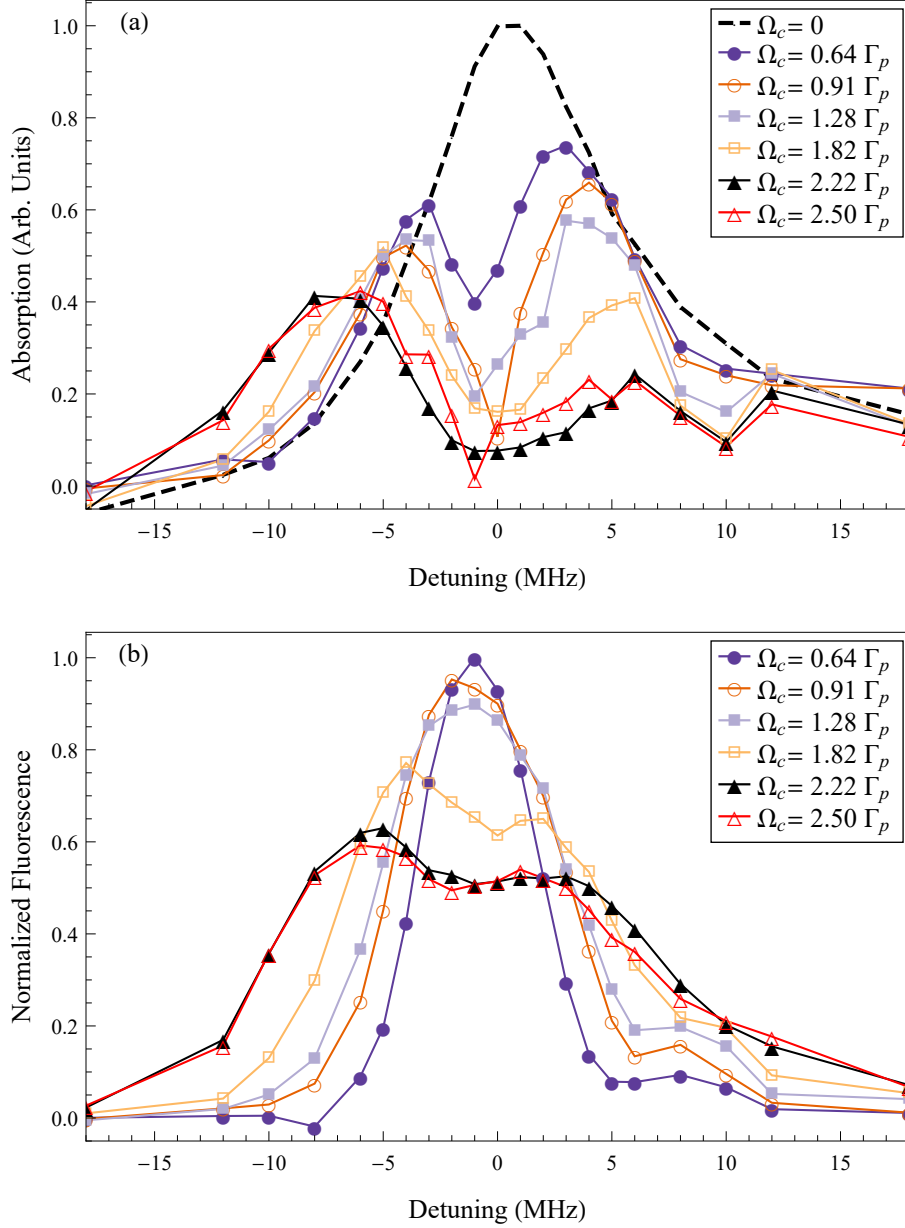


FIG. 24: Counterpropagating EIT with control detuning $\Delta_c = 0$ and probe Rabi frequency $\Omega_p = 0.18\Gamma_p$. (a) Probe absorption as a function of probe detuning at various control Rabi frequencies. (b) Fluorescence of the $6P_{3/2}$ energy level as a function of probe detuning at various control Rabi frequencies.

It is clear to see that as the control field Rabi frequency increases, the more pronounced the window of probe transmission becomes. The frequency band in which transmission occurs broadens as control power increases, while also allowing for more transmission close to resonance. This effect is shown more clearly in Fig. 24, with the depth and width of the EIT profile increasing with control power.

The detected fluorescence at 420 nm also broadens as a function of probe detuning as control Rabi frequency increases. The total fluorescence decreases near resonance at higher control power, while the total fluorescence further from resonance increases.

4.1.1.2 Polarization Dependence

The effect of using various polarizations of the control and probe beam were also studied to investigate the variation in which it would display on the results of EIT, to extend to the CBS experiment. Figure 25 shows various combinations of probe and control beam polarizations, displaying probe absorption as a function of probe detuning. For each polarization, the control Rabi frequency was $\Omega_c = 2.22\Gamma_p$ and probe Rabi frequency $\Omega_p = 0.18\Gamma_p$. For reference, the typical polarizations used when involving CBS for the H_\perp channel are σ_- for the probe, and linear (π) for the control field.

The results of the probe absorption are superimposed for each combination of probe and control polarizations in Fig. 26(a), with the fluorescence of the $6P_{3/2}$ state in (b) at each combination of polarizations, with the legend representing the probe and control polarizations respectively (p:c).

From Fig. 26, there does not seem to be a significant effect due to various combinations of probe and control polarization. Each probe absorption curve is roughly similar, with only the fluorescence from the σ_+ probe and linear control varying slightly from the rest.

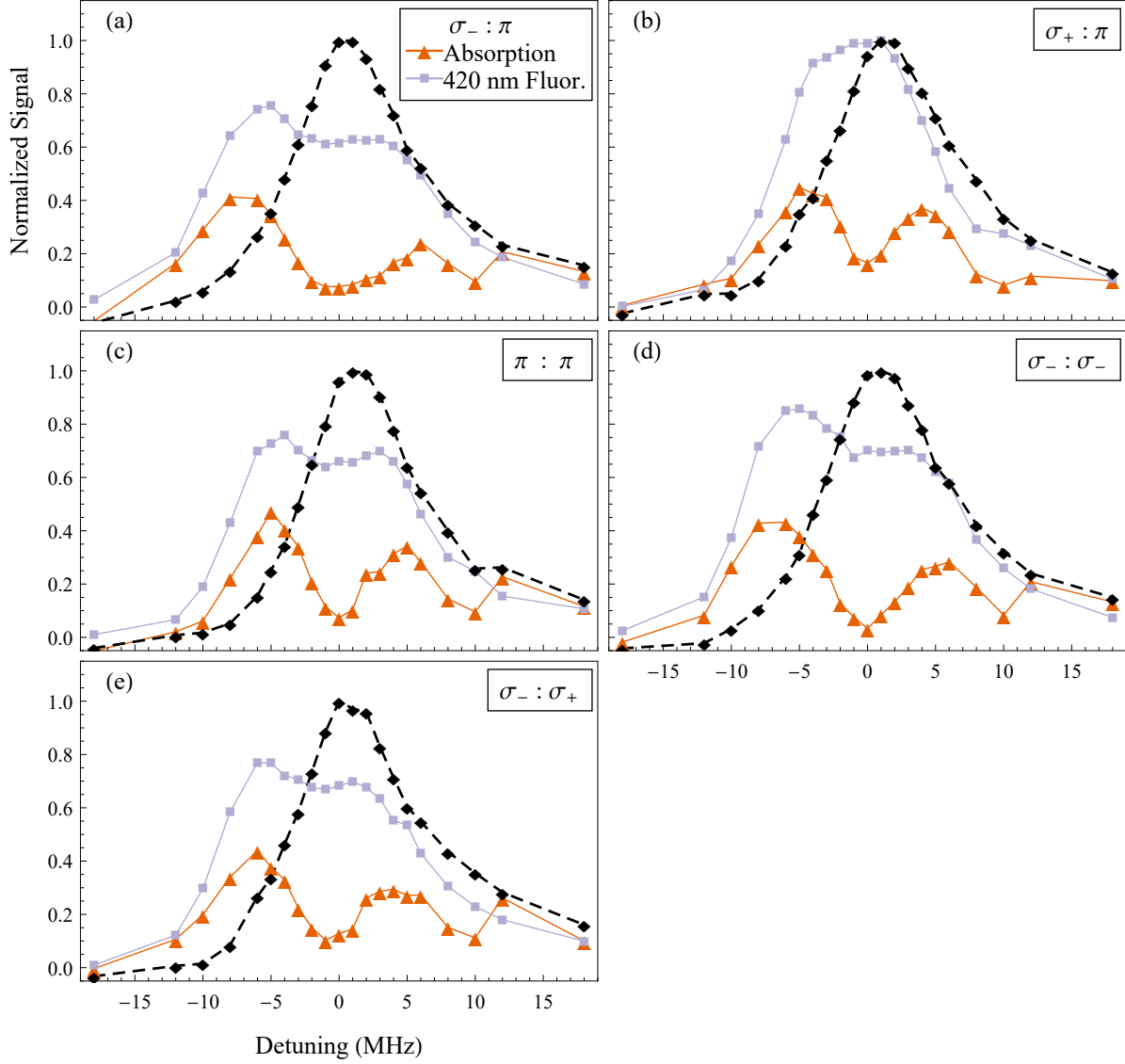


FIG. 25: All data as a function of probe detuning in the counterpropagating EIT geometry with probe Rabi frequency $\Omega_p = 0.18\Gamma_p$ and control Rabi frequency $\Omega_c = 2.22\Gamma_p$ with control detuning $\Delta_c = 0$. (a)-(e) display various combinations of probe and control polarizations specified in the legends with σ_- , σ_+ , and π corresponding to left handed circular, right handed circular, and linear polarization respectively. In the legend left is probe polarization and right is control (probe : control).

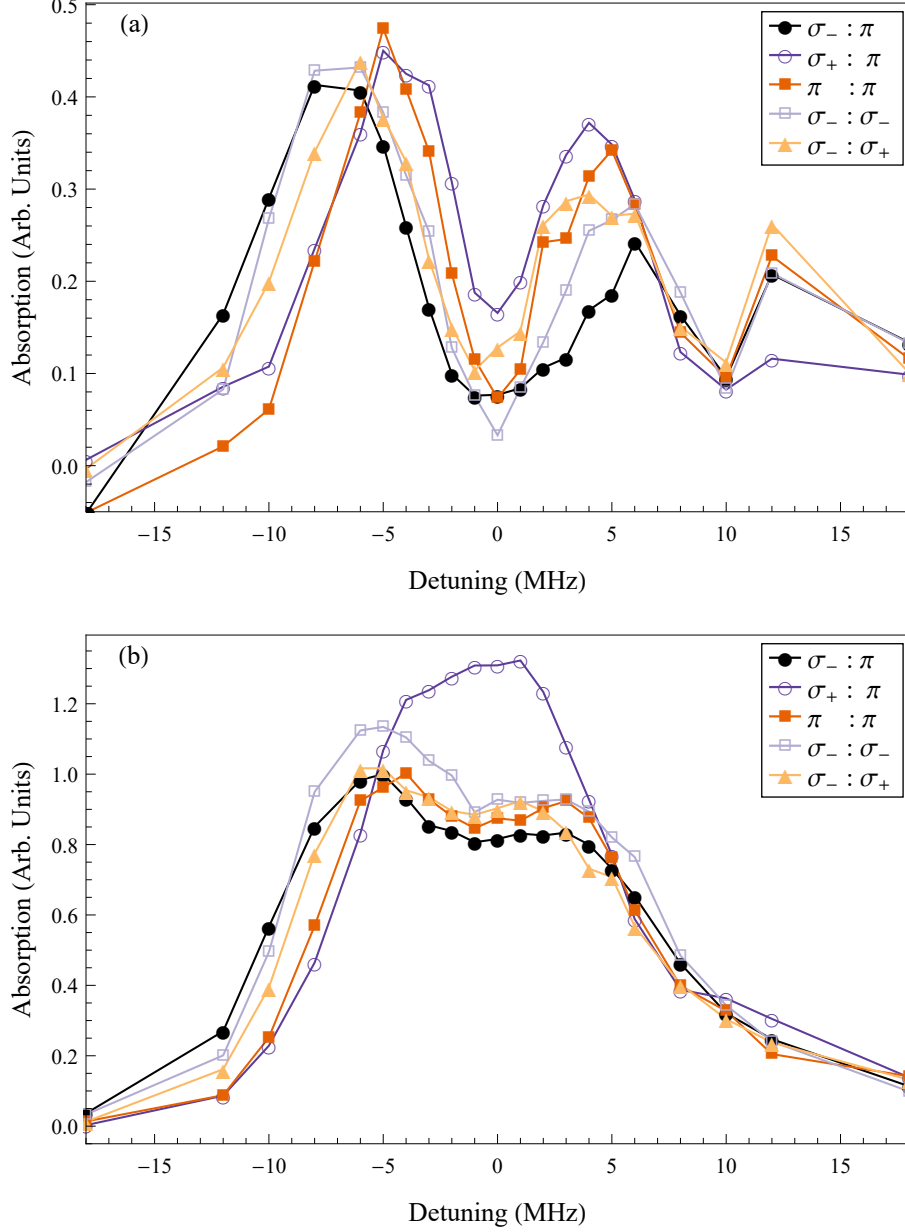


FIG. 26: In the legend, the left side consists of the probe polarization while the right side is the control polarization (probe polarization : control polarization), with σ_- , σ_+ , and π corresponding to left handed circular, right handed circular, and linear polarization respectively. Data corresponding to counterpropagating EIT geometry. Control detuning $\Delta_c = 0$ and probe and control Rabi frequency $\Omega_p = 0.18\Gamma_p$ and $\Omega_c = 2.22\Gamma_p$ respectively. (a) Probe absorption as a function of probe detuning. (b) Fluorescence of the $6P_{3/2}$ state as a function of probe detuning.

4.1.1.3 Control Detuning Dependence

Figure 27 displays the probe absorption (orange triangles) and the $6P_{3/2}$ state fluorescence (light purple squares) at 9.5 MHz control detuning and 18.5 MHz control detuning, which roughly correspond to the $F'' = 4$ and $F'' = 3$ hyperfine levels respectively within the $5D_{5/2}$ manifold. Plots in Fig. 27 are as a function of probe detuning.

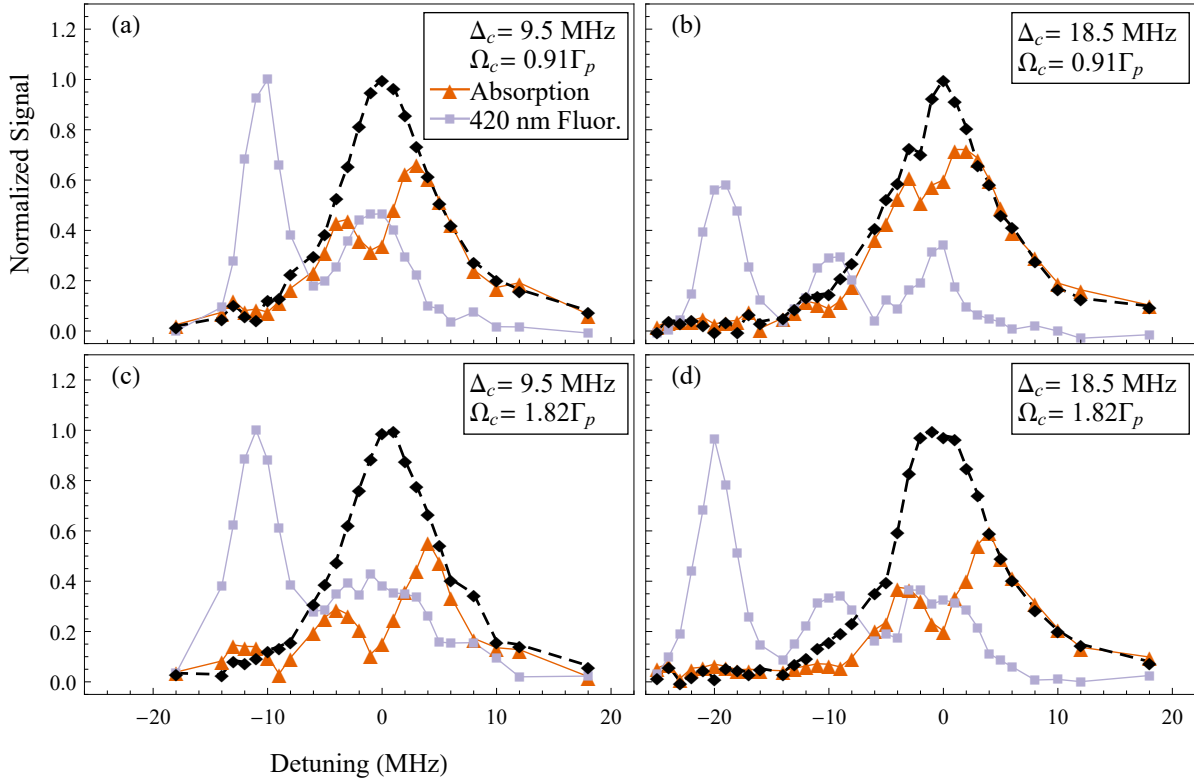


FIG. 27: Counterpropagating EIT geometry with a σ_- probe and horizontal π control polarization with probe Rabi frequency $\Omega_p = 0.18\Gamma_p$. Black: probe absorption as a function of probe detuning with no control field present. Orange: Probe absorption as a function of probe detuning with control field present. Purple: Fluorescence of the $6P_{3/2}$ state as a function of probe detuning. (a) $\Delta_c = 9.5$ MHz, $\Omega_c = 0.91\Gamma_p$ (1 mW). (b) $\Delta_c = 18.5$ MHz, $\Omega_c = 0.91\Gamma_p$. (c) $\Delta_c = 9.5$ MHz, $\Omega_c = 1.82\Gamma_p$ (4 mW). (d) $\Delta_c = 18.5$ MHz, $\Omega_c = 1.82\Gamma_p$.

As expected, with the control detuned, the probe is detuned negatively to meet the

cascade excitation condition and the probe appears to show some signature of transmission, while there is fluorescence from the $6P_{3/2}$ state at the corresponding detunings. In Fig. 28, the plots for each control detuning are compared directly.

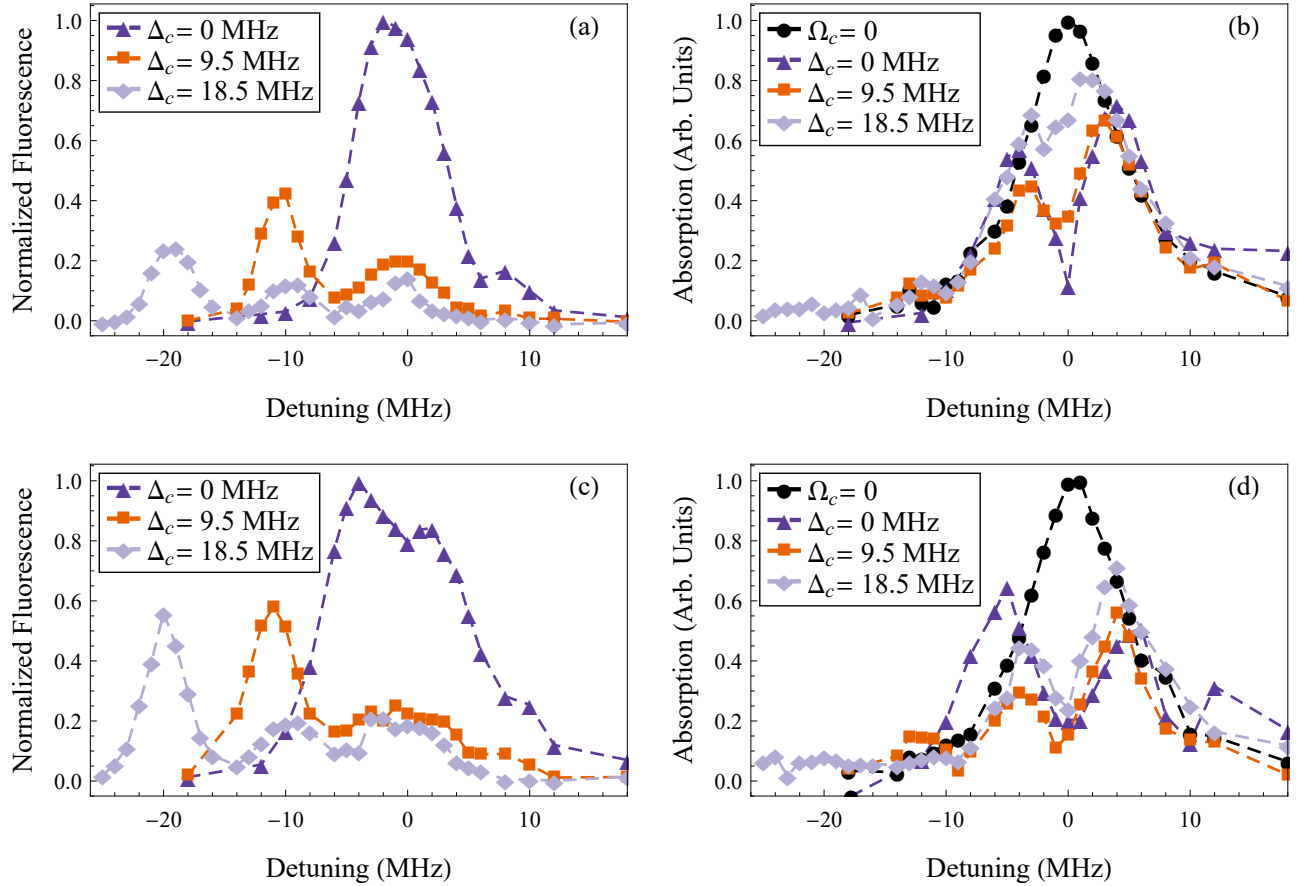


FIG. 28: Counterpropagating EIT geometry with probe rabi frequency of $\Omega_p = 0.18\Gamma_p$. (a) Fluorescence of the $6P_{3/2}$ state as a function of probe detuning at various control detunings with control Rabi frequency $\Omega_c = 0.91\Gamma_p$. (b) Probe absorption as a function of probe detuning at various control detunings with $\Omega_c = 0.91\Gamma_p$. (c) Fluorescence of the $6P_{3/2}$ state as a function of probe detuning at various control detunings with control Rabi frequency $\Omega_c = 1.82\Gamma_p$. (d) Probe absorption as a function of probe detuning at various control detunings with $\Omega_c = 1.82\Gamma_p$.

4.1.1.4 Probe Power Dependence

The dependence of the intensity of the probe was also investigated as a function of probe detuning at three probe intensities. These results are shown in Fig. 29.

We must note that this range of probe Rabi frequencies was used due to experimental constraints. The minimum probe intensity in terms of the Rabi frequency $\Omega_p = 0.10\Gamma_p$ corresponds to $5 \mu\text{W}$, which was the lowest power that could be consistently achieved, while the highest probe intensity of Rabi frequency $\Omega_p = 0.22\Gamma_p$ was limited by the recollection of the MOT. Any probe intensity with higher Rabi frequency than $\Omega_p = 0.22\Gamma_p$ would force the atomic cloud out of the recollection region, within the duty cycle of the experiment, limited by the constraints of the CBS data collection cycle. The probe intensity corresponding to a Rabi frequency of $\Omega_p = 0.18\Gamma_p$ ($\sim 17 \mu\text{W}$) is the standard probe power for other measurements within the parameter space. The absorption data and $6P_{3/2}$ fluorescence are overlaid in Fig. 30.

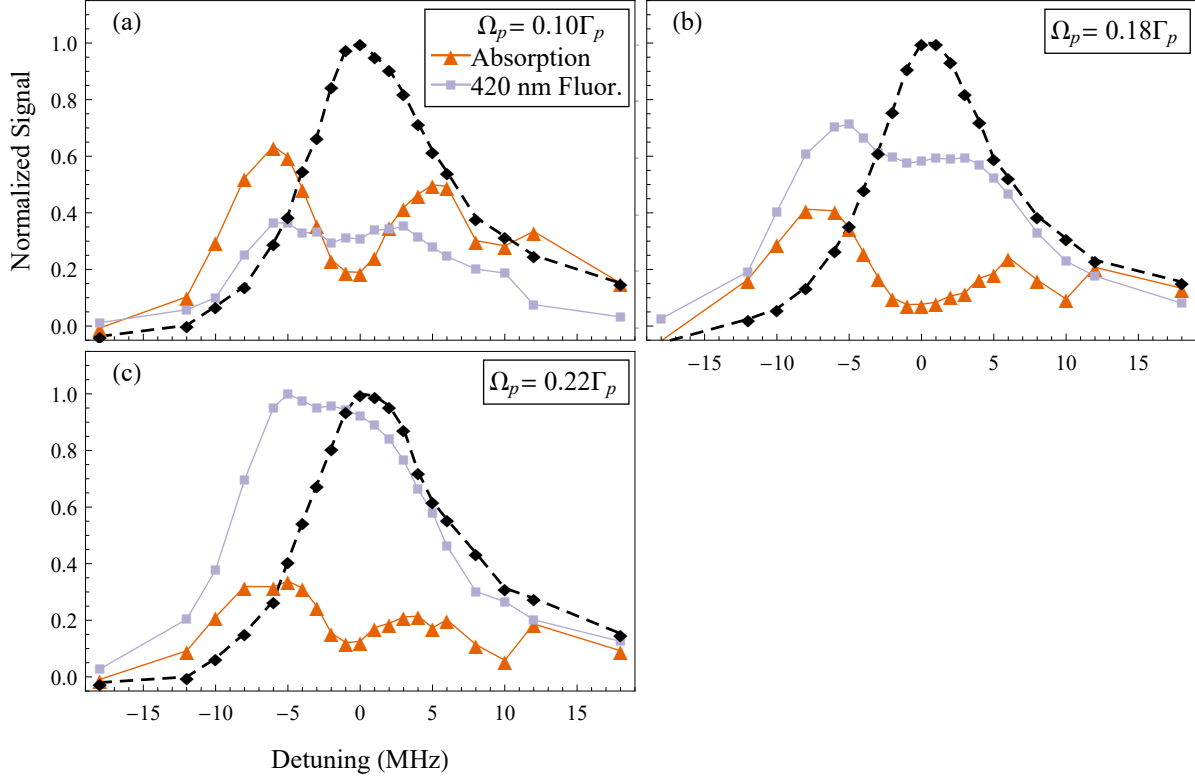


FIG. 29: Probe absorption without EIT (black), probe absorption with EIT conditions (orange), and $6P_{3/2}$ fluorescence (purple) at various probe Rabi frequencies as a function of probe detuning at $\Omega_c = 2.22\Gamma_p$ with control detuning $\Delta_c = 0$. (a) $\Omega_p = 0.10\Gamma_p$ ($5 \mu\text{W}$). (b) $\Omega_p = 0.18\Gamma_p$ ($17 \mu\text{W}$). (c) $\Omega_p = 0.22\Gamma_p$ ($25 \mu\text{W}$). Data collected in counterpropagating EIT geometry.

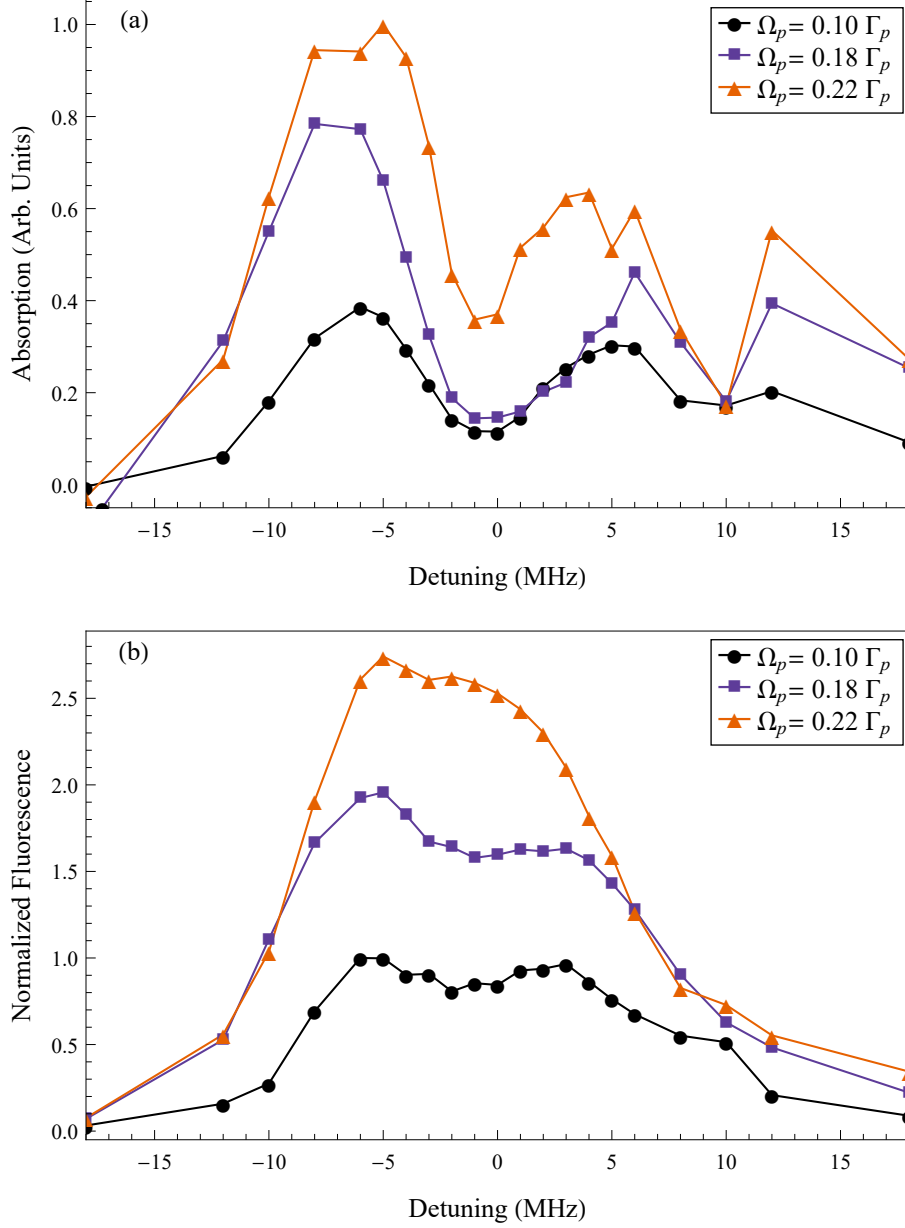


FIG. 30: Counterpropagating EIT probe intensity dependence in terms of probe Rabi frequency with control detuning $\Delta_c = 0$. (a) Probe absorption vs probe detuning at various probe Rabi frequencies, with a control Rabi frequency of $\Omega_c = 2.22\Gamma_p$. (b) Fluorescence of the $6P_{3/2}$ state as a function of probe detuning at various probe intensities with $\Omega_c = 2.22\Gamma_p$. Data collected in counterpropagating EIT geometry.

4.1.2 ORTHOGONAL EIT GEOMETRY

Here the EIT in the orthogonal geometry is presented to be compared with that of the counterpropagating geometry, but also to provide insight on the effects taking place during CBS while the control beam is present.

4.1.2.1 Control Intensity Dependence

The results of EIT in the orthogonal scheme are shown in Fig. 31, with ascending control field intensity in terms of Rabi frequency from (a) to (e). As before, each plot shows the probe absorption with no control field present (black dashed), probe absorption with the control field present (orange), and the resulting 420 nm fluorescence from the $6P_{3/2}$ state (purple) recorded during EIT measurements, as functions of probe detuning. There was a slight reduction in optical power in the orthogonal arrangement compared to that of the counterpropagating geometry, hence the reasoning of the highest Rabi frequency from the counterpropagating data not being included here. Furthermore, it will be shown that at such intensities, CBS signals are mostly nonexistent, so it is not an extremely vital measurement as those at higher intensities.

The dependence on control intensity seems to have roughly the same scaling as before in the counterpropagating regime, indicating that geometry in this case may not have an effect.

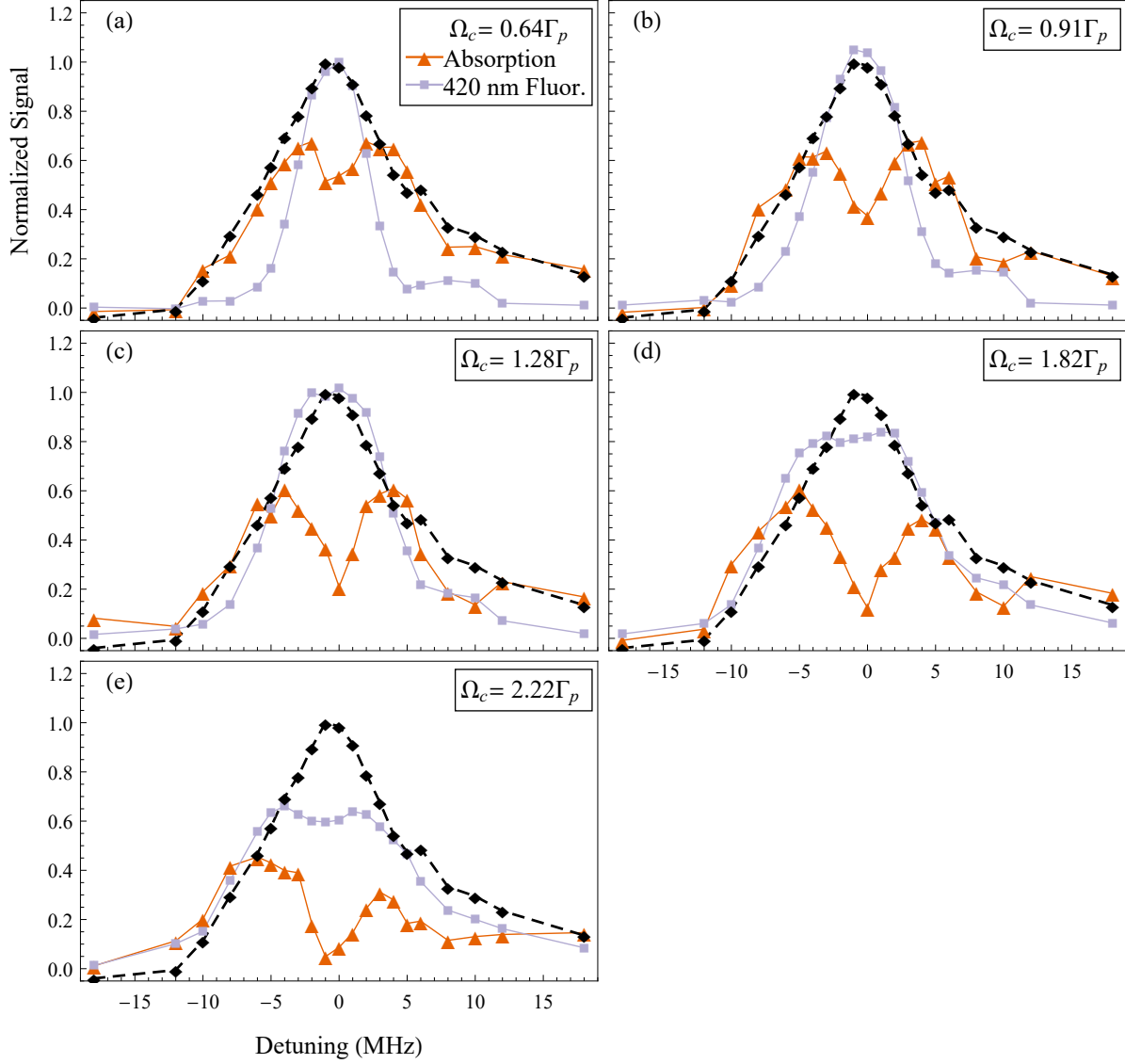


FIG. 31: All data represented as a function of probe detuning with σ_- probe polarization and horizontal π control polarization in the orthogonal EIT geometry with probe Rabi frequency $\Omega_p = 0.18\Gamma_p$ and control detuning $\Delta_c = 0$. Black: probe absorption with no control field present. Orange: Probe absorption with control field present. Purple: Fluorescence of the $6P_{3/2}$ state. (a)-(e) display various control intensities specified in terms of Rabi frequency in the legends.

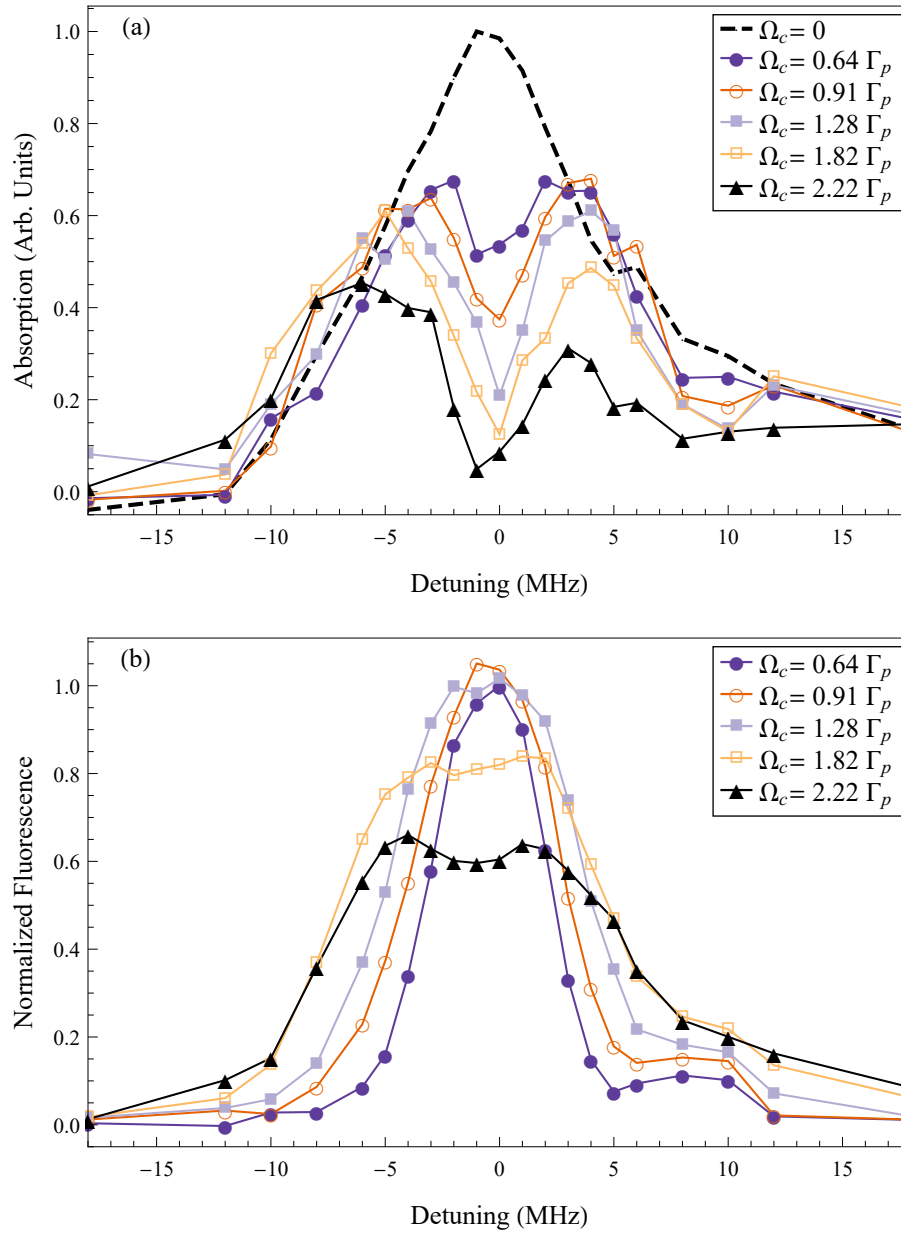


FIG. 32: Orthogonal EIT with control detuning $\Delta_c = 0$ and probe Rabi frequency $\Omega_p = 0.18\Gamma_p$. (a) Probe absorption as a function of probe detuning at various control Rabi frequencies. (b) Fluorescence of the $6P_{3/2}$ energy level as a function of probe detuning at various control Rabi frequencies.

4.1.2.2 Polarization Dependence

As for the orthogonal geometry polarization dependence, Fig. 33 shows various combinations of probe and control beam polarizations, displaying probe absorption as a function of probe detuning. The Rabi frequency of the probe and control are $\Omega_p = 0.18\Gamma_p$ and $\Omega_c = 2.22\Gamma_p$ respectively for each given polarization, with a control detuning of $\Delta_c = 0$.

Similar to the counterpropagating geometry, the polarizations in the legend correspond to probe on the left and control on the right (p:c), where σ_+ , σ_- are right handed and left handed circular polarization respectively and π is linear polarization.

Again as with the counterpropagating geometry, there does not seem to be a significant dependence on the polarization of the probe or control beams.

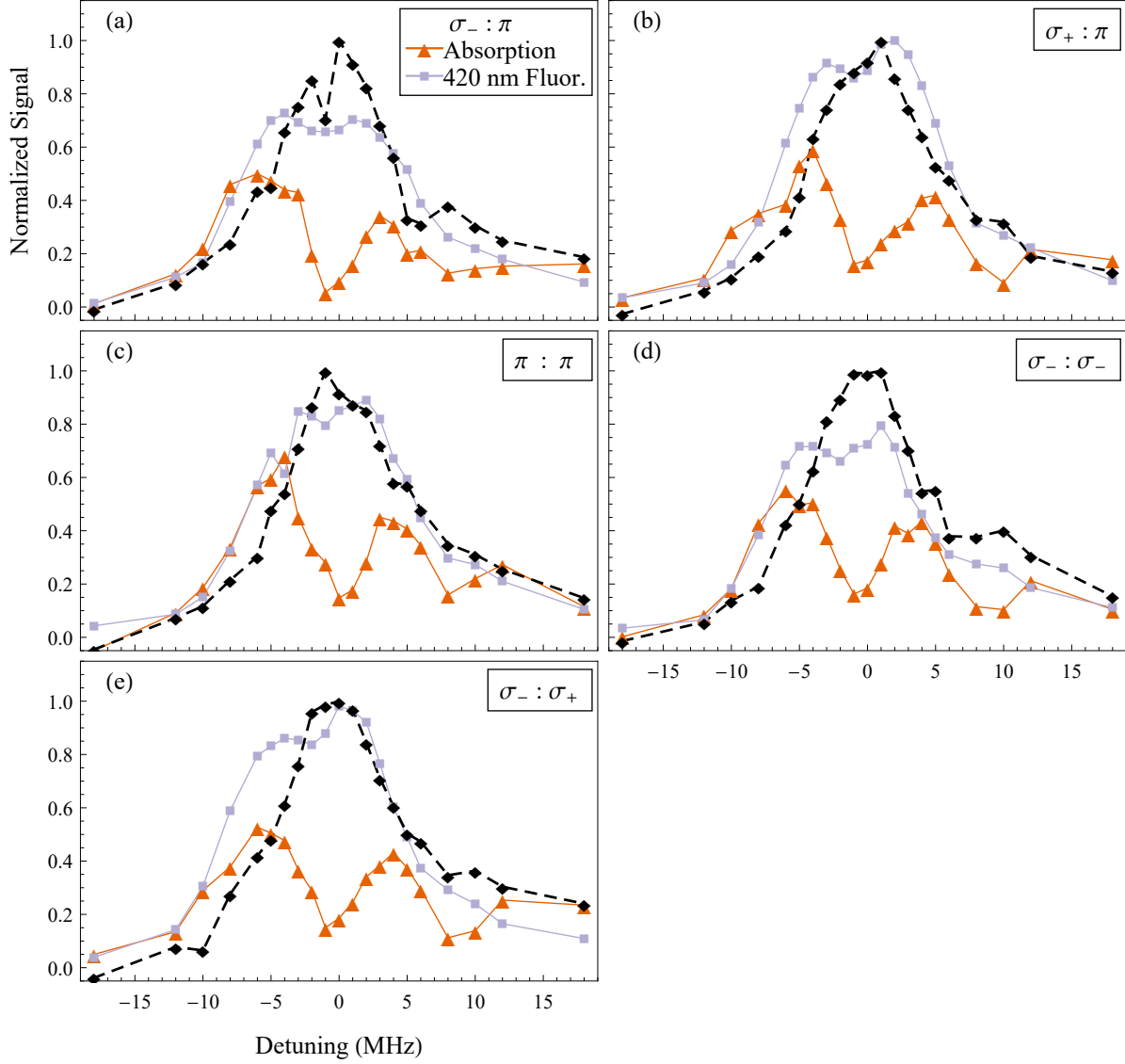


FIG. 33: All data as a function of probe detuning in the orthogonal EIT geometry with a probe and control Rabi frequency of $\Omega_p = 0.18\Gamma_p$ and $\Omega_c = 2.22\Gamma_p$ respectively, with control detuning $\Delta_c = 0$. (a)-(e) display various combinations of probe and control polarizations specified in the legends with σ_- , σ_+ , and π corresponding to left handed circular, right handed circular, and linear polarization respectively.

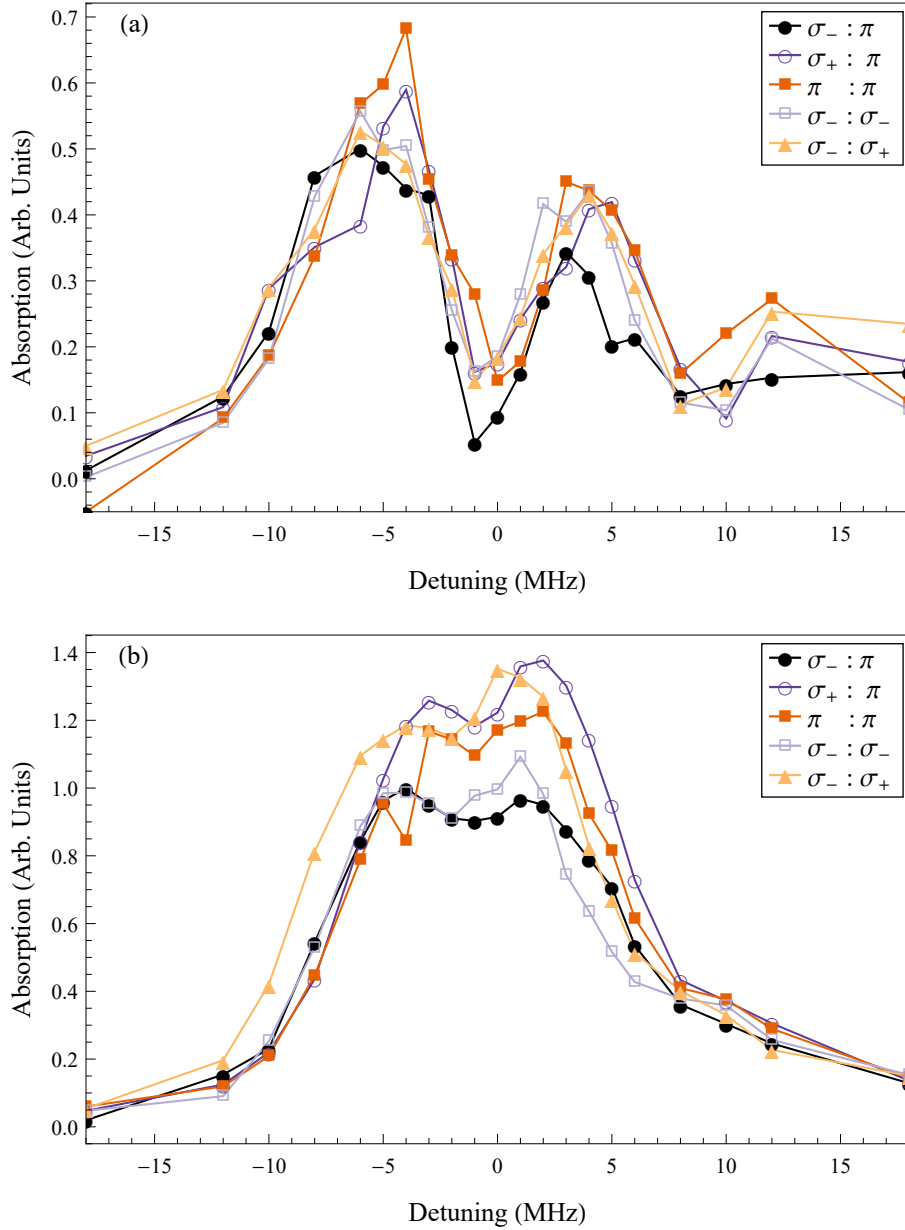


FIG. 34: In the legend, the left side consists of the probe polarization while the right side is the control polarization (probe polarization : control polarization), with σ_- , σ_+ , and π corresponding to left handed circular, right handed circular, and linear polarization respectively. Data corresponding to orthogonal EIT geometry. Control detuning $\Delta_c = 0$ and probe and control Rabi frequency $\Omega_p = 0.18\Gamma_p$ $\Omega_c = 2.22\Gamma_p$ respectively. (a) Probe absorption as a function of probe detuning. (b) Fluorescence of the $6P_{3/2}$ state as a function of probe detuning.

4.1.2.3 Control Detuning Dependence

Figure 35 displays the probe absorption (orange triangles) and the $6P_{3/2}$ state fluorescence (light purple squares) at 9.5 MHz control detuning and 18.5 MHz control detuning as functions of probe detuning.

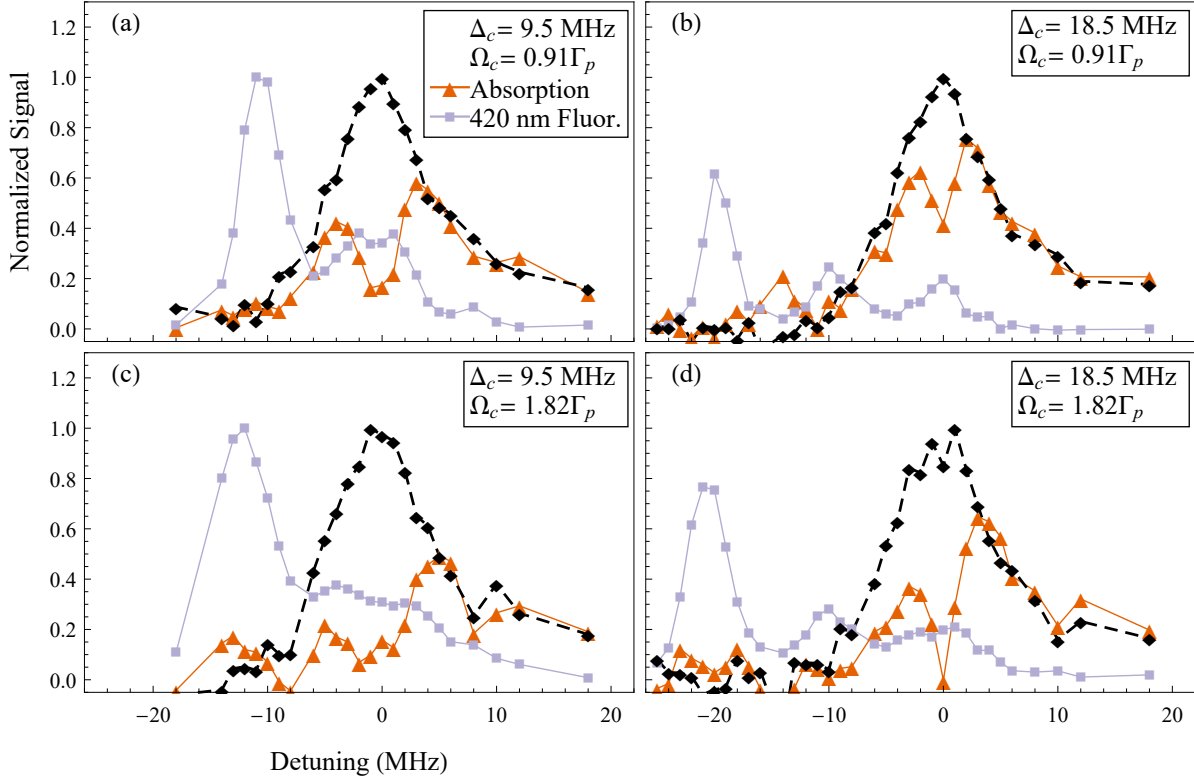


FIG. 35: Orthogonal EIT geometry with a σ_- probe and horizontal π control polarization with probe Rabi frequency $\Omega_p = 0.18\Gamma_p$. Black: probe absorption as a function of probe detuning with no control field present. Orange: Probe absorption as a function of probe detuning with control field present. Purple: Fluorescence of the $6P_{3/2}$ state as a function of probe detuning. (a) $\Delta_c = 9.5$ MHz, $\Omega_c = 0.91\Gamma_p$ (1 mW). (b) $\Delta_c = 18.5$ MHz, $\Omega_c = 0.91\Gamma_p$. (c) $\Delta_c = 9.5$ MHz, $\Omega_c = 1.82\Gamma_p$ (4 mW). (d) $\Delta_c = 18.5$ MHz, $\Omega_c = 1.82\Gamma_p$. Orthogonal EIT geometry with a σ_- probe and horizontal π control polarization.

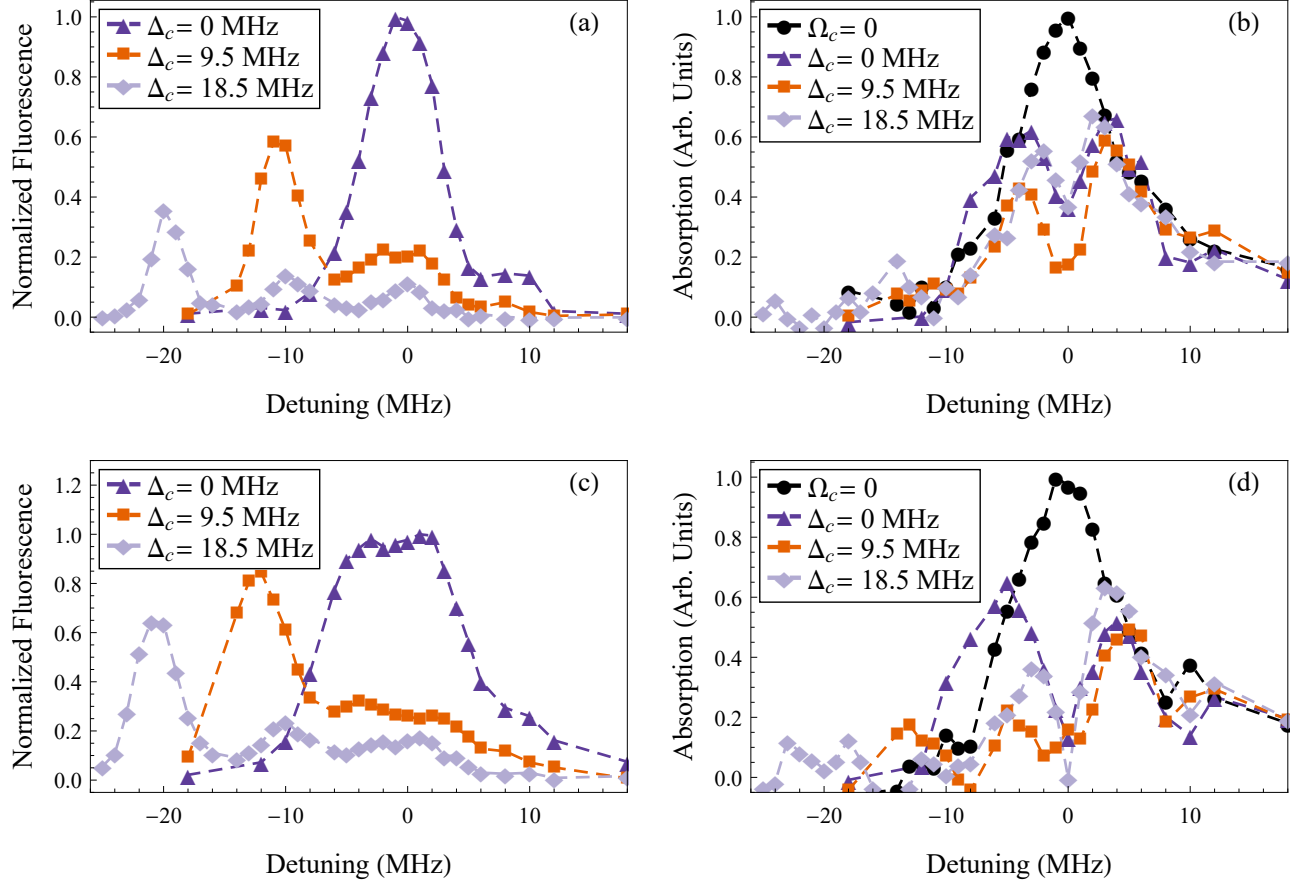


FIG. 36: Orthogonal EIT geometry with probe Rabi frequency of $\Omega_p = 0.18\Gamma_p$. (a) Fluorescence of the $6P_{3/2}$ state at various control detunings with control Rabi frequency $\Omega_c = 0.91\Gamma_p$. (b) Probe absorption as a function of probe detuning at various control detunings with $\Omega_c = 0.91\Gamma_p$. (c) Fluorescence of the $6P_{3/2}$ state at various control detunings with control Rabi frequency $\Omega_c = 1.82\Gamma_p$. (d) Probe absorption as a function of probe detuning at various control detunings with $\Omega_c = 1.82\Gamma_p$. Data collected in orthogonal EIT geometry.

The effect on EIT at various control detunings seems to align with what was observed in the counterpropagating geometry, eluding to no noticeable difference depending on beam geometry.

4.1.2.4 Probe Intensity Dependence

The dependence of probe intensity as a function of probe detuning is shown in Fig. 37 at the three probe Rabi frequencies, as before in the counterpropagating regime.

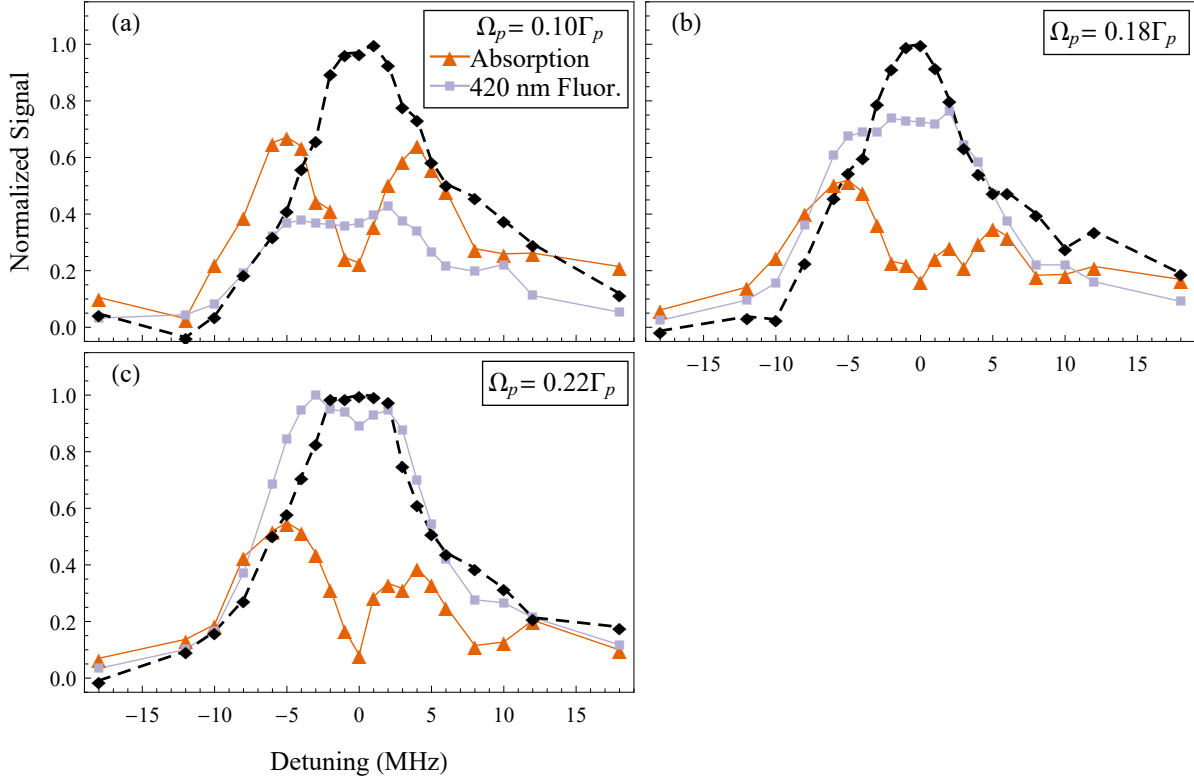


FIG. 37: Probe absorption without EIT (black), probe absorption with EIT conditions (orange), and $6P_{3/2}$ fluorescence (purple) at various probe Rabi frequencies as a function of probe detuning at $\Omega_c = 2.22\Gamma_p$ with control detuning $\Delta_c = 0$. (a) $\Omega_p = 0.10\Gamma_p$. (b) $\Omega_p = 0.18\Gamma_p$. (c) $\Omega_p = 0.22\Gamma_p$. Data collected in orthogonal EIT Geometry.

As previously observed, the effect of EIT increases with probe power. This can be more directly compared in Fig. 38. Higher probe intensities show higher absorption, except for within the EIT window. Higher intensities also give rise to more fluorescence of the $6P_{3/2}$ state.

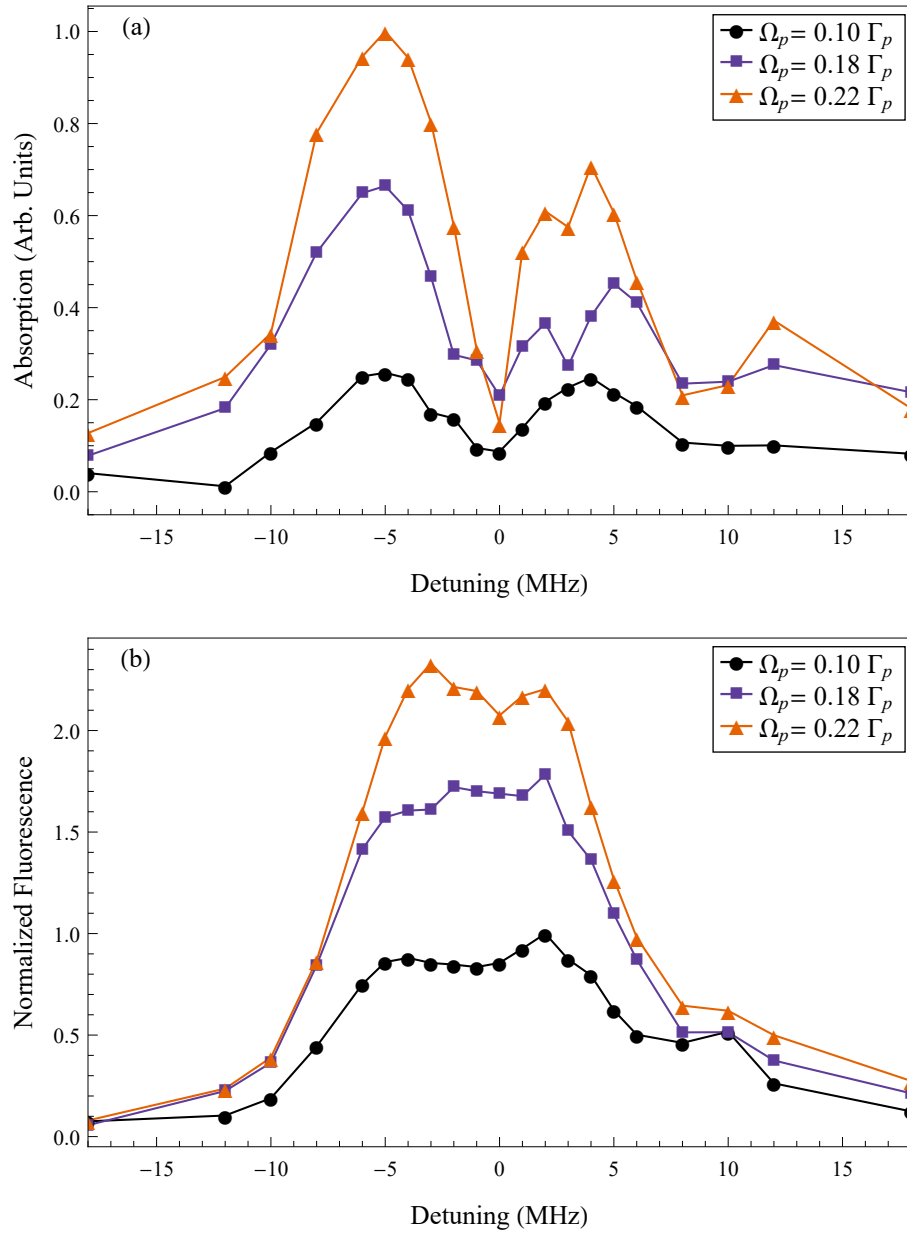


FIG. 38: Orthogonal EIT probe intensity dependence in terms of probe Rabi frequency with control detuning $\Delta_c = 0$. (a) Probe absorption vs probe detuning at various probe Rabi frequencies, with a control Rabi frequency of $\Omega_c = 2.22\Gamma_p$. (b) Fluorescence of the $6P_{3/2}$ state as a function of probe detuning at various probe Rabi frequencies with $\Omega_c = 2.22\Gamma_p$. Data collected in orthogonal EIT geometry.

4.1.3 AN ASIDE ON ALIGNMENT

It should be stated that for EIT experiments of this type, the alignment of the probe and control beam overlap is crucial. In Fig. 39, the data in (a) presents a set of data with a slightly misaligned control beam, which occurred naturally over time due likely due to mechanical variations in the optical setup. The data in (b) is under the same conditions of that of (a), but with optimal alignment of the control and probe beam overlap. Nearly imperceptible variations in either beam path can result in significant alterations of EIT signals. A slight change in alignment can cause a significant change in the effective Rabi frequency that the atoms are subject to, due to laser intensity being Gaussian in nature.

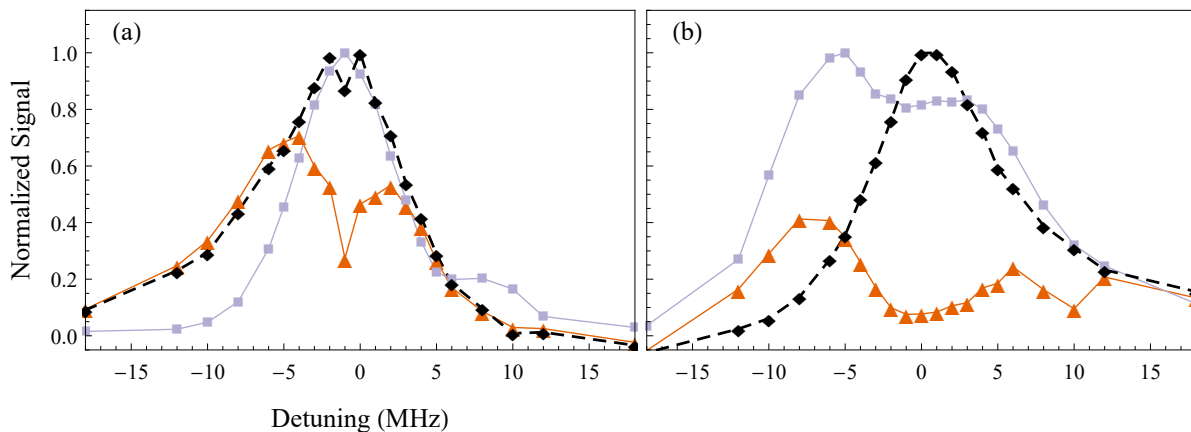


FIG. 39: Data taken at same parameters with the only difference being alignment. (a) Unoptimized probe and control beam alignment. (b) Optimally aligned probe and control beam overlap.

Clearly, the effect of an optimized alignment as in Fig. 39(b) drastically increases the EIT effect. Alignment procedure corresponded to maximizing 420 nm fluorescence at -6 MHz where it is maximized at high control intensities.

4.2 NUMERICAL EIT RESULTS

For the numerical EIT plots, a 9-level optical Bloch equation system was used with the levels corresponding to the levels in Fig. 40. In the calculation of the transition strengths of the $5D_{5/2}$ hyperfine levels, the square root of the relative strength factors, normalized to the largest strength factor value were used for the relevant Rabi frequencies. More specifically, the weighting values

$$\{W_{45}, W_{44}, W_{43}\} = \left\{ \sqrt{\frac{S_{45}}{S_{45}}}, \sqrt{\frac{S_{44}}{S_{45}}}, \sqrt{\frac{S_{43}}{S_{45}}} \right\} = \{1, 0.45, 0.15\} , \quad (120)$$

where the relative strength factors are defined as

$$S_{FF'} = (2F' + 1)(2J + 1) \left\{ \begin{matrix} J & J' & 1 \\ F' & F & I \end{matrix} \right\}^2 . \quad (121)$$

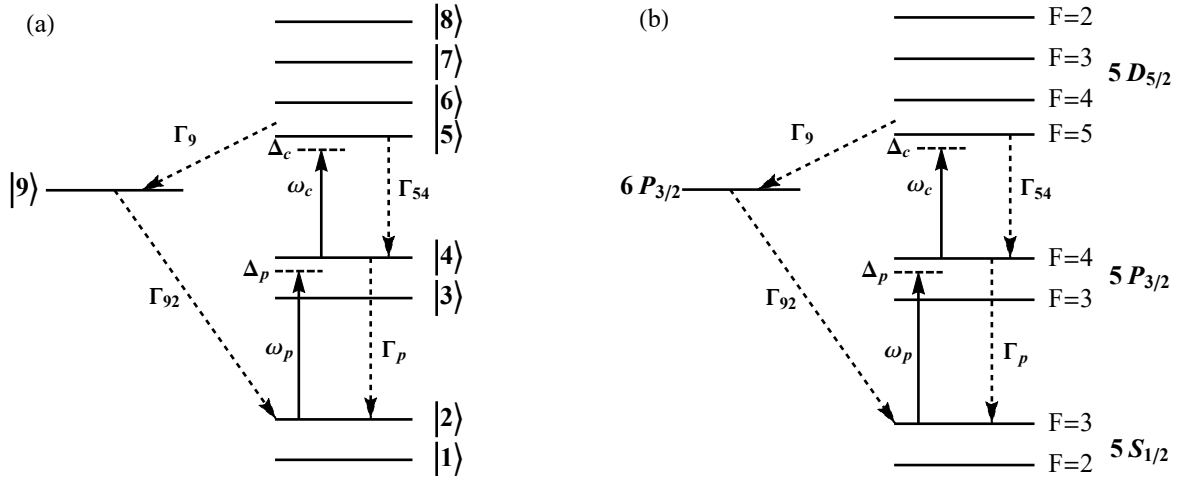


FIG. 40: (a) Level labeling used in the numerical calculation of the optical Bloch equations. (b) The rubidium 85 energy levels corresponding to those used in the numerical calculation of the optical Bloch equations.

A few of the relevant equations of motion from the simulation are:

$$\dot{\sigma}_{42} = \frac{1}{2}i \left\{ 2R_{24}^p (\sigma_{22} - \sigma_{44}) + 2(-R_{23}^p \sigma_{43} + R_{45}^c \sigma_{52} + R_{46}^c \sigma_{62} + R_{47}^c \sigma_{72}) + \sigma_{42} (2\Delta_{24}^p + i\Gamma_N) \right\} \quad (122)$$

$$\begin{aligned} \dot{\sigma}_{44} = & iR_{24}^p (\sigma_{24} - \sigma_{42}) + iR_{45}^c (\sigma_{54} - \sigma_{45}) + iR_{46}^c (\sigma_{64} - \sigma_{46}) \\ & - iR_{47}^c (\sigma_{47} - \sigma_{74}) + \Gamma_{54}\sigma_{55} + \Gamma_{64}\sigma_{66} + \Gamma_{74}\sigma_{77} - \Gamma_N\sigma_{44} , \end{aligned} \quad (123)$$

$$\begin{aligned} \dot{\sigma}_{54} = & \frac{1}{2}i \left\{ -2R_{24}^p \sigma_{52} + 2R_{45}^c (\sigma_{44} - \sigma_{55}) - 2(R_{46}^c \sigma_{56} + R_{47}^c \sigma_{57}) \right. \\ & \left. + \sigma_{54} [2\Delta_{45}^c + i(\Gamma_{54} + \Gamma_9 + \Gamma_N)] \right\} , \end{aligned} \quad (124)$$

$$\dot{\sigma}_{55} = -(\Gamma_{54} + \Gamma_9)\sigma_{55} + iR_{45}^c (\sigma_{45} - \sigma_{54}) , \quad (125)$$

$$\dot{\sigma}_{99} = \Gamma_9 (\sigma_{55} + \sigma_{66} + \sigma_{77} + \sigma_{88}) - \Gamma_{92}\sigma_{99} , \quad (126)$$

where the scripts correspond to the diagram in Fig. 40(a). The Rabi frequencies are in terms of the weighting factor W_{ij} that is determined by the square root of the transition strength factors to give proper weighting to hyperfine transitions, i.e.,

$$R_{ij}^\alpha = \frac{\Omega_{ij}}{2} W_{ij} . \quad (127)$$

We only display these equations due to the fact that there are 81 equations of motion in a 9-level system such as this and that these are equations corresponding to probe absorption ($\text{Im}[\sigma_{54}]$) and the populations of the $5P_{3/2}F' = 4$ (σ_{44}), $5D_{5/2}F'' = 5$ (σ_{55}), and $6P_{3/2}$ (σ_{99}).

4.2.1 CONTROL INTENSITY DEPENDENCE

In the following subsection, the solutions for the 9-level OBEs are shown at the end of the probe pulse in (a) and the integrated solutions over the time of the pulse are shown in (b). The integrated solutions physically follow closer to that of the data collected in the experimental EIT data section as shown in Fig. 16, where there was some signal change over the pulse length and are shown here for comparison to the OBEs solved in the traditional manner.

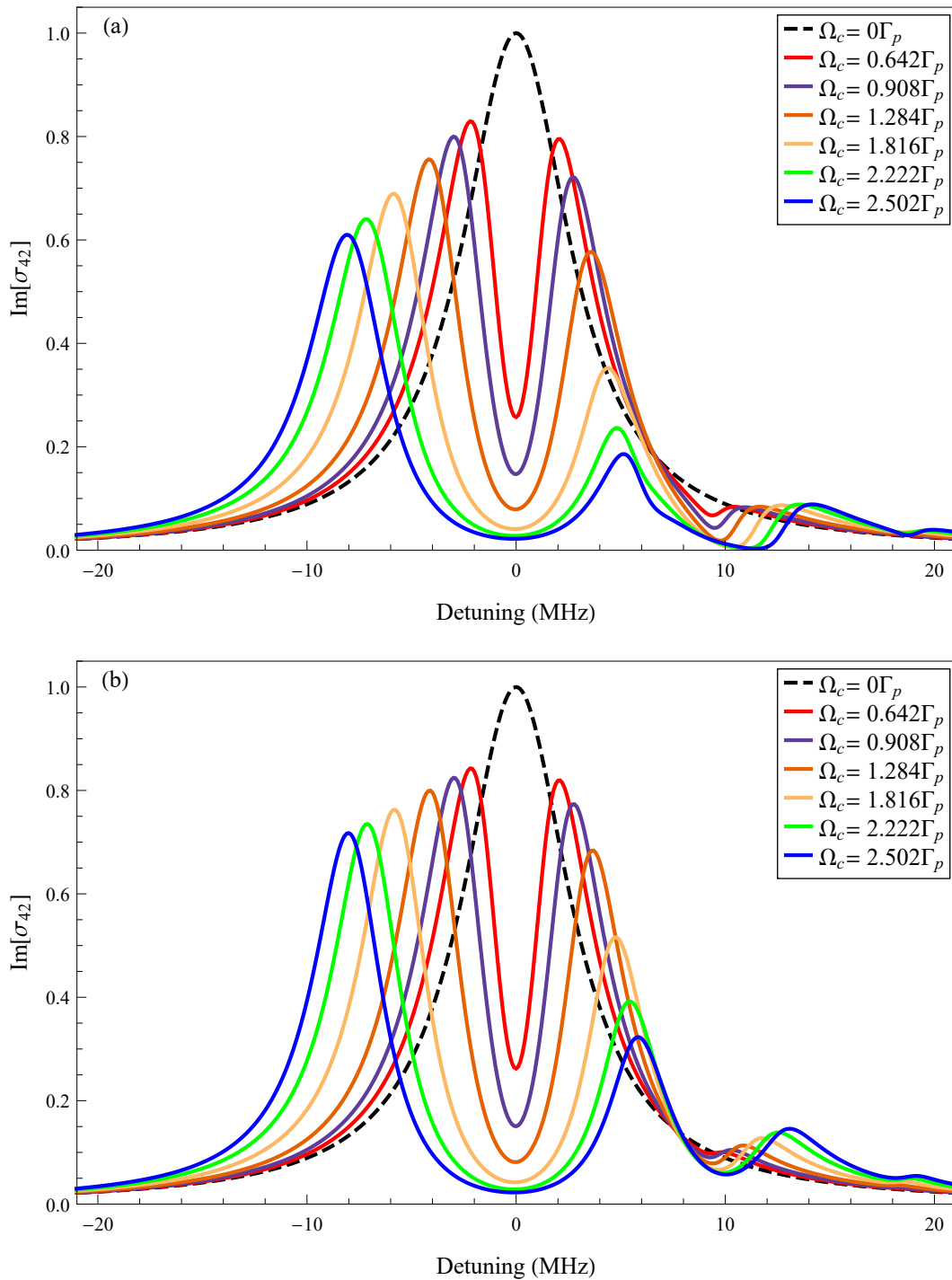


FIG. 41: Numerical solutions of the OBE simulated probe absorption channel ($\text{Im}[\sigma_{42}]$) with $\Delta_c = 0$ MHz and $\Omega_p = 0.18\Gamma_p$ at various control field Rabi frequencies. (a) Numerical solution at end of light pulse. (b) Integration of numerical solutions over entire pulse.

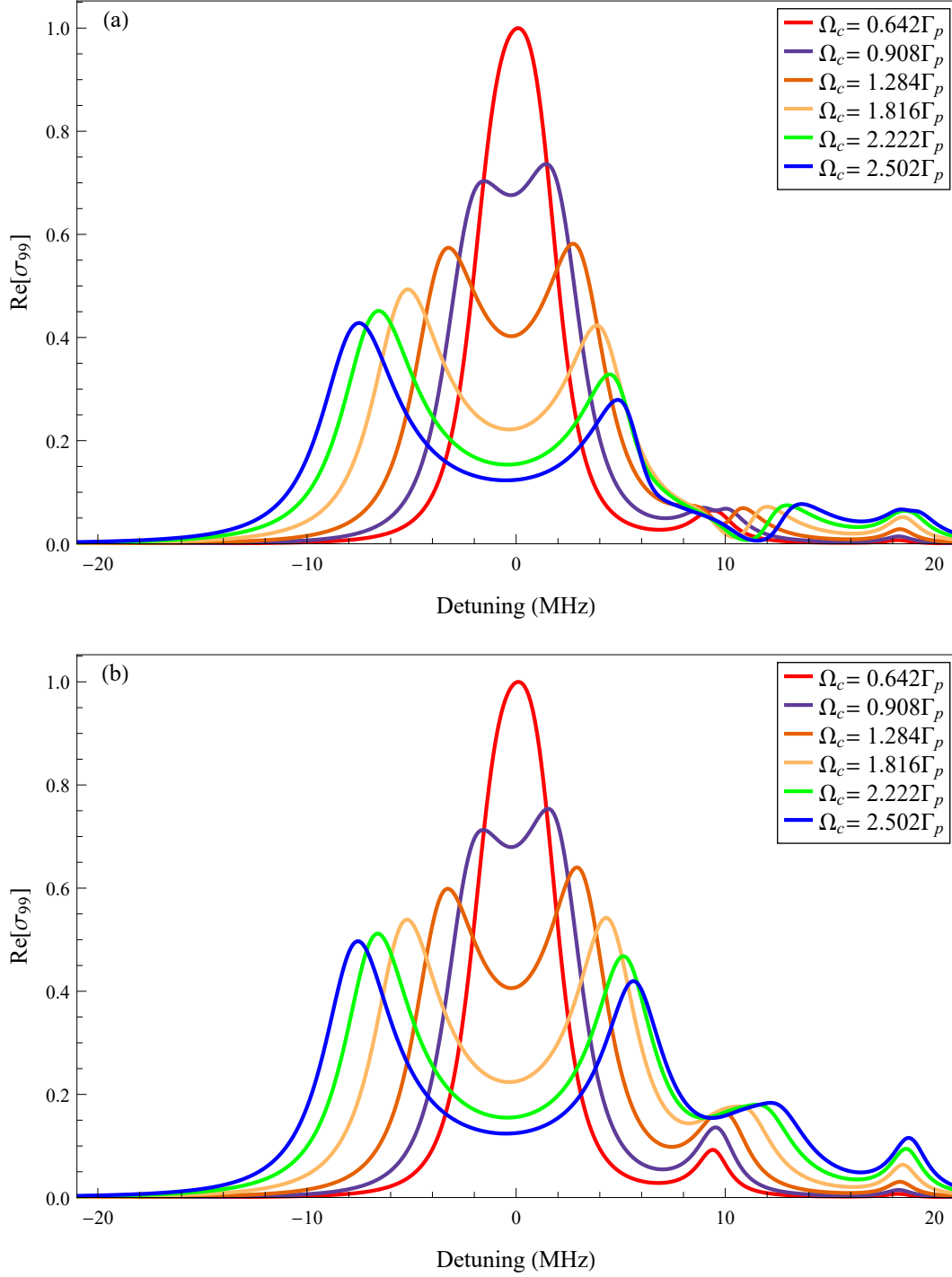


FIG. 42: Numerical solutions of the OBE simulated $6P_{3/2}$ state fluorescence ($\text{Re}[\sigma_{99}]$) with $\Delta_c = 0$ MHz and $\Omega_p = 0.18\Gamma_p$ at various control field Rabi frequencies. (a) Numerical solution at end of light pulse. (b) Integration of numerical solutions over entire pulse.

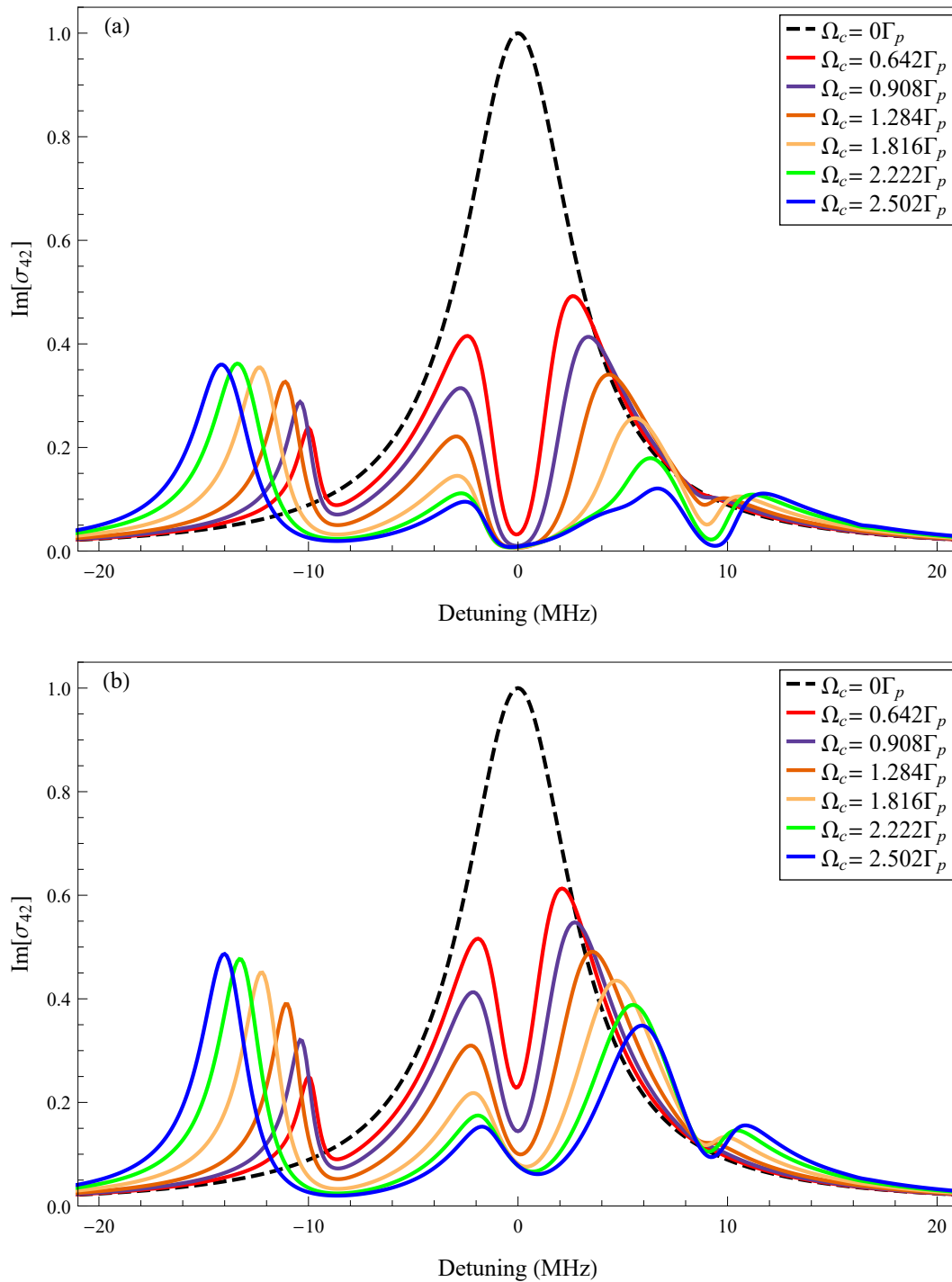


FIG. 43: Numerical solutions of the OBE simulated probe channel ($\text{Im}[\sigma_{42}]$) with $\Delta_c = 9.5$ MHz and $\Omega_p = 0.18\Gamma_p$ at various control field Rabi frequencies. (a) Numerical solution at end of light pulse. (b) Integration of numerical solutions over entire pulse.

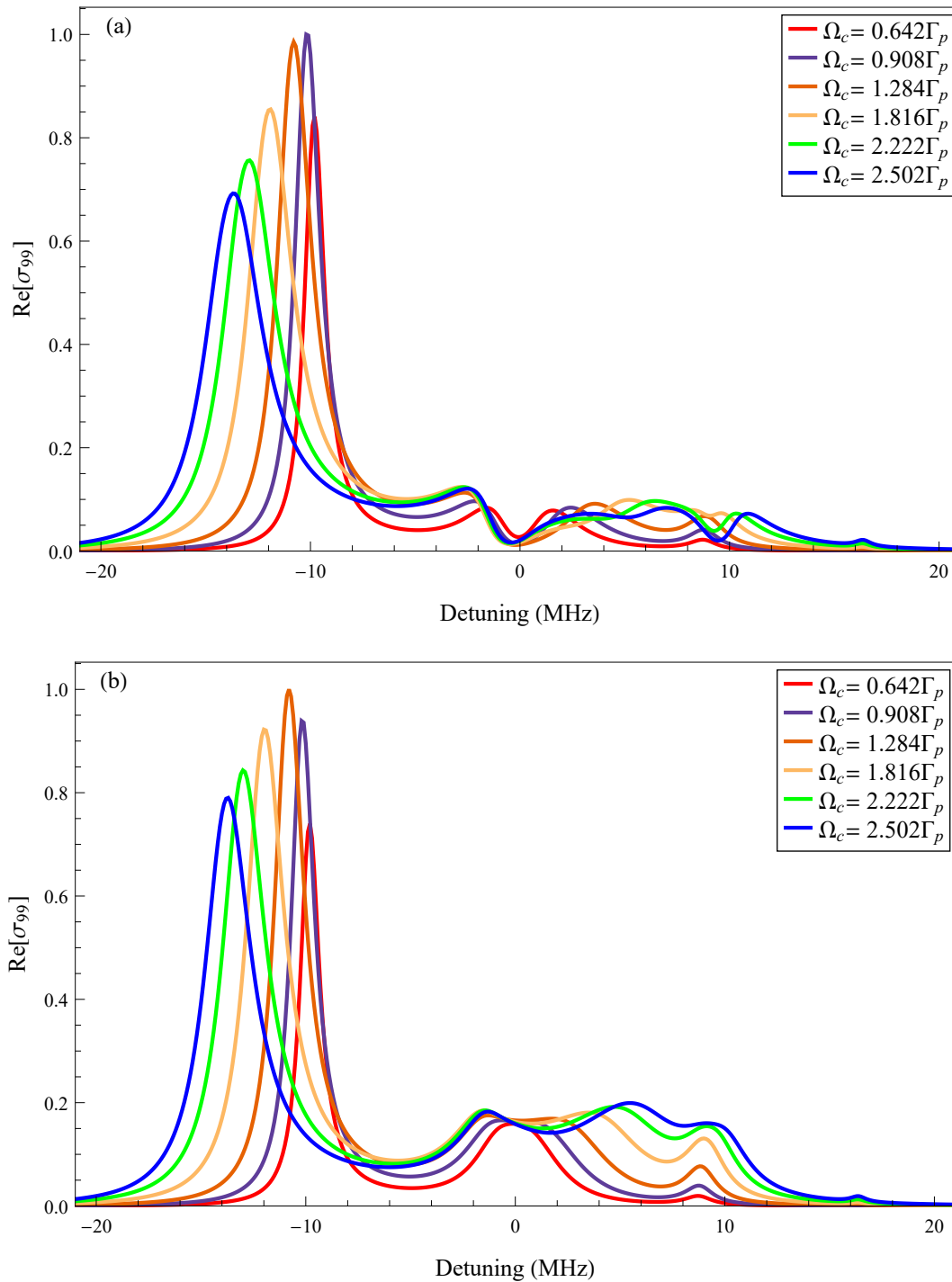


FIG. 44: Numerical solutions of the OBE simulated $6P_{3/2}$ state fluorescence ($\text{Re}[\sigma_{99}]$) with $\Delta_c = 9.5$ MHz and $\Omega_p = 0.18\Gamma_p$ at various control field Rabi frequencies. (a) Numerical solution at end of light pulse. (b) Integration of numerical solutions over entire pulse.

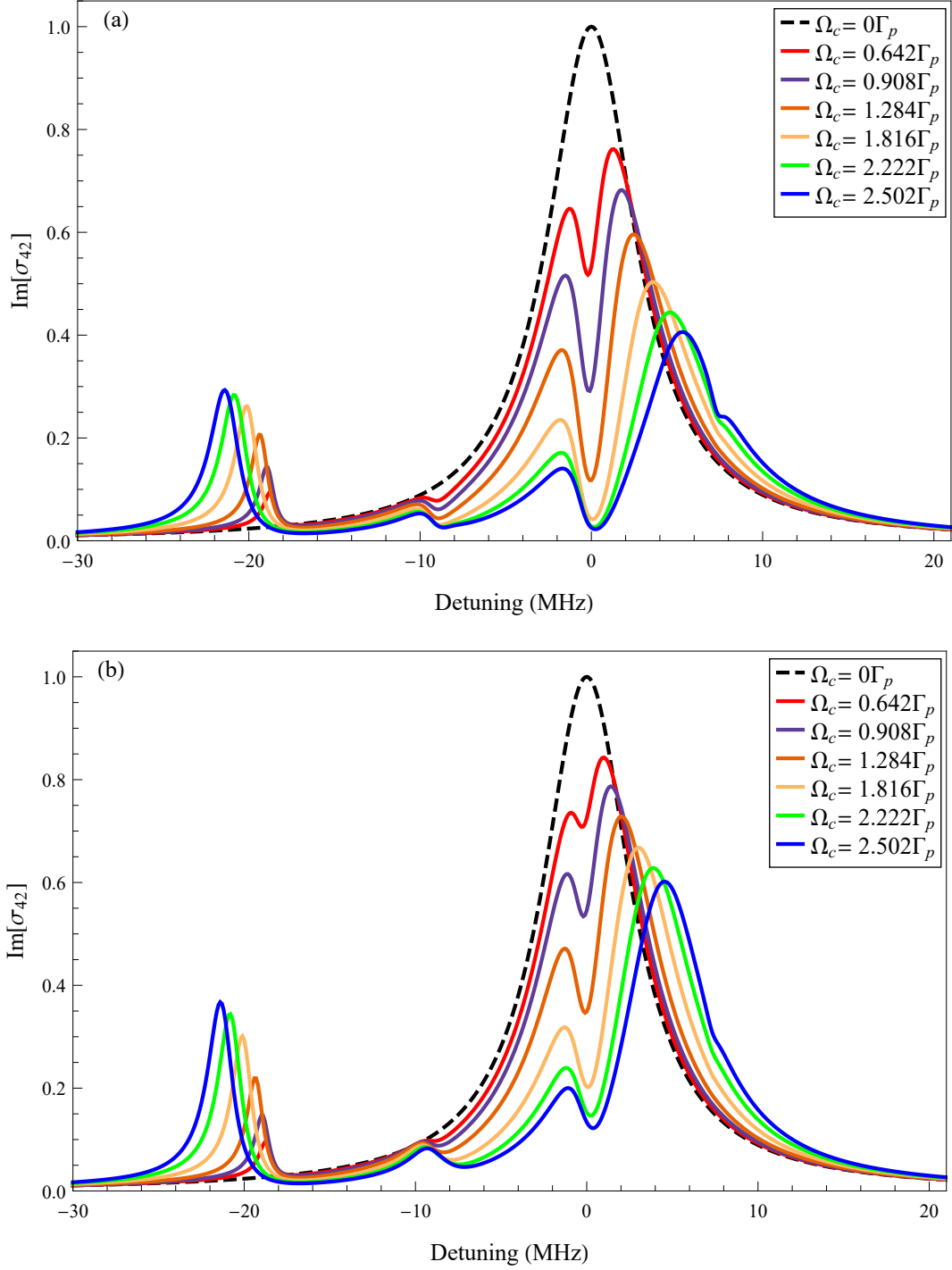


FIG. 45: Numerical solutions of the OBE simulated probe channel ($\text{Im}[\sigma_{42}]$) with $\Delta_c = 18.5$ MHz and $\Omega_p = 0.18\Gamma_p$ at various control field Rabi frequencies. (a) Numerical solution at end of light pulse. (b) Integration of numerical solutions over entire pulse.

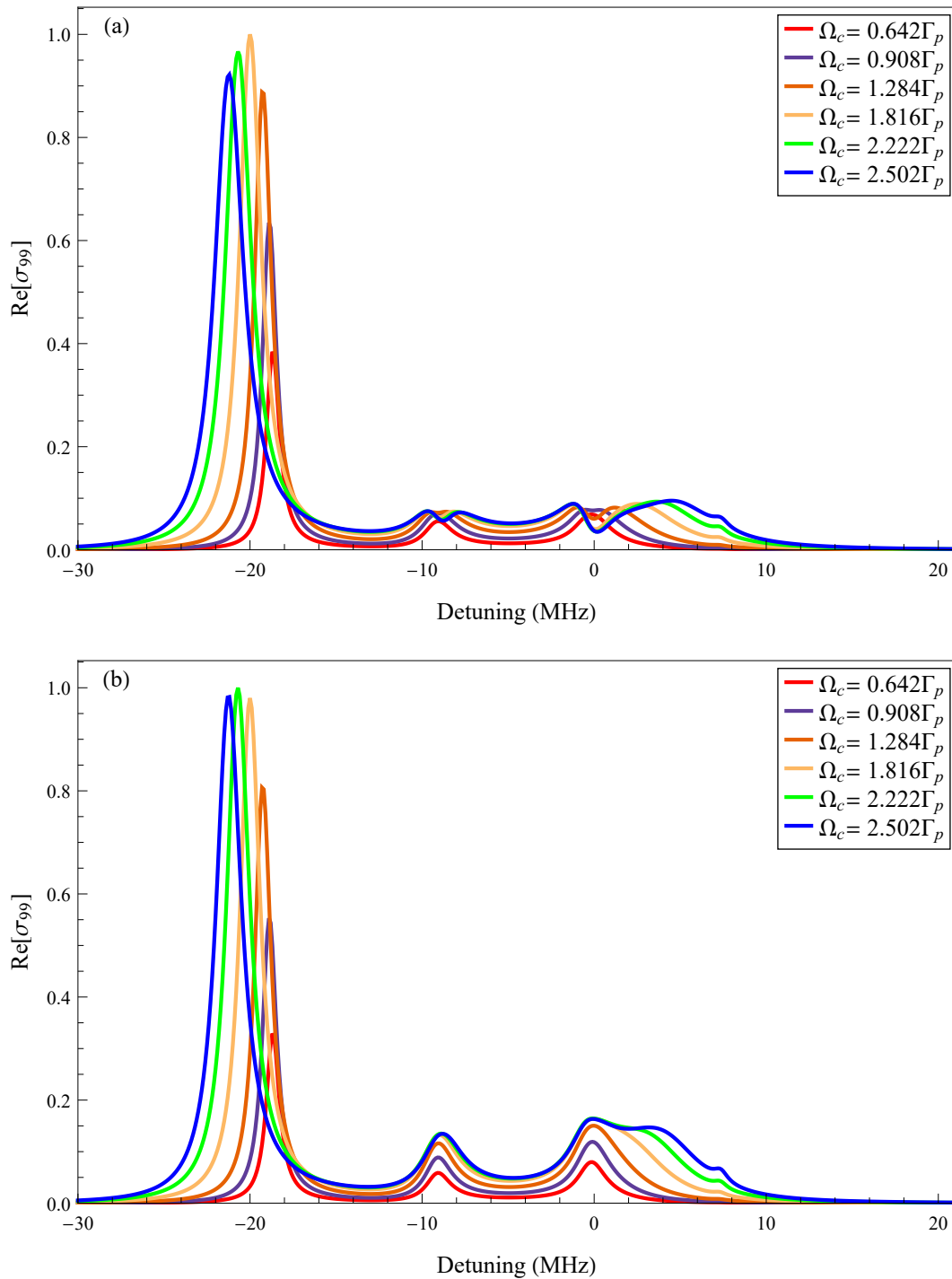


FIG. 46: Numerical solutions of the OBE simulated $6P_{3/2}$ state fluorescence ($\text{Re}[\sigma_{99}]$) with $\Delta_c = 18.5$ MHz and $\Omega_p = 0.18\Gamma_p$ at various control field Rabi frequencies. (a) Numerical solution at end of light pulse. (b) Integration of numerical solutions over entire pulse.

From the comparison between the numerical solutions at the end of the pulse to the integrated solutions, there are only slight differences, with most differences occurring away from resonance. As for the comparison to experimental data, qualitatively they agree, but simulated results show a steeper, thinner EIT window.

4.2.2 PROBE INTENSITY DEPENDENCE

Here the EIT dependence of the probe intensity was investigated, with intensities approximately equal to the experimental values with (a) displaying the solution at the end of the light pulse and (b) the integrated solution over the duration of the pulse. Figure 47 is the solution portraying probe beam absorption and Fig. 48 is the solution of the population of the $6P_{3/2}$ state, which is directly proportional to the fluorescence emitted.

The comparison of the solution at the end of the pulse shows little to no difference to that of the integrated solutions. The difference in probe power in experiment showed a much more noticeable difference in that of the numerical solutions, but still trended similarly in the order of total amplitudes on and off resonance. The fluorescence solutions also trend similarly, but show a deep, wide window near resonance, where experiment displayed little to no evidence of this effect.

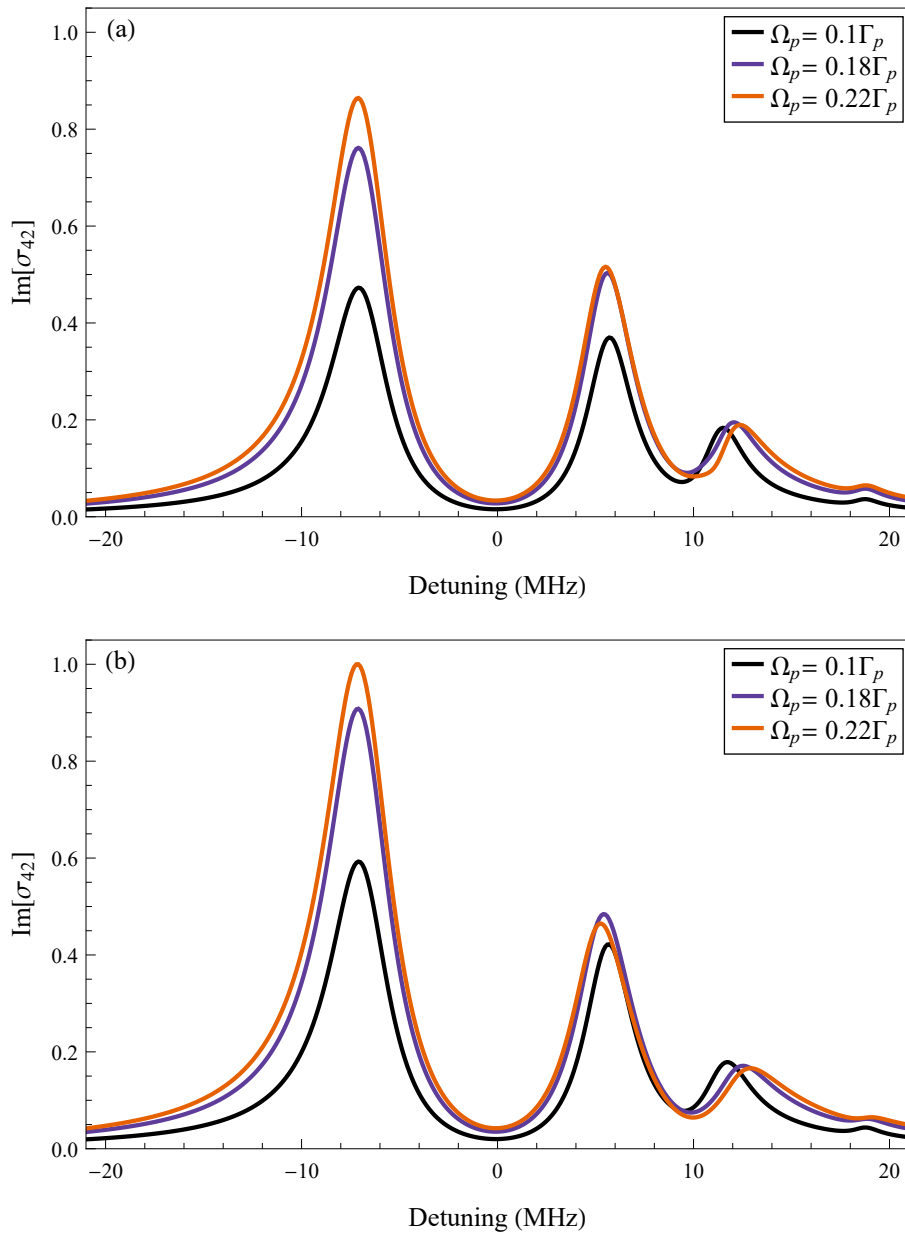


FIG. 47: Numerical solutions of the OBE simulated probe absorption channel ($\text{Im}[\sigma_{42}]$) at various probe Rabi frequencies and control Rabi frequency $\Omega_c = 2.22\Gamma_p$ with control detuning $\Delta_c = 0$. (a) Numerical solution at end of light pulse. (b) Integration of numerical solutions over entire pulse.

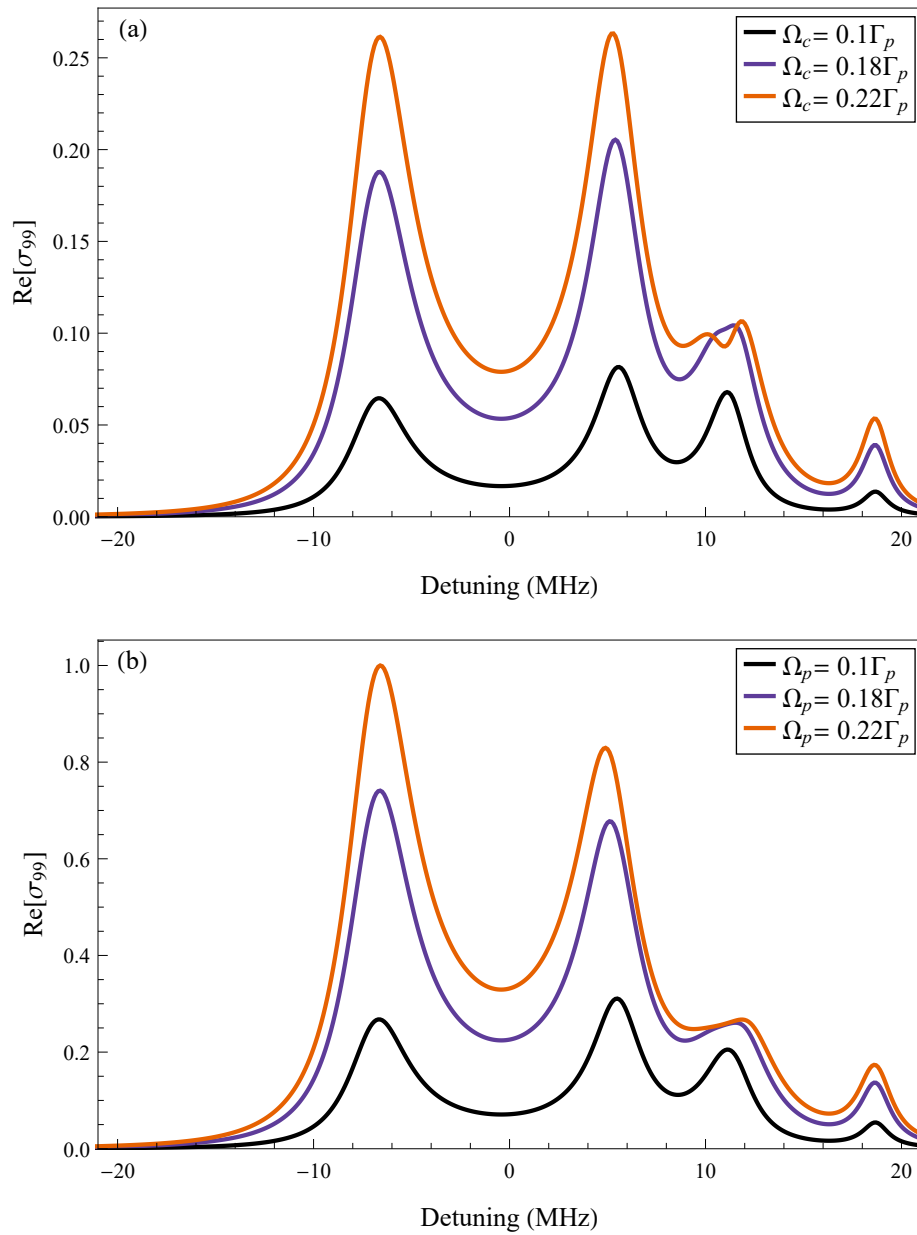


FIG. 48: Numerical solutions of the OBE simulated $6P_{3/2}$ state fluorescence ($\text{Re}[\sigma_{99}]$) control Rabi frequency $\Omega_c = 2.22\Gamma_p$ with control detuning $\Delta_c = 0$. (a) Numerical solution at end of light pulse. (b) Integration of numerical solutions over entire pulse.

4.2.3 CONTROL DETUNING COMPARISON

Here we compare the solutions of the OBEs at the end of the pulse in a similar representation of that of Figs. 28 and 36.

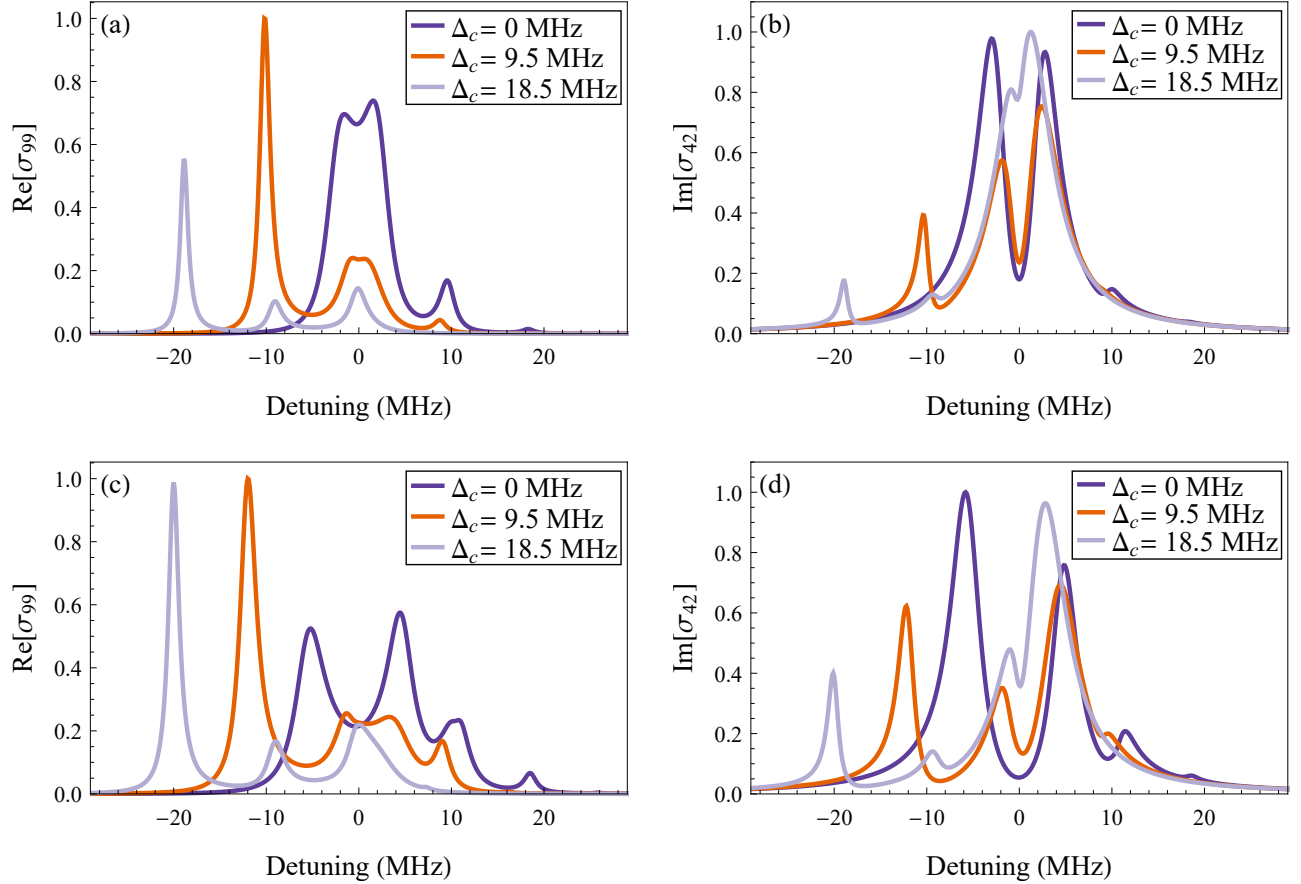


FIG. 49: Numerical solutions of the OBE simulated $6P_{3/2}$ state fluorescence ($\text{Re}[\sigma_{99}]$) as a function of probe detuning at various control detunings with probe Rabi frequency $\Omega_p = 0.18\Gamma_p$ overlaid for comparison with (a) $\Omega_c = 0.91\Gamma_p$ and (c) $\Omega_c = 1.82\Gamma_p$. Simulated probe absorption as a function of probe detuning at various control detunings with (b) $\Omega_c = 0.91\Gamma_p$ and (d) $\Omega_c = 1.82\Gamma_p$.

4.3 EXPERIMENTAL AND NUMERICAL RESULTS COMPARISON

Normalization conventions for the EIT absorption data are based on the peak value of the corresponding absorption, without the control beam present, as portrayed in all other plots showing absorption. This normalization is calculated separately for both experimental and theoretical data for every given parameter (Ω_c, Δ_c) , unless otherwise stated.

For data of the 420 nm fluorescence decaying from the $6P_{3/2}$ state, we've chosen to rescale the data to fit the fluorescence corresponding to a Control Rabi frequency of $\Omega_c = 0.91\Gamma_p$. For the fluorescence data, there is no way to have a standardized normalization as there is with absorption, so this value was chosen due to amplitudes showing some agreement.

4.3.1 ORTHOGONAL EIT

Here we present experimental data from the orthogonal EIT geometry overlaid with theoretical calculations. In Fig. 50, the experimental data corresponding to probe absorption as a function of probe detuning is shown with comparison to theory, at various control Rabi frequencies.

Figure 51 shows the $6P_{3/2}$ fluorescence as a function of probe detuning at various control Rabi frequencies as shown in the legend.

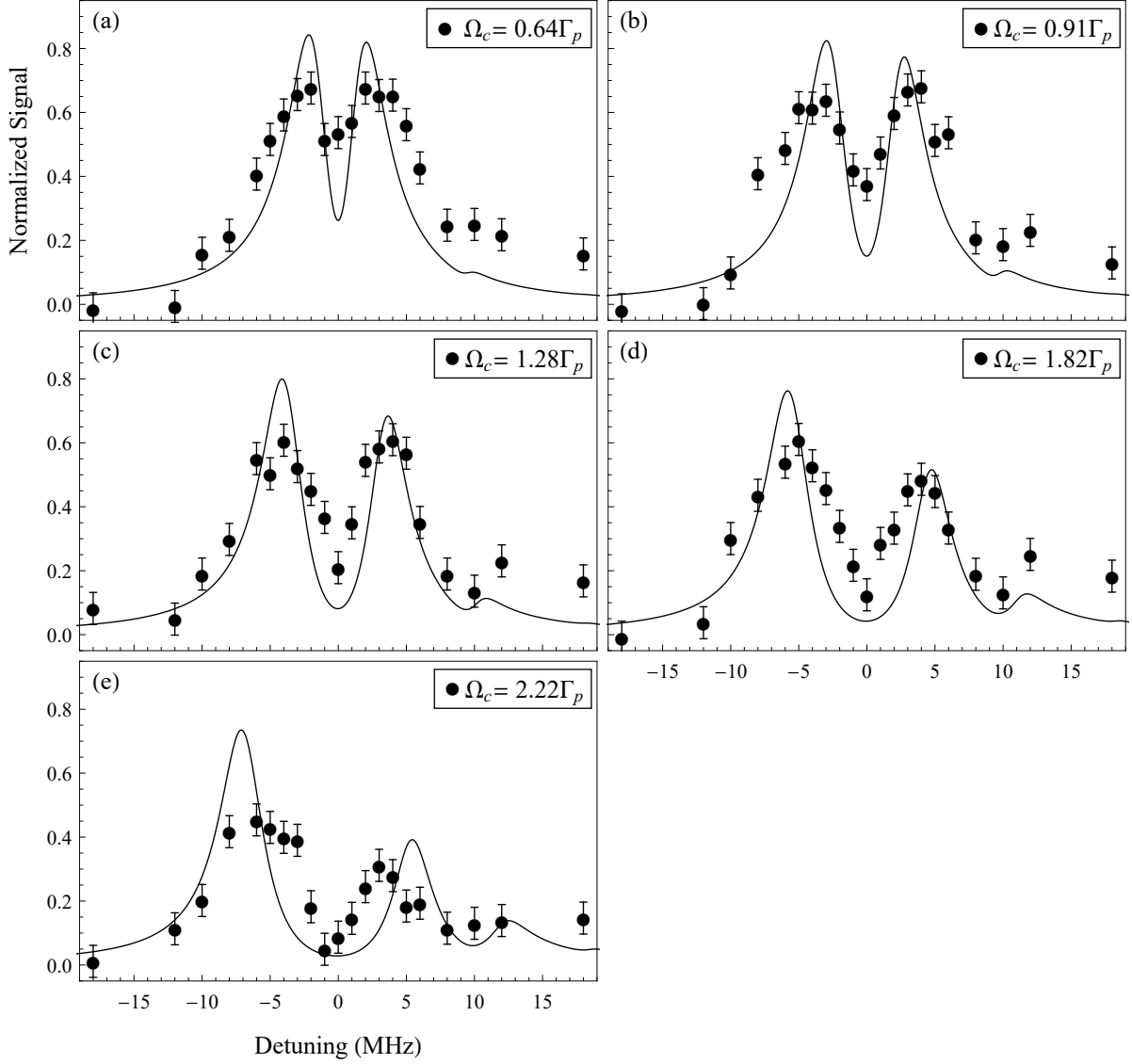


FIG. 50: Comparison of orthogonal EIT probe absorption as a function of probe detuning to theory with $\Delta_c = 0$ and $\Omega_p = 0.18\Gamma_p$ at various control Rabi frequencies. Points correspond to data. Experimental data and theoretical data are normalized to the peak value of probe absorption without EIT, respectively, as described in the text.

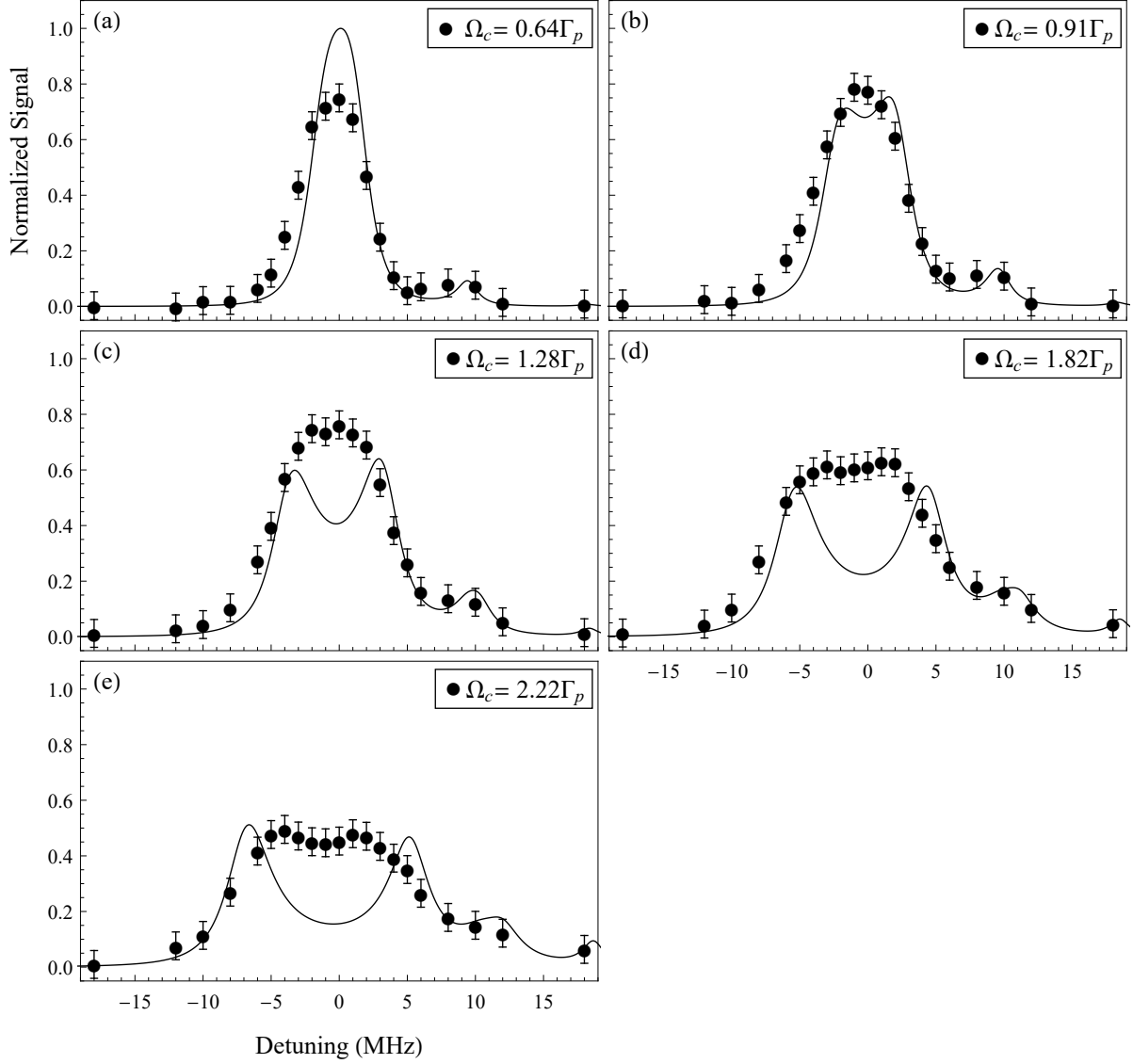


FIG. 51: Comparison of orthogonal EIT $6P_{3/2}$ fluorescence as a function of probe detuning to theory with $\Delta_c = 0$ and $\Omega_p = 0.18\Gamma_p$ at various control Rabi frequencies. Points correspond to data. Experimental data is scaled to the Rabi frequency $\Omega_c = 0.91\Gamma_p$ as described in text.

In Fig. 52, the experimental data corresponding to probe absorption as a function of probe detuning is shown with comparison to theory, at multiple control detunings and Rabi frequencies, as shown in the legend.

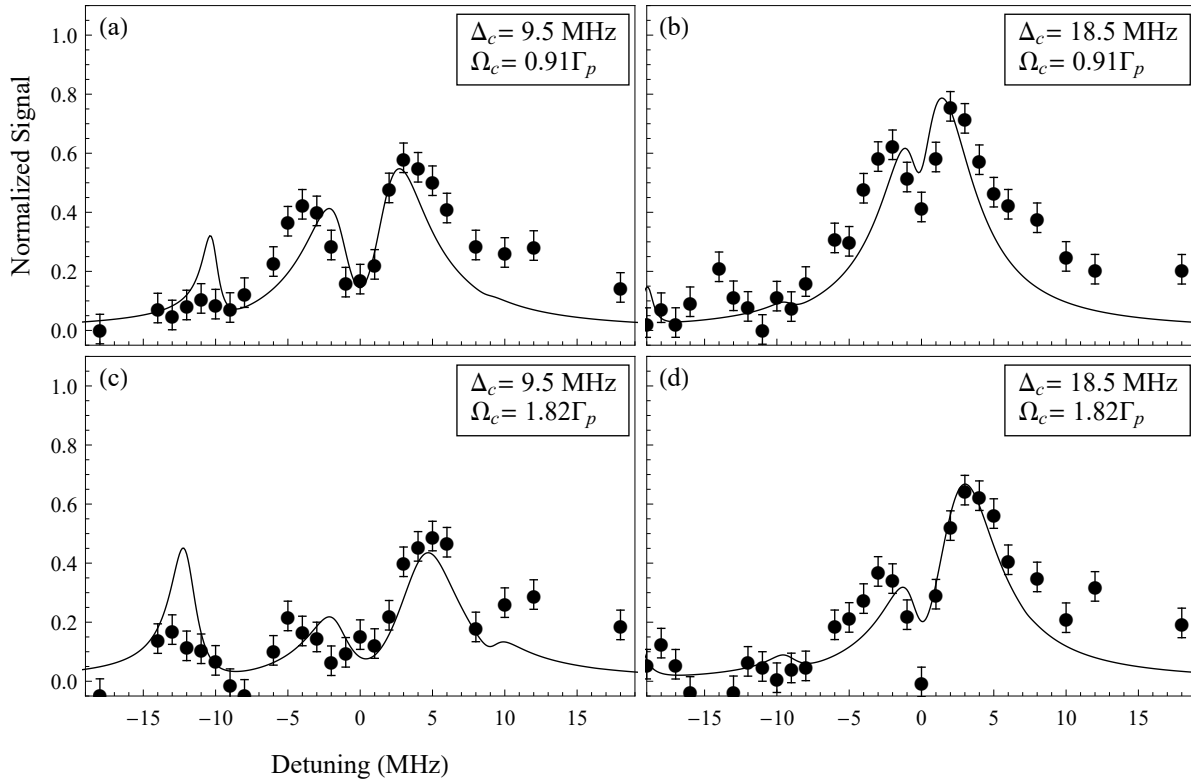


FIG. 52: Comparison of orthogonal EIT probe absorption to theory as a function of probe detuning at multiple control detunings and control Rabi frequencies as displayed in legend. Probe Rabi frequency $\Omega_p = 0.18\Gamma_p$. Points correspond to data. Experimental data and theoretical data are normalized to the peak value of probe absorption without EIT, respectively, as described in the text.

Figure 53 displays the experimental data corresponding to fluorescence from the $6P_{3/2}$ state as a function of probe detuning with comparison to theory at multiple control detunings and Rabi frequencies, as shown in the legend.

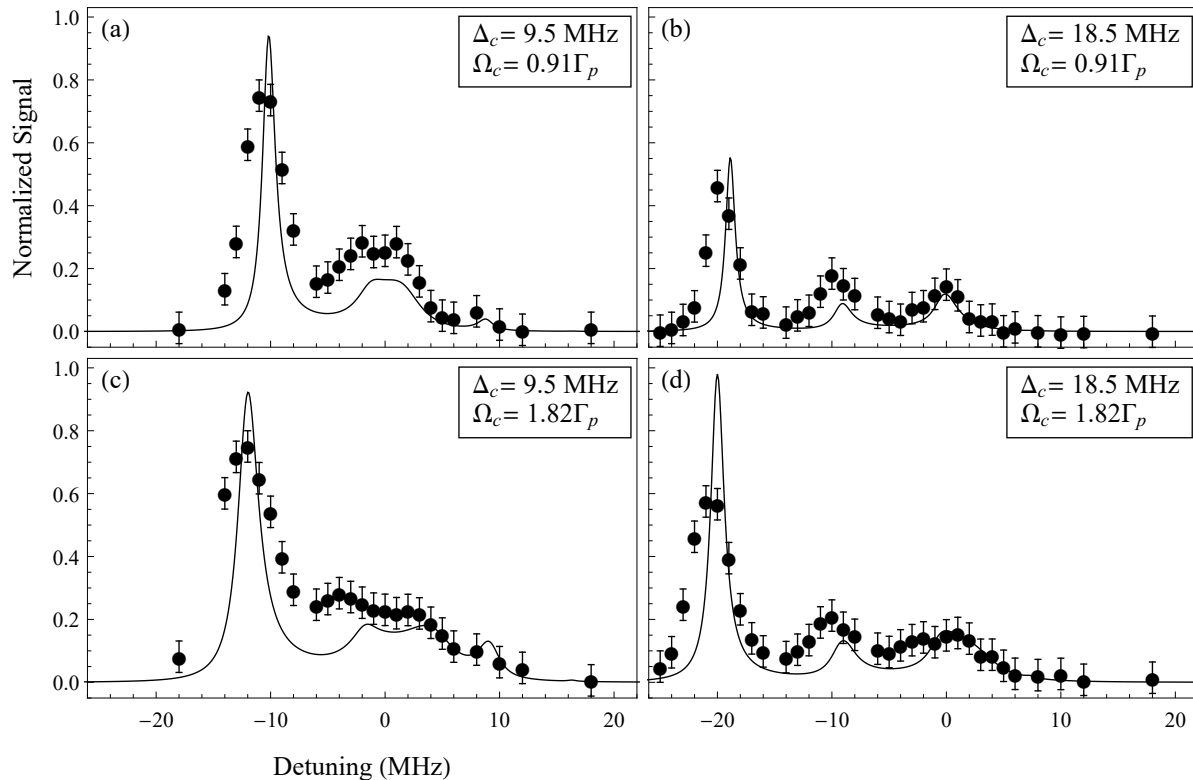


FIG. 53: Comparison of orthogonal EIT $6P_{3/2}$ fluorescence to theory as a function of probe detuning at multiple control detunings and control Rabi frequencies as displayed in legend. Probe Rabi frequency $\Omega_p = 0.18\Gamma_p$. Points correspond to data. Experimental data is scaled to the Rabi frequency $\Omega_c = 0.91\Gamma_p$ as described in text.

In Fig. 54, the experimental data corresponding to probe absorption as a function of probe detuning is shown with comparison to theory, at multiple probe Rabi frequencies, as shown in the legend.

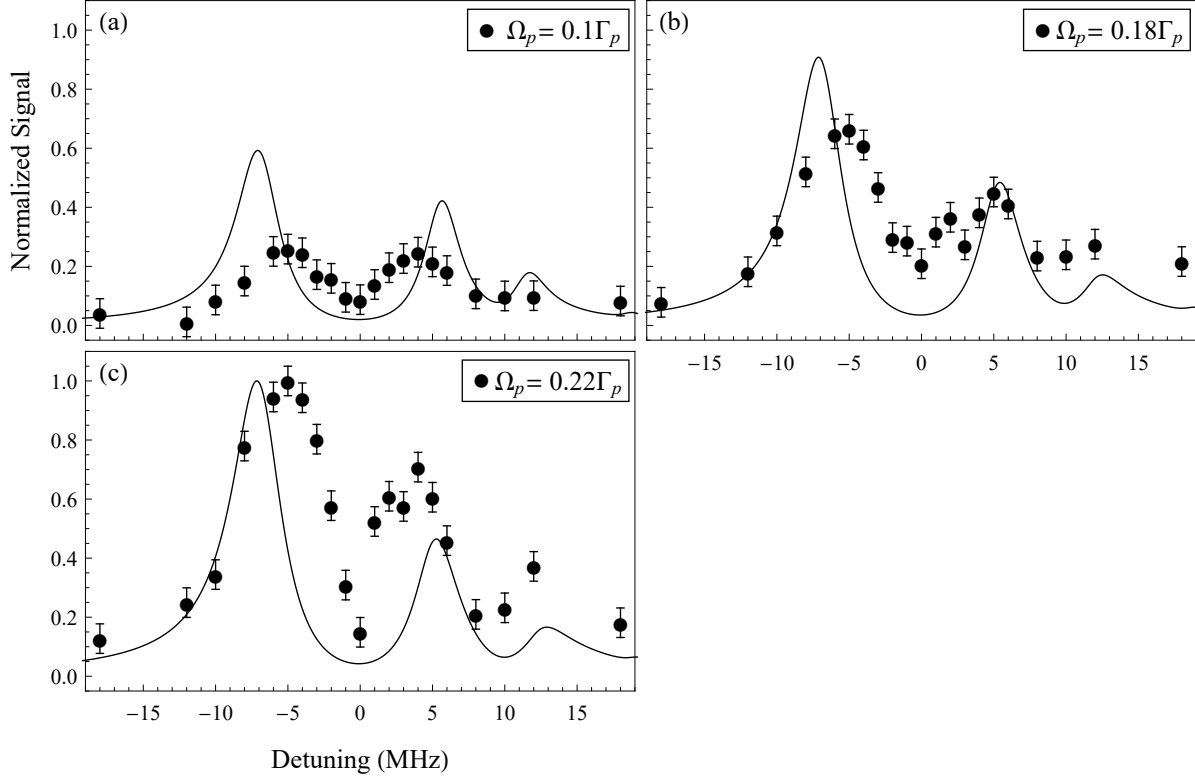


FIG. 54: Comparison of orthogonal EIT probe absorption to theory as a function of probe detuning at multiple probe intensities displayed in terms of the Rabi frequency in legends. Control Rabi frequency $\Omega_c = 2.22\Gamma_p$ and detuning $\Delta_c = 0$. Points correspond to data. Experimental data and theoretical data are normalized to the peak value of probe absorption without EIT, respectively, as described in the text.

Figure 55 displays the experimental data corresponding to fluorescence from the $6P_{3/2}$ state as a function of probe detuning with comparison to theory at multiple probe Rabi frequencies, as shown in the legend. The fluorescence signals were normalized to the data corresponding to the probe Rabi frequency of $\Omega_p = 0.22\Gamma_p$.

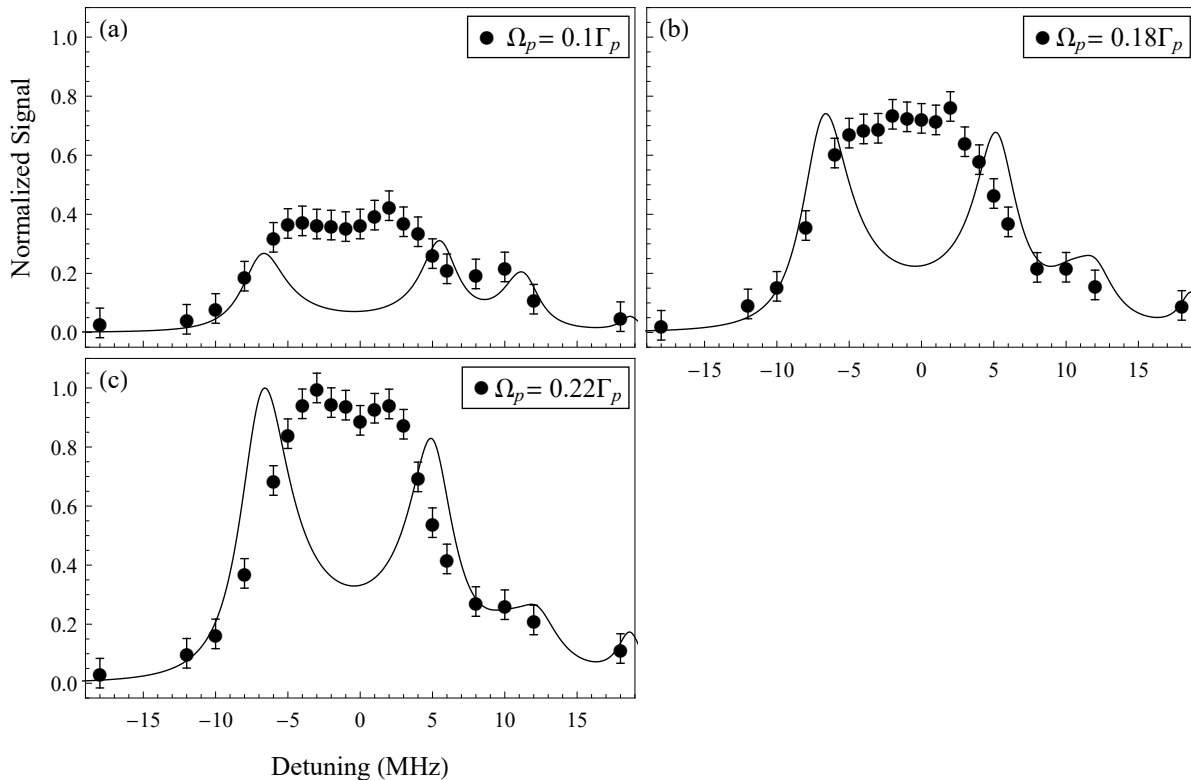


FIG. 55: Comparison of orthogonal EIT $6P_{3/2}$ fluorescence to theory as a function of probe detuning at multiple probe intensities displayed in terms of the Rabi frequency in legends. Control Rabi frequency $\Omega_c = 2.22\Gamma_p$ and detuning $\Delta_c = 0$. Points correspond to data. Fluorescence was normalized to probe Rabi frequency $\Omega_p = 0.22\Gamma_p$ data.

4.3.2 COUNTERPROPAGATING EIT

Here we present experimental data from the counterpropagating EIT geometry with theoretical calculations overlaid. In Fig. 56, the experimental data corresponding to probe absorption as a function of probe detuning is shown with comparison to theory, at various control Rabi frequencies.

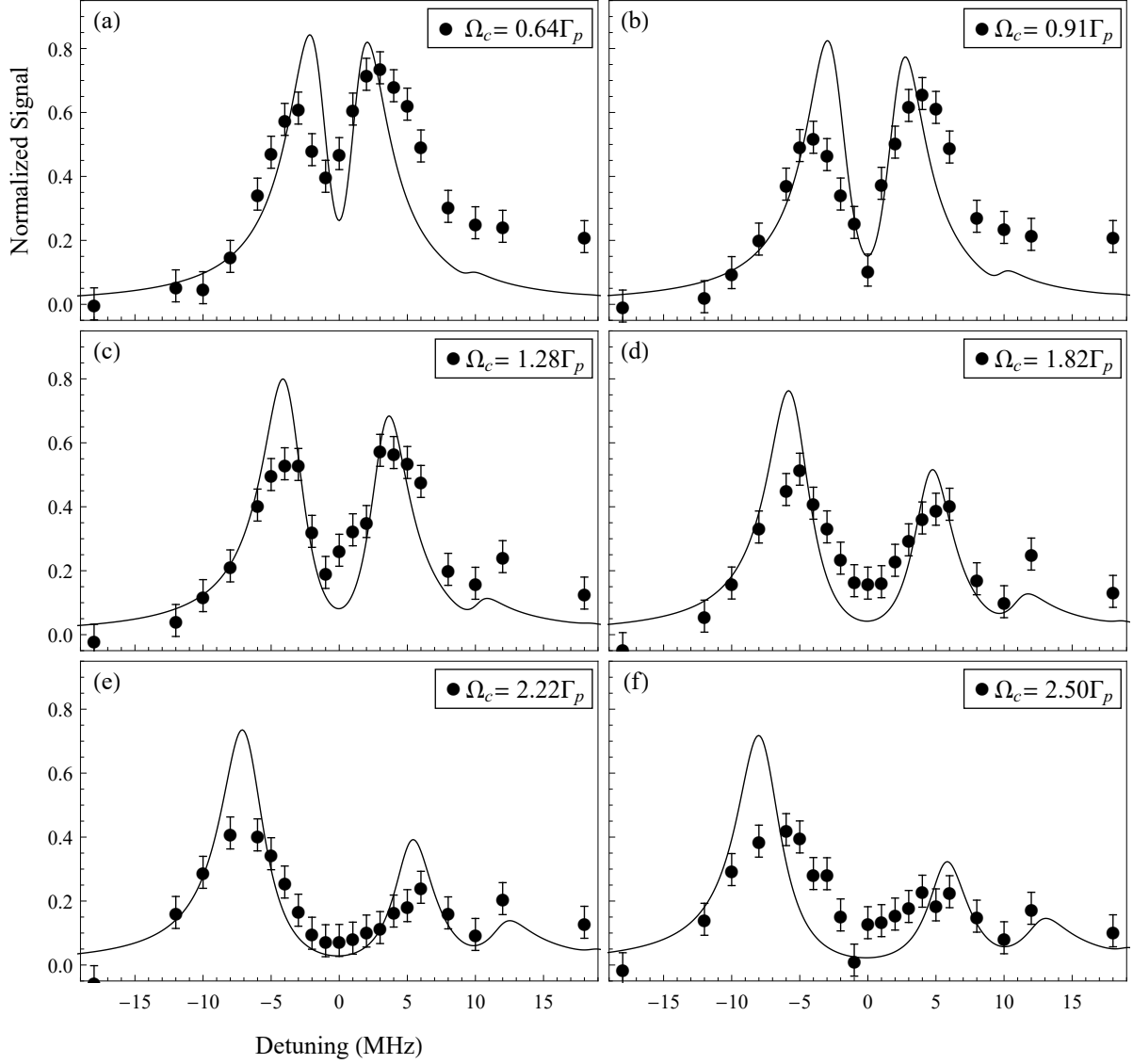


FIG. 56: Comparison of counterpropagating EIT probe absorption as a function of probe detuning to theory with $\Delta_c = 0$ and $\Omega_p = 0.18\Gamma_p$ at various control Rabi frequencies. Points correspond to data. Experimental data and theoretical data are normalized to the peak value of probe absorption without EIT, respectively, as described in the text.

Figure 57 shows the $6P_{3/2}$ fluorescence as a function of probe detuning at various control Rabi frequencies as shown in the legend. Data is normalized to the fluorescence of control Rabi frequency $\Omega_c = 0.91\Gamma_p$.

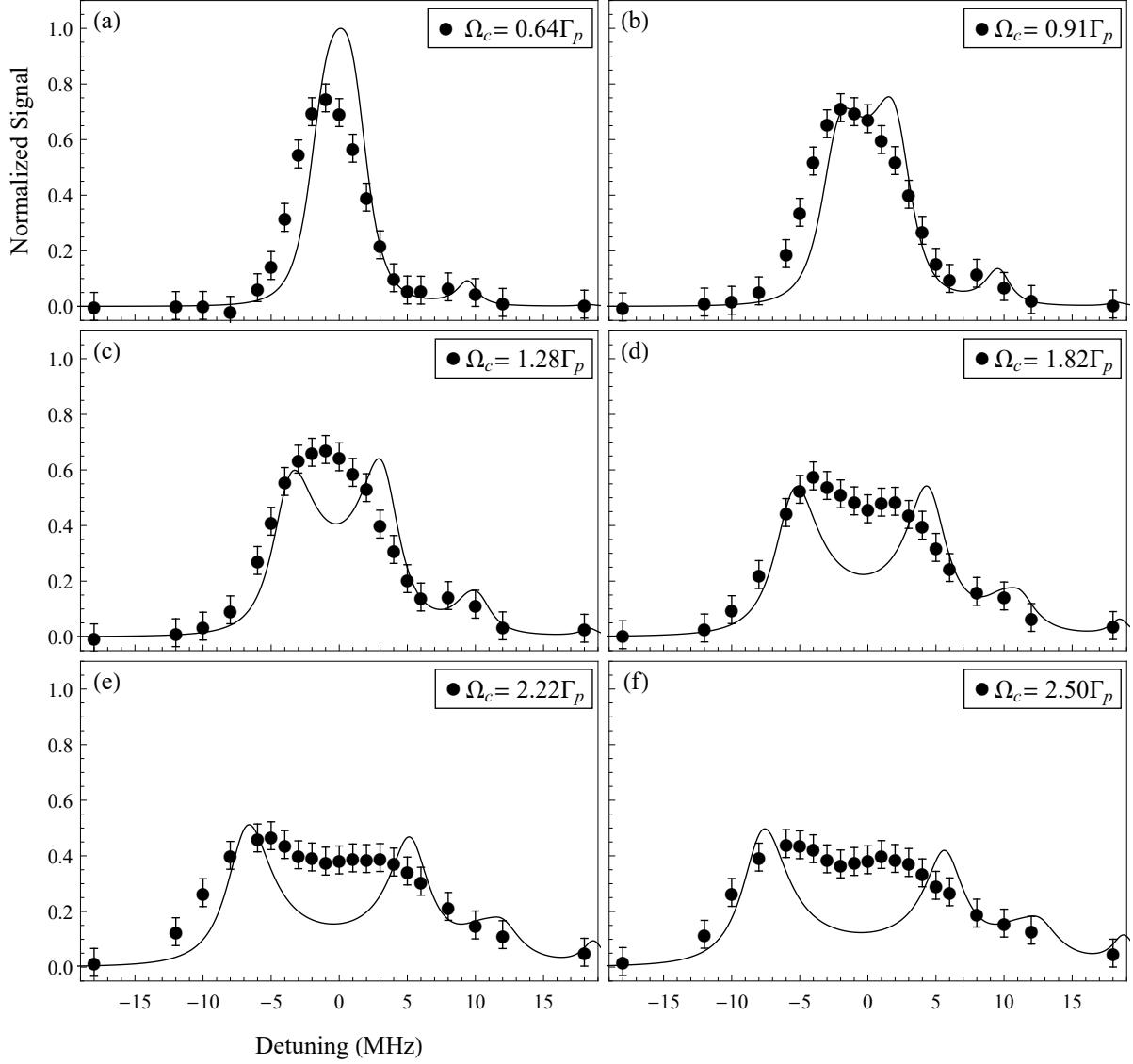


FIG. 57: Comparison of counterpropagating EIT $6P_{3/2}$ fluorescence as a function of probe detuning to theory with $\Delta_c = 0$ and $\Omega_p = 0.18\Gamma_p$ at various control Rabi frequencies. Points correspond to experimental data. Experimental data is scaled to the Rabi frequency $\Omega_c = 0.91\Gamma_p$ as described in text.

In Fig. 58, the experimental data corresponding to probe absorption as a function of probe detuning is shown with comparison to theory, at multiple control detunings and Rabi frequencies, as shown in the legend.

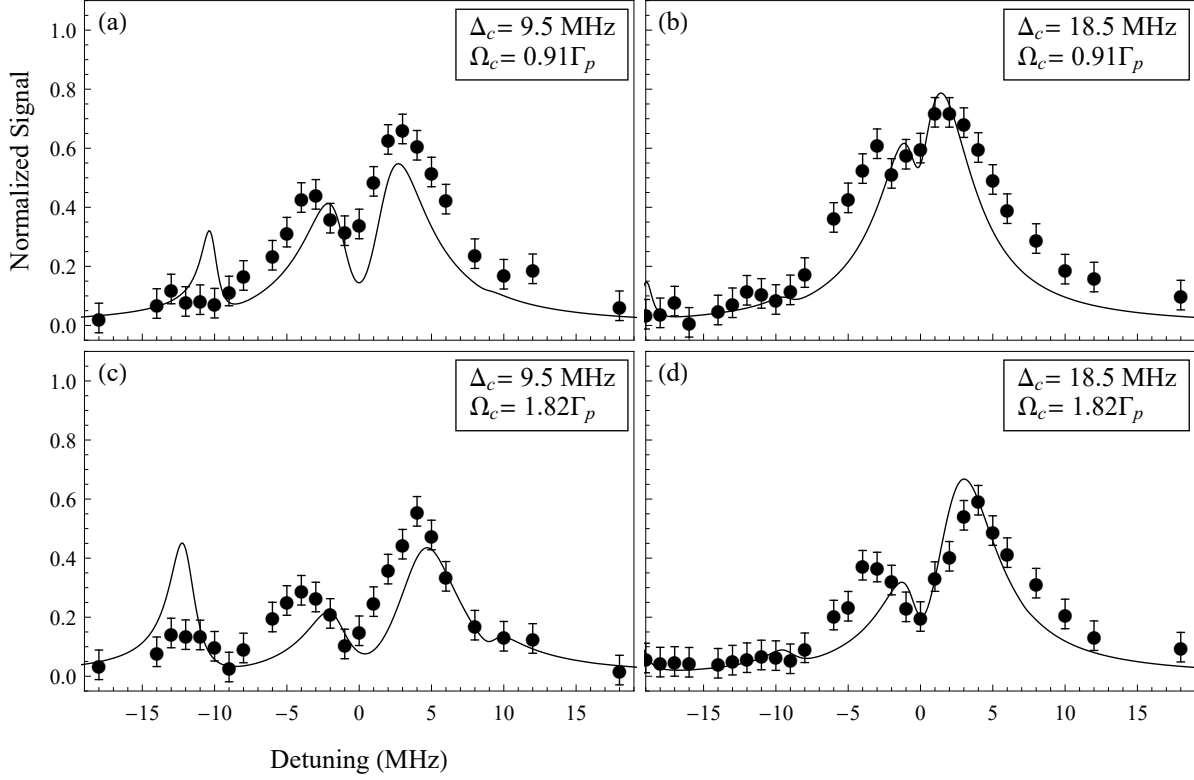


FIG. 58: Comparison of counterpropagating EIT probe absorption to theory as a function of probe detuning at multiple control detunings and control Rabi frequencies as displayed in legend. Probe Rabi frequency $\Omega_p = 0.18\Gamma_p$. Points correspond to experimental data. Experimental data and theoretical data are normalized to the peak value of probe absorption without EIT, respectively, as described in the text.

Figure 59 displays the experimental data corresponding to fluorescence from the $6P_{3/2}$ state as a function of probe detuning with comparison to theory at multiple control detunings and Rabi frequencies, as shown in the legend.

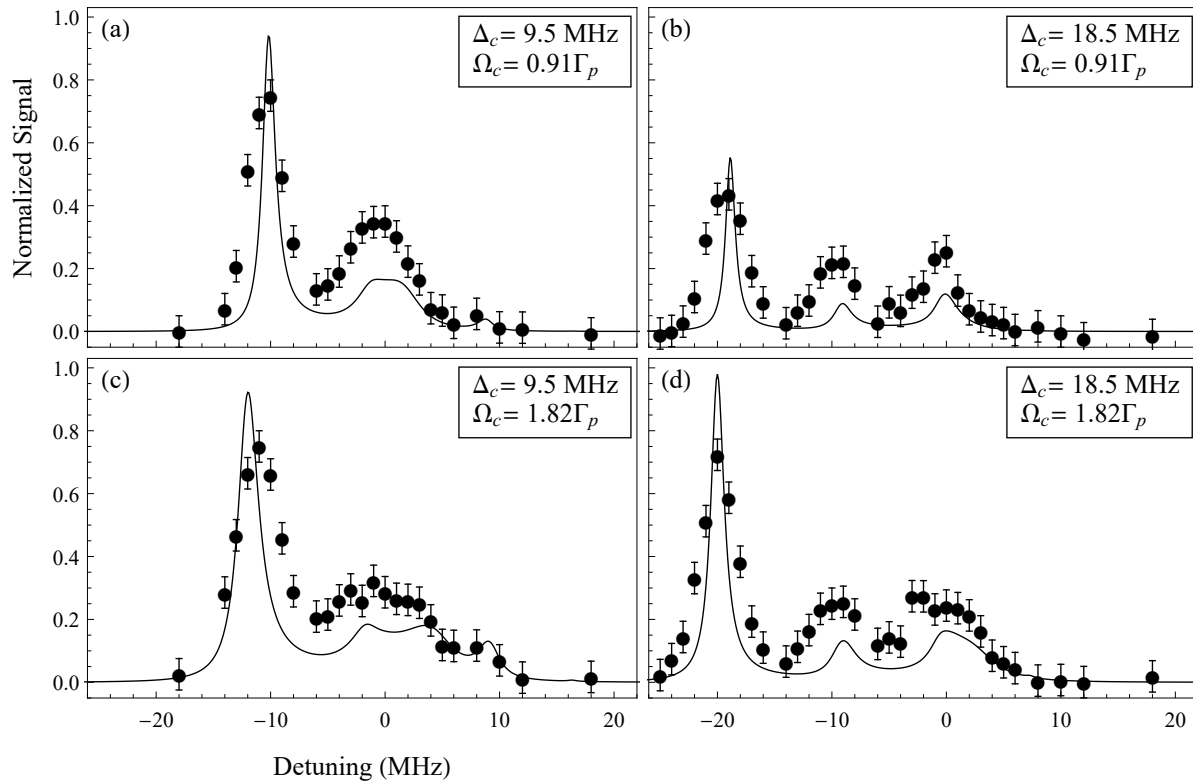


FIG. 59: Comparison of orthogonal EIT $6P_{3/2}$ fluorescence to theory as a function of probe detuning at multiple control detunings and control Rabi frequencies as displayed in legend. Probe Rabi frequency $\Omega_p = 0.18\Gamma_p$. Points correspond to data. Experimental data is scaled to the Rabi frequency $\Omega_c = 0.91\Gamma_p$ as described in text.

In Fig. 60, the experimental data corresponding to probe absorption as a function of probe detuning is shown with comparison to theory, at multiple probe Rabi frequencies, as shown in the legend.

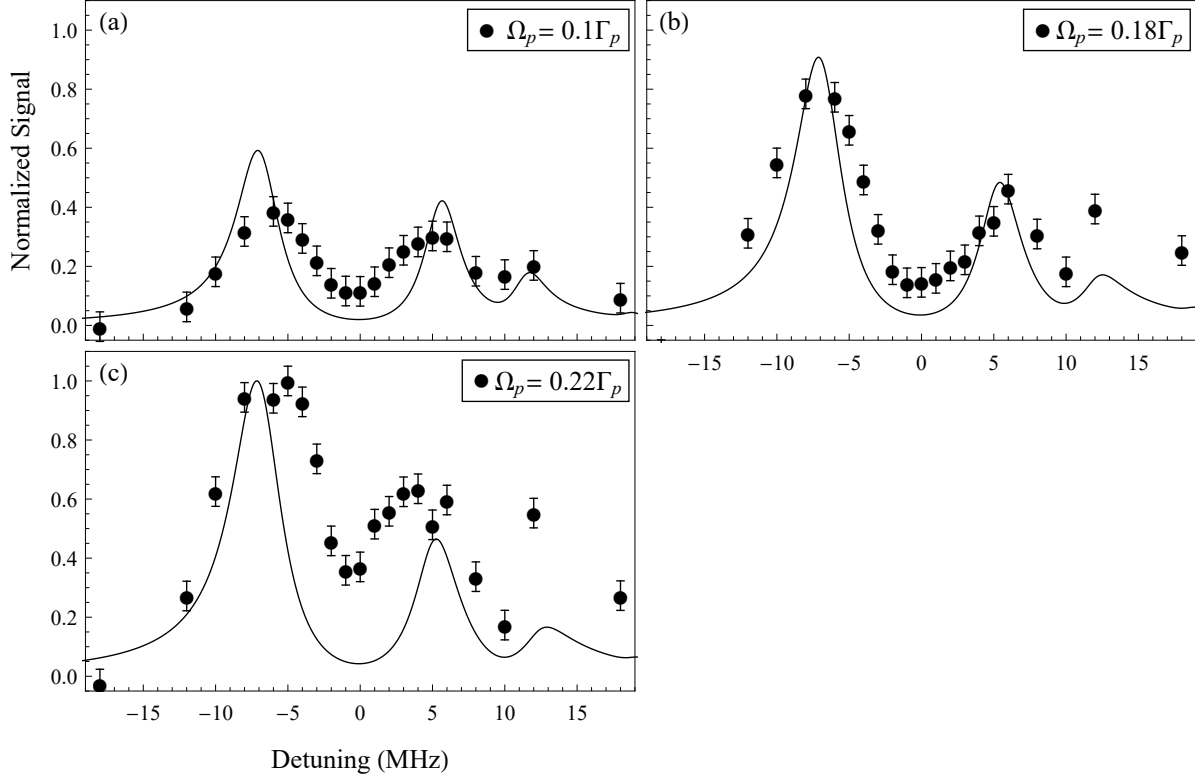


FIG. 60: Comparison of orthogonal EIT probe absorption to theory as a function of probe detuning at multiple probe intensities displayed in terms of the Rabi frequency in legends. Control Rabi frequency $\Omega_c = 2.22\Gamma_p$ and detuning $\Delta_c = 0$. Points correspond to data. Experimental data and theoretical data are normalized to the peak value of probe absorption without EIT, respectively, as described in the text.

Figure 61 displays the experimental data corresponding to fluorescence from the $6P_{3/2}$ state as a function of probe detuning with comparison to theory at multiple probe Rabi frequencies, as shown in the legend. The fluorescence signals were normalized to the data corresponding to the probe Rabi frequency of $\Omega_p = 0.22\Gamma_p$.

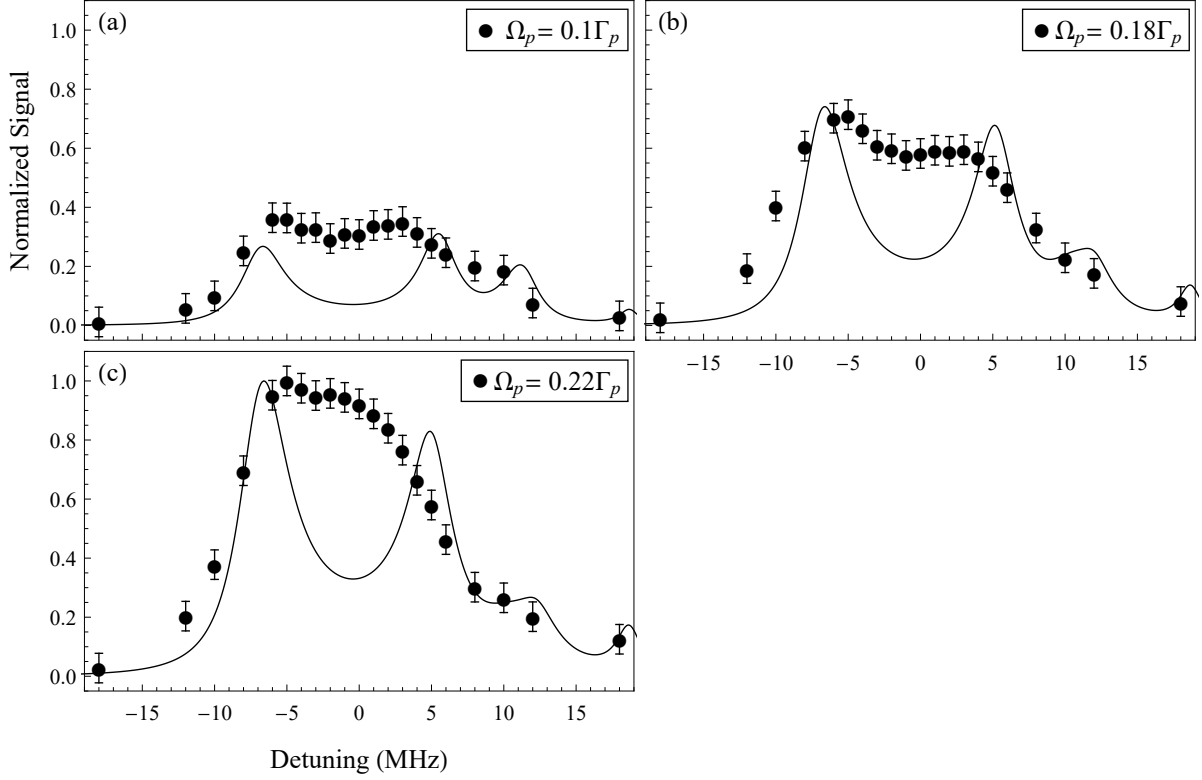


FIG. 61: Comparison of orthogonal EIT $6P_{3/2}$ fluorescence to theory as a function of probe detuning at multiple probe intensities displayed in terms of the Rabi frequency in legends. Control Rabi frequency $\Omega_c = 2.22\Gamma_p$ and detuning $\Delta_c = 0$. Points correspond to data. Fluorescence was normalized to probe Rabi frequency $\Omega_p = 0.22\Gamma_p$ data.

Qualitatively there is some agreement with experiment, but the numerical results show sharper, thinner bands in frequency. The largest discrepancy however is in the predicted $6P_{3/2}$ fluorescence curves compared to experimental results. The experimental results do not show the explicit “dip” that the theoretical results suggest. In some of the experimental data at control Rabi frequencies $\Omega_c > 2$, there is some slight signature of a dip there, but not nearly on the scale of the theory. This leads us to believe that there is some significant broadening mechanism occurring within the experimental domain. Broadening can occur from a variety of reasons including, but not limited to laser linewidth, collision broadening, laser frequency locking instability, and residual magnetic fields lifting the degeneracy of Zeeman substates. The aforementioned broadening mechanisms were not included in the

theory calculations presented here.

To summarize the comparison of the numerical results to experimental, in general numerical solutions showed much more pronounced effects than what was shown in experiment, with EIT windows being much thinner and more steep. There was some variance in off resonant fluorescence amplitudes, but displayed qualitative agreement. These inaccuracies between the numerical simulation and experiment could be attributed to a vast variety of reasons, one being the non-zero linewidth of lasers in the experimental setting, sensitivity to beam alignment, and also due to OBEs describing the effect of a single atom subject to electric fields treated as a “population” as opposed to a Gaussian distributed sample of atoms as in a MOT.

CHAPTER 5

COHERENT BACKSCATTERING EXPERIMENTAL

RESULTS

As previously mentioned, CBS can occur from a variety of different objects. For comparison, the CCD images of CBS from a macroscopic object (Styrofoam ball) is compared with the CBS from a cold atomic sample in Fig. 62. As expected, the macroscopic object shows a much more pronounced CBS profile than the cold atomic sample. This is partly due to the atomic gas being more dilute than typical solid objects that CBS is usually observed from, allowing for less multiple scattering, along with the motion of the cold atoms (~ 10 cm/s) which in turn causes dephasing of time reversed wave trajectories, along with depolarization and other effects mentioned in Chapter 2. For images and therefore data points within this section, light was collected for 10 minutes, corresponding to ~ 11 seconds of CBS light collection, as eluded in the experimental timing description. The primary measurement of CBS will be the enhancement value, which as discussed in Chapter 2 is ratio the total reflected light (coherent and incoherent) to the incoherent background contribution. Specifically in terms of the albedo,

$$\text{enhancement} = \frac{\alpha}{\alpha_D} = \frac{\alpha_C + \alpha_D}{\alpha_D} . \quad (128)$$

The various parameters of CBS data to be covered in this chapter are:

- Probe detuning dependence of CBS without EIT.
- Control intensity dependence of CBS during EIT.
- Probe detuning dependence of CBS with EIT at various control intensities in terms of Rabi frequency.
- Probe detuning dependence of CBS with EIT at various control polarizations.
- Control detuning dependence of CBS with EIT.

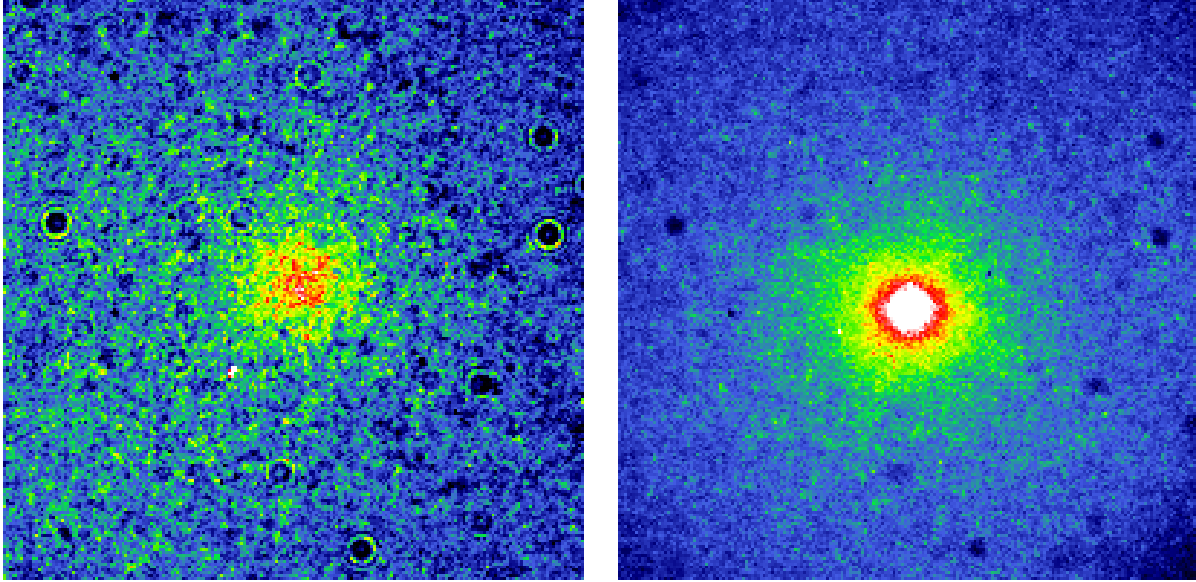


FIG. 62: Left: Collection period of 10 minutes of coherent backscattering on the H_{\perp} channel of a cold rubidium sample. Right: Collection period of 60 s of coherent backscattering off of a spinning Styrofoam ball.

5.1 ATOMIC CBS WITHOUT EIT

First, we present CBS data to give a baseline of the effect without a control beam present. Images of CBS for the four studied channels, H_{\perp} , H_{\parallel} , L_{\perp} , and L_{\parallel} , are shown in Fig. 63.

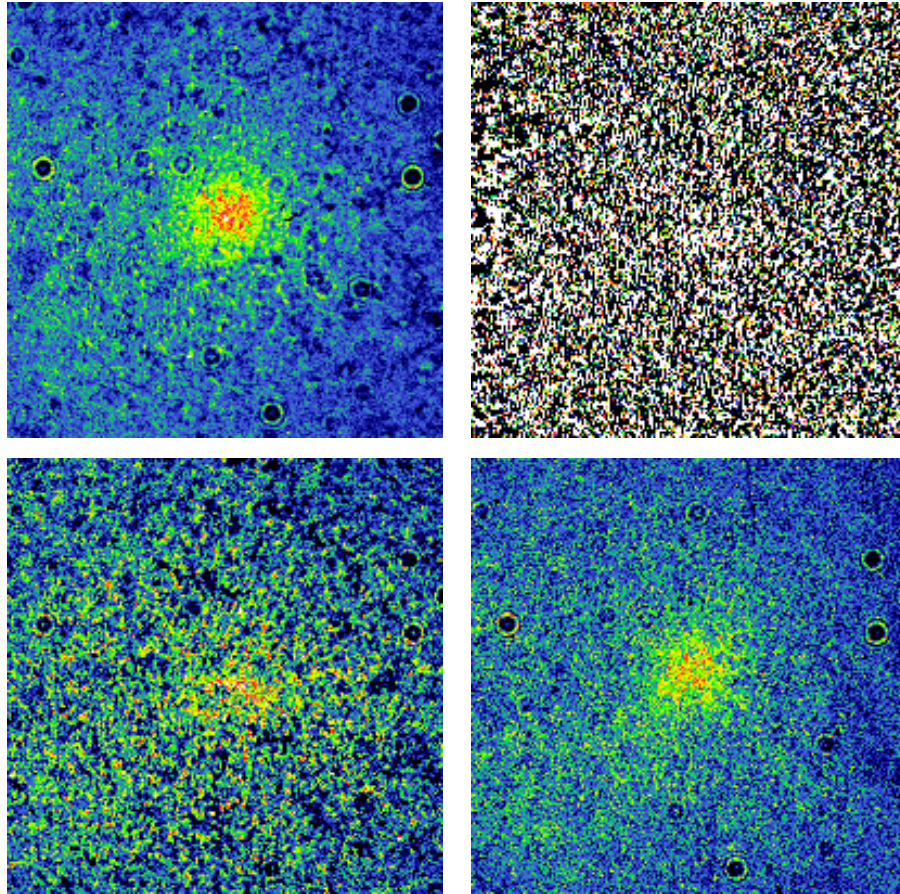


FIG. 63: Top left: H_{\perp} channel. Top right: H_{\parallel} channel. Bottom left: L_{\perp} channel. Bottom right: L_{\parallel} channel. All channels collected for a 10 minute period.

Upon examining the four channels of CBS, it is clear to see that the H_{\perp} channel has the most distinguishable signal to noise, as was eluded to previously. For that reason, most of the experiments involving CBS under electromagnetically induced transparent conditions were performed primarily on the H_{\perp} channel, with some further analysis of the L_{\perp} and L_{\parallel} channels as well. Over the course of data acquisition, the H_{\parallel} showed little to no CBS signals as displayed in Figs. 63, 64, so this channel was eliminated from this study. A more quantitative method for analyzing CBS is by using the counts vs pixel of a single strip of pixels through the peak of the CBS profile, as shown in Fig. 64. From this, the angular width of the CBS cone and enhancement factor can be determined. Pure CCD counts are displayed as orange points in the following plots and the smoothed counts are displayed in

purple, which give an averaged value of counts. Also, there is an alternative method of determining the cone, based on angular integration of the CCD. The angular integration is performed by taking concentric “rings” of pixels, starting from the center pixel iterating each ring being just outside the last, larger than the last. Each ring of pixels is normalized to the number of pixels contained within the ring. The angular integration method is shown in black in each of the counts vs pixel plots and as one can see, follows the averaged counts over a single pixel slice quite closely.

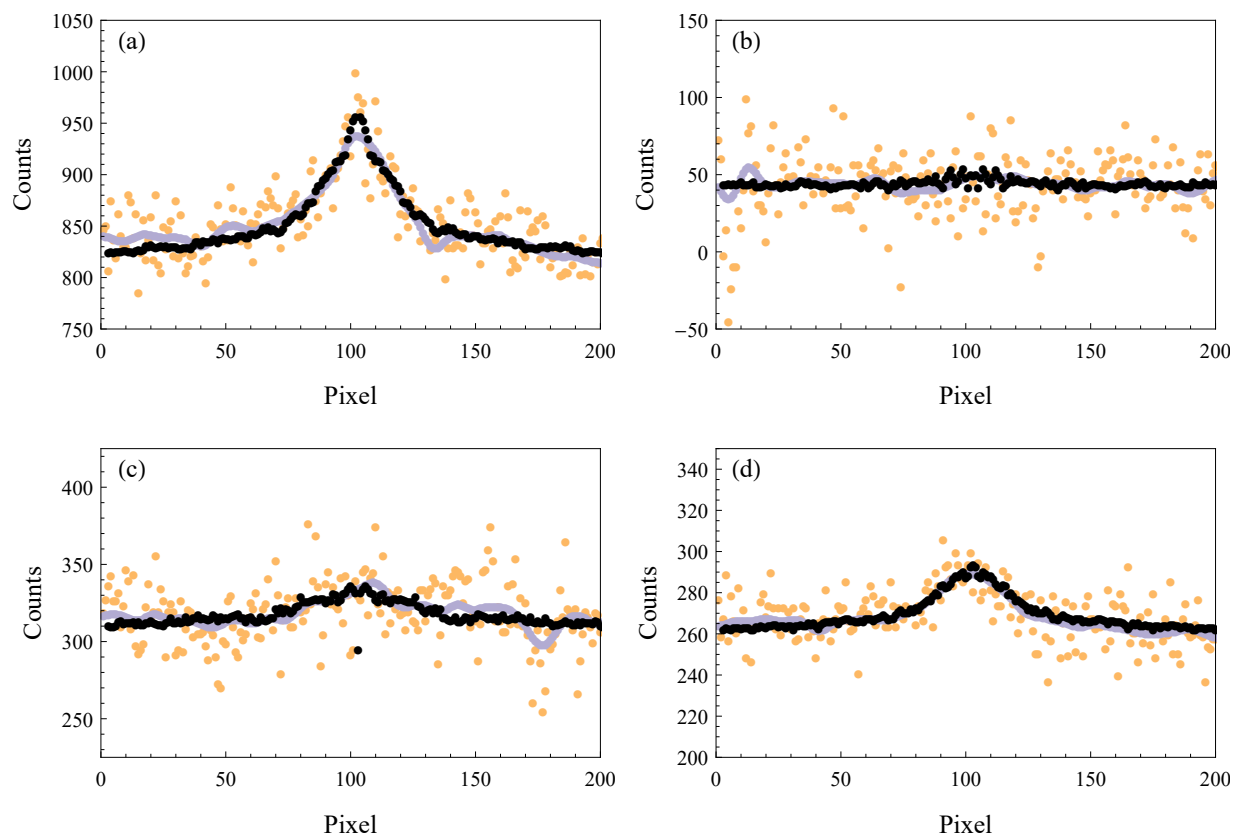


FIG. 64: CCD counts with respect to pixel. (a) H_{\perp} channel. (b) H_{\parallel} channel. (c) L_{\perp} channel. (d) L_{\parallel} channel. These profiles correspond to the CCD images in Fig. 63

5.1.1 CBS DETUNING DEPENDENCE

To further survey the effect of coherent backscattering, the frequency detuning of the probe beam was measured as a baseline to compare with that of coherent backscattering under electromagnetic induced transparency.

The probe field detuning dependence of the H_{\perp} channel is shown in Fig. 65. A total of 11 detunings were measured for each of the probe detuning data sets, with sample CCD profiles shown in Fig. 65 and further analysis in Fig. 66.

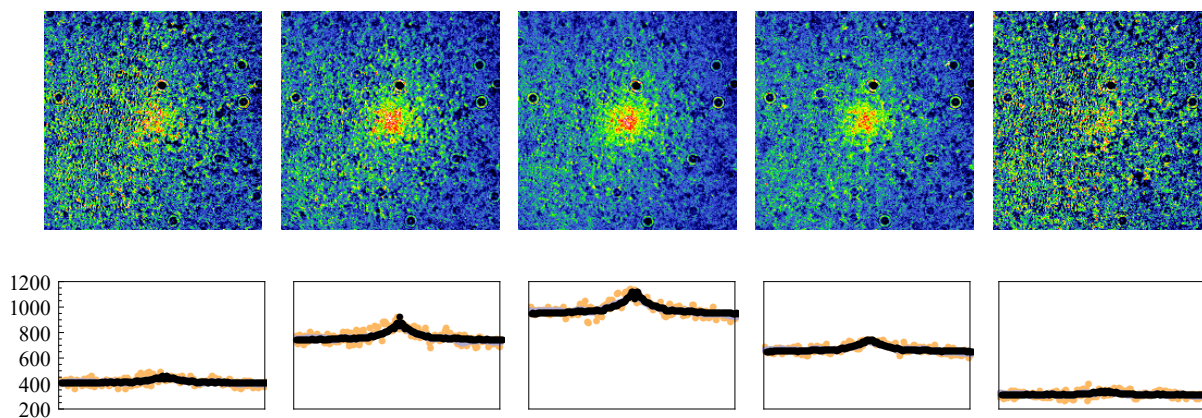


FIG. 65: Top: CCD images from the H_{\perp} channel probe detuning dependence. Bottom: Detuning dependence of CBS profiles with angular integration overlaid. Detunings from left to right for top and bottom are: -6 MHz, -3 MHz, 0 MHz, 3 MHz, 6 MHz.

With no control beam present, CBS is more observable near resonance, and tapers off as probe detuning diverges from zero. This is quantitatively shown in Fig. 66. In (a), the background and peak counts are shown on the same scale, with (b) showing the ratio of those values to determine the enhancement factor.

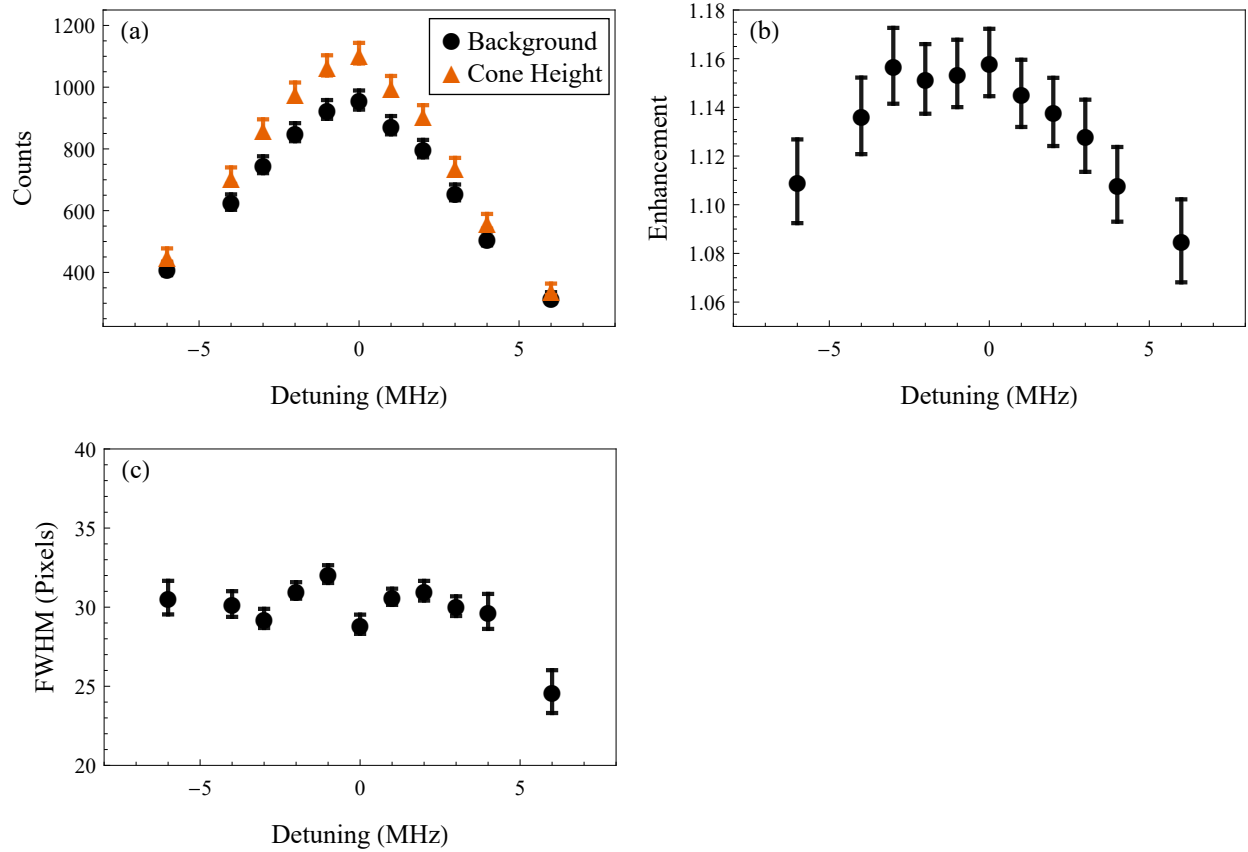


FIG. 66: Data corresponding to the H_{\perp} channel with no control beam present. (a) CBS background level and cone height as a function of probe detuning. (b) CBS enhancement as a function of probe detuning. (c) CBS cone width as a function of probe detuning.

From Fig. 66(b), the enhancement factor near resonance is around 1.15, with the value converging to one as the probe is detuned. Figure 66(c) displays the width of the CBS cone at each detuning in pixels. The cone width appears to be roughly 30 pixels across the detuning range, which corresponds to roughly 1.6 mrad.

The same probe detuning dependent measurements were repeated for the L_{\parallel} channel, with CCD images and CBS profiles shown in Fig. 67.

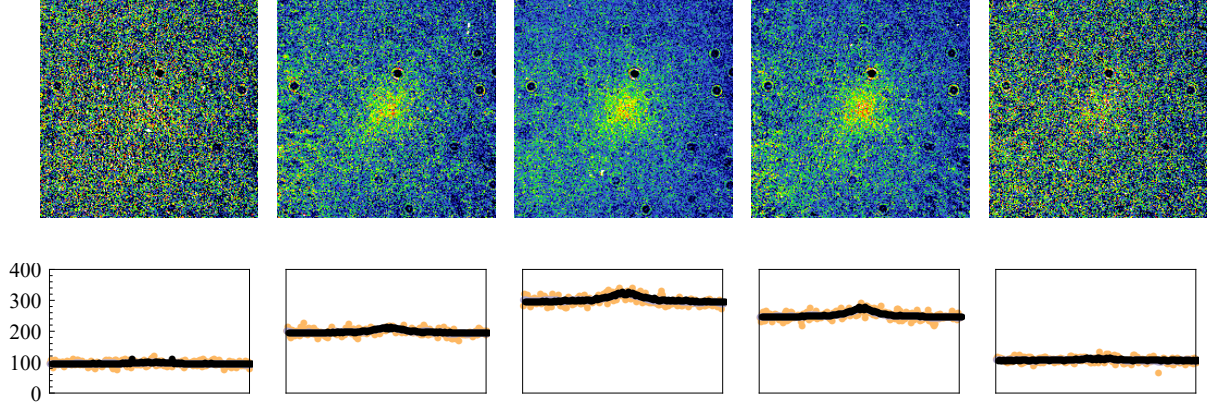


FIG. 67: Top: CCD images from the L_{\parallel} channel probe detuning dependence with no control beam present. Bottom: Detuning dependence of CBS profiles with angular integration overlaid. Detunings from left to right for top and bottom are: -6 MHz, -3 MHz, 0 MHz, 3 MHz, 6 MHz.

The images of the L_{\parallel} channel trend similarly to those of the H_{\perp} channel, but with less counts at all detunings. From the CBS profile in the bottom of Fig. 67, the counts are roughly a third or less in all cases as compared to the H_{\perp} channel. Further analysis of the L_{\parallel} channel is shown in Fig. 68. The probe detuning dependence of CBS in the L_{\parallel} channel has an asymmetry, that could be due to laser frequency lock point, but more than likely due to the lower fidelity of the CBS profiles, as compared to when CBS signals are much stronger. At lower count levels, the CBS “cone” and incoherent background levels are much closer to that of the natural random counts accumulated by the CCD over the 10 minute span of data acquisition. From Fig. 68(b), the enhancement factor near resonance is around 1.1, with the value decreasing towards negative detuning and increasing for positive detuning up until 6 MHz which is the aforementioned asymmetry. Figure 68(c) displays the width of the CBS cone at each detuning in pixels. The cone width appears to be roughly between 30 and 40 pixels across the detuning range, which corresponds to roughly 1.6-2.1 mrad.

The L_{\perp} and H_{\parallel} channels were not studied further in terms of detuning dependence due to poor quality of signal to noise.

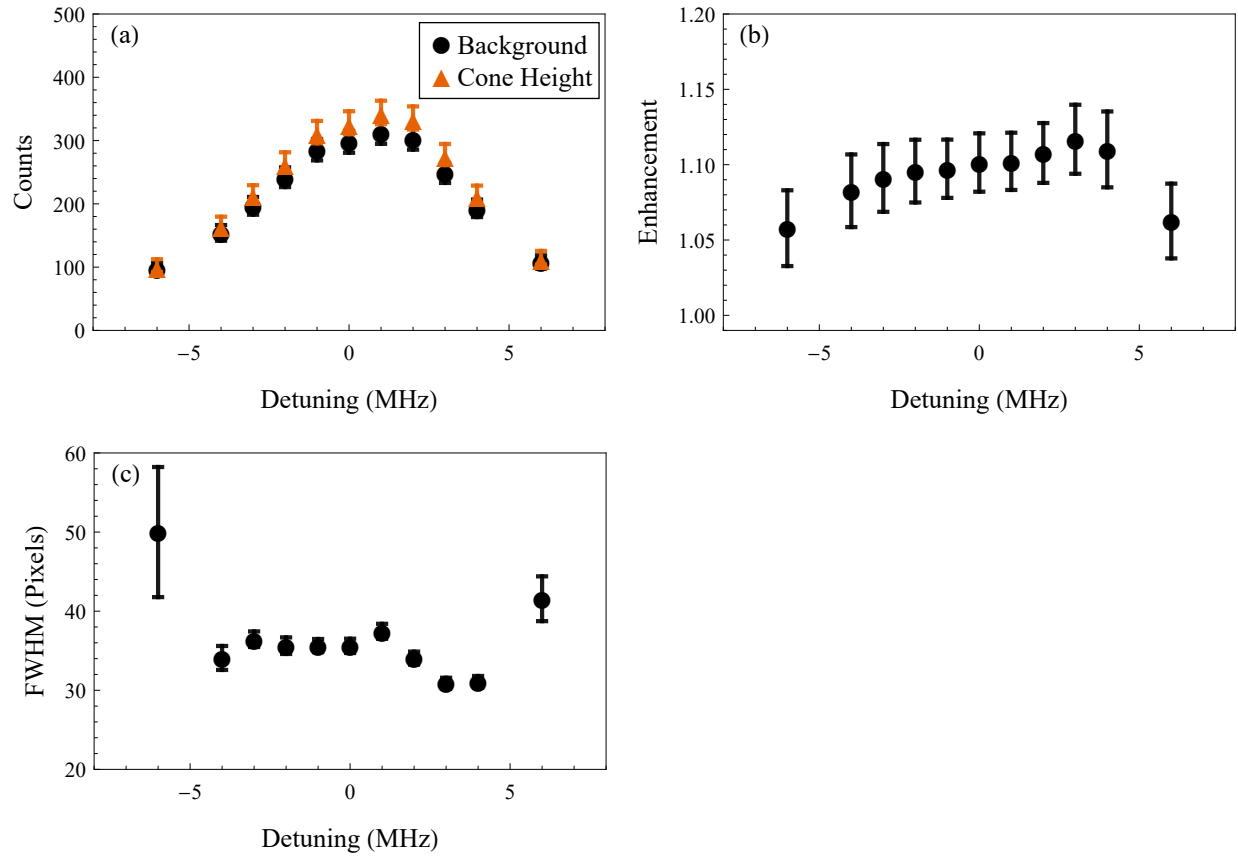


FIG. 68: Data corresponding to the L_{\parallel} channel with no control beam present. The top left shows the CBS background level and cone height as a function of probe detuning. The top right shows the CBS enhancement as a function of probe detuning. The bottom shows the CBS cone width as a function of probe detuning.

5.2 CBS WITH EIT

With coherent backscattering under normal conditions covered briefly, we now move to the primary topic of this dissertation, coherent backscattering under electromagnetically induced transparent conditions. Here, unless otherwise stated, the control field detuning is $\Delta_c = 0$ and the probe Rabi frequency is $\Omega_p = 0.18\Gamma_p$.

5.2.1 CBS WITH EIT CONTROL INTENSITY DEPENDENCE

To express the full variation of CBS during EIT conditions, Fig. 69 displays the CCD images of CBS at each measured control Rabi frequency, up to $1.82\Gamma_p$.

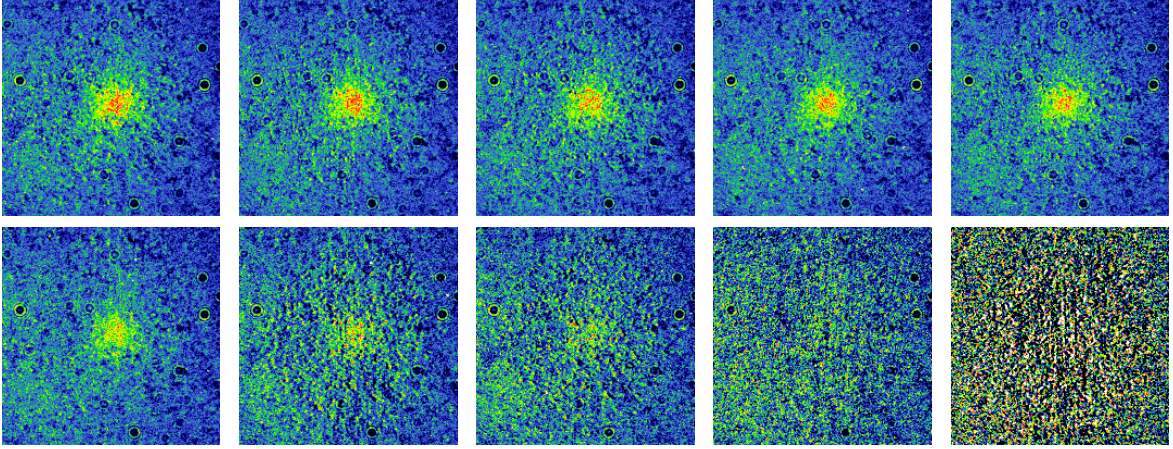


FIG. 69: Control beam intensity dependence of the H_{\perp} channel with control beam intensities in ascending order with $\Delta_c = 0$ and probe Rabi frequency $\Omega_p = 0.18\Gamma_p$. The intensities in terms of Rabi frequencies are: $\Omega_c = 0, 0.11\Gamma_p, 0.16\Gamma_p, 0.22\Gamma_p, 0.32\Gamma_p, 0.45\Gamma_p, 0.64\Gamma_p, 0.91\Gamma_p, 1.28\Gamma_p, 1.82\Gamma_p$.

The corresponding CBS profiles from Fig. 69 are shown in Fig. 69, with 10 images and CBS profiles to fully represent the effect of control laser Rabi frequency on CBS. The number of images and CBS profiles will be reduced from here. Unless otherwise stated, the control field detuning is $\Delta_c = 0$. Also, control Rabi frequencies beyond $\Omega_c = 1.82\Gamma_p$ were not used due to the reduction in signal to noise past that value.

Further analysis of the H_{\perp} channel as a function of control field power is shown in Fig. 71, displaying the background and CBS cone height, CBS enhancement value, and full width at half maximum (FWHM) as functions of control beam power.

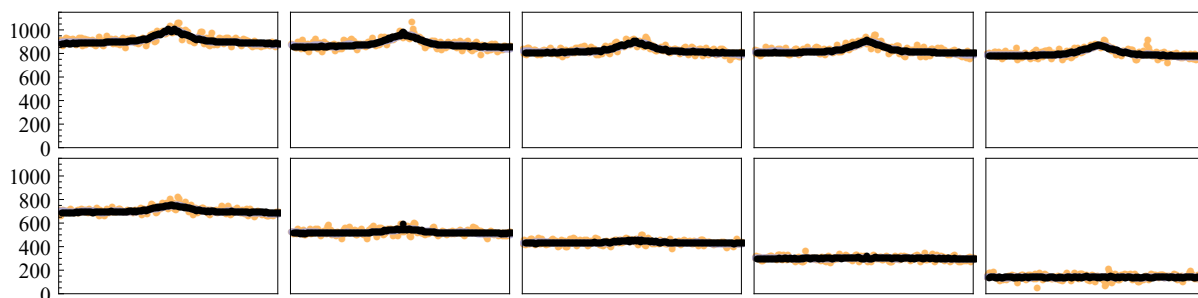


FIG. 70: CBS profiles corresponding to the images in Fig. 69

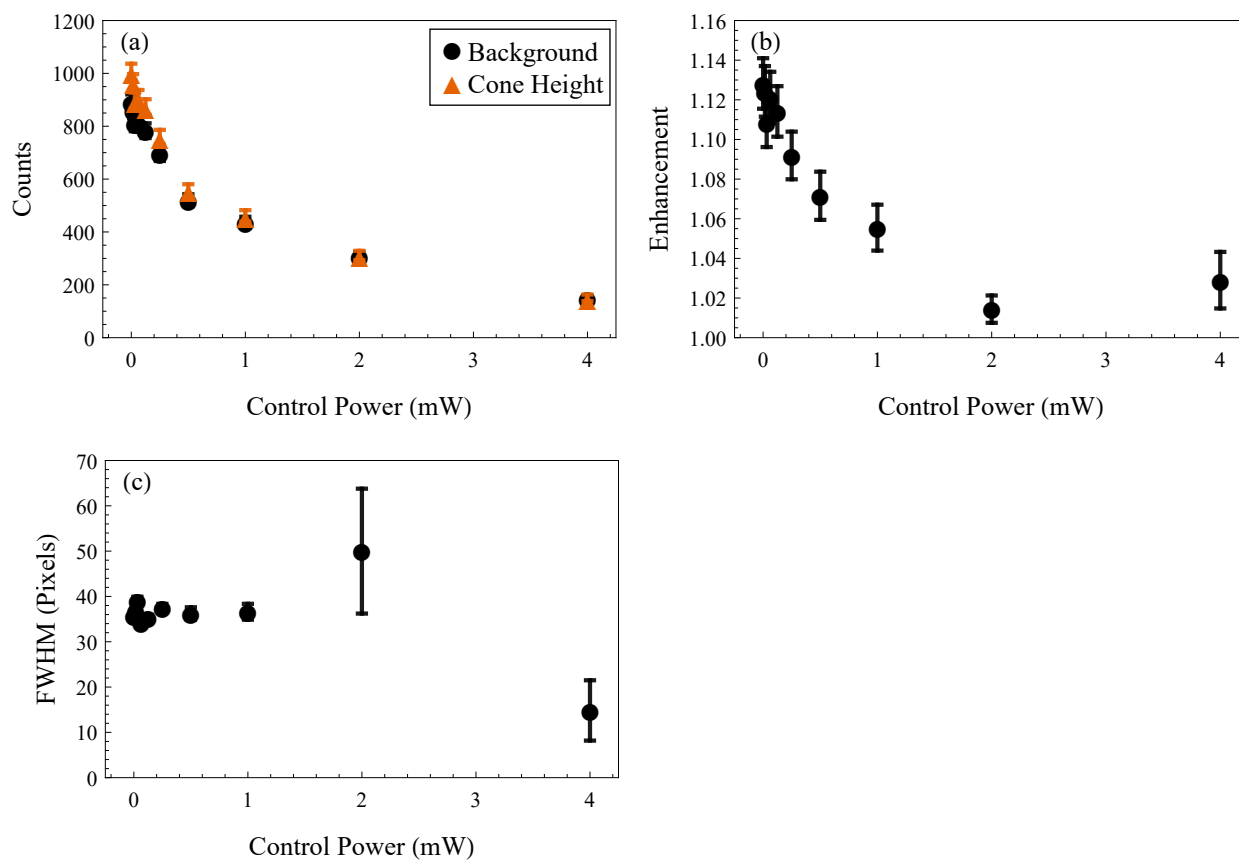


FIG. 71: Control power dependence of the H_{\perp} channel with control detuning $\Delta_c = 0$ and probe Rabi frequency $\Omega_p = 0.18\Gamma_p$. (a) the CBS background level and cone height. (b) the CBS enhancement. (c) CBS cone width.

From Fig. 71(a), it is clear that the control beam being present reduces the amount of total scattering, incoherent background and coherent backscattering, as the power of the control beam increases. While not immediately intuitive from total scattering reduction, the enhancement factor also is reduced as control power increases. However, the width of the CBS profile appears to be consistent across the range of powers, within the 30-40 pixel range (1.6-2.1 mrad).

Next, the same measurements were taken, but with a vertically polarized control field. These results are shown in Fig. 72 and further analyzed in Fig. 73.

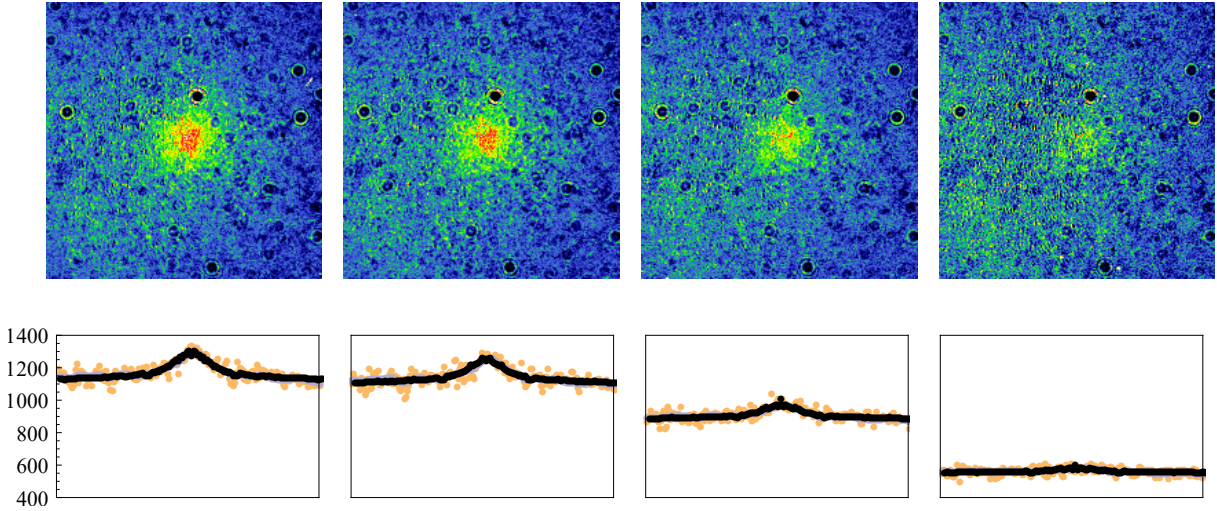


FIG. 72: Top: CCD images of vertically polarized control field intensity dependence of H_{\perp} channel with control detuning $\Delta_c = 0$ and probe Rabi frequency $\Omega_p = 0.18\Gamma_p$. Bottom: CBS profiles as a function of control intensity. Corresponding control intensity in terms of Rabi frequency from left to right: $\Omega_c = 0, 0.22\Gamma_p, 0.45\Gamma_p, 0.91\Gamma_p, 1.28\Gamma_p$.

The vertically polarized control beam seems to increase the amount of CCD counts, as opposed to the horizontally polarized beam. However, it must be noted that slight variations in probe beam power, MOT beam power, current in the getter circuit and more can all attribute to count differences from day to day in the laboratory environment. A higher getter current can easily increase the number of atoms in the MOT, which increases counts,

and in turn increases the amount of coherent backscattering as well.

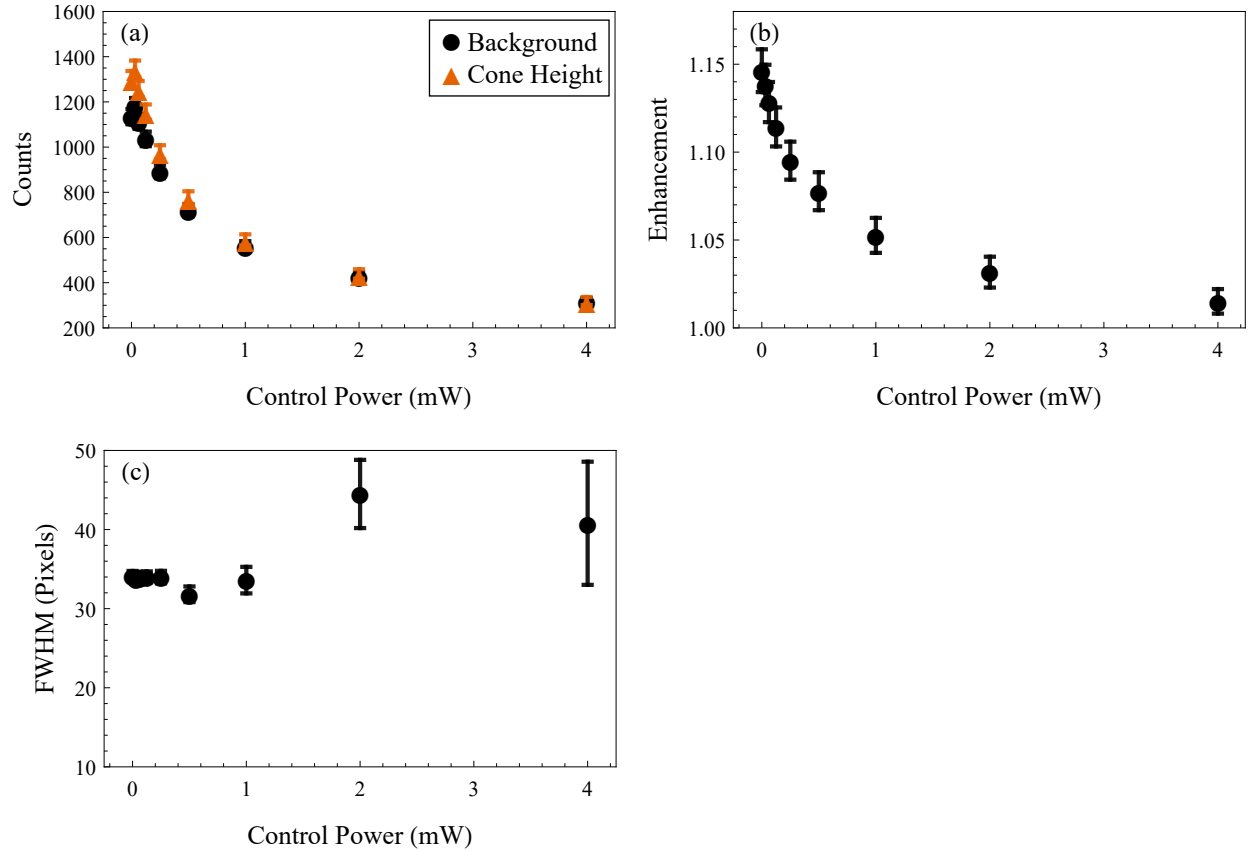


FIG. 73: Control power dependence of the H_{\perp} channel with a vertically polarized control field with control detuning $\Delta_c = 0$ and probe Rabi frequency $\Omega_p = 0.18\Gamma_p$. (a) CBS background level and cone height as a function of control field power. (b) CBS enhancement as a function of control field power. (c) CBS cone width as a function of control field power.

The trend of the vertically polarized control beam in Fig. 73, follows similarly to that of the horizontally polarized control field, with counts and enhancement decreasing as a function of control power. The backscattering profile width also follows closely, being in the 30-40 pixel range (1.6-2.1 mrad).

Lastly, of the control field polarization comparisons, is a circularly polarized control. Sample images and CBS profiles are shown in Fig. 74.

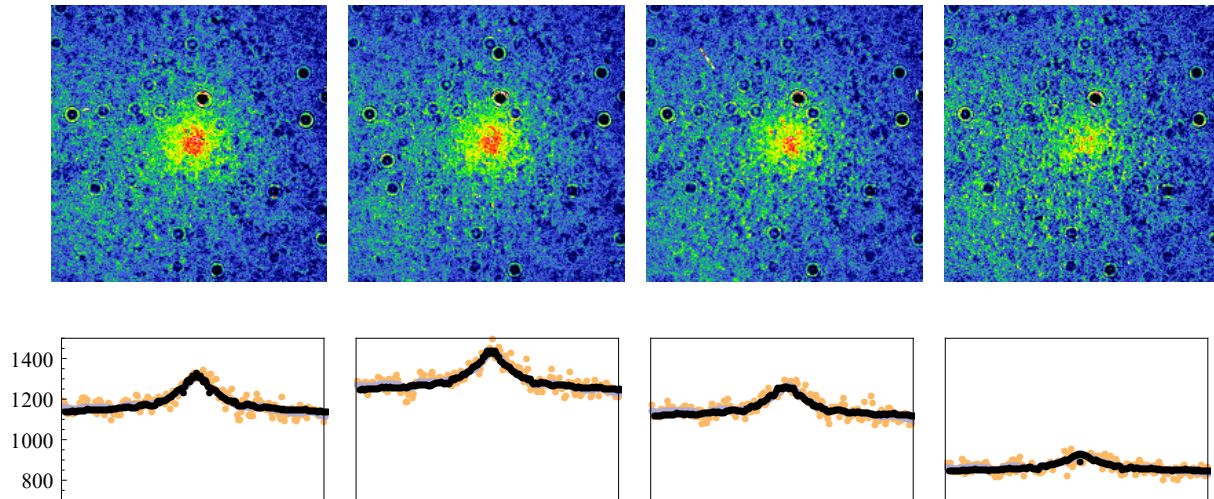


FIG. 74: Top: CCD images of circularly polarized control field intensity dependence of H_{\perp} channel with control detuning $\Delta_c = 0$ and probe Rabi frequency $\Omega_p = 0.18\Gamma_p$. Bottom: CBS profiles as a function of control field Rabi frequency. Corresponding control intensity in terms of Rabi frequency from left to right: $\Omega_c = 0, 0.22\Gamma_p, 0.45\Gamma_p, 0.91\Gamma_p, 1.28\Gamma_p$.

Further analysis of the circularly polarized control field is shown in Fig. 75. As with the vertically polarized control beam, there was an increase in counts from the horizontally polarized beam. The counts for the Rabi frequency of $\Omega_c = 0.22\Gamma_p$ were greater than the counts with no control present, which could be due to fluctuations in laser power, or lack thereof during the measurement.

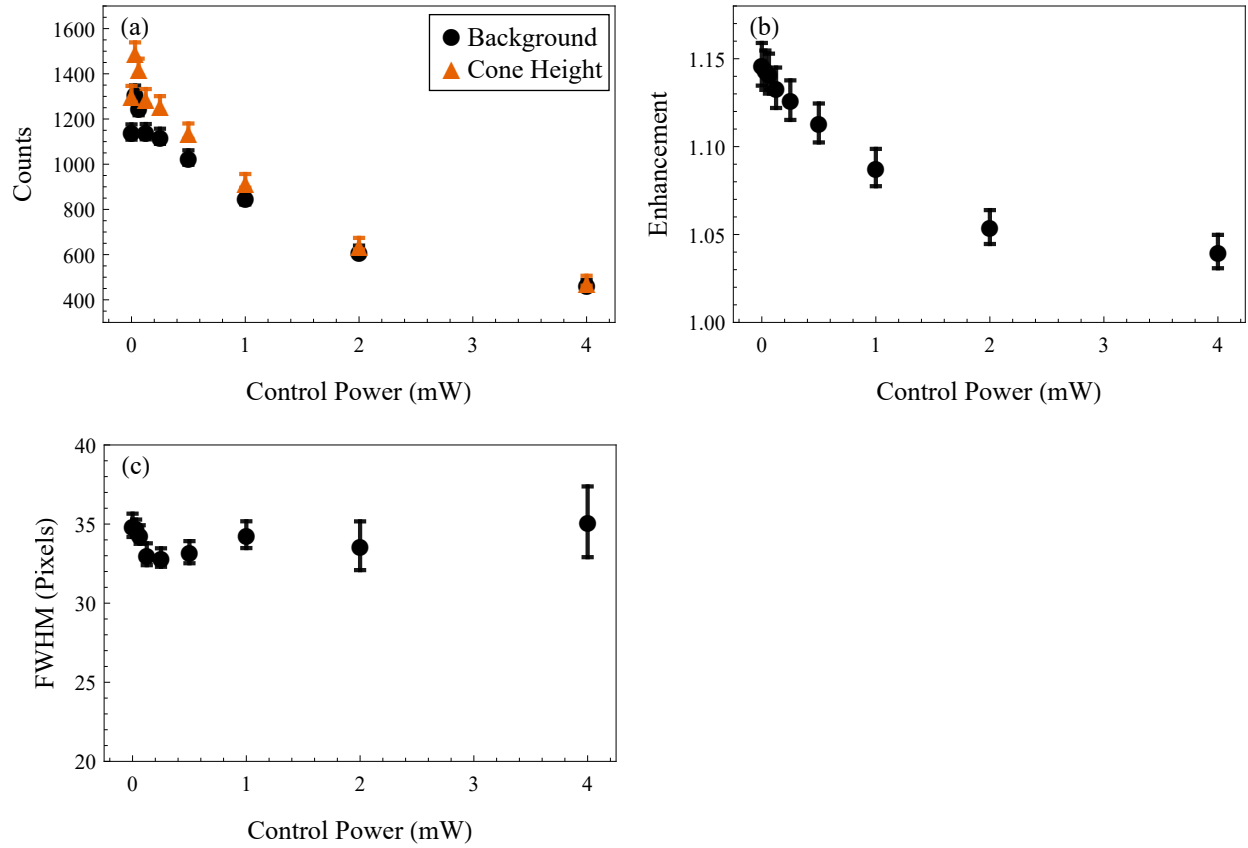


FIG. 75: Control power dependence of the H_{\perp} channel with a circularly polarized control field with control detuning $\Delta_c = 0$ and probe Rabi frequency $\Omega_p = 0.18\Gamma_p$. (a) CBS background level and cone height as a function of control field power. (b) CBS enhancement as a function of control field power. (c) CBS cone width as a function of control field power.

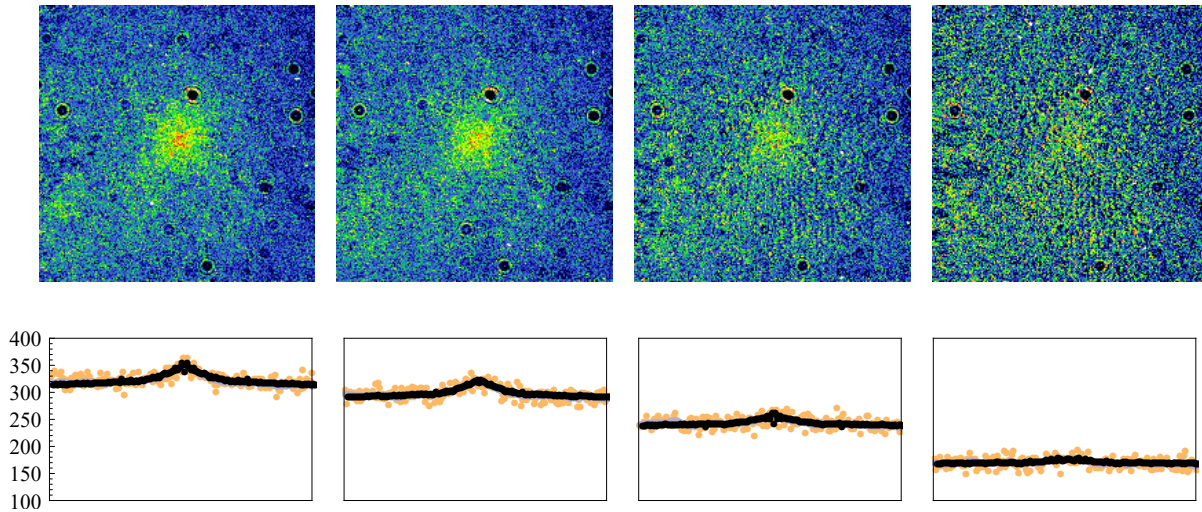


FIG. 76: Top: CCD images of horizontally polarized control field intensity dependence of L_{\parallel} channel with control detuning $\Delta_c = 0$ and probe Rabi frequency $\Omega_p = 0.18\Gamma_p$. Bottom: CBS profiles as a function of control field Rabi frequency. Corresponding control field intensity from left to right in terms of Rabi frequency: $\Omega_c = 0, 0.22\Gamma_p, 0.45\Gamma_p, 0.91\Gamma_p, 1.28\Gamma_p$.

The circularly polarized control beam has similar count levels to that of the vertically polarized beam, and shows similar trends to the aforementioned polarizations in CBS profile enhancement and widths, with enhancement being around 1.15 at its peak, and the width being within the 30 to 40 pixel range (1.6-2.1 mrad).

The control power dependence of the L_{\parallel} channel is shown in Fig. 76. From this, it is immediately evident that the quality of the CBS cone is diminished from that of the H_{\perp} channel. Further analysis of the L_{\parallel} channel is shown in Fig. 77.

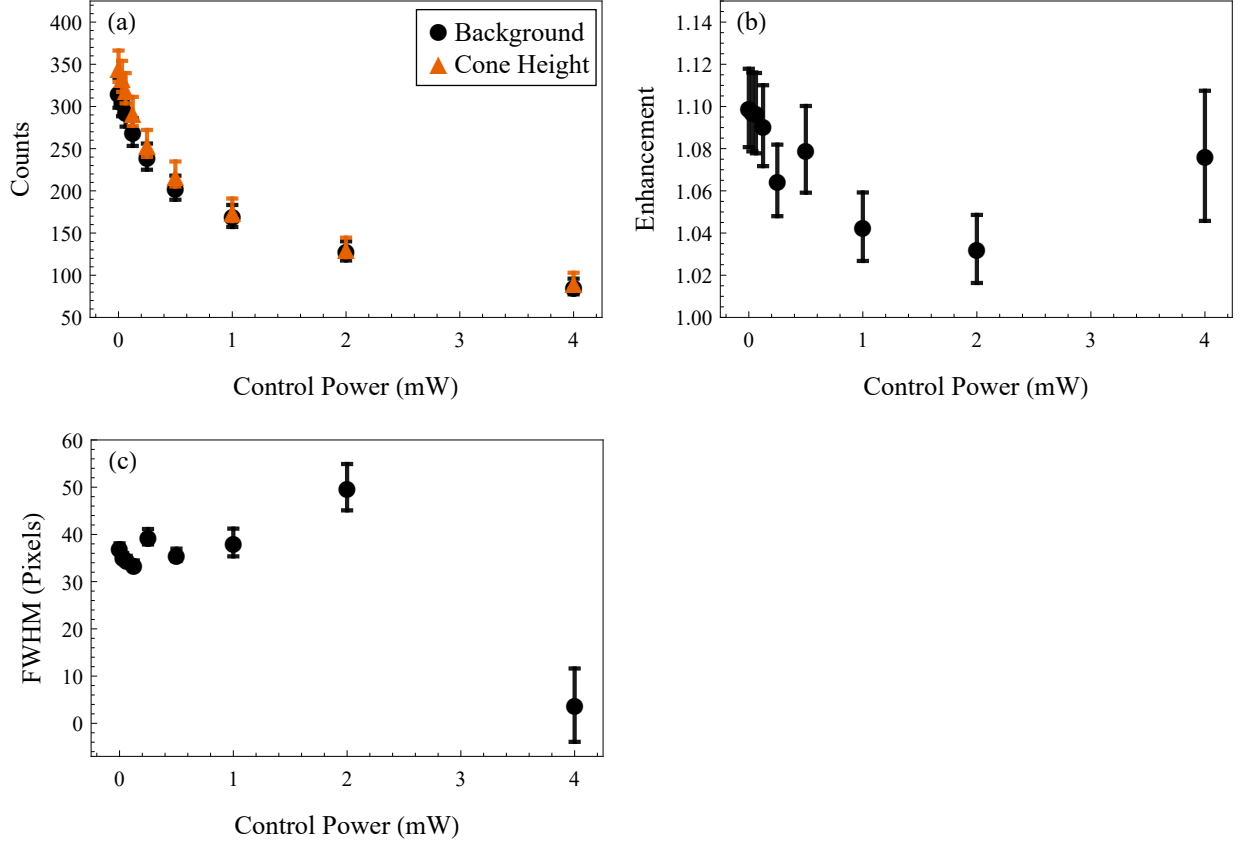


FIG. 77: Control power dependence of the L_{\parallel} channel with a horizontally polarized control field with control detuning $\Delta_c = 0$ and probe Rabi frequency $\Omega_p = 0.18\Gamma_p$. (a) CBS background level and cone height as a function of control field power. (b) CBS enhancement as a function of control field power. (c) CBS cone width as a function of control field power.

In Fig. 78, the control power dependence of CBS of the L_{\perp} channel is shown. Clearly, CBS in general is not strong enough in this channel to be studied much further from this. The total counts in the L_{\parallel} detection channel trend similarly to that of the H_{\perp} channel, but with significantly lower counts. However, the trend of the CBS profile enhancement is slightly less at all points, peaking around the 1.1 mark, with more irregularity as control power increases. The CBS profile width of the L_{\parallel} detection channel is within the 30-40 pixel range as the other channels are until the higher control power completely eliminates any remnant of coherent backscattering. From Fig. 76, it is easy to see that the CBS profile, or lack thereof, makes measurements at higher control power less suitable for in depth study with

the current apparatus.

The L_{\perp} channel shows minimal resemblance of a CBS cone, as shown in Fig. 78, with further detail given in Fig. 79. Control beam powers greater than 1 mW were omitted in this data collection channel due to lack of signal vs noise.

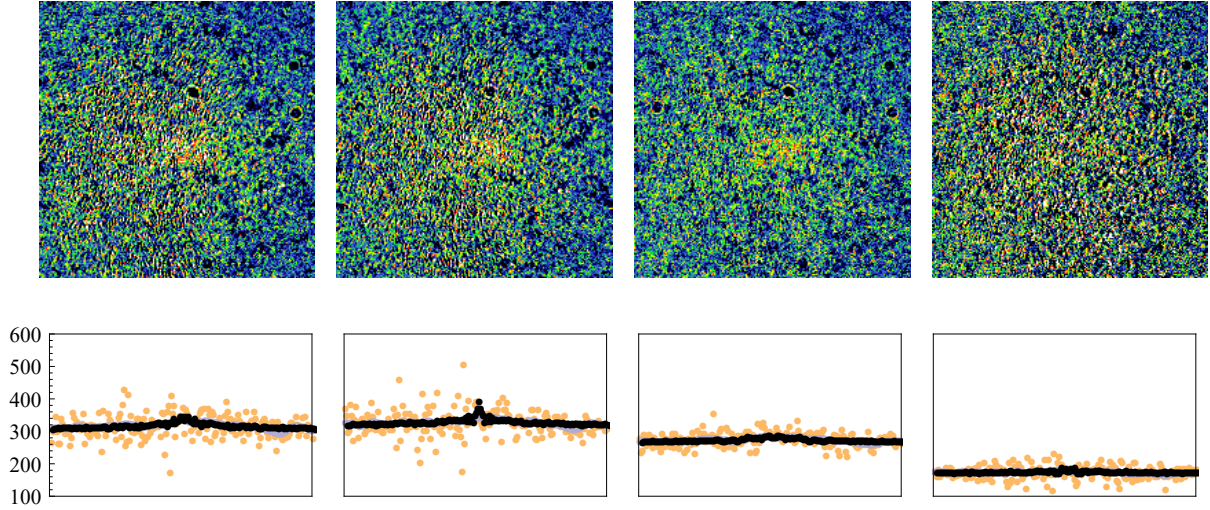


FIG. 78: Top: CCD images of horizontally polarized control field power dependence of L_{\perp} channel with control detuning $\Delta_c = 0$ and probe Rabi frequency $\Omega_p = 0.18\Gamma_p$. Bottom: CBS profiles as a function of control field Rabi frequency. Corresponding control field Rabi frequency from left to right: $\Omega_c = 0, 0.22\Gamma_p, 0.45\Gamma_p, 0.91\Gamma_p, 1.28\Gamma_p$.

Figure 79 shows the L_{\perp} channel counts, enhancement, and cone widths as a function of control power. It is interesting to note that the cone widths seem larger than previous measurements, but that is likely due to the poor fidelity of CBS cones that this channel allows for.

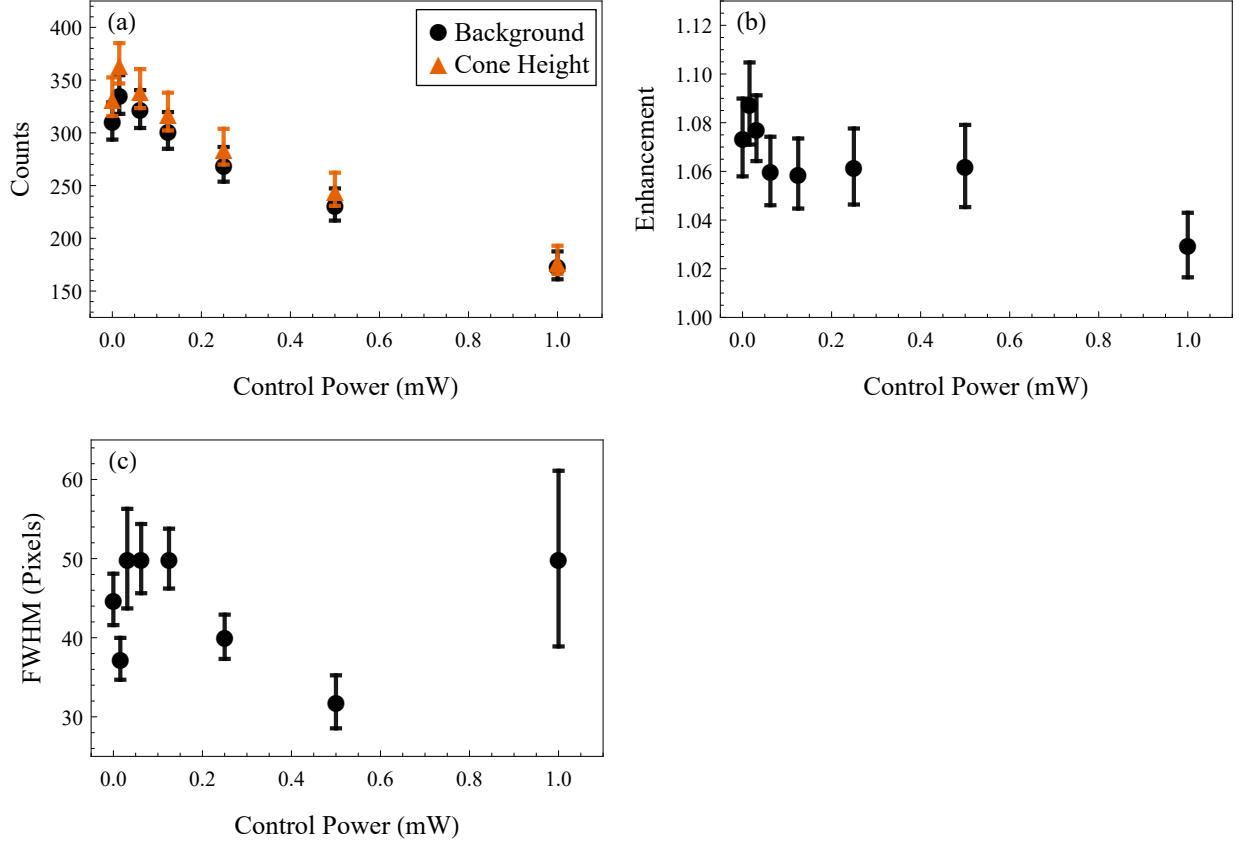


FIG. 79: Control power dependence of the L_{\perp} channel with a horizontally polarized control field with control detuning $\Delta_c = 0$ and probe Rabi frequency $\Omega_p = 0.18\Gamma_p$. (a) CBS background level and cone height as a function of control field power. (b) CBS enhancement as a function of control field power. (c) CBS cone width as a function of control field power.

As shown in Fig. 78 the CBS profile is poorly defined due to much lower signal to noise than the H_{\perp} and L_{\parallel} channels. Like the L_{\parallel} channel, the L_{\perp} is less suitable for in-depth study.

It is clear from the results in this subsection, that the intensity of the control directly affects the amount of coherent backscattering, with higher intensities corresponding to less total scattering and enhancement.

5.2.2 CBS WITH EIT PROBE DETUNING DEPENDENCE AT VARIOUS CONTROL INTENSITIES

Here we investigated coherent backscattering over a range of probe detuning at various control intensities. Here the data is presented as it was in the previous section, but now with horizontal polarization of the control beam. Each set of images and data will be presented in ascending control field intensity in terms of the Rabi frequency.

The first set of images in Fig. 80 corresponds to a control Rabi frequency of $\Omega_c = 0.64\Gamma_p$ (0.5 mW).

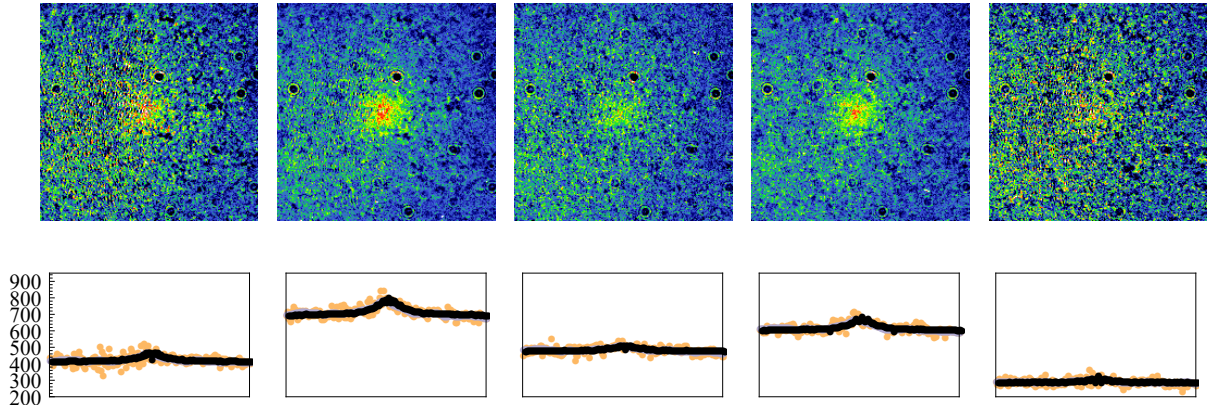


FIG. 80: Top: CCD images from the H_{\perp} channel probe detuning dependence with $\Omega_c = 0.64\Gamma_p$ (0.5 mW) control beam present with control detuning $\Delta_c = 0$ and probe Rabi frequency $\Omega_p = 0.18\Gamma_p$. Bottom: Detuning dependence of CBS profiles with angular integration overlaid. Detunings from left to right for top and bottom are: -6 MHz, -3 MHz, 0 MHz, 3 MHz, 6 MHz.

As with the previously displayed polarization data, there appears to be a decrease in CBS near resonance and further from resonance in both directions. Further analysis of the H_{\perp} channel at $\Omega_c = 0.64\Gamma_p$ is shown in Fig. 81.

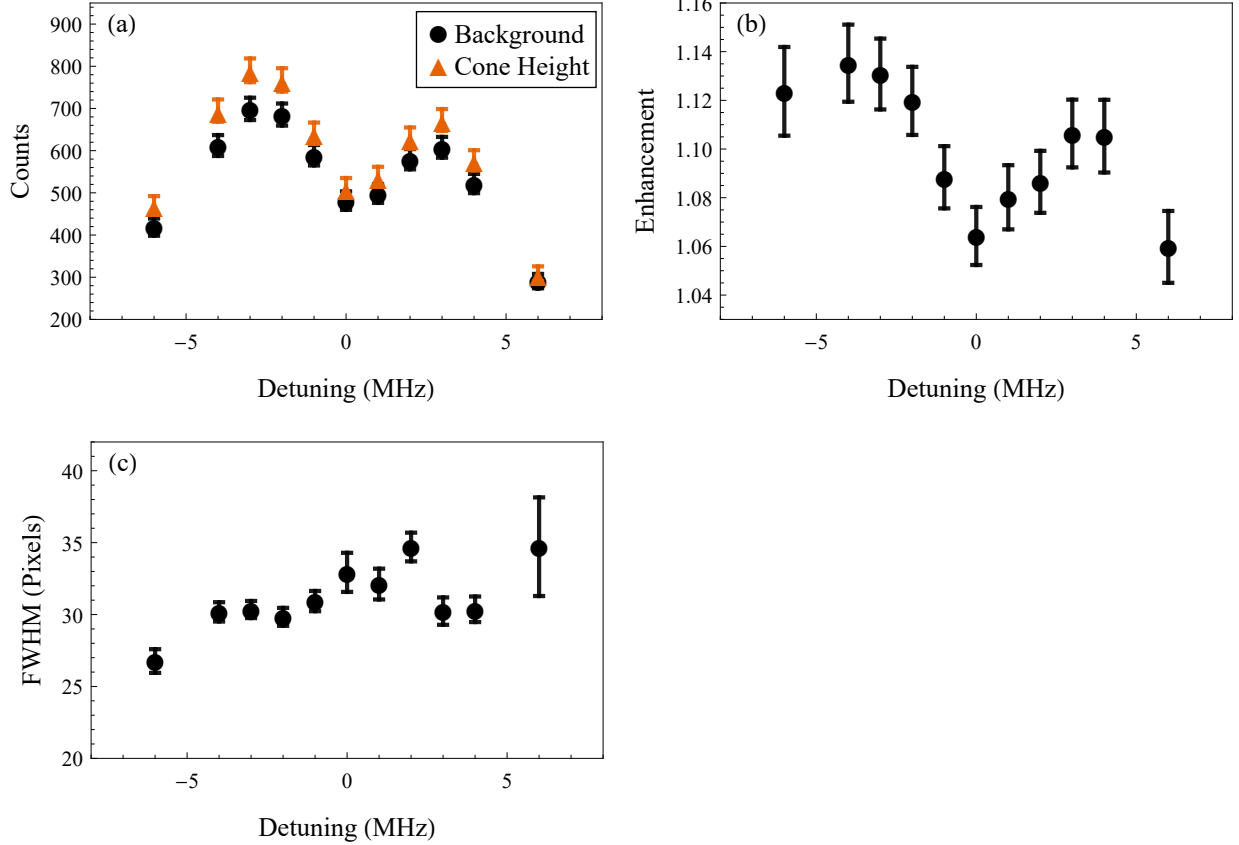


FIG. 81: H_{\perp} CBS channel with a $\Omega_c = 0.64\Gamma_p$ (0.5 mW) control beam with control detuning $\Delta_c = 0$ and probe Rabi frequency $\Omega_p = 0.18\Gamma_p$. (a) CBS background level and cone height as a function of detuning. (b) CBS enhancement as a function of detuning. (c) CBS cone width as a function of detuning.

From Fig. 81(a), there is a decrease in counts for the background and CBS cone near resonance. In (b), the enhancement is about 1.07 at resonance and shows asymmetry with detuning, but increases up to roughly 1.13 at -4 MHz. From (c), the cone width is roughly around 30 pixels, corresponding to 1.6 mrad, showing consistency with previously observed cone widths. On resonance, there is a reduction of about 7% in enhancement, eluding to a reduction in coherent scattering with the control beam present.

In Fig. 82, the results are shown for a control beam of Rabi frequency $\Omega_c = 0.91\Gamma_p$ (1 mW).

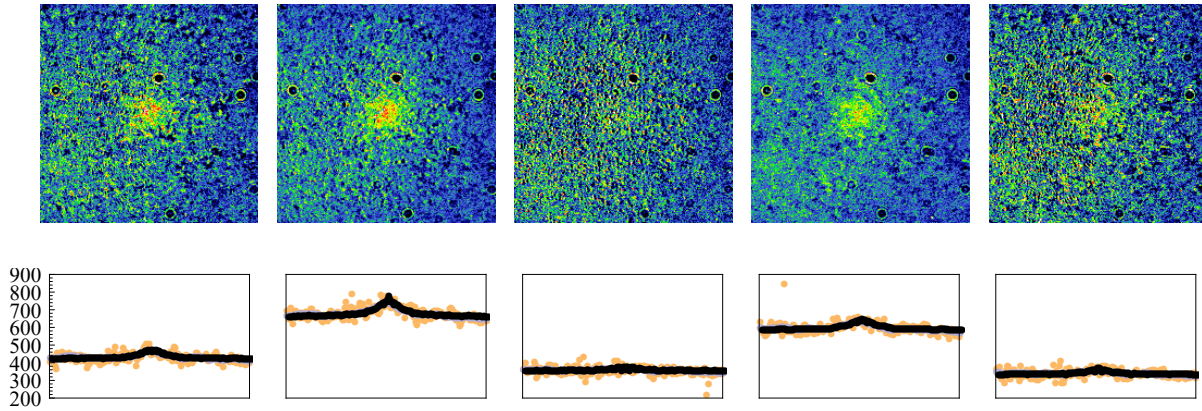


FIG. 82: Top: CCD images from the H_{\perp} CBS channel probe detuning dependence with $\Omega_c = 0.91\Gamma_p$ (1 mW) control beam with control detuning $\Delta_c = 0$ and probe Rabi frequency $\Omega_p = 0.18\Gamma_p$. Bottom: Detuning dependence of CBS profiles with angular integration overlaid. Detunings from left to right for top and bottom are: -6 MHz, -3 MHz, 0 MHz, 3 MHz, 6 MHz.

There is a decrease in the CBS effect near resonance. The effects of EIT on the H_{\perp} channel at $\Omega_c = 0.91\Gamma_p$ are more quantitatively displayed in Fig. 83.

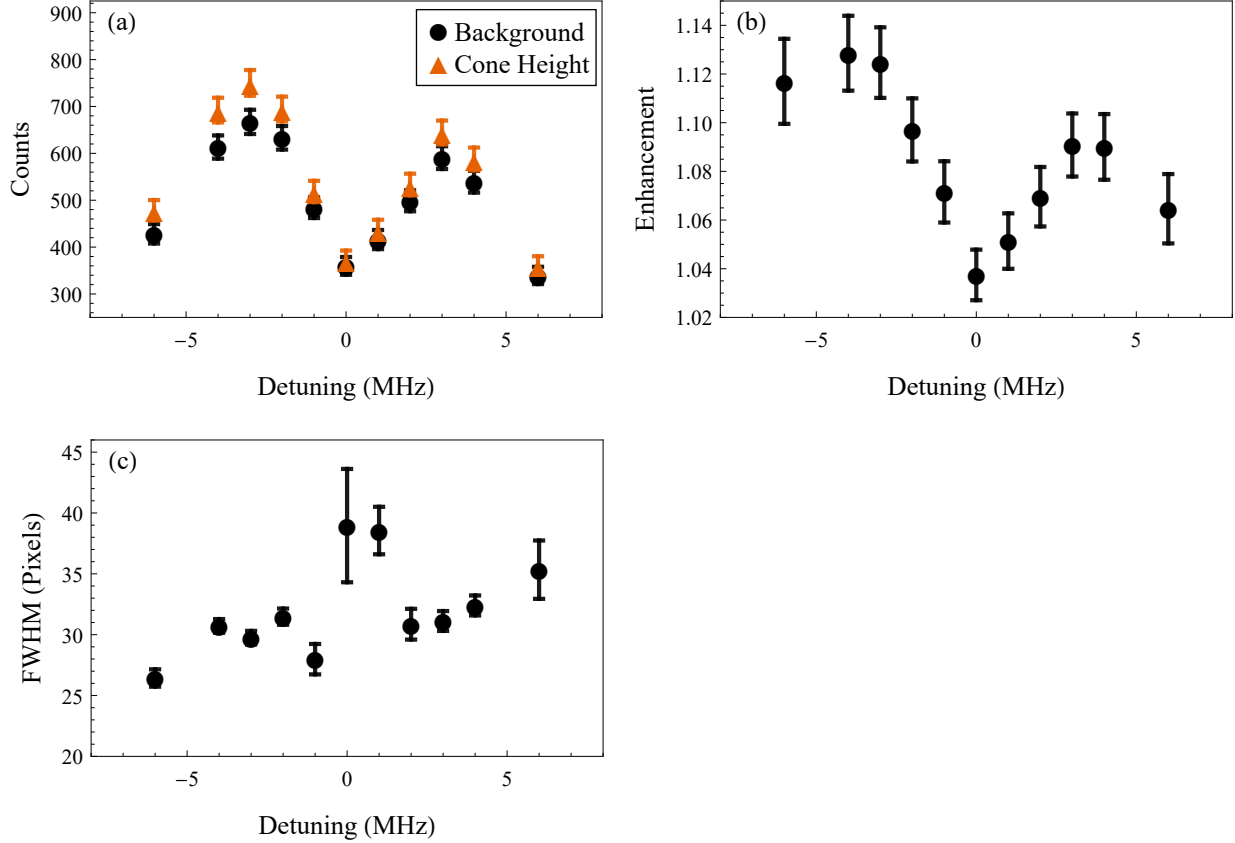


FIG. 83: H_{\perp} CBS channel with a $\Omega_c = 0.91\Gamma_p$ (1 mW) control beam with control detuning $\Delta_c = 0$ and probe Rabi frequency $\Omega_p = 0.18\Gamma_p$. (a) CBS background level and cone height as a function of detuning. (b) CBS enhancement as a function of detuning. (c) CBS cone width as a function of detuning.

From Fig. 83(a), there is a decrease in counts for the background and CBS cone near resonance. In (b), the enhancement is just under 1.04 at resonance and shows asymmetry with detuning, but increases up to roughly 1.13 at -4 MHz. From (c), the cone width is roughly around 30 pixels as before, corresponding to 1.6 mrad. Widths near resonance do not reflect the actual value due to low signal to noise and lack of a CBS cone. On resonance, there is a reduction of about 9.5% in enhancement, further giving rise to a reduction in coherent scattering with the control beam present.

In Fig. 84, images and CBS profiles are displayed for a control beam with Rabi frequency $\Omega_c = 1.28\Gamma_p$ (2 mW).

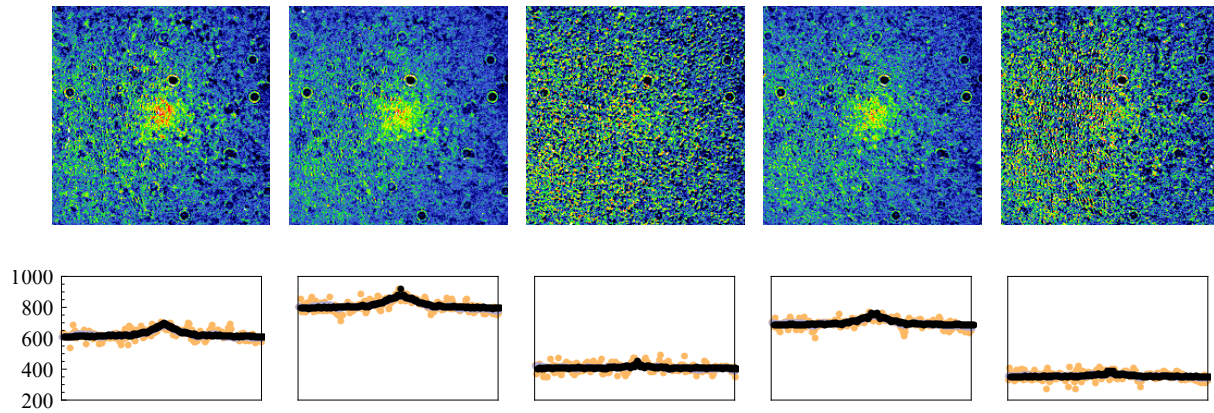


FIG. 84: Top: CCD images from the H_{\perp} channel probe detuning dependence with $\Omega_c = 1.28\Gamma_p$ (2 mW) control beam with control detuning $\Delta_c = 0$ and probe Rabi frequency $\Omega_p = 0.18\Gamma_p$. Bottom: Detuning dependence of CBS profiles with angular integration overlaid. Detunings from left to right for top and bottom are: -6 MHz, -3 MHz, 0 MHz, 3 MHz, 6 MHz.

At higher intensity, less signature of the CBS cone exists near resonance. Figure 85 displays further analysis of the H_{\perp} channel under the effect of a control beam of $\Omega_c = 1.28\Gamma_p$.

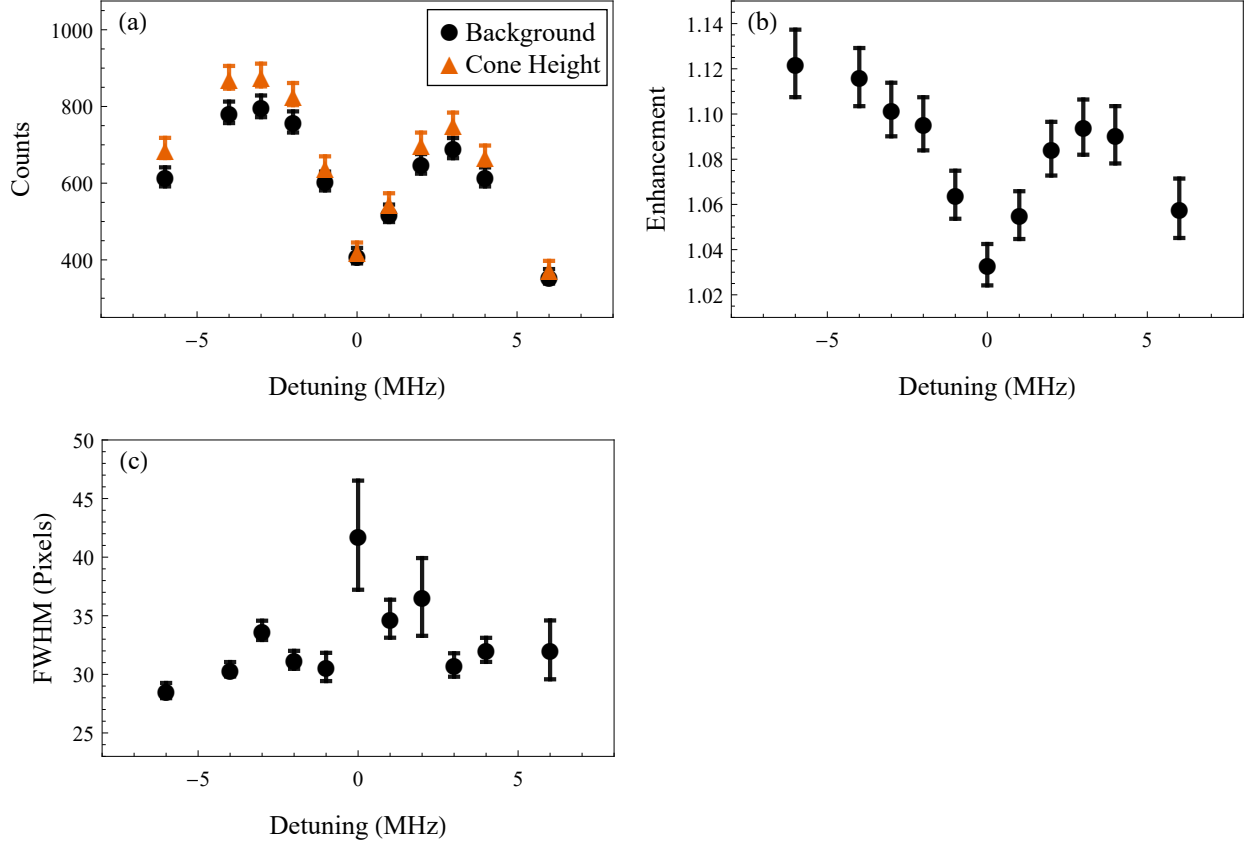


FIG. 85: H_{\perp} CBS channel with a $\Omega_c = 1.28\Gamma_p$ (2 mW) control beam with control detuning $\Delta_c = 0$ and probe Rabi frequency $\Omega_p = 0.18\Gamma_p$. (a) CBS background level and cone height as a function of detuning. (b) CBS enhancement as a function of detuning. (c) CBS cone width as a function of detuning.

As shown at lower intensities, Fig. 85(a) displays a significant decrease in background and cone height counts. In (b), the enhancement on resonance is just under 1.04, with the enhancement rising to 1.12 on the negative detuning side. The cone width FWHM in (c) is around 30 pixels (1.6 mrad). On resonance, there is a reduction of about 10% in enhancement with an on resonance enhancement factor of 1.035 at $\Omega_c = 1.28\Gamma_p$, displaying reduction in coherent scattering with EIT occurring.

The CBS signals with the largest control Rabi frequency of $\Omega_c = 1.82\Gamma_p$ (4 mW) is shown in Fig. 86, showing a significant decrease in collected light on resonance. Further analysis of the H_{\perp} channel under the effect of a $\Omega_c = 1.82\Gamma_p$ control beam is shown in Fig. 87.

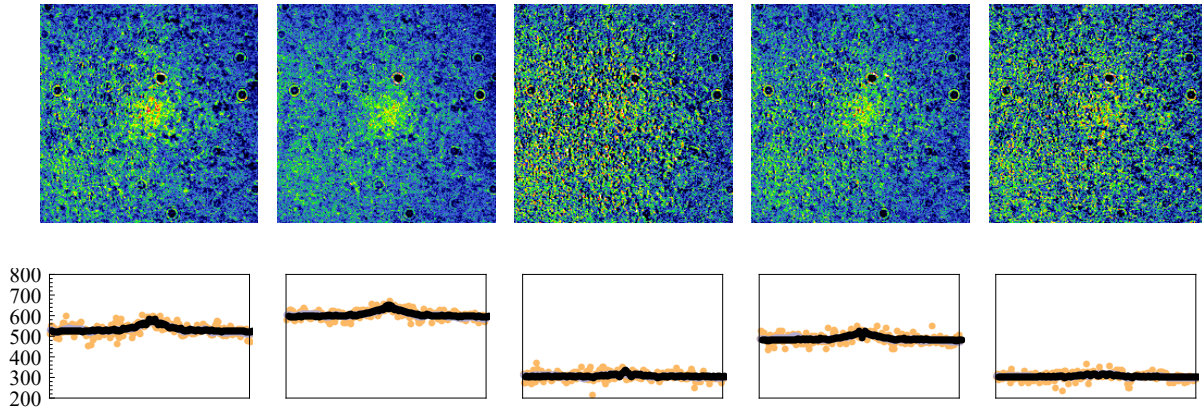


FIG. 86: Top: CCD images from the H_{\perp} channel probe detuning dependence with $\Omega_c = 1.82\Gamma_p$ (4 mW) control beam with control detuning $\Delta_c = 0$ and probe Rabi frequency $\Omega_p = 0.18\Gamma_p$. Bottom: Detuning dependence of CBS profiles with angular integration overlaid. Detunings from left to right for top and bottom are: -6 MHz, -3 MHz, 0 MHz, 3 MHz, 6 MHz.

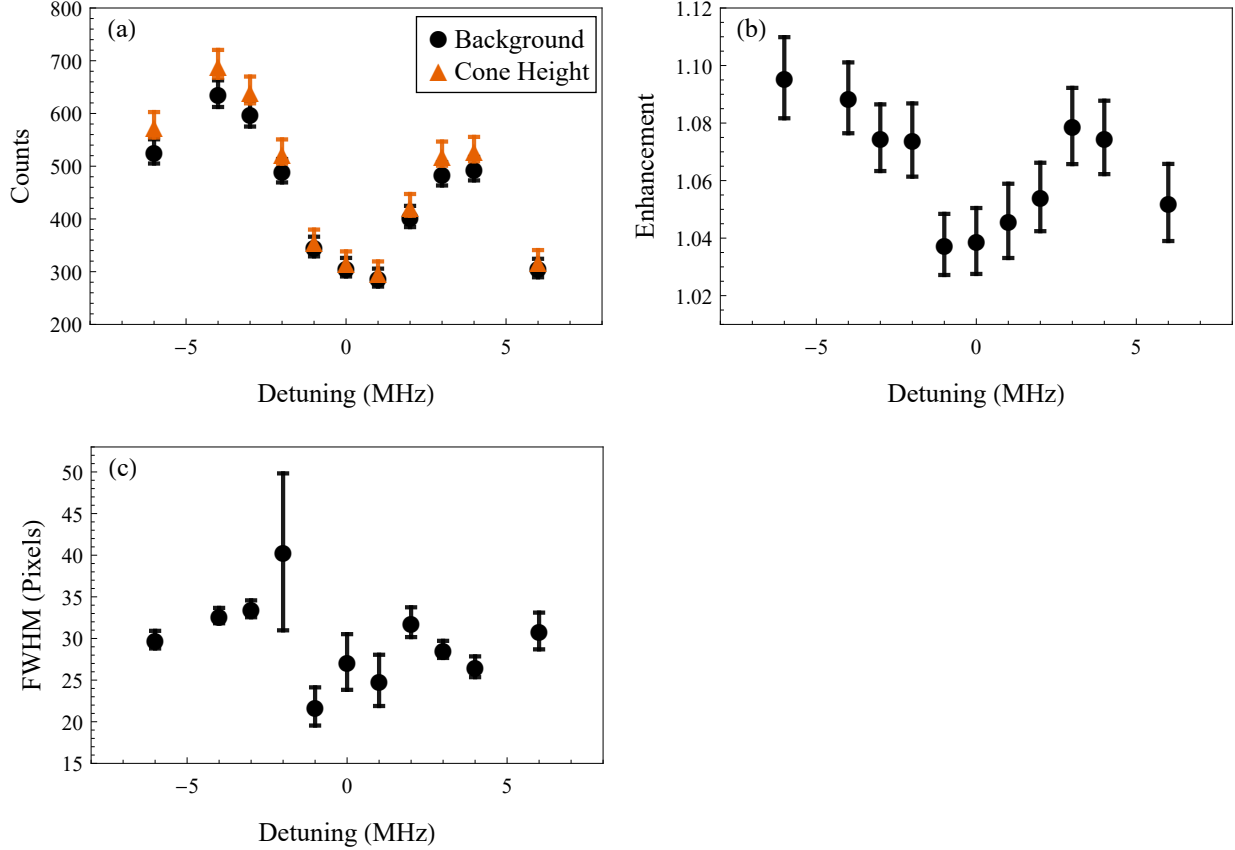


FIG. 87: H_{\perp} CBS channel with a $\Omega_c = 1.82\Gamma_p$ (4 mW) control beam with control detuning $\Delta_c = 0$ and probe Rabi frequency $\Omega_p = 0.18\Gamma_p$. (a) CBS background level and cone height as a function of detuning. (b) CBS enhancement as a function of detuning. (c) CBS cone width as a function of detuning.

Figure 87(a) shows similar behavior to the previous measurements at lower Rabi frequencies (Figs. 85, 83, and 81), but seems to show a more broadened window in frequency, which could be expected due to the effects of EIT at higher control intensities. In (b), the enhancement is around 1.04 at resonance and increases up to 1.09 as detuned negatively from resonance. From (c), the FWHM of the CBS cone is roughly 30 pixels, or 1.6 mrad, as previously observed at lower control intensities. Again, the change in enhancement is 9.5% due to the effect of the control field, suggesting EIT reduces coherent scattering.

As control intensity increased, there seemed to be a signature of less enhancement for the entire frequency range measured. The changes in counts and enhancement were subtle, until

the highest intensity, where a more noticeable change occurred, especially in terms of the EIT window width. The FWHM of the CBS cone remained consistently around 30 pixels, or 1.6 mrad, at all control intensities. Furthermore, at all control intensities, the presence of a control field seemed to reduce the coherent scattering processes more than that of the classical diffusive scattering, as shown by the reduction in enhancement near resonance.

5.2.3 CBS WITH EIT PROBE DETUNING DEPENDENCE AT VARIOUS POLARIZATIONS

Here the experimental results of the detuning dependence of CBS under the effect of EIT are shown for a control with vertical and circular polarization with a Rabi frequency of $\Omega_c = 0.91\Gamma_p$. For the images and CBS profiles, detunings of -6 MHz, -3 MHz, 0 MHz, 3 MHz, and 6 MHz will be shown as before.

Figure 88 shows CCD images of CBS with EIT due to a vertically polarized control beam. The counts of the background and CBS cone height are shown as a function of detuning in Fig. 89(a).

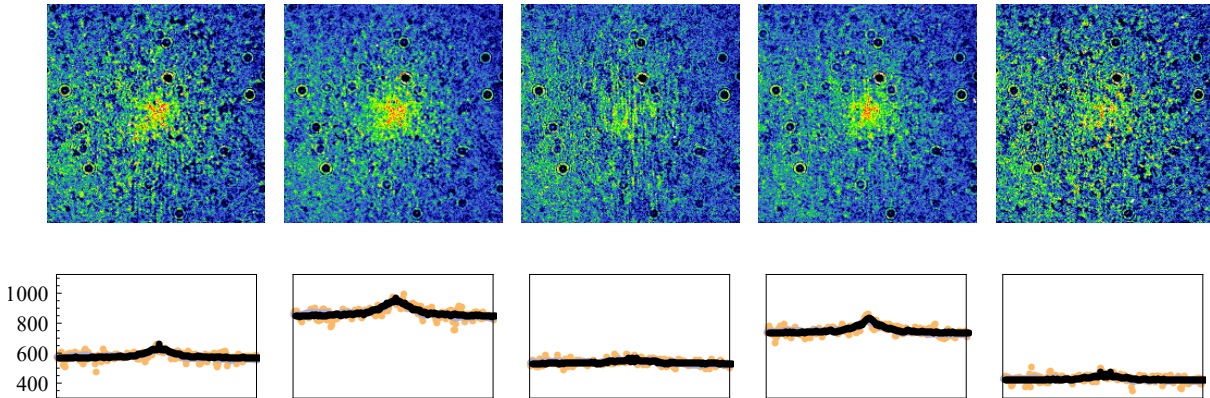


FIG. 88: Top: CCD images from the H_{\perp} channel probe detuning dependence with $\Omega_c = 0.91\Gamma_p$ vertically polarized control beam with control detuning $\Delta_c = 0$ and probe Rabi frequency $\Omega_p = 0.18\Gamma_p$. Bottom: Detuning dependence of CBS profiles with angular integration overlaid. Detunings from left to right for top and bottom are: -6 MHz, -3 MHz, 0 MHz, 3 MHz, 6 MHz.

There is a clear reduction in coherent scattering near resonance for the vertically polarized control beam of $\Omega_c = 0.91\Gamma_p$, as observed with horizontal polarization.

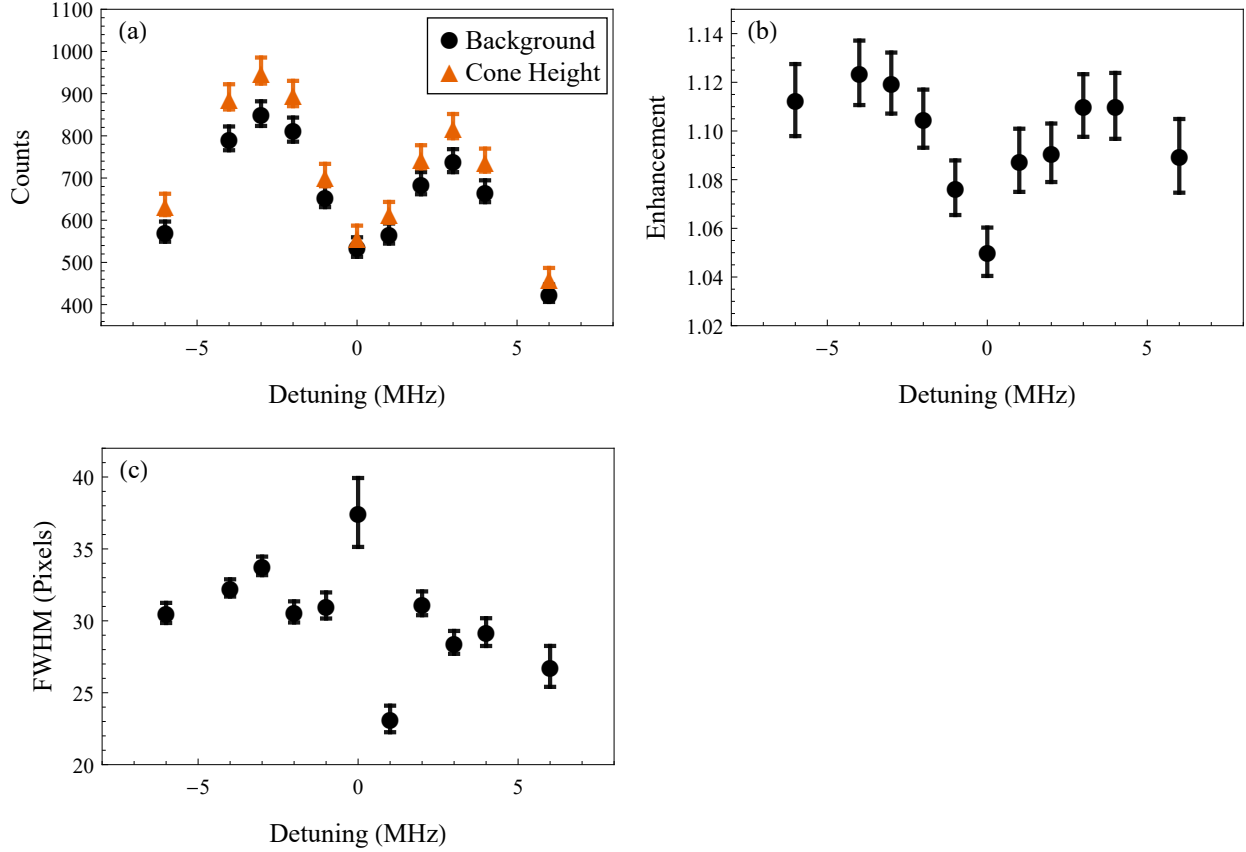


FIG. 89: H_{\perp} CBS channel with a $\Omega_c = 0.91\Gamma_p$ vertically polarized beam present with control detuning $\Delta_c = 0$ and probe Rabi frequency $\Omega_p = 0.18\Gamma_p$. (a) CBS background level and cone height as a function of detuning. (b) CBS enhancement as a function of detuning. (c) CBS cone width as a function of detuning.

From the results in Fig. 89(a), there is a decrease in CCD counts near resonance for both the CBS cone and background signals. In (b), the total enhancement is shown. A non obvious result is that there is less enhancement near resonance where the EIT condition occurs. Less enhancement suggests that the height of the cone is reduced more than the the background is reduced. On resonance, the enhancement is roughly 1.05, while the enhance

reaches around 1.12 off resonance. The FWHM of the cone in (c) appears to roughly be 30 pixels, corresponding to 1.6 mrad.

Images with the associated CBS profiles are shown of the detuning dependence results for the H_{\perp} with a circularly polarized control beam Rabi frequency of $\Omega_c = 0.91\Gamma_p$ in Fig. 90.

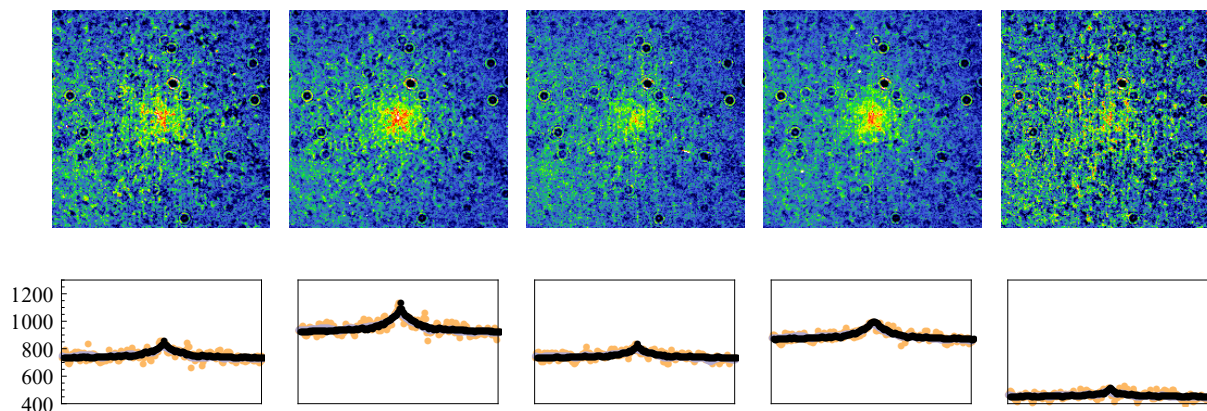


FIG. 90: Top: CCD images from the H_{\perp} channel probe detuning dependence with $\Omega_c = 0.91\Gamma_p$ circularly polarized control beam with control detuning $\Delta_c = 0$ and probe Rabi frequency $\Omega_p = 0.18\Gamma_p$. Bottom: Detuning dependence of CBS profiles with angular integration overlaid. Detunings from left to right for top and bottom are: -6 MHz, -3 MHz, 0 MHz, 3 MHz, 6 MHz.

As with the vertically polarized light, it is evident from Fig. 90 that CBS is decreased on resonance due to EIT with circularly polarized light as well. Further quantitative analysis of CBS under the effect of a $\Omega_c = 0.91\Gamma_p$ circularly polarized control is displayed in Fig. 91.

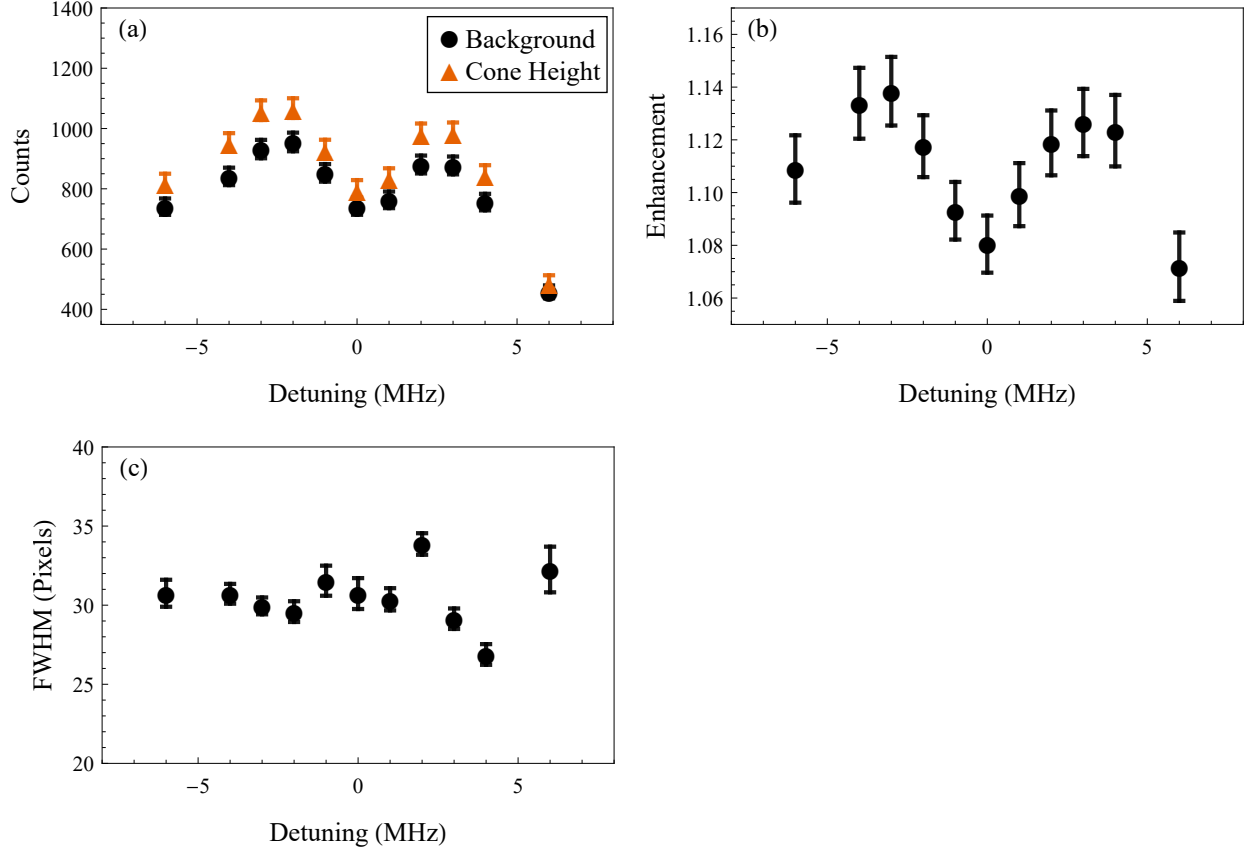


FIG. 91: H_{\perp} CBS channel with a $\Omega_c = 0.91\Gamma_p$ circularly polarized beam present with control detuning $\Delta_c = 0$ and probe Rabi frequency $\Omega_p = 0.18\Gamma_p$. (a) CBS background level and cone height as a function of detuning. (b) CBS enhancement as a function of detuning. (c) CBS cone width as a function of detuning.

In Fig. 91(a), there is a decrease in CCD counts near resonance for both the CBS cone and background signals. Qualitatively, it shows similar behavior to a linearly polarized control beam, whether vertical or horizontally polarized. In 91(b), the total enhancement is shown. As with the vertically polarized control beam, there is less enhancement near resonance where the EIT condition occurs. Near resonance the enhancement is about 1.08 and up to roughly 1.14 further from resonance which shows more enhancement than that of the horizontal and vertical polarizations at $\Omega_c = 0.91\Gamma_p$. Table 4 shows each enhancement at measured control polarizations with Rabi frequencies of $\Omega_c = 0.91\Gamma_p$.

TABLE 4: Enhancement and CBS cone FWHM for the three measured control polarizations at $\Omega_c = 0.91\Gamma_p$.

Control Polarization	Enhancement	CBS cone FWHM (mrad)
\rightarrow	1.04	1.6
σ_+	1.09	1.6
\uparrow	1.05	1.6

The width of the cone is consistent here with that of the circularly polarized beam at roughly 30 pixels (1.6 mrad). Measurements with a vertically polarized beam and circularly polarized beam were consistent with the measurements with a horizontally polarized control, showing a consistent dip in coherent enhancement around resonance.

5.2.4 CBS WITH EIT CONTROL DETUNING DEPENDENCE

Here we present the absorption as a function of control detuning, as opposed to the previous measurements with probe detuning at a control Rabi frequency of $\Omega_c = 1.82\Gamma_p$ (4 mW). Generally probe detuning is used for measuring the effects of EIT, but we present preliminary data on CBS under the effect of EIT as a function of control detuning in Fig. 92.

Figure 92(a) displays probe absorption as a function of control detuning. There is a significant drop in counts where EIT normally occurs on resonance, corresponding to the $5D_{5/2}F'' = 5$, another at 9.5 MHz, consisting of where the $5D_{5/2}F'' = 4$ hyperfine level is, and then a very slight signature of a dip around 18 MHz, likely corresponding to the $5D_{5/2}F'' = 3$ hyperfine level. Reduction of the effect at those values is likely due to the line strength factors, as mentioned in Eq. (120). Figure 92(b) corresponds to the enhancement as a function of control detuning. There appears to be a reduction in enhancement near resonance and around 9 MHz, and a slight indication of an alteration of enhancement around 18 MHz, corresponding with the observed effect in (a). Lastly, (c) shows the FWHM of the CBS cone as a function of control detuning. While previous measurements of probe detuning displayed a FWHM of 30 pixels, here only near resonance was around 30 pixels, while the remainder of data points had a width of roughly 50 pixels according to the fits of the CBS cones. With signals of CBS decreasing significantly at detunings further from resonance, the

fitting error of the weak CBS cones could have played a role in these large values.

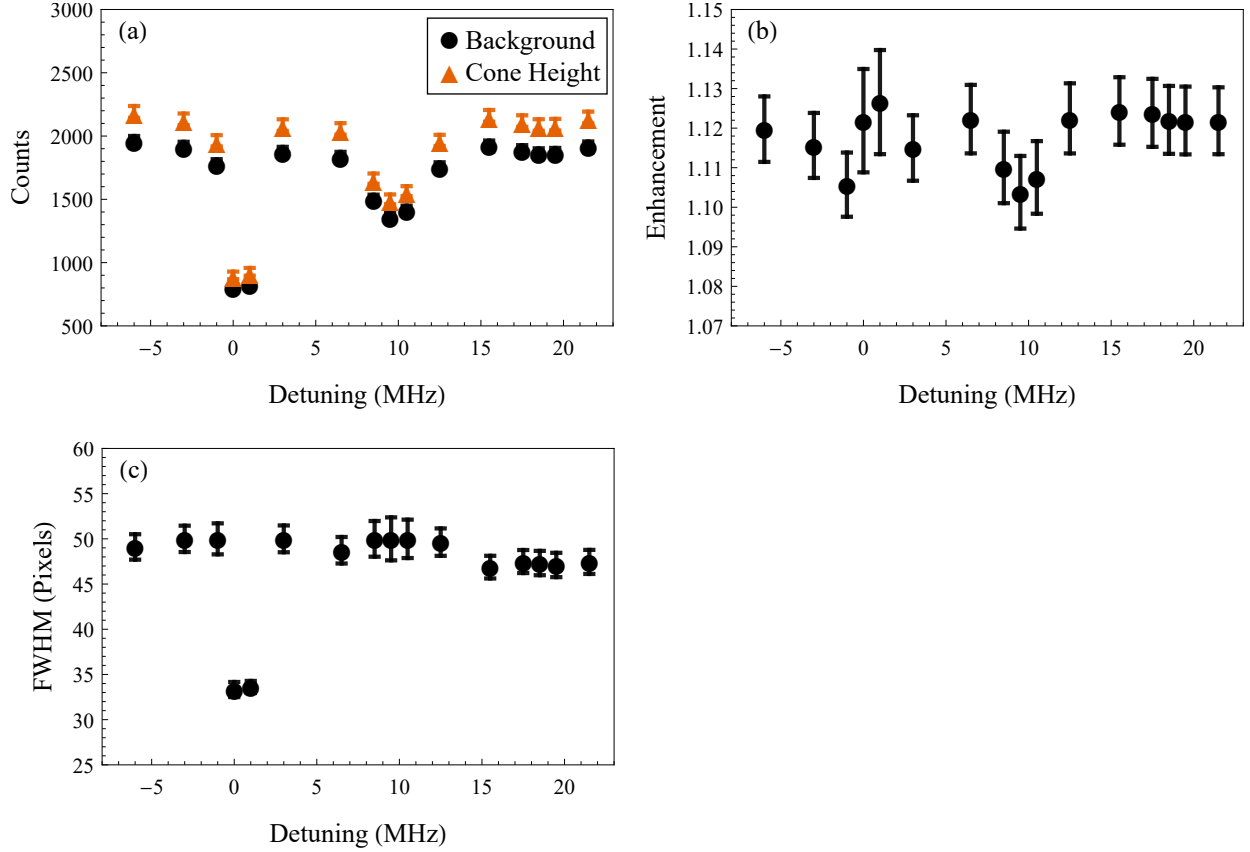


FIG. 92: Control beam detuning dependence of the H_{\perp} channel with a $\Omega_c = 1.82\Gamma_p$ (4 mW) horizontally polarized control beam with probe Rabi frequency $\Omega_p = 0.18\Gamma_p$. (a) CBS background level and cone height as a function of control detuning. (b) CBS enhancement as a function of control detuning. (c) CBS cone width as a function of control detuning.

5.2.5 SUMMARY OF RESULTS

First, we presented results of CBS without a control beam present to establish baseline measurements. Here we reported enhancement of 1.15 with cone widths of 1.6 mrad for the H_{\perp} channel. The L_{\parallel} channel had an enhancement of 1.11 and a cone width in the range

of 1.6-2.1 mrad. The channels of L_{\perp} and H_{\parallel} were not studied here due to poor fidelity of signals.

We then moved to data with a control beam introduced, starting with the dependence of control intensity, and the effect of the control beam on CBS signals observed. The effect of control intensity with a vertical and circularly polarized beam aligned with the results of a horizontally polarized control. Here we saw the enhancement decrease as control power increased for each parameter explored. The results in the L_{\perp} channel seemed to decrease in a similar way as control beam power increased, but with less signal to noise, more data and experimental work could be necessary.

Then we reported the probe detuning dependence of CBS with EIT at various control intensities in terms of the control Rabi frequency. Here we displayed the enhancement being decreased near resonance due to the presence of the control beam, which is consistent with the effects of EIT. Interestingly though, the amount of coherent scattering seemed to be reduced more than that of incoherent background scattering, based on the dip in enhancement approaching one, near resonance. At the lowest control intensity, corresponding to a Rabi frequency of $\Omega_c = 0.64\Gamma_p$, we observed an enhancement of about 1.07, equivalent a difference of about 7% from enhancement without EIT. At the highest intensity, corresponding to $\Omega_c = 1.82\Gamma_p$, the enhancement was around 1.04, which is about a 9.5% decrease from the results without EIT.

We measured the probe detuning of CBS under the effect of EIT with circular and vertically polarized control beams, which did not show any significant difference from a horizontally polarized beam in overall behavior, but the circularly polarized beam appeared to show more enhancement on resonance than that of the other control polarizations as shown in Table 4.

Lastly, we presented preliminary data for probe absorption as a function of control detuning, over a larger range of detuning to observe effects over multiple hyperfine levels. There appeared to be a decrease in light scattering near hyperfine resonances. The enhancement showed a slight decrease near resonances, but more data is needed for further analysis.

CHAPTER 6

CONCLUSIONS

Measurements of coherent backscattering under the conditions of electromagnetically induced transparency in a ladder configuration were presented in this dissertation. Coherent backscattering, probe absorption, and fluorescence at 420 nm were measured with respect to detuning, intensity, and polarization of both probe and control, to determine the overarching effect. This allowed for exploration of a nearly boundless parameter space, so here we concentrated on fundamental measurements typically involving detuning the probe, while looking at various other parameters. To obtain understanding of the physical processes, we measured EIT in a ^{85}Rb MOT, in a counterpropagating beam geometry of probe and control, and then in an orthogonal geometry as was the setup when simultaneously observing CBS. The counterpropagating EIT measurements were used to provide a check of consistency and to determine if there was any geometrical dependence of probe and control in cold rubidium. From our measurements, the geometry did not show a significant difference. In these measurements, there was not a significant effect on EIT due to the various combinations of polarization of both probe and control fields for either geometry. Probe detuning measurements of EIT were taken at set control detunings, corresponding to the hyperfine splittings of the $5D_{5/2}$ state, which displayed relatively consistent EIT windows and fluorescence of the $6P_{3/2}$ state for both counterpropagating and orthogonal beam geometries. The dependence on probe intensity was also observed, which behaved consistently in both geometries, showing a larger EIT effect at higher probe intensities and more fluorescence from the $6P_{3/2}$ state. We compared a theoretical model of a 9 level simulated system with that of the EIT process in the experiment and it agreed qualitatively with experimental results. With consistent experimental and theoretical results in EIT, we then presented measurements of CBS without a control beam present as a baseline for comparison. The results from CBS under the effect of EIT showed consistent results with the reduction of light scattering processes near resonances where EIT occurs. This effect reduced the total amount of scattering in both the incoherent and coherent contributions to the backscattered signals, which was directly measured. The values of the enhancement decreasing near resonance also suggests that the effect of EIT influences the coherent contribution more than the incoherent contribution to the measured albedo. The decrease of coherent scattering processes on resonance was in

the range of 7-10%. This is an important result in agreement with early theoretical work that our group was previously involved with [83], which predicted the dip in enhancement as shown in Chapter 5.

There were a number of experimental hurdles involved in bringing this research together. The apparatus was developed completely from the ground up. Significant effort was required pertaining to optical, electrical, and mechanical systems in order to design and construct the laser configuration and data collection processes used in this experiment. Several lasers at different wavelengths had to work harmoniously to facilitate such an experiment, within very specific timing windows, all while maintaining a consistent atomic sample.

Future prospects continuing upon this work could consist of exploring the parameter space further, especially with measurements in the control detuning domain. A cascade-type EIT system could also be implemented with a strong field on the lower transition instead, to investigate differences in systems that are EIT dominant versus ATS dominant [48]. Another possibility would be to alter the current pulse dynamics in such a way as to study CBS under the effects of slowed and stopped light. Theoretical work could be done to include polarization effects in the optical Bloch equations and developing a simulation of the coherent backscattering process with polarization effects included. Further experimental work could be continued, using the method of a strong magnetic field as in [75] to increase the coherent backscattering signals in order to study all polarization channels equally. Also, a full theoretical treatment from theory colleagues or a theoretical dissertation could explore the effects of EIT under conditions of CBS further, under the specific case that was studied here.

BIBLIOGRAPHY

- [1] A. Shaheen and M. S. Anwar, Electromagnetically induced transparency in rubidium a theoretical overview, 2011, (unpublished).
- [2] S. E. Harris, J. E. Field, and A. Kasapi, *Phys. Rev. A* **46**, R29 (1992).
- [3] S. E. Harris, *Phys. Rev. Lett.* **70**, 552 (1993).
- [4] R. R. Moseley, S. Shepherd, D. J. Fulton, B. D. Sinclair, and M. H. Dunn, *Opt. Commun.* **119**, 61 (1995).
- [5] S. E. Harris, *Opt. Lett.* **19**, 2018 (1994).
- [6] G. Vemuri and K. Vasavada, *Opt. Commun.* **129**, 379 (1996).
- [7] S. Hopkins, E. Usadi, H. Chen, and A. Durrant, *Opt. Commun.* **138**, 185 (1997).
- [8] H. S. Moon, L. Lee, and J. B. Kim, *J. Opt. Soc. Am. B* **22**, 2529 (2005).
- [9] D. McGloin, M. H. Dunn, and D. J. Fulton, *Phys. Rev. A* **62**, 053802 (2000).
- [10] J. Gea-Banacloche, Y. qing Li, S. zheng Jin, and M. Xiao, *Phys. Rev. A* **51**, 576 (1995).
- [11] J.-Y. Gao, S.-H. Yang, D. Wang, X.-Z. Guo, K.-X. Chen, Y. Jiang, and B. Zhao, *Phys. Rev. A* **61**, 023401 (2000).
- [12] F. Cataliotti, C. Fort, T. Hänsch, M. Inguscio, and M. Prevedelli, *Phys. Rev. A* **56**, 2221 (1997).
- [13] G. Bian, B. Shan, L. Huang, and J. Zhang, *Chinese Optics Letters* **21**, 100201 (2023).
- [14] K. Kowalski, K. Vaseva, S. Gateva, M. Glódz, L. Petrov, and J. Szonert (SPIE, 2007) pp. 66040K–66040K–5.
- [15] G. S. Agarwal and W. Harshawardhan, *Phys. Rev. Lett.* **77**, 1039 (1996).
- [16] D. Wang, J. Y. Gao, J. H. Xu, G. C. L. Rocca, and F. Bassani, *EPL* **54**, 456 (2001).
- [17] A. M. Akulshin, S. Barreiro, and A. Lezama, *Phys. Rev. A* **57**, 2996 (1998).

- [18] D. V. Brazhnikov, A. M. Tumaikin, V. I. Yudin, and A. V. Taichenachev, *J. Opt. Soc. Am. B* **22**, 57 (2005).
- [19] S. Vdović, T. Ban, D. Aumiler, and G. Pichler, *Opt. Commun.* **272**, 407 (2007).
- [20] P. S. Light, F. Benabid, G. J. Pearce, F. Couny, and D. M. Bird, *Appl. Phys. Lett.* **94**, 10.1063/1.3115143 (2009).
- [21] J. Zhao, L. Wang, L. Xiao, Y. Zhao, W. Yin, and S. Jia, *Opt. Commun.* **206**, 341 (2002).
- [22] D. J. Fulton, S. Shepherd, R. R. Moseley, B. D. Sinclair, and M. H. Dunn, *Phys. Rev. A* **52**, 2302 (1995).
- [23] J. R. Boon, E. Zekou, D. J. Fulton, and M. H. Dunn, *Phys. Rev. A* **57**, 1323 (1998).
- [24] H. H. Jen, B. Xiong, I. A. Yu, and D.-W. Wang, *J. Opt. Soc. Am. B* **30**, 2855 (2013).
- [25] M. N. Winchester, M. A. Norcia, J. R. Cline, and J. K. Thompson, *Phys. Rev. Lett.* **118**, 263601 (2017).
- [26] M. Fleischhauer, A. Imamoglu, and J. P. Marangos, *Rev. Mod. Phys.* **77**, 633 (2005).
- [27] A. H. Safavi-Naeini, T. P. Alegre, J. Chan, M. Eichenfield, M. Winger, Q. Lin, J. T. Hill, D. E. Chang, and O. Painter, *Nature* **472**, 69 (2011).
- [28] J. Mompert and R. Corbalan, *J. Opt. B* **2**, R7 (2000).
- [29] Y. V. Radeonychev, M. A. Erukhimova, O. A. Kocharovskaya, and R. Vilaseca, *Radio-physics and Quantum Electronics* **47**, 795 (2004).
- [30] H. Wu, M. Xiao, and J. Gea-Banacloche, *Phys. Rev. A* **78**, 041802 (2008).
- [31] L. Ma, O. Slattery, and X. Tang, *J. Opt.* **19**, 043001 (2017).
- [32] L. Karpa and M. Weitz, *Nature Physics* **2**, 332 (2006).
- [33] Y. qing Li and M. Xiao, *Opt. Lett.* **21**, 1064 (1996).
- [34] J. Clarke, H. Chen, and W. A. van Wijngaarden, *Appl. Opt.* **40**, 2047 (2001).
- [35] N. H. Bang, D. X. Khoa, D. H. Son, and L. V. Doai, *J. Opt. Soc. Am. B* **36**, 3151 (2019).

- [36] R. Coussement, M. V. D. Bergh, G. S'heeren, G. Neyens, R. Nouwen, and P. Boolchand, *Hyperfine Interactions* **80**, 1307 (1993).
- [37] K.-J. Boller, A. Imamoglu, and S. E. Harris, *Phys. Rev. Lett.* **66**, 2593 (1991).
- [38] A. J. Olson and S. K. Mayer, *Am. J. of Phys.* **77**, 116 (2009).
- [39] N. Thaicharoen, K. R. Moore, D. A. Anderson, R. C. Powel, E. Peterson, and G. Raithel, *Phys. Rev. A* **100**, 063427 (2019).
- [40] Y. qing Li and M. Xiao, *Phys. Rev. A* **51**, R2703 (1995).
- [41] S. K. Nath, V. Naik, A. Chakrabarti, and A. Ray, *J. Opt. Soc. Am. B* **36**, 2610 (2019).
- [42] M. Yan, E. G. Rickey, and Y. Zhu, *J. Opt. Soc. Am. B* **18**, 1057 (2001).
- [43] J. Wang, L. B. Kong, X. H. Tu, K. J. Jiang, K. Li, H. W. Xiong, Y. Zhu, and M. S. Zhan, *Phys. Lett.* **328**, 437 (2004).
- [44] B. C. Sanders, *AVS Quantum Science* **5**, 10.1116/5.0149908 (2023).
- [45] P. M. Anisimov, J. P. Dowling, and B. C. Sanders, *Phys. Rev. Lett.* **107**, 163604 (2011).
- [46] P. Anisimov and O. Kocharovskaya, *Journal of Modern Optics* **55**, 3159 (2008).
- [47] R. Finkelstein, S. Bali, O. Firstenberg, and I. Novikova, *New Journal of Physics* **25**, 035001 (2023).
- [48] T. Y. Abi-Salloum, *Phys. Rev. A* **81**, 053836 (2010).
- [49] T. Abi-salloum, J. P. Davis, C. Lehman, E. Elliott, and F. A. Narducci, *Journal of Modern Optics* **54**, 2459 (2007).
- [50] T. Abi-Salloum, *Journal of Modern Optics* **57**, 1366 (2010).
- [51] H. S. Rawat, S. K. Dubey, and V. N. Ojha, *J. of Phys. B* **51**, 155401 (2018).
- [52] H. Wu, Y. Ruan, Z. Li, M. Dong, M. Cai, J. Tang, L. Tang, H. Zhang, M. Xiao, and K. Xia, *Laser and Photonics Reviews* **16**, 10.1002/lpor.202100708 (2022).
- [53] Z. Ji, Y. Jiao, Y. Xue, L. Hao, J. Zhao, and S. Jia, *Optics Express* **29**, 11406 (2021).

- [54] L. Giner, L. Veissier, B. Sparkes, A. S. Sheremet, A. Nicolas, O. S. Mishina, M. Scherman, S. Burks, I. Shomroni, D. V. Kupriyanov, P. K. Lam, E. Giacobino, and J. Laurat, *Phys. Rev. A* **87**, 013823 (2013).
- [55] H. Lee, Y. Rostovtsev, and M. O. Scully, *Phys. Rev. A* **62**, 063804 (2000).
- [56] E. O. Nyakang'o, D. Shylla, K. Indumathi, and K. Pandey, *The European Physical Journal D* **74**, 187 (2020).
- [57] A. W. Laskar, P. Adhikary, N. Singh, and S. Ghosh, *J. Opt. Soc. Am. B* **41**, 29 (2024).
- [58] L. Margerin, M. Campillo, and B. A. van Tiggelen, *Geophysical Journal International* **145**, 593 (2001).
- [59] M. Segev, Y. Silberberg, and D. N. Christodoulides, *Nature Photonics* **7**, 197 (2013).
- [60] P. W. Anderson, *Phys. Rev.* **109**, 1492 (1958).
- [61] K. M. Yoo, G. C. Tang, and R. R. Alfano, *Appl. Opt.* **29**, 3237 (1990).
- [62] M. Safadi, O. Lib, H. C. Lin, C. W. Hsu, A. Goetschy, and Y. Bromberg, *Nature Physics* **19**, 562 (2023).
- [63] G. Jacucci, O. D. Onelli, A. D. Luca, J. Bertolotti, R. Sapienza, and S. Vignolini, *Interface Focus* **9**, 20180050 (2019).
- [64] N. M. Estakhri, N. M. Estakhri, and T. B. Norris, *Scientific Reports* **12**, 22256 (2022).
- [65] P. H. Moriya, R. F. Shiozaki, R. C. Teixeira, C. E. Máximo, N. Piovella, R. Bachelard, R. Kaiser, and P. W. Courteille, *Phys. Rev. A* **94**, 053806 (2016).
- [66] E. E. Gorodnichev, K. A. Kondratiev, and D. B. Rogozkin, *Phys. Rev. B* **105**, 104208 (2022).
- [67] P. Hank, F. Foschum, S. Geiger, and A. Kienle, *J. Quant. Spectrosc. Radiat. Transfer* **287**, 108230 (2022).
- [68] T. Vaisanen, A. Penttila, J. Markkanen, and K. Muinonen (IEEE, 2016) pp. 396–399.
- [69] V. M. Datsyuk and I. M. Sokolov, *Journal of Experimental and Theoretical Physics* **102**, 724 (2006).

- [70] E. Akkermans, P. E. Wolf, and R. Maynard, *Phys. Rev. Lett.* **56**, 1471 (1986).
- [71] V. N. Shatokhin, R. Blattmann, T. Wellens, and A. Buchleitner, *Phys. Rev. A* **90**, 023850 (2014).
- [72] R. Lenke and G. Maret, *Eur. Phys. J. B* **17**, 171 (2000).
- [73] G. Labeyrie, F. de Tomasi, J.-C. Bernard, C. A. Müller, C. Miniatura, and R. Kaiser, *Phys. Rev. Lett.* **83**, 5266 (1999).
- [74] G. Labeyrie, C. A. Müller, D. S. Wiersma, C. Miniatura, and R. Kaiser, *J. Opt. B: Quantum Semiclass* **2**, 672 (2000).
- [75] O. Sigwarth, G. Labeyrie, T. Jonckheere, D. Delande, R. Kaiser, and C. Miniatura, *Phys. Rev. Lett.* **93**, 143906 (2004).
- [76] D. Wilkowski, Y. Bidet, T. Chanelière, R. Kaiser, B. Klappauf, G. Labeyrie, C. Müller, and C. Miniatura, *Physica B: Condensed Matter* **328**, 157 (2003).
- [77] P. B. Kulatunga, Ph.D. thesis, Old Dominion University (2002).
- [78] D. V. Kupriyanov, I. M. Sokolov, P. Kulatunga, C. I. Sukenik, and M. D. Havey, *Phys. Rev. A* **67**, 013814 (2003).
- [79] D. V. Kupriyanov, I. M. Sokolov, N. V. Larionov, P. Kulatunga, C. I. Sukenik, S. Balik, and M. D. Havey, *Phys. Rev. A* **69**, 033801 (2004).
- [80] P. Kulatunga, C. I. Sukenik, S. Balik, M. D. Havey, D. V. Kupriyanov, and I. M. Sokolov, *Phys. Rev. A* **68**, 033816 (2003).
- [81] S. Balik, P. Kulatunga, C. I. Sukenik, M. D. Havey, D. V. Kupriyanov, and I. M. Sokolov, *Journal of Modern Optics* **52**, 2269 (2005).
- [82] D. V. Kupriyanov, I. M. Sokolov, C. I. Sukenik, and M. D. Havey, *Laser Physics Letters* **3**, 223 (2006).
- [83] I. Sokolov, D. Kupriyanov, and M. Havey, *Journal of Modern Optics* **58**, 1928 (2011).
- [84] R. Loudon, *The Quantum Theory of Light*, 3rd ed. (Oxford University Press, 2000).
- [85] H. J. Metcalf and P. van der Straten, *Laser Cooling and Trapping* (Springer, 2001).

- [86] D. A. Steck (2008), *Rubidium 85 D Line Data* (ver. 2.3.2), [Online]. Available: <http://steck.us/alkalidata> [2016, August 1].
- [87] K. Fujii, *Journal of Modern Physics* **08**, 2042 (2017).
- [88] E. Akkermans and G. Montambaux, *Mesoscopic Physics of Electrons and Photons* (Cambridge University Press, 2007).
- [89] E. Akkermans, C. Miniatura, and C. A. Müller, arXiv:cond-mat/0206298 (2002).
- [90] E. Robertson, N. Šibalić, R. Potvliege, and M. Jones, *Comput. Phys. Commun.* **261**, 107814 (2021).
- [91] C. H. Greene and R. N. Zare, *Annual Review of Physical Chemistry* **33**, 119 (1982).
- [92] B. Jones, Ph.D. thesis, Old Dominion University (2024).
- [93] D. Doweck and P. Decleva, *Physical Chemistry Chemical Physics* **24**, 24614 (2022).

APPENDIX A

OTHER OPTICAL BLOCH NUMERICAL SOLUTIONS

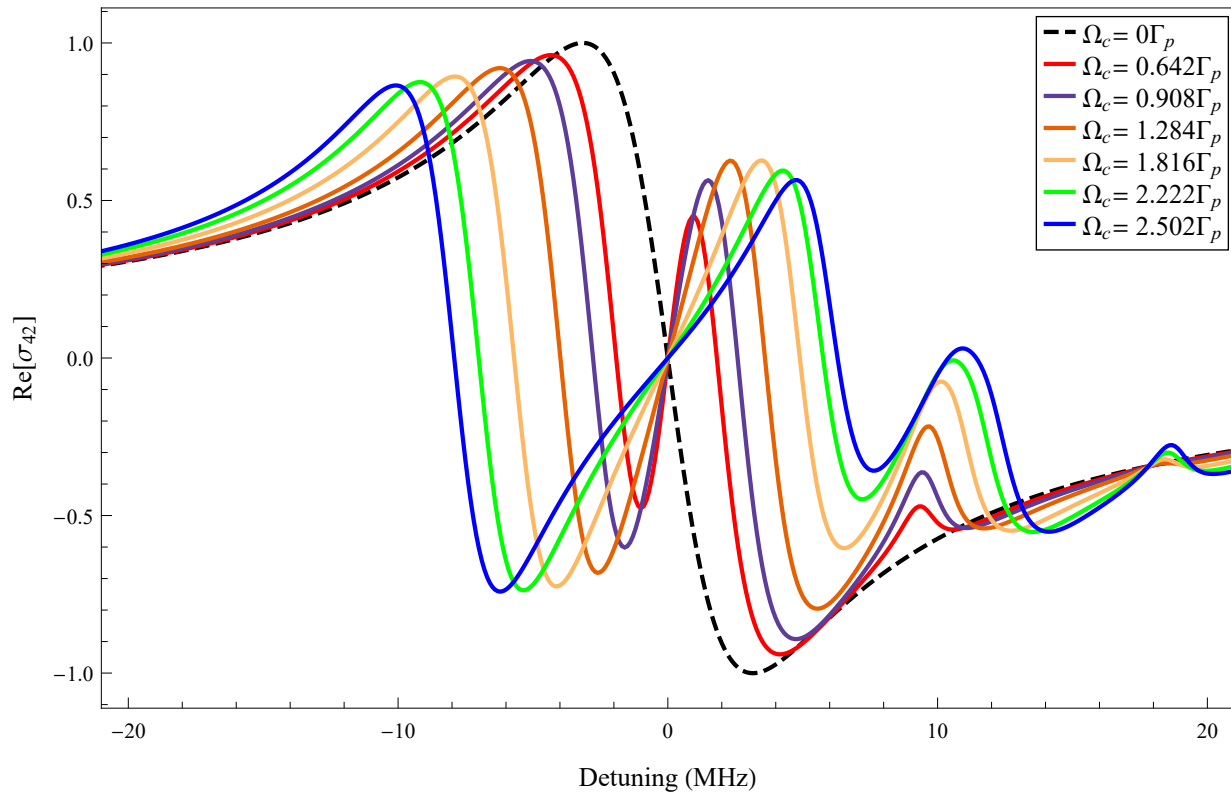


FIG. 93: $\text{Re}[\sigma_{42}]$ as a function of probe detuning at various control Rabi frequencies with $\Delta_c = 0$. Probe Rabi frequency $\Omega_p = 0.18\Gamma_p$.

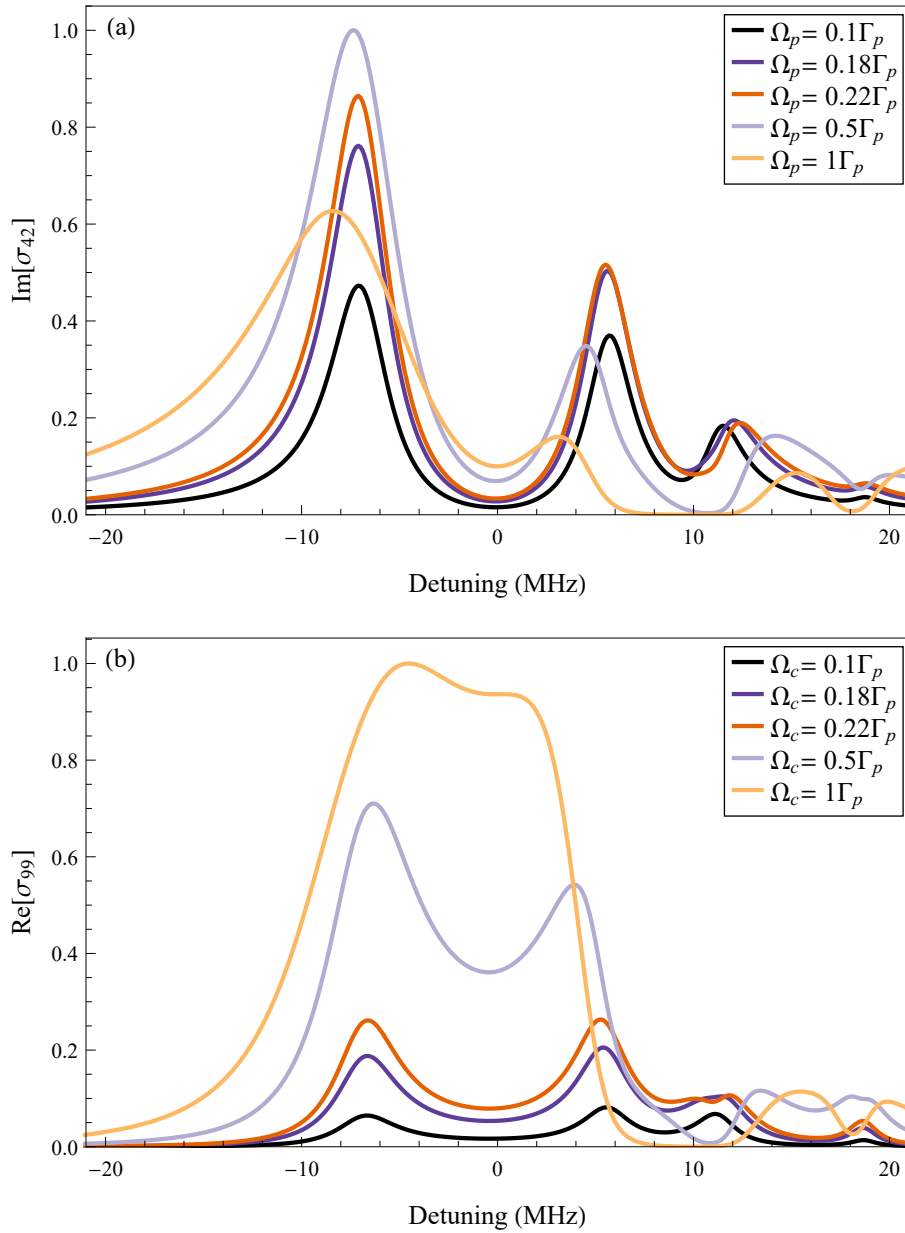


FIG. 94: (a) Numerical solution of $\text{Im}[\sigma_{42}]$ as a function of probe detuning at various probe intensities with $\Delta_c = 0$ and $\Omega_c = 2.22\Gamma_p$. Simulated fluorescence of the $6P_{3/2}$ state ($\text{Re}[\sigma_{99}]$) as a function of probe detuning at various probe intensities with $\Delta_c = 0$ and $\Omega_c = 2.22\Gamma_p$.

APPENDIX B

OPTICAL DIAGRAM LEGEND


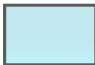









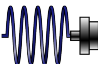

	Wave Plate		Vapor Cell
	Polarizer		Optical Isolator
	Beam Splitter Cube		Lenses
	Beam Splitter		Laser Source
	Mirror		Acousto-Optic Modulator
	Beam Block		Fiber Optic Cable with Coupler
	Iris		

FIG. 95: Legend for optical diagrams used in this dissertation.

VITA

Joshua D. Carter
 Department of Physics
 Old Dominion University
 Norfolk, VA 23529

EDUCATION

Ph. D. Physics, *Coherent Backscattering Under Conditions of Electromagnetically Induced Transparency in Ultracold ^{85}Rb* , Old Dominion University, Norfolk, VA, August 2024. **Advisor:** Dr. Charles Sukenik
M.S. Physics, Old Dominion University, Norfolk, VA, May 2018.
B.S. Physics, Old Dominion University, Norfolk, VA, August 2016.

PUBLICATIONS

Atom Counting by Hyperfine Raman Optical Pumping in Cold ^{87}Rb , J. D. Carter, B. M. Jones, S. J. Roof, K. J. Kemp, M. D. Havey, DAMOP 2019 Milwaukee, Wisconsin.
Coherent Backscattering Under Conditions of Electromagnetically Induced Transparency in ^{85}Rb , J. D. Carter, B. M. Jones, C. I. Sukenik, M. D. Havey, In preparation.
Observation of Cooperative Subradiance in Dense Atomic ^{87}Rb Ensembles, B. M. Jones, J. D. Carter, C. I. Sukenik, M. D. Havey, In preparation.
Raman Scattering and Atom Counting in Cold Rubidium Gas, B. M. Jones, J. D. Carter, M. D. Havey, C. I. Sukenik, In preparation.

AFFILIATIONS

Physics Graduate Student Association

Typeset using L^AT_EX.